

Energy and Charge Transfer in Donor- Acceptor Substituted Hexaarylbenzenes



Dissertation zur Erlangung des
naturwissenschaftlichen Doktorgrades
der Julius-Maximilians-Universität Würzburg

vorgelegt von
Markus Steeger
aus Groß-Umstadt

Würzburg 2015

Eingereicht bei der Fakultät für Chemie und Pharmazie am

Gutachter der schriftlichen Arbeit

1. Gutachter: _____

2. Gutachter: _____

Prüfer des öffentlichen Promotionskolloquiums

1. Prüfer: _____

2. Prüfer: _____

3. Prüfer: _____

Datum des öffentlichen Promotionskolloquiums

Doktorurkunde ausgehändigt am

Die experimentellen Arbeiten wurden von Oktober 2008 bis März 2014 am Institut für Organische Chemie der Universität Würzburg durchgeführt.

Mein besonderer Dank gilt

Herrn Prof. Dr. Christoph Lambert

für die Möglichkeit dieses faszinierende Thema zu erforschen, die anregenden Diskussionen und die immerwährende Hilfsbereitschaft und Unterstützung

Content

1. Introduction	1
2. Scope of the work	1
3. Theory	5
3.1. Charge transfer theory	5
3.1.1. <i>Marcus</i> theory and the adiabatic solvent-controlled limit	6
3.1.2. <i>Jortner</i> Theory.....	8
3.1.3. <i>Mulliken-Hush</i> theory	12
3.1.4. Bridge effects	13
3.2. Energy transfer	16
3.2.1. Weak coupling limit	17
3.2.1.1 Coulomb interactions.....	18
3.2.1.2 Electron exchange interactions.....	21
3.2.2. Strong coupling limit.....	23
3.3. Ultrafast spectroscopy	25
3.3.1. Measurement setups	25
3.3.1.1 Fluorescence upconversion	26
3.3.1.2 Transient absorption	29
3.3.2. Nonlinear optical processes.....	35
3.3.2.1 Second order nonlinear effects	36
3.3.2.2 Uniaxial crystals	39
3.3.2.3 Third order nonlinear effects	44
3.3.3. Polarisation/Anisotropy	51
3.3.4. Devices to change the polarisation characteristics of light beams	59
3.3.5. Measurement issues.....	62
3.3.5.1 Fluorescence upconversion	62
3.3.5.2 Transient absorption	65
4. Multidimensional chromophores containing PCTMs	68
4.1. Introduction	68

4.2.	Synthesis.....	68
4.3.	Electrochemistry.....	73
4.4.	Electron paramagnetic resonance.....	75
4.5.	Absorption spectroscopy.....	79
4.6.	Spectroelectrochemistry.....	85
4.7.	Transient absorption spectra.....	91
4.8.	Transient absorption anisotropy measurement.....	100
4.9.	Conclusion.....	106
5.	Hexaarylbenzenes containing TABs	111
5.1.	Introduction.....	111
5.2.	Synthesis.....	112
5.3.	Electrochemistry.....	113
5.4.	Absorption and emission spectroscopy.....	116
5.5.	Time-resolved fluorescence spectroscopy.....	118
5.6.	Transient absorption spectroscopy.....	119
5.7.	Steady-state fluorescence anisotropy spectroscopy.....	122
5.8.	Titration with fluoride.....	123
5.9.	Ultrafast TA and FUC measurements.....	130
5.9.1.	Model compound B3	130
5.9.2.	HABs B1 and B2	137
6.	Hexaarylbenzene containing squaraine chromophores	149
6.1.	Introduction.....	149
6.2.	Retrosynthetic analysis.....	149
6.3.	Synthesis.....	153
6.3.1.	Attempted synthesis of S2b (pathway III).....	153
6.3.2.	Synthesis of S2a (pathway IV).....	154
6.3.3.	Attempted synthesis of S1a (pathway I).....	156
6.3.4.	Attempted synthesis of S3 (pathway II).....	157
6.3.5.	Synthesis of model compound S20	157
6.4.	Absorption spectroscopy.....	158

7. Summary	160
8. Experimental section	163
8.1. Methods	163
8.2. Synthesis	167
9. Literature	191
10. Table of formulas	204
11. Zusammenfassung	208
12. Appendix 1	211
13. Appendix 2	221
14. Appendix 3	225
15. Appendix 4	231
16. Appendix 5	234

ABBREVIATIONS

BBO	beta-barium borate
CARS	coherent anti- <i>Stokes-Raman</i> scattering
CSRS	coherent <i>Stokes-Raman</i> scattering
CMOS	Complementary metal-oxide-semiconductor
CT	charge transfer
CV	cyclic voltammetry
DFG	difference frequency generation
DPV	differential pulse voltammetry
DSC	differential scanning calorimetry
EA	ethyl acetate
EN	energy transfer
ESI	electrospray ionisation
Fc	ferrocene
FES	free energy surface
FUC	fluorescence upconversion
GMH	generalised <i>Mulliken-Hush</i>
GPC	gel permeation chromatography
IRF	instrument response function
IV-CT	intervalence charge transfer
KDP	potassium dihydrogen phosphate
lp	long-pass
MALDI	matrix assisted laser desorption/ionisation
MV	mixed valence
ND	neutral density
OD	optical density
PE	petrol ether
PMT	photomultiplier tube
SFG	sum frequency generation

SHG	second harmonic generation
SOA	sucrose octaacetate
SWV	square wave voltammetry
TAA	triarylamine
TAB	triarylborane
TDSS	time dependent spectral shift
TS	transition state
TBAHFP	tetrabutylammonium hexafluorophosphate
THF	tetrahydrofurane
TIR	total internal reflection
WLC	white light continuum

COPYRIGHTS REMARKS

Parts of this thesis have already been published in the following articles:

Charge-Transfer Interactions in Tris-Donor–Tris-Acceptor Hexaarylbenzene Redox Chromophores, M. Steeger and C. Lambert, *Chem. Eur. J.*, **2012**, *18*, 11937-11948.

On the relation of Energy Transfer Between IV-CT States and Electron Transfer Between Redox Centres in Multidimensional Chromophores Based on Polychlorinated Triphenylmethyl Radicals and Triarylaminines, M. Steeger, S. Griesbeck, A. Schmiedel, M. Holzapfel, I. Krummenacher, C. Lambert and H. Braunschweig, *Phys. Chem. Chem. Phys.*, **2015**, submitted.

1. Introduction*

Energy transfer is an extensively investigated phenomenon particularly in regard to the natural light-harvesting process.¹⁻⁴ Accordingly, both natural⁵⁻⁸ and artificial⁹⁻¹⁸ antenna systems were examined to gain insight into the energy transfer mechanisms and their dependencies on electronic and geometric variables. There are generally two ways chromophores can interact with each other to exchange energy. First, “through bond” exchange of two electrons and second, Coulomb interactions where there is no formal electron exchange between the chromophores.¹ The former “through bond” energy transfer mechanism is strongly related to the concept of charge transfer. Hence, some relevant variables like the conjugation of the bridge connecting the two chromophores/redox centres play an essential role in both mentioned processes. In order to investigate this correlation the theories of energy and charge transfer are discussed in detail in the theory section. But for a better understanding of these topics, first the aim of this thesis is presented.

2. Scope of the work*

In this work energy transfer (EN) between charge transfer (CT = charge transfer between redox centres) states shall be investigated in multidimensional chromophores. In these chromophores, optically induced charge transfer between two different redox centres *via* a connecting bridge is possible which, after electron transfer, leads to a reduced and an oxidised redox centre. The main focus lies on the influence of the charge transfer parameters on associated energy transfer properties. In order to do so homogeneous energy transfer between IV-CT states shall be examined in which the “through-bond” interaction pathways of energy transfer coincide with the IV-CT interactions. This is the case if the two IV-CT states transferring energy share one redox centre (see Figure 1).

*Parts of this section have already been published in M. Steeger and C. Lambert, *Chem. Eur. J.*, **2012**, **18**, 11937-11948 and M. Steeger, S. Griesbeck, A. Schmiedel, M. Holzapfel, I. Krummenacher, C. Lambert and H. Braunschweig, *Phys. Chem. Chem. Phys.*, **2015**, submitted.

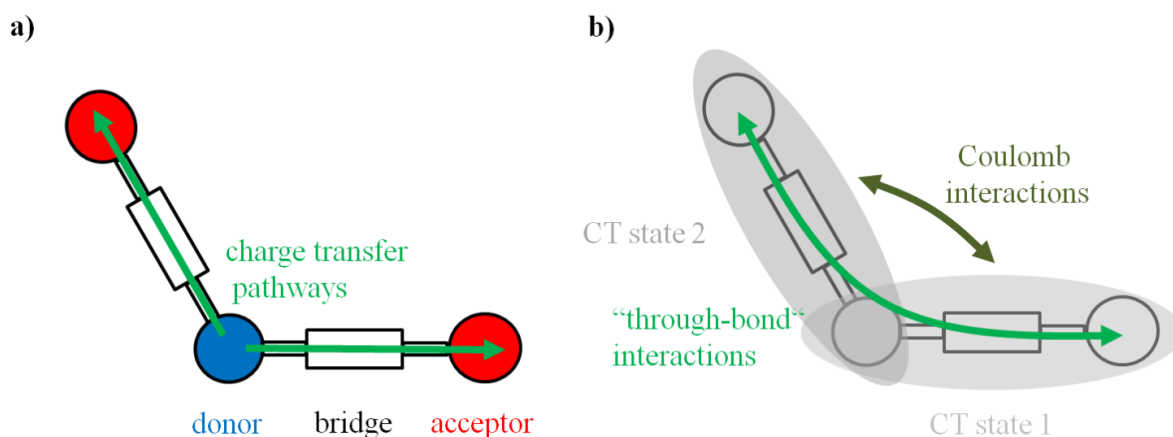


Figure 1 a) Charge transfer pathways and b) energy transfer interactions in a multidimensional system consisting of three redox centres.

Thus, the “through-bond“ energy transfer process shall be treated by conventional electron transfer theory and insights how to control electron transfer processes should be directly adaptive to the energy transfer process. Furthermore, the examination of IV-CT states has the advantage that the transition moment directions of the IV-CT transitions are known to be parallel to the electron donor-acceptor vector. This facilitates the analysis of dipole-dipole interactions and therewith the discrimination between the Coulomb and “through bond” mechanisms.

For the EN investigations both the redox centres as well as the bridge connecting the redox centres shall be altered providing varying degree of interaction (see Figure 2). This shall be achieved by synthesising one set of compounds based on the hexaarylbenzene (HAB) framework, which allows the symmetric (**HAB-S** and **B1**) and asymmetric (**HAB-A** and **B2**) covalent linkage of three electron donor and three electron acceptor centres. These multidimensional molecules adopt a propeller like arrangement^{12,19-21} to minimise sterical repulsion of the six π -systems. In this respect through space interactions and direct p_z -orbital overlap are made responsible for a weak electronic coupling between neighbouring branches.¹⁹ Due to its geometric and electronic properties the HAB framework has been in focus of several energy^{13,14,21-23} and electron transfer^{12,20,24-30} studies. Moreover, a HAB substituted with six squaraine chromophores (**S1a/b**) shall be synthesised. Squaraines can be in general regarded as donor-acceptor-donor structures with the charge density completely delocalised throughout the whole system. They show a strong absorption band in the red to NIR region which should facilitate the EN by Coulomb interactions. In the other set of compounds, the star-like framework with tolan bridging units (**Star**) shall provide a much better electronic communication between the central electron acceptor and the three surrounding donor groups.³¹ Triarylamines (TAA) shall be used in all cases as electron donors as they are easily oxidisable and have a very low internal reorganization energy.³² Therefore, TAAs are attractive candidates for hole transport materials in optoelectronic applications.³³⁻⁴² Either triarylboranes (TAB) or polychlorinated triphenylmethyl radicals (PCTM) shall be used as electron acceptors.⁴³ In order to discriminate pure charge transfer characteristics from

energy transfer processes in the multidimensional systems **HAB-S(A)**, **B1(B2)** and **Star**, three model compounds (**HAB-Model**, **B3** and **Star-Model**) shall be synthesised in which only a single charge transfer pathway is possible (Figure 2).

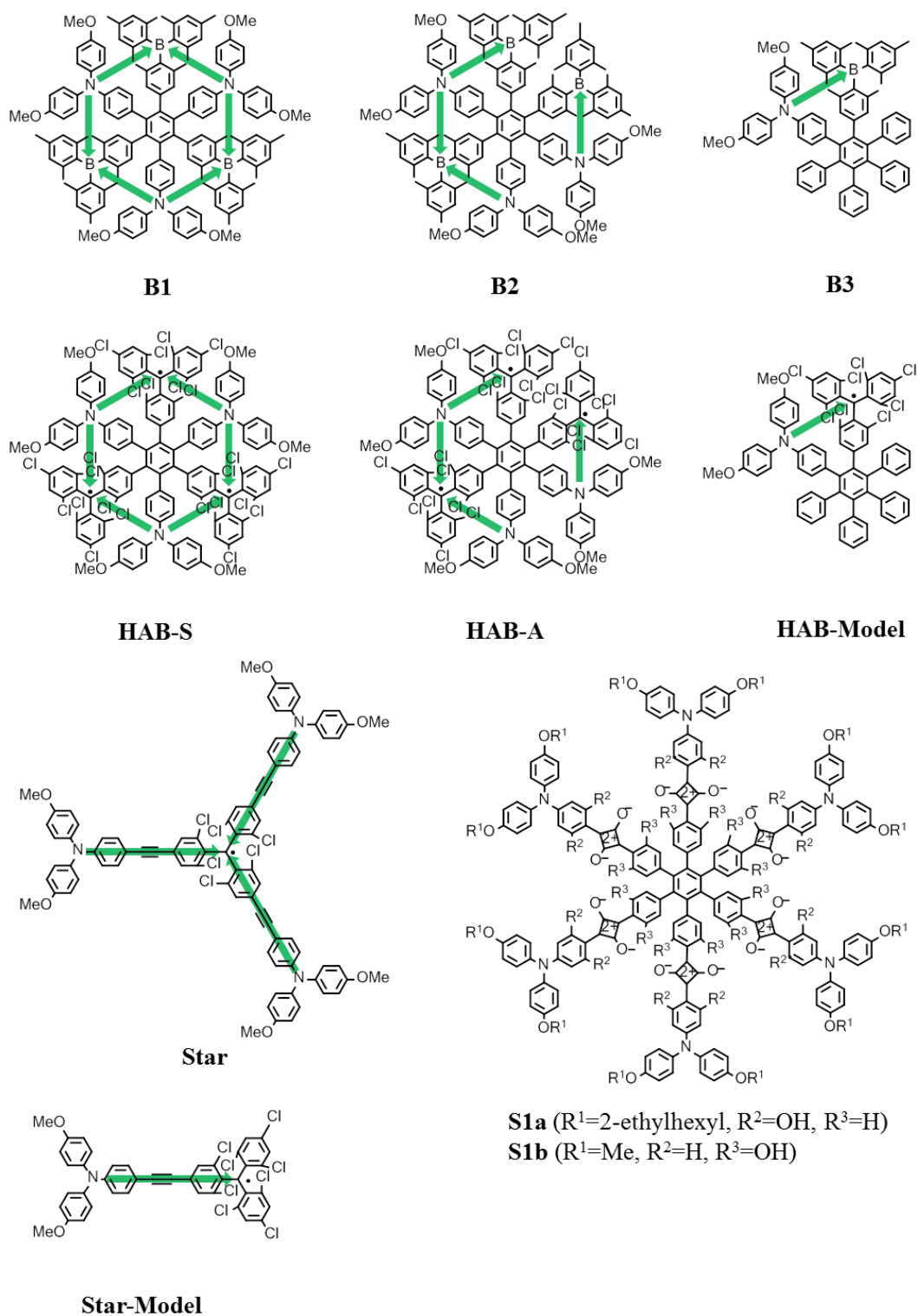


Figure 2 Possible IV-CT pathways (green arrows) in **B1**, **B2** and **B3**, in **HAB-S**, **HAB-A** and **HAB-Model** and in **Star** and **Star-Model**. In addition, **S1a/b** is depicted consisting of six squaraine chromophores.

The electronic interactions between electron donor and acceptor centres shall be investigated by electrochemistry, EPR spectroscopy and by optical methods such as steady-state absorption, steady-state fluorescence, spectroelectrochemistry and isotropic transient absorption and fluorescence upconversion measurements. Energy transfer shall be monitored by anisotropic transient absorption spectroscopy, anisotropic fluorescence upconversion measurements and anisotropic steady-state fluorescence spectroscopy.

3. Theory

To address the relationship between energy and charge transfer their theoretical background shall be reviewed in the following. Moreover, insights into the experimental characterisation of charge and energy transfer by fluorescence upconversion and ultrafast transient absorption spectroscopy will be provided.

3.1. Charge transfer theory

Intramolecular charge transfer (CT) from an electron rich to an electron poor redox centre can either be described by transitions between or motions on free energy surfaces (FESs).^{31,44} With FESs the free energy of the whole electron donor-acceptor system, including the solvent environment, is given as a function of the reaction coordinate q (Figure 3).

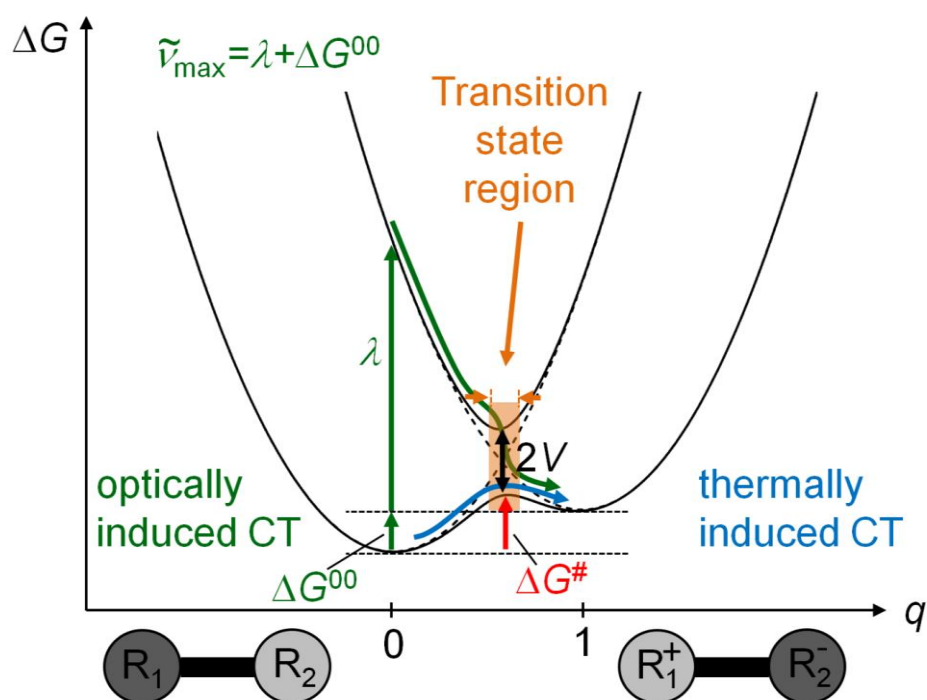


Figure 3 Diabatic (dashed) and adiabatic (solid line) free energy surfaces (FESs) of an electron donor-acceptor compound. The optically induced (green) and thermally induced (blue) charge transfers are shown.

The FESs can be treated either diabatically or adiabatically. This distinction is introduced by the quantumchemical description of charge transfer. In general, the total Hamiltonian of the system H can be divided into a zeroth-order part H_0 and a perturbation term V . With the zeroth-order part H_0 the situations in which the charge to be transferred is either completely localised at the electron donor (reactant state) or at the electron acceptor redox centres (product state) are described. The diabatic

FESs are the *Born-Oppenheimer* approximated solutions to the zeroth-order part H_0 . For reactant and product state a single FES is obtained. These FESs are displaced along the reaction coordinate and intersect in the transition state (TS) region. The transition between reactant and product state is enabled by the electronic coupling term V . In contrast, the adiabatic FESs are the *Born-Oppenheimer* approximated solutions to the entire Hamiltonian H and can be obtained by linear combination of the diabatic states coupled by V . Due to the electronic coupling the adiabatic FESs show no intersection but a splitting by about $2V$. As a result, an upper and a lower adiabatic FES is obtained with the local minima of the lower adiabatic FES representing the reactant and product states. The displacement on the q coordinate between these states can be rationalised by the change of the solvent position and orientation as well as intramolecular bond lengths and angles due to the oxidation and reduction of the respective redox centres. In general, a large number of nuclear coordinates is needed to describe all these processes. Therefore a theoretical treatment of all the coordinates is impossible. Hence, these nuclear coordinates are combined in the reaction coordinate q . One way to do this shall be described in the following. For each nuclear coordinate setting the diabatic free energy of the product and reactant states is given by the respective multidimensional, diabatic FESs. Moreover, there is a specific vertical energy gap between these two FESs for each setting. The coordinate system can be simplified when defining the reaction coordinate q by this vertical energy gap between the multidimensional, diabatic FESs of product and reactant.⁴⁴ This means, each position at the reaction coordinate q corresponds to a huge number of nuclear coordinate settings which feature all the same beformentioned energy gap. Accordingly, a change in q corresponds therewith to a complex change of the intramolecular and solvent coordinates.

3.1.1. Marcus theory and the adiabatic solvent-controlled limit

Charge transfer can be either thermally or optically induced. Following the *Frank-Condon* principle, electron motion is much faster than nuclear motion, so that the optically induced charge transfer occurs from the minimum of the reactant state vertically to the product FESs, whereas the thermally induced charge transfer can occur only in the TS region. In this region the nuclear momenta and the free energy of the system are nearly conserved. As a result, in the case of thermally induced charge transfer, the system has to move along the reaction coordinate to the TS region, resulting in an activation barrier. The barrier height can be estimated by parameters for the optically induced charge transfer using simple geometric considerations. In the diabatic limit the FESs for reactant and product can be approximated by quadratic functions of q with equal shape. Accordingly, the free energy of activation ΔG^\ddagger can be calculated by the intersection point of the two parabolas (equation 1).

$$\Delta G^\ddagger = \frac{(\Delta G^{00} + \lambda)^2}{4\lambda} \quad \text{with } \lambda = \lambda_o + \lambda_v \quad (1)$$

The free energy difference between the minima of the reactant and product states is represented by ΔG^{00} and λ is the reorganisation energy which is composed of the inner and outer reorganisation energies λ_v and λ_o , respectively. The free energies λ_v and λ_o are accounting for the intramolecular and solvent coordinate changes in the optically induced charge transfer process, respectively, and $\Delta G^{00} + \lambda$ is the total energy needed to optically induce the charge transfer. While λ_v cannot be calculated in a simple manner, λ_o can be estimated within the dielectric continuum model by equation 2.^{31,44,45}

$$\lambda_o = \frac{e^2}{4\pi\epsilon_0} \left[\frac{1}{2r_+} + \frac{1}{2r_-} - \frac{1}{d} \right] \left[\frac{1}{n^2} - \frac{1}{D} \right] \quad (2)$$

The radii of the electron donor and electron acceptor redox centres r_{\pm} are assumed to be spherical. The distance between these redox centres is represented by d . The solvent continuum is described by its refractive index n , permittivity D and the dielectric constant ϵ_0 . In the adiabatic case, the free energy of activation $\Delta G^{\#}$ is reduced in comparison to the diabatic limit. This is a result of the FES splitting in the TS region and due to resonance delocalisation of the adiabatic ground state. If a degenerate charge transfer is considered ($\Delta G^{00} = 0$), $\Delta G^{\#}$ can be calculated by equation 3.³¹

$$\Delta G^{\#} = \frac{\lambda}{4} - V + \frac{V^2}{\lambda} \quad (3)$$

Motion on the FESs can be considered as both intramolecular and solvent fluctuations which alter the free energy of the electron donor-acceptor system. However, the overall free energy remains unchanged due to energy exchange with the bath. Although the system resides predominantly near the minimum of the reactant FES, the mentioned fluctuations can push the system across the activation barrier to the intersection point of the diabatic reactant and product FESs. In this TS region the charge transfer process may occur with a given probability, so the system changes from the diabatic reactant to the diabatic product FESs or crosses the peak in the adiabatic lower FES. Afterwards, the system relaxes to the minimum of the product FES by dispensing free energy to the bath. The rate constant of charge transfer k is therefore governed by the barrier height given by $\Delta G^{\#}$, the probability to change the state P when the system is in the TS region, and the motion on the FESs. The probability P can be rationalised by the time the system needs to cross the TS region, compared to the time the system needs to change from the reactant to the product state. In the diabatic regime, the change of states is slow regarding the motion through the TS region. Accordingly, the system remains most of the time on the reactant FESs when crossing the TS region. Thus, the probability for the transition from the reactant to the product state P is low. On that account, the overall charge transfer is limited by P , which in turn is proportional to the square of the electronic coupling element V^2 . In the diabatic limit $hcV < kT$, the rate constant of charge transfer k_{na} (na = non-adiabatic) can thus be described by the Arrhenius-type equation 4 formulated by Marcus,⁴⁶⁻⁴⁹

$$k_{\text{na}} = 4\pi^2 hc^2 \frac{1}{\sqrt{4\pi hc \lambda k_b T}} V^2 \exp\left(-\frac{hc(\lambda + \Delta G^{00})^2}{4\lambda k_b T}\right) \quad (4)$$

where k_b is the *Boltzmann* constant, c the speed of light in vacuum, h the *Planck* constant and T the temperature. In contrast, if the system remains long enough in the TS region so that a transition of states certainly occurs when the TS region is reached, the rate constant depends no more on P . The system will leave the TS region always on the product FESs for energetic reasons marking this reaction adiabatic. In this case the rate constant is limited by the motion on the FESs escaping the TS region.⁵⁰ This time dependent relaxation process is presumably governed mainly by the longitudinal dielectric relaxation time of the solvent τ_1 , characterising its response to an added charge.⁴⁴ In this limiting case the charge transfer is thus a solvent-controlled, adiabatic process. By measuring time dependent spectral shifts (TDSS) of the absorption or fluorescence of specific probe molecules, τ_1 can be obtained experimentally.⁵¹ Values for τ_1 range from 250 fs to 50 ps.⁴⁴ As non-exponential decays can in general be observed in these TDSS experiments, it is often not obvious which component of the decays can be attributed to τ_1 . Furthermore, it is under discussion if very fast inertial motion of the solvents ($\tau_1 < 300$ fs) is constituting to the relaxation.⁴⁴ Nevertheless, the respective rate constant $k_{\text{sc-ad}}$ is given by equation 5, which shows that $1/\tau_1$ represents the upper limit to charge transfer.

$$k_{\text{sc-ad}} = \sqrt{\frac{hc\lambda}{16\pi k T}} \frac{1}{\tau_1} \exp\left(-\frac{hc(\lambda + \Delta G^{00})^2}{4\lambda k_b T}\right) \quad (5)$$

In several cases (e.g. in intramolecular systems with a twisted charge transfer state), charge transfer rates faster than the upper limit $1/\tau_1$ were observed.⁴⁴ It may be assumed that in these cases charge transfer is coupled to very fast solvent relaxation processes, which could not be measured.⁴⁴

To describe the charge transfer rate constant k in the intermediate situation the limiting cases of diabatic and solvent controlled adiabatic charge transfer (equation 4 and equation 5) are interpolated to equation 6.

$$k = \frac{1}{1 + \kappa} k_{\text{na}} \quad \text{with} \quad \kappa = \frac{8\pi^2 c V^2}{\lambda} \tau_1 \quad (6)$$

When the electronic coupling V is strong and/or the solvent relaxation time τ_1 long, the adiabaticity parameter κ can be much larger than unity, $\kappa \gg 1$, so that equation 6 simplifies to equation 5, which is independent on V . In the opposite situation, if $\kappa \ll 1$, the diabatic equation 4 is obtained.

3.1.2. Jortner Theory

If high energy intramolecular vibrations can be excited, the intramolecular degrees of freedom can be treated quantumchemically, as shown by *Bixon* and *Jortner*.⁵² This is possible, because large amounts

of energy can be released to the surrounding environment (bath) by the high energy vibrations. This theory is restricted to the diabatic case with $hcV < kT$. In general, it is sufficient to treat the intramolecular high energy vibrations by a single averaged molecular vibration mode $\tilde{\nu}_v$. Within the framework of the *Marcus* theory both the inner and outer reorganisation energies are treated classical. On that account, they are described by the position and momentum on the FESs. *Bixon* and *Jortner* kept this description for the low energy solvent vibrations, but they treated the intramolecular degrees of freedom as discrete vibronic quantum states. If $\hbar c\tilde{\nu}_v \gg kT$ is valid, only the vibronic ground state of the reactant state is populated. The overall charge transfer rate k is now calculated by the sum of all the charge transfer rates from the reactant vibronic ground state to the j -th product vibronic state. Hence, the electronic coupling element V has to be extended by the vibronic overlap matrix element $\langle 0|j\rangle$, which can be considered as a *Frank-Condon* factor for the transition between the vibronic states. The square of the matrix element $\langle 0|j\rangle$ can be represented by a *Poisson* distribution incorporating the *Huang-Rhys* factor S . As a result the diabatic charge transfer rate k_{na} can be calculated according to *Bixon* and *Jortner* by equation 7.

$$k_{na} = 4\pi^2 hc^2 \sqrt{\frac{1}{4\pi\hbar c\lambda_o k_b T}} \sum_{j=0}^{\infty} V^2 \langle 0|j\rangle^2 \exp\left(-\frac{hc(j\tilde{\nu}_v + \lambda_o + \Delta G^{00})^2}{4\lambda_o k_b T}\right) \quad (7)$$

$$\text{with } \langle 0|j\rangle^2 = \frac{e^{-S} S^j}{j!} \text{ and } S = \frac{\lambda_v}{\tilde{\nu}_v}$$

If equation 7 is substituted into equation 6 the rate constant for the intermediate case is obtained (equation 8).⁵²

$$k = 4\pi^2 hc^2 \sqrt{\frac{1}{4\pi\hbar c\lambda_o k_b T}} \sum_{j=0}^{\infty} \frac{V^2 \langle 0|j\rangle^2 \exp\left[-\frac{hc(j\tilde{\nu}_v + \lambda_o + \Delta G^{00})^2}{4\lambda_o k_b T}\right]}{1 + \kappa \langle 0|j\rangle^2} \quad (8)$$

$$\text{with } \kappa \langle 0|j\rangle^2 = \frac{8\pi^2 c V^2 \langle 0|j\rangle^2 \tau_1}{\lambda_o}$$

Due to the quantumchemical treatment of the intramolecular motion, the theory of *Bixon* and *Jortner* is able to account for nuclear tunneling effects. In general, the activation barrier height is dependent on the mutual position of the reactant and product FESs. This effect is important in the so called *Marcus* inverted region, where the activation barrier rises with increasing ΔG^{00} . In this region the reactant state can intersect with higher vibronic states of the product FESs much nearer to the reactant FES minimum so that the effective activation barrier is decreased (see Figure 4). Thus, the *Bixon-Jortner* theory leads to higher charge transfer rates in the *Marcus* inverted region.

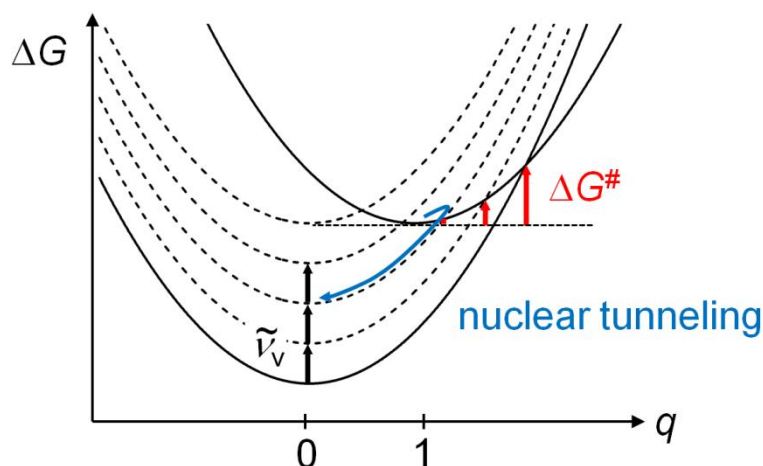


Figure 4 Diabatic reactant and product FESs (line) in the *Marcus* inverted region. The nuclear tunneling occurs from the vibronic ground state of the reactant FES to high energy vibrational levels (dashed) of the product FES with energies $j\tilde{\nu}_v$.

In case the energy of the averaged high energy vibration is in the range or lower than k_bT , it has to be assumed that the reactant state may be vibrational excited. It follows that a charge transfer from a manifold of reactant states to a manifold of product states has to be considered. Similar to the description above, the charge transfer is now calculated by the sum of all charge transfer rates from the i -th reactant vibronic state to the j -th product vibronic state. The associated equations for this charge transfer consideration are much more complex and can be found elsewhere.⁵² By using these equations, nuclear tunneling effects in the *Marcus* normal region (the activation barrier decreases with increasing ΔG^{00}) can be explained (see Figure 5).

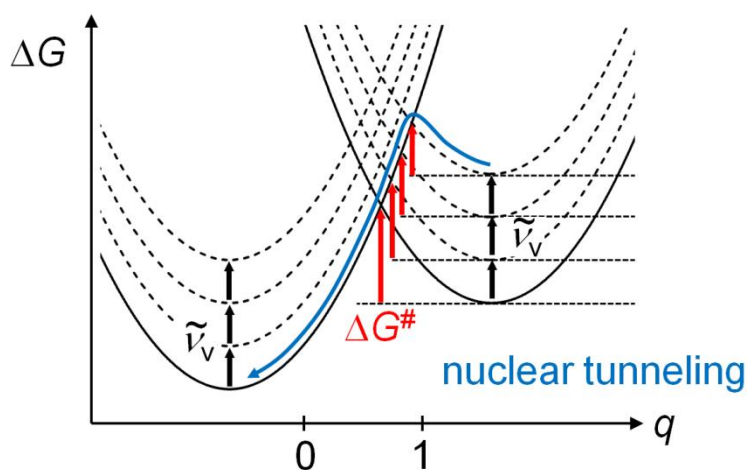


Figure 5 Diabatic reactant and product FESs in the *Marcus* normal region. The nuclear tunneling occurs from high energy vibrational levels (dashed) of the reactant FES to lower energy vibrational levels (dashed) of the product FES.

In the high temperature limit, $\hbar c\tilde{\nu}_v \ll kT$, the influence of the quantumchemical treated high energy vibrations on the charge transfer rate is negligible and thus equation 7 can be reduced to the fully classical treatment described by the *Marcus* theory (equation 4).

To this point it was demonstrated that the thermal charge transfer rates can be calculated by using the parameters V , ΔG^{00} , $\tilde{\nu}_v$, λ_v and λ_o . In the following, possibilities to determine these quantities experimentally, with optical methods, will be shown. This can be done in case the absorption spectrum of the investigated electron donor-acceptor compound shows a band featuring the optical induced charge transfer. With this optical excitation information about the FESs of the product and reactant states is gained, so that the back-charge transfer rates can be calculated using equation 6 or 8. Thereby, it is assumed that the excited state undergoes no geometric reorientations before relaxing to the ground state. If the system can be treated diabatically, with $hcV < kT$, and if $\hbar c\tilde{\nu}_v \gg kT$ so only the vibronic ground state is populated, the charge transfer absorption band can be analysed using equation 9 formulated by *Jortner*,^{53,54}

$$\frac{\varepsilon}{\tilde{\nu}} = \frac{2000N\pi^2}{3\varepsilon_0 \ln 10} \frac{(n^2 + 2)^2}{9n} \mu_{ab}^2 \sqrt{\frac{1}{4\pi\hbar c\lambda_o k_b T}} \sum_{j=0}^{\infty} \frac{e^{-S} S^j}{j!} \exp\left(-\frac{\hbar c(j\tilde{\nu}_v + \lambda_o - \tilde{\nu} + \Delta G^{00})^2}{4\lambda_o k_b T}\right) \quad (9)$$

with ε being the extinction coefficient of the charge transfer absorption band at an absorption energy of $\tilde{\nu}$, μ_{ab} the adiabatic transition moment between the ground and the charge transfer states and ε_0 the dielectric constant. With this equation the optically induced charge transfer is described as solvent broadened transitions from the ground state to *Frank-Condon* weighted vibronic states of the charge transfer state. The vibronic states differ in energy by $\tilde{\nu}_v$. The solvent broadening is represented by a *Gaussian* and the *Frank-Condon* factor $\langle 0|j\rangle^2$ by a *Poisson* distribution. Thereby, the *Huang-Rhys* factor S plays a critical role because it dictates the shape of the *Poisson* distribution. If S is small the charge transfer absorption band is asymmetric. In case S is large, the *Poisson* distribution approaches a *Gaussian* distribution rendering the charge transfer band to be symmetric. Due to ambiguous dependency of the fit parameters, a symmetric charge transfer band cannot be fitted with equation 9. If the *Jortner* theory is performed successfully, values for ΔG^{00} , $\tilde{\nu}_v$, λ_v and λ_o are obtained. The advantage of this approach is that λ_v and λ_o can be determined separately and that this theory is likewise applicable to fluorescence spectra. However, the electronic coupling element V is not directly obtained.

3.1.3. Mulliken-Hush theory

In contrast to the *Jortner* theory, *Mulliken* and *Hush* derived equations to analyse charge transfer absorption bands in the adiabatic limit, $hc\tilde{\nu} > kT$.^{47,55-57} As a result, the transition from the *Boltzmann* weighted vibrational levels of the low-energy minimum of the lower adiabatic FES to the vibrational manifold of the upper FES is described (see Figure 3). The subsequent relaxation process leads from the upper adiabatic FES to the high-energy minimum of the lower adiabatic FES, describing the completion of the charge transfer. Due to the assumption of a *Boltzmann* distribution the high temperature limit, $\hbar c\tilde{\nu} \ll kT$, has to be fulfilled. For this reason, the *Mulliken-Hush* theory can be applied to *Gaussian* shaped charge transfer absorption bands. It should be noted that charge transfer absorption bands may have an asymmetric shape although the high temperature limit is complied. A cut-off at the low energy side can be observed when the limiting transition energy of $2V$ is reached.

To construct adiabatic FESs, the wave functions of the upper and lower adiabatic states Ψ_a and Ψ_b are generated by linear combination of the wavefunctions Ψ_1 and Ψ_2 of the diabatic reactant and product states, respectively (equation 10),

$$\Psi_a = c_1\Psi_1 + c_2\Psi_2 \text{ and } \Psi_b = c_1\Psi_1 - c_2\Psi_2 \quad (10)$$

with c_1 and c_2 being mixing coefficients. To calculate the energies E_a and E_b of the adiabatic states describing the shape of the upper and lower adiabatic FESs, respectively, the secular determinant shown in equation 11 has to be solved.

$$\begin{vmatrix} V_{11} - E & V_{12} \\ V_{12} & V_{22} - E \end{vmatrix} = 0 \quad (11)$$

V_{11} and V_{22} are the energies of the diabatic zeroth-order reactant and product states and V_{12} is the coupling element. Furthermore, the adiabatic transition moment of the optically induced charge transfer μ_{ab} can be represented by equation 12,

$$\mu_{ab} = -e \left\langle \Psi_a \left| \sum r_i \right| \Psi_b \right\rangle \quad (12)$$

with r_i being the vector distance of the i -th electron to the chosen origin. Combining equations 10 – 12, the coupling element V_{12} can be related to μ_{ab} , the energy difference $E_a - E_b$ between the two adiabatic FESs at the minimum of the reactant state, given by the energy of the absorption band maximum $\tilde{\nu}_{\max}$, and the difference in the dipole moments of the diabatic reactant and product states $\Delta\mu_{12}$ (equation 13).

$$V_{12} = \frac{\hbar c\tilde{\nu}_{\max}\mu_{ab}}{\Delta\mu_{12}} \quad \text{with} \quad \tilde{\nu}_{\max} = \Delta G^{00} + \lambda_o + \lambda_v \quad (13)$$

$$\mu_{ab} = \frac{3hc\varepsilon_0 \ln 10}{2000\pi^2 N} \frac{9n}{(n^2 + 2)^2} \int \frac{\varepsilon}{\tilde{\nu}} d\tilde{\nu} \quad (14)$$

$$\Delta\mu_{12} = \sqrt{\Delta\mu_{ab}^2 + 4\mu_{ab}^2} \quad (15)$$

consequently, the coupling element V_{12} can be calculated by this adiabatic theory. The transition moment μ_{ab} can be obtained by integration of the reduced charge transfer absorption band described by equation 14, which is corrected for the refractive index n of the solvent. However, $\Delta\mu_{12}$ cannot be determined by experiment. It has to be calculated by the adiabatic dipole moment difference $\Delta\mu_{ab}$ using equation 15, which in turn is not easily accessible. $\Delta\mu_{ab}$ can be approximated by $e \cdot r$, with r being the distance the participating electron has to cover during the charge transfer process. Nevertheless, it has been shown that in general r is overestimated. Furthermore, $\Delta\mu_{ab}$ can be obtained by quantumchemical calculations or by electro-optical absorption measurements, both methods inheriting considerable inaccuracies. To conclude, the electronic coupling element V cannot precisely be determined by the *Mulliken-Hush* analysis, although a rough estimate is obtained.

3.1.4. Bridge effects

It may be important to consider the bridge connecting the electron rich and electron poor redox centres to describe the intramolecular charge transfer correctly. This is particularly necessary when a second charge transfer band is observed in the absorption spectrum of the electron donor-acceptor compound, which can be attributed to an optically induced charge transfer to the bridge. To do so a third FES is introduced, describing the charge localisation at the bridge, which is in general higher in energy compared to the reactant and product states. The FESs of the three states are then positioned as shown in Figure 6.

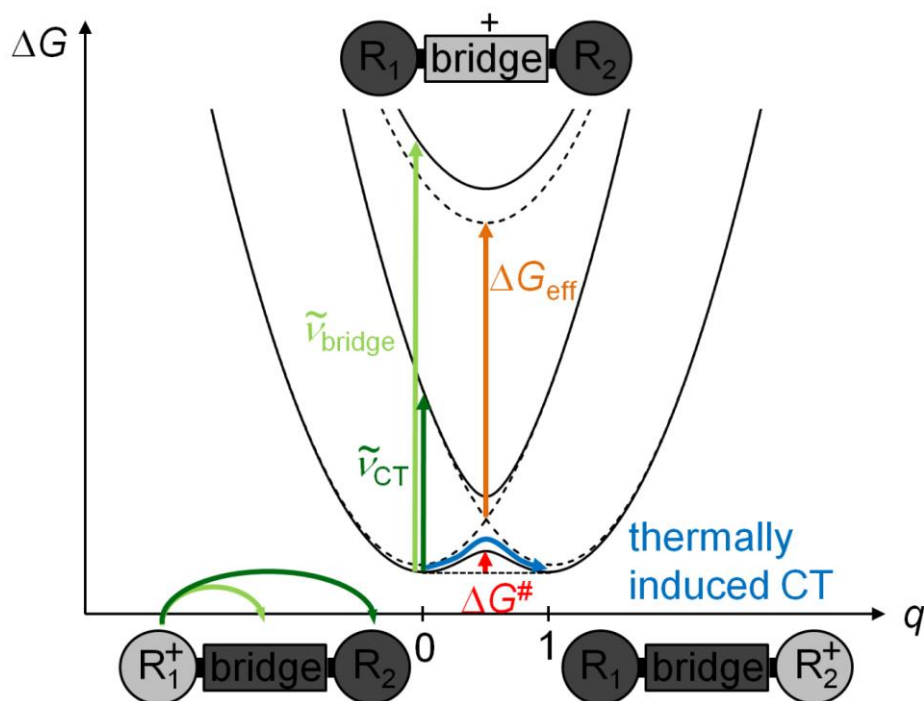


Figure 6 Diabatic (dashed line) and adiabatic (solid line) free energy surfaces (FESs) of a three state system consisting of reactant, bridge and product states (from left to right).

Although the bridge state can influence the activation barrier ΔG^\ddagger of the thermally induced charge transfer between reactant and product states,³³ the bridge state itself is not populated during the thermal process. To describe this system, the total Hamiltonian has to be extended for the bridge state (see equation 16)

$$H = \begin{vmatrix} V_{11} & V_{12} & V_{13} \\ V_{12} & V_{22} & V_{23} \\ V_{13} & V_{23} & V_{33} \end{vmatrix} \quad (16)$$

with V_{11} , V_{22} and V_{33} being the energies of the diabatic zeroth-order reactant, product and bridge states, respectively, and V_{12} , V_{13} and V_{23} the associated coupling elements. To calculate these energies the Generalised *Mulliken-Hush* (GMH) theory can be utilised, which is able to treat more than two states.^{31,33,58,59} The approach is similar to that described for the *Mulliken-Hush* analysis. Basically, the adiabatic transition dipole moments between the three states, the adiabatic and diabatic dipole moments of the three states and the transition energies $\tilde{\nu}_{CT}$ and $\tilde{\nu}_{bridge}$ (see Figure 6) between the reactant and product and reactant and bridge states, respectively, are used to calculate V_{12} , V_{13} and V_{23} . The mathematical treatment can be found elsewhere.^{33,58,59} As the experimental determination of all relevant quantities is almost impossible, the GMH analysis is performed with a mixture of experimental and quantumchemically calculated quantities.^{33,60}

In addition, the bridge state actually can render the charge transfer possible, in case the coupling element between the reactant and product states V_{12} is negligible. Two mechanisms are discussed in this regard.⁶¹ First, the charge may be transferred without populating the bridge state. This single-step nuclear tunneling is called “superexchange” mechanism and is observed when the bridge state is considerably higher in energy than the reactant state. In other words, the free energy difference between reactant and bridge states is distinctly positive, $\Delta G_{13} \gg 0$ (see Figure 7).

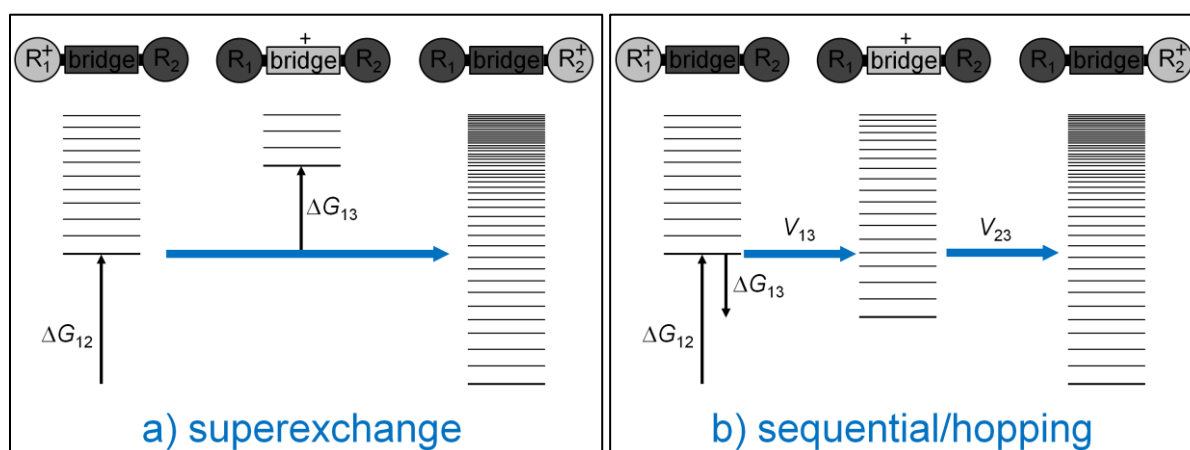


Figure 7 Vibronic level structure of the electronic three state system consisting of reactant, bridge and product states (from left to right). In the case the free energy difference $\Delta G_{13} \gg 0$, the “superexchange” mechanism (a) is dominant, whereas the charge transfer can be described by a sequential/hopping (b) scheme when $\Delta G_{13} < 0$.

Second, the sequential/hopping mechanism is observed when $\Delta G_{13} < 0$, which implies that the charge is consecutively transferred to the bridge state, a genuine chemical intermediate, and afterwards to the product state. In this case, the bridge state is found to be populated even when the charge transfer from the bridge to the product state is faster than the vibrational relaxation within the bridge state.

Assuming V_{13} and V_{23} are small compared to ΔG_{13} , the superexchange can basically be treated as a diabatic two state system. This means that the bridge state induces an electronic coupling between reactant and product states, but is otherwise not considered in constructing the adiabatic FESs. The induced electronic coupling is dependent on the electronic coupling elements between the bridge and the reactant/product states V_{13}/V_{23} and on the free energy difference between the intersection point of the diabatic reactant and product FESs and the minimum of the diabatic bridge FES ΔG_{eff} (Figure 6).^{56,62,63}

$$V_{12} = \frac{V_{13}V_{23}}{\Delta G_{\text{eff}}} \quad (17)$$

The coupling element V_{12} , calculated by equation 17, can then be substituted into equations 4 or 7 to obtain the rate constant for the “superexchange” charge transfer.

The theoretical description of the sequential/hopping mechanism is split into the transition from a “doorway” vibrational state of the reactant FES to a quasicontinuum of vibrational states of the bridge FES and subsequently from that quasicontinuum of vibrational states of the bridge FES to the quasicontinuum of vibrational states of the product FES.⁶¹ The first step, the reactant to bridge charge transfer, can be treated in a straightforward manner using equation 4 or 7 with the coupling element V_{13} , the free energy difference ΔG_{13} , and the respective reorganisation energies.^{61,63} The theoretical description of the second step, the transition from the bridge state to the product state, is much more demanding and can be found elsewhere.^{61,64} This is for two reasons: first, this transition originates from a high energy quasicontinuum of vibrational states in contrast to a single “doorway” state. Second, relaxation/dephasing processes within the bridge state may be of importance. It has to be pointed out that the sequential charge transfer from reactant to product state is only observed when the reverse processes, the charge transfer from bridge to reactant and from product to bridge state, are not dominating. Hence, the free energy differences of the three states should follow the relation $\Delta G_{12} \leq \Delta G_{13} \leq 0$.

3.2. Energy transfer

Energy transfer between two chromophores can be classified into three categories. To do so two processes are compared, (i) the motion of the excitation energy between the two chromophores and (ii) vibrational relaxation at the chromophore centres.⁶⁵ The former can be quantified by the energy transfer coupling element V_{EN} of the chromophores, whereas the latter can be approximated by the homogeneous line width Γ of the chromophore absorption band, which itself is a function of the reorganisation energy λ_o .⁶⁶⁻⁶⁸ An upper limit for Γ can be obtained by equation 18.

$$\Gamma = \frac{\sqrt{4\pi\lambda_o k_b T}}{\pi} \quad (18)$$

If the energy motion is much faster than vibrational relaxation ($V_{EN} \gg \Gamma$), the excitation energy oscillates coherently between the two chromophores. Therefore, the excitation energy is delocalised over the bichromophoric system, which is the strong coupling limit (first category). The reversed case, that the vibrational relaxation is faster than the motion of the excitation energy ($V_{EN} \ll \Gamma$), describes the weak coupling limit (second category). That is, the relaxed excited state is trapped at one chromophore and the excitation energy may hop irreversibly to the other chromophore centre. In the intermediate region (third category), both concepts are combined so that a coherent, oscillatory behavior is partly observed but quickly dies off due to the vibrational relaxation. In the following, theoretical models for the weak and the strong coupling limit will be reviewed. The intermediate case is much more complex and can be described by quantumchemical calculations.⁶⁸

3.2.1. Weak coupling limit

Energy transfer between a donor and an acceptor centre can be rationalised in the weak interaction limit as a transition between two states (see Figure 8).

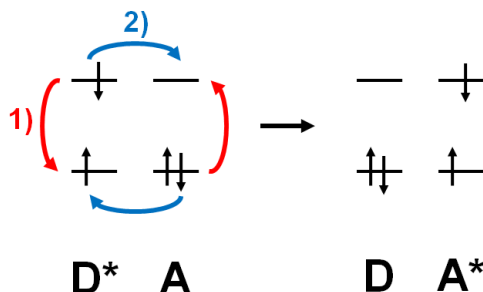


Figure 8 Schematic presentation of the two pathways of energy transfer between the initial $D^* + A$ and final $D + A^*$ states. The energy can be transferred by 1) Coulomb interactions or 2) by electron exchange.

The initial state depicts the situation that the donor centre is electronically excited (marked with an asterix) whereas the acceptor centre is in the ground state and the final state characterises the reversed situation. The transition can then take place either by Coulomb interactions or by exchanging electrons. In both cases two electrons are involved so that the initial state can be described by the two-electron antisymmetric wave function Ψ_i (equation 19)⁶⁹

$$\Psi_i = \frac{1}{\sqrt{2}} [\Psi_{D^*}(1)\Psi_A(2) - \Psi_{D^*}(2)\Psi_A(1)] \quad (19)$$

and the final state by the wave function Ψ_f (equation 20)

$$\Psi_f = \frac{1}{\sqrt{2}} [\Psi_D(1)\Psi_{A^*}(2) - \Psi_D(2)\Psi_{A^*}(1)] \quad (20)$$

where Ψ is the total wave function. If the Born-Oppenheimer approximation is met, Ψ can be divided into an electronic ϕ and a vibrational χ part (equation 21):

$$\Psi = \phi\chi \quad (21)$$

In the weak interaction limit the energy transfer can be regarded as a perturbation. Hence, the total Hamiltonian H can be divided into a zeroth-order part H_0 and the perturbation part V given by equation 22,

$$V = \frac{e^2}{r_{12}} \quad (22)$$

with the distance between the electrons r_{12} . The coupling element V_{EN} , which induces the energy transfer, can then be obtained (equation 23) by uniting equation 19, 20 and 22.

$$V_{\text{EN}} = \langle \Psi_i | V | \Psi_f \rangle = \left\langle \Psi_{\text{D}^*}(1)\Psi_{\text{A}}(2) \left| \frac{e^2}{r_{12}} \right| \Psi_{\text{D}}(1)\Psi_{\text{A}^*}(2) \right\rangle - \left\langle \Psi_{\text{D}^*}(1)\Psi_{\text{A}}(2) \left| \frac{e^2}{r_{12}} \right| \Psi_{\text{D}}(2)\Psi_{\text{A}^*}(1) \right\rangle \quad (23)$$

The first term on the right side describes the Coulomb interaction. That is the excited donor centre relaxes to the ground state and simultaneously the acceptor centre gets excited (Figure 8). One can imagine that in this case the energy is transferred by a virtual photon. Although an actual photon is not emitted or absorbed, this mechanism is nevertheless only relevant when these transitions are spin-allowed. The second term on the right side describes the energy transfer as a concerted two electron exchange process (Figure 8). Accordingly, the orbitals of the donor and acceptor centres need to overlap, so that the two electrons can be transported between the chromophores. It follows that this mechanism is only relevant at short interchromophore distances. The overall coupling element V_{EN} is therefore divided into a Coulomb part $V_{\text{EN}}^{\text{Coul}}$ and an exchange part $V_{\text{EN}}^{\text{exch}}$ (equation 24).

$$V_{\text{EN}} = V_{\text{EN}}^{\text{Coul}} + V_{\text{EN}}^{\text{exch}} \quad (24)$$

3.2.1.1 Coulomb interactions

Long-range intermolecular energy transfer ($10 \text{ nm} > r > 1 \text{ nm}$) is predominantly induced by the Coulomb coupling as the electron exchange term can be neglected due to the lack of orbital overlap.⁶⁵ For this case Förster derived an expression for the energy transfer rate constant.^{69,70} Therefore, the Coulomb integral (first term on the right side in equation 23) is approximated by the dipole-dipole term of the multipole expansion (equation 25),

$$V_{\text{EN}} = V_{\text{EN}}^{\text{Coul}} = \frac{\mu_{\text{D}}\mu_{\text{A}}}{r^3} \kappa \quad (25)$$

with $\mu_{\text{D}} = \langle \varphi_{\text{D}} | e\vec{r}_{\text{D}} | \varphi_{\text{D}^*} \rangle \langle \chi_{\text{D}^*} | \chi_{\text{D}} \rangle$, $\mu_{\text{A}} = \langle \varphi_{\text{A}} | e\vec{r}_{\text{A}} | \varphi_{\text{A}^*} \rangle \langle \chi_{\text{A}} | \chi_{\text{A}^*} \rangle$

and $\kappa = (\mathbf{e}_{\text{D}}\mathbf{e}_{\text{A}}) - 3(\mathbf{e}_{\text{D}}\mathbf{e}_{\text{DA}})(\mathbf{e}_{\text{A}}\mathbf{e}_{\text{DA}}) = \cos \alpha_{\text{DA}} - 3\cos \alpha_{\text{D}} \cos \alpha_{\text{A}}$

where μ_{D} and μ_{A} are the transition dipole moments for the for the $\text{D}^* \rightarrow \text{D}$ and $\text{A} \rightarrow \text{A}^*$ transitions, respectively, r is the distance between the D and A centres and κ is an orientation factor. The latter is defined by the unit vectors \mathbf{e}_{D} , \mathbf{e}_{A} and \mathbf{e}_{DA} of μ_{D} , μ_{A} and r , respectively, and can be expressed furthermore by the angles α_{D} , α_{A} and α_{DA} between the unit vectors (see Figure 9).⁷¹

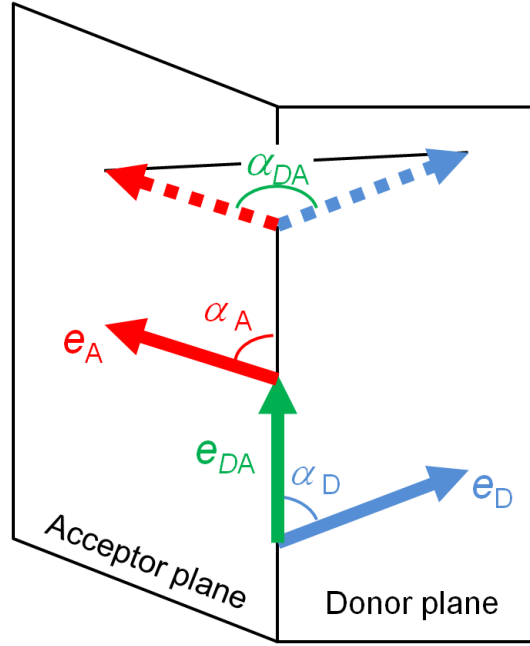


Figure 9 Directions of the unit vectors e_D , e_A and e_{DA} and the angles α_D , α_A and α_{DA} used to calculate κ

The orientation vector κ can have absolute values between 0 and 2. The minimum value of zero is obtained for the orthogonal orientation of the donor and acceptor transition moments ($\alpha_D = 90^\circ$, $\alpha_A = 90^\circ$ and $\alpha_{DA} = 90^\circ$). Consequently, the Coulomb interaction vanishes in this case. A parallel orientation of the transition moments ($\alpha_D = 90^\circ$, $\alpha_A = 90^\circ$ and $\alpha_{DA} = 0^\circ$) leads to the maximal value of 2. With a random orientation of the transition moments κ can be assigned to a value of $\sqrt{2/3}$.

The rate constant for energy transfer can be obtained by applying the *Fermis* Golden Rule expression (equation 26),

$$k_{\text{EN}} = \frac{2\pi}{\hbar} \sum_i \sum_f V_{\text{EN}}^2 P_i \delta(E_i - E_f) \quad (26)$$

with P_i being a *Boltzman* distribution representing all thermally available, initial states. The last term in equation 26 is a Dirac delta function of the initial and final energies E_i and E_f considering the conservation of energy during the energy transfer process. If equation 25 is inserted into equation 26 and the transition dipole moments μ_D and μ_A in equation 25 are expressed in terms of spectroscopically measurable quantities (equation 27a and 27b), then the formula for the rate constant of energy transfer according to Förster is obtained (equation 28),

$$\mu_A^2 \sum_f \langle \chi_A | \chi_{A^*} \rangle^2 \delta(E - E_f) \propto \frac{\varepsilon(\tilde{\nu})}{\tilde{\nu}} \quad (27a)$$

$$\mu_D^2 \sum_i \langle \chi_{D^*} | \chi_D \rangle^2 \delta(E_i - E) \propto \frac{\Phi_D}{\tau_D} \frac{\bar{I}_{fl,D}(\tilde{\nu})}{\tilde{\nu}^3} \quad (27b)$$

$$k_{EN}^{Coul} = \frac{9000 \ln(10) \Phi_D \kappa^2}{128 \pi^5 N_A n^4 \tau_D r^6} \int_{-\infty}^{\infty} \bar{I}_{fl,D}(\tilde{\nu}) \varepsilon(\tilde{\nu}) \frac{\partial \tilde{\nu}}{\tilde{\nu}^4} \quad (28)$$

where Φ_D and τ_D are the quantum yield and lifetime of the separated donor centre, respectively. The integral in equation 28 includes the area normalised fluorescence intensity of the donor $\bar{I}_{fl,D}(\tilde{\nu})$ and the extinction coefficient of the acceptor $\varepsilon(\tilde{\nu})$ and is called overlap integral J . With the exception of r and τ_D , the constants and variables can be combined to the Förster critical transfer radius R_0 (equation 29).

$$k_{EN}^{Coul} = \frac{1}{\tau_D} \left(\frac{R_0}{r} \right)^6 \quad (29)$$

$$\text{with } R_0^6 = \frac{9000 \ln(10) \Phi_D \kappa^2}{128 \pi^5 N_A n^4} J \text{ and } J = \int_{-\infty}^{\infty} \bar{I}_{fl,D}(\tilde{\nu}) \varepsilon(\tilde{\nu}) \frac{\partial \tilde{\nu}}{\tilde{\nu}^4}$$

The critical transfer radius defines the distance between donor and acceptor at which the fluorescence rate constant of the donor equals the energy transfer rate constant. From equation 28 it follows that the energy transfer induced by Coulomb interaction is significantly fast when the involved transitions are spin-allowed, overlap spectrally and their transition moment directions are oriented non-orthogonal. Furthermore, the rate constant decreases with the distance separating the donor and acceptor centres to the power of 6.

It has to be pointed out that the expression for the rate constant of energy transfer according to Förster is strictly valid only for donor acceptor distances greater than the chromophore sizes. Despite the fact that with very small interchromophore distances the electron exchange interaction gains in importance and can no more be excluded, the dipole-dipole approximation no longer holds true.^{4,72} That is because the donor and acceptor see each other no more as transition dipoles but in the shape of transition densities. In other words, the molecular charge distribution has an effect on the Coulomb interactions. These transition densities can be calculated quantumchemically.^{65,73,74} When lifting the dipole-dipole approximation and utilising instead transition densities, Coulomb interactions could be even verified between dark states of closely neighboured chromophores.⁷⁵ Furthermore, the influence of the solvent on the energy transfer is insufficiently described by Förster at very small interchromophore distances. Basically, the solvent surrounding the donor and acceptor centres screen the energy transfer interaction, which is accounted for by the fixed factor $1/n^4$ in equation 28. However, at small distances between donor and acceptor, when they share a common solvent cavity, the screening decreases and ultimately vanishes.⁷⁶

It has been shown that energy transfer can occur in the same time domain as relaxation processes in the excited state of the donor chromophore (< 50 ps).^{67,71} These relaxation processes are for example solvation dynamics or intramolecular vibrational redistributions. During the relaxation processes, changes in the fluorescence energy have been observed in proteins⁷¹ and compounds with charge transfer states.^{67,77} This leads to time dependent spectral overlap integrals $J(t)$ between the fluorescence of the relaxing donor and the absorption of the acceptor and thus to time dependent, non-equilibrium energy transfer rate constants (see Figure 10). By performing ultrafast fluorescence measurements the time dependency of the spectral overlap can be determined experimentally.^{67,71} The donor fluorescence directly after excitation can be estimated by the fluorescence of the donor in an apolar solvent, when charge transfer states are involved.⁶⁷

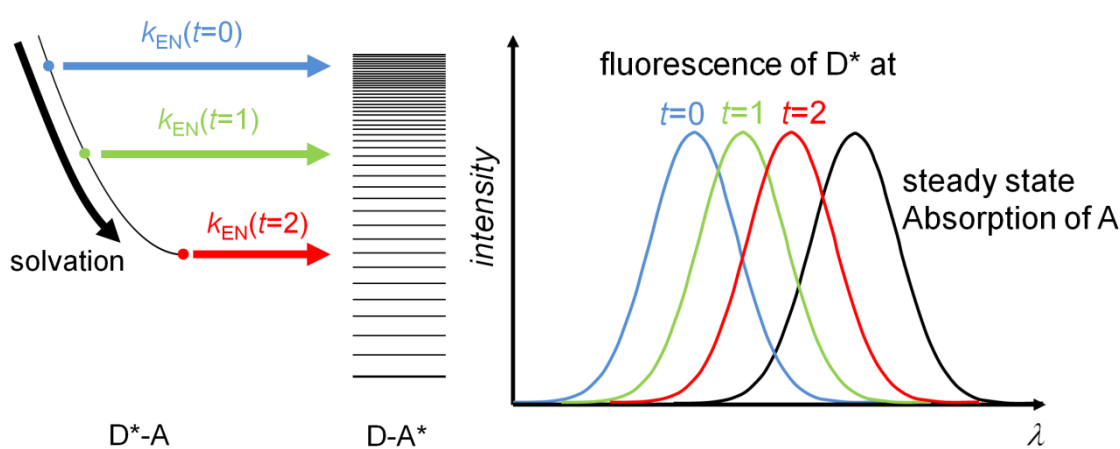


Figure 10 Schematic model (left side) of non-equilibrium energy transfer from unrelaxed (at time $t = 0$ and $t = 1$) and relaxed ($t = 2$) D^*-A state to the vibronic level structure of the $D-A^*$ state. On the right side the spectral overlap (coloured area) of the time dependent fluorescence of the D^*-A state and the steady-state absorption of the $D-A^*$ state is illustrated.

Besides the spectral overlap the mentioned relaxation may furthermore induce time dependent changes in the interchromophore distance⁷¹ and the direction^{71,78} and magnitude^{77,79} of the fluorescence transition moment of D^*-A may be altered, too. These processes are difficult to monitor experimentally and hence the expression for the energy transfer according to *Förster* seems to be incapable of describing these ultrafast phenomena.

3.2.1.2 Electron exchange interactions

If energy transfer is considered between triplet states, the Coulomb interaction is negligible due to the spin forbidden electronic transitions. In this case the coupling element V_{EN} in equation 24 reduces to the electron exchange part V_{EN}^{exch} (equation 30).

$$V_{EN} = V_{EN}^{\text{exch}} = \left\langle \Psi_{D^*}(1)\Psi_A(2) \left| \frac{e^2}{r_{12}} \right| \Psi_D(2)\Psi_{A^*}(1) \right\rangle \quad (30)$$

Dexter understood equation 30 as electrostatic interaction between two charge clouds, where the electron densities of the involved wave functions decrease exponentially with the distance to their centres.⁸⁰ He derived under the assumption of hydrogen like orbitals and on the basis of *Fermis* Golden Rule expression (equation 26) a formula for the energy transfer rate constant *via* electron exchange $k_{\text{EN}}^{\text{exch}}$ (equation 31),⁸⁰

$$k_{\text{EN}}^{\text{exch}} = \frac{2\pi}{\hbar} K \exp(-2r/L) \bar{J} \quad (31)$$

$$\text{with } \bar{J} = \int_0^\infty \bar{I}_{\beta,D}(\tilde{\nu}) \bar{\mathcal{E}}(\tilde{\nu}) d\tilde{\nu}$$

where L is the average *van der Waals* radius of the D*-A and D-A* molecular orbitals and \bar{J} the spectral overlap of the normalised donor fluorescence and acceptor absorption. In contrast to the *Förster* equation, in the *Dexter* expression a parameter K is present, which cannot be determined by spectroscopic measurements. Combined with the difficulties to determine $V_{\text{EN}}^{\text{exch}}$ directly, the expression of *Dexter* (equation 31) is useless to determine the contribution of the exchange mechanism to the overall energy transfer rate.⁶⁹ It should however be noted that the rate constant for energy transfer *via* electron exchange interaction decreases exponentially with the interchromophore distance. This rate behavior confirms that the electron exchange mechanism is present only at very short interchromophore distances.

Furthermore, it has been remarked by *May* that besides the direct electron exchange coupling, described by *Dexter*, the superexchange mechanism as well as charge transfer states might considerably contribute to the through bond interactions (Figure 11).¹

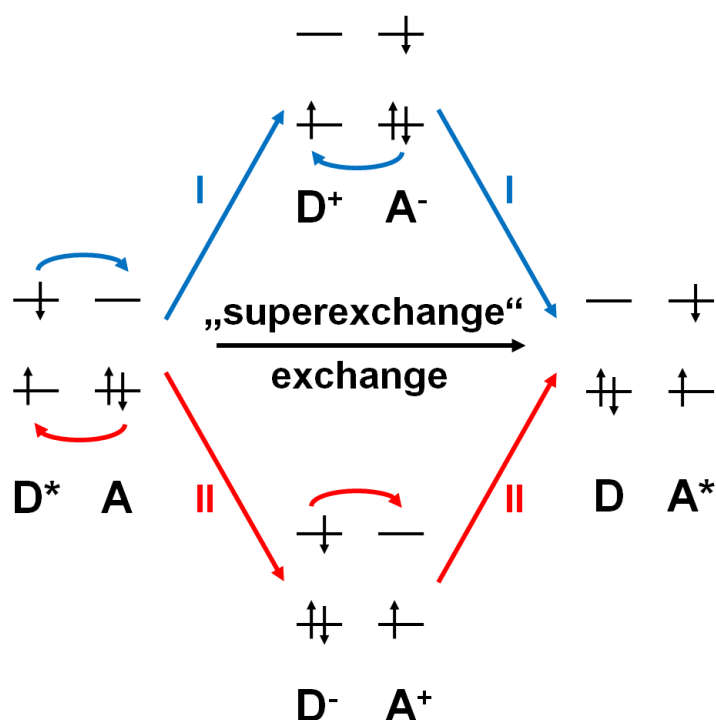


Figure 11 Schematic presentation of the energy transfer between the initial $D^* + A$ and final $D + A^*$ states by through bond interactions. The energy can be transferred by direct electron exchange or superexchange contributions or *via* the charge transfer states $D^+ + A^-$ (pathway I) and $D^- + A^+$ (pathway II).

With the charge transfer states a sequential/hopping mechanism is described,¹ where the transition between D^*-A and D^+-A^- (pathway I in Figure 11) has the appearance of a photoinduced electron transfer from the donor to the acceptor and the subsequent transition between D^+-A^- and $D-A^*$ of a photoinduced hole transfer from the donor to the acceptor. The reversed situation can be noticed for pathway II in Figure 11. Within the “superexchange” mechanism the charge transfer states are considered as virtual intermediate states.^{1,69}

3.2.2. Strong coupling limit

A strong Coulomb interaction between two chromophores (monomers) C_1 and C_2 leads to a situation where the excitation is no more localised at a single chromophore (monomer) but is delocalised over the complete system (dimer).^{81,82} One can regard this situation as a bound electron-hole pair which is also named exciton. In the following the two chromophores are assumed to be identical, as this situation is encountered in the molecules investigated in this thesis. Both the excited and the ground states are stabilised due to *van der Waals* interactions between the two monomers. Furthermore, the excited state energy levels are split into a lower and a higher exciton energy level because of the strong Coulomb coupling (electron exchange interactions are neglected). The splitting energy equals twice the coupling term V_{ex} (Figure 12).

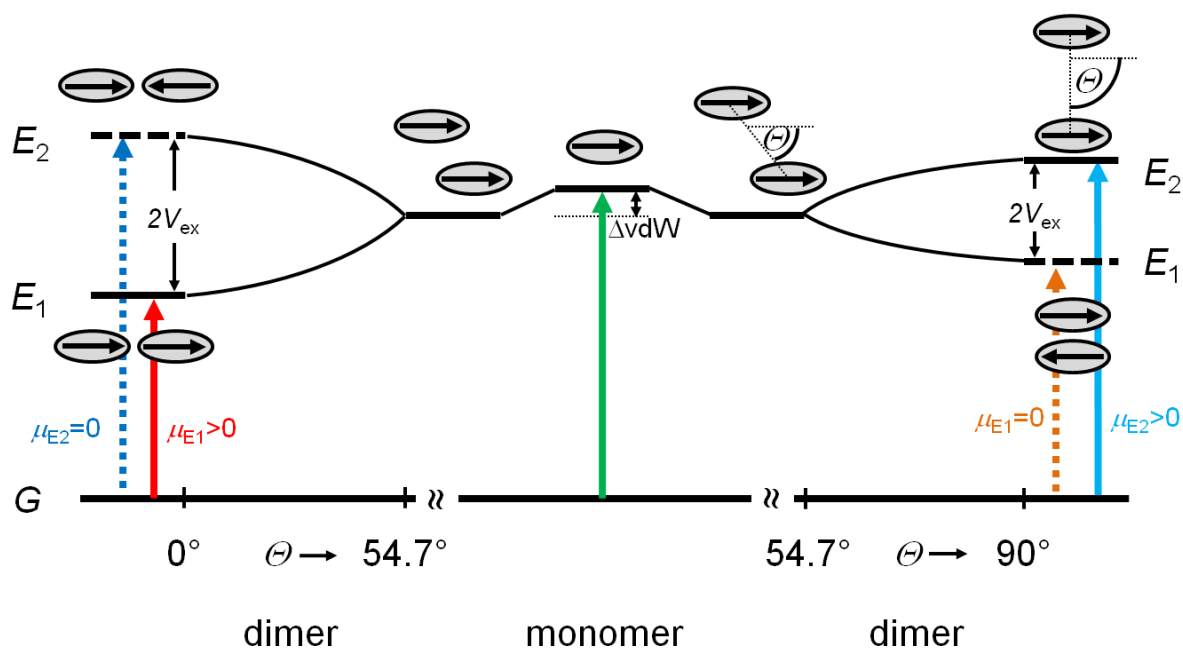


Figure 12 Ground and excited state energy diagram for the monomer and a molecular dimer depending on the angle Θ describing the mutual position of the two coplanar transition moments. The difference in the excited and ground state *van der Waals* stabilisation Δvdw is shown relative to a fixed ground state. The excitonic energy levels E_1 and E_2 are splitted by $2V_{ex}$ in the case Θ has a value different from the magic angle 54.7° . The transition moment vectors are shown as black arrows. For the limiting cases of parallel ($\Theta = 90^\circ$) and in-line ($\Theta = 0^\circ$) transition moments, the excitation energies are illustrated as coloured arrows, which are dashed when the transition moments have a magnitude of zero.

In these systems energy transfer is basically no more possible due to the intrinsic delocalisation of the excited states. The theoretical treatment of excitons is very similar to the description of adiabatic charge transfer (see charge transfer section). That is, the two excitonic states E_1 and E_2 are constructed by linear combination of the zeroth-order excited states $C_1^*-C_2$ and $C_1-C_2^*$, with the excitation localised at one chromophore. These zeroth-order states are coupled furthermore by a perturbation term V . The Coulomb coupling element for exciton interactions V_{ex} can be approximated in the exact same way as shown for the Förster energy transfer, by the dipole-dipole term of the multipole expansion (equation 25).

$$V_{ex} = V_{EN}^{Coul} = \frac{\mu_{C1}\mu_{C2}}{r^3} \kappa \quad (25)$$

It follows that the energy splitting of the exciton states $2V_{ex}$ is dependent on the magnitude and mutual orientation of the absorption transition moments of the involved chromophores. The same relationship is applicable as well to the magnitude of the transition moments between the ground and the exciton states E_1 and E_2 and can be evaluated qualitatively by simple geometric considerations. Optical

transitions between two states can basically be regarded as induced oscillations of dipoles. If multiple transitions are simultaneously considered, as is done for transitions from/to exciton states, these oscillations can be in or out-of-phase which is illustrated by vector diagrams in Figure 12. The magnitude of the transition moment is proportional to the square root of the dipole oscillator strength (illustrated by the length of the vector). Moreover, the direction of the oscillations (vector orientation) and the respective transition moments coincide. Hence, the transition moments related to the E_1 and E_2 states can be evaluated by vector superposition of the two monomer transition moments. In the following two limiting cases shall be reviewed (see Figure 12). If the transition moments of the two chromophores $\vec{\mu}_m$ are aligned parallel, the in-phase oscillation of the dipoles (the vectors point in the same direction) is electrostatically unfavourable so that the energy is increased marking this state to be E_2 . Moreover, the transition from the ground state to E_2 is allowed with $\mu_{E_2} = \sqrt{2}\mu_m$. In contrast, the out-of-phase situation leads to the lower energy exciton state E_1 with $\mu_{E_1} = 0$. It follows that the absorption of this dimer is shifted to higher energies compared to that of the monomer and that the fluorescence from the lowest energy excited state is quenched. When the transition moments of the two chromophores are oriented in-line, the situation is reversed so that the absorption of the dimer is shifted to lower energies and the fluorescence transition moment is by the square of two greater than that of a monomer $\mu_{E_1} = \sqrt{2}\mu_m$.

It should be pointed out that the exciton coupling theory can be expanded to account for any number of interacting chromophores.

3.3. Ultrafast spectroscopy

In this chapter first the measurement setups and then the functional principles for ultrafast transient absorption (TA) and fluorescence upconversion (FUC) will be discussed. Furthermore, adjustments of the measurement parameters to the characteristics of the monitored molecules will be presented.

3.3.1. Measurement setups

The energy transfer and charge transfer processes under investigation (see the scope of the work) all involve the excited states of the presented molecules. Hence, these phenomena can be tracked over time by monitoring the temporal evolution of the respective excited states. Two possibilities are presented in the following. Either the emitting (fluorescence) or the absorption characteristics (transient absorption) of the excited states can be recorded with time. As energy transfer and charge transfer processes can be very fast (<10 ps) the time dependent measurements have to have an even better time resolution. To monitor dynamics in the sub picosecond time regime the recording of data has to be translated from the time domain to the space domain. This is because the photoelectric effect

that is used in detectors to monitor light intensities in real time is limited to a time resolution in the picoseconds regime.⁸³ To trace processes in the femtosecond time regime at least two ultrashort light pulses have to be correlated. The time resolution is indirectly obtained by the differing path lengths of the pulses. In the following the utilised setups are described to monitor ultrafast fluorescence and transient absorption.

3.3.1.1 Fluorescence upconversion

In the fluorescence upconversion measurement a pump pulse is used to excite the sample (see Figure 13).

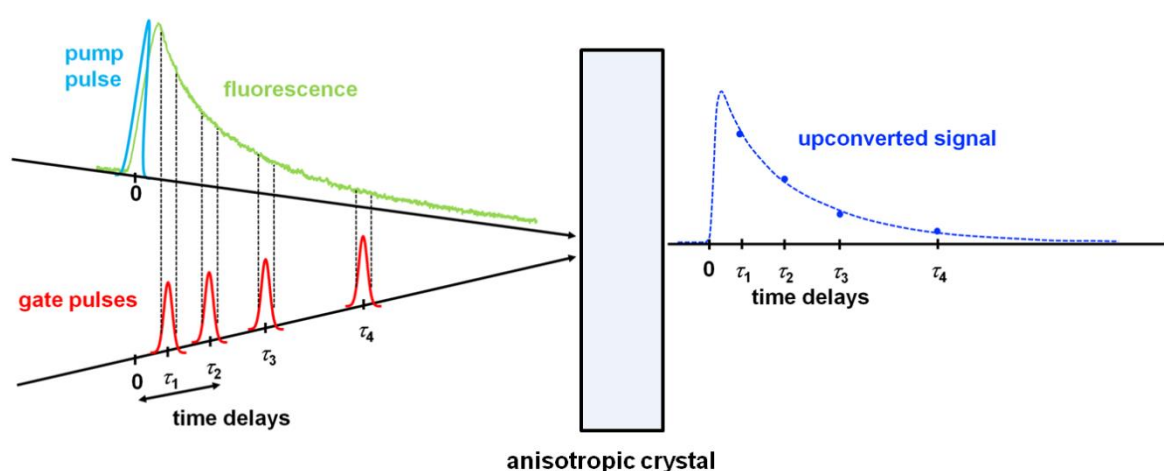


Figure 13 Schematic diagram of upconversion.

The emitted fluorescence is then overlapped with a gate pulse in an anisotropic medium to generate the sum frequency/upconverted signal. The path length of the gate pulse is thereby varied to obtain a time delay to the pump pulse. The monitored intensity of the sum frequency signal correlates to the fluorescence intensity at the respective delay time between the pump and gate pulses with a time resolution determined by the instrument response function (IRF). The IRF is dependent on the temporal pulse width of the pump and gate pulses and can be furthermore lengthened by dispersion in the sample volume and optics and by phase mismatch in the anisotropic crystal. However, the IRF is not dependent on the temporal response of the detector. The complete fluorescence decay can be reconstructed by monitoring the sum frequency signal at various delay times.

The actual fluorescence upconversion measurement setup used in this work is depicted in Figure 14.

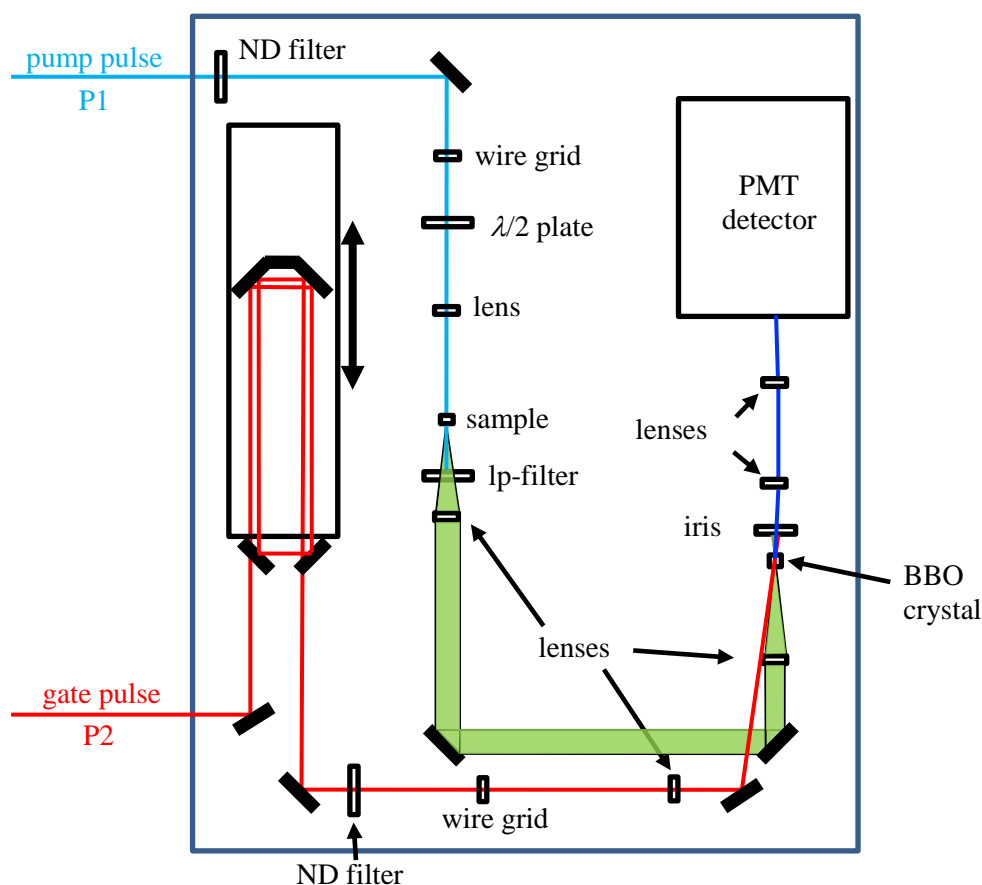


Figure 14 Layout of the fluorescence upconversion measurement setup. Lp-filter stands for long-pass filter and ND filter for neutral density filter.

This detection system called “Halcyone” was purchased from Ultrafast Systems. The source of the ultrashort pulses was an ultrafast amplified Ti:Sapphire laser (Solstice from Newport-Spectra-Physics). The generated pulses have a central wavenumber of 12500 cm^{-1} (800 nm) and a length of 100 fs with a repetition rate of 1 kHz. The laser output was split into the pump and probe beam. The wavelength of the pump pulse was subsequently set to 26700 cm^{-1} (375 nm) or 24700 cm^{-1} (405 nm) in an optical parametric amplifier (TOPAS from Light Conversion / Newport-Spectra-Physics) whereat the pulse length changed to 140 fs. With a neutral density filter (ND) the power of the pump pulse was reduced to $\leq 250\text{ nJ}$. Thereafter the beam was focused (spot diameter at $1/e^2$ intensity ca. $100\text{ }\mu\text{m}$) onto the sample solution stirred in a 2 mm path length quartz cuvette. The molecules under investigation were dissolved in Uvasol solvents, the OD adjusted to 0.5-0.7 at the excitation wavelength and the solution purged with argon prior measurement. After exciting the sample volume the pump pulse was blocked by a colored glass 400 nm long-pass (lp) filter whereas the fluorescence (16700 cm^{-1} (600 nm)) was imaged onto a 0.5 mm BBO type 1 anisotropic crystal by two quartz lenses ($f = 100\text{ mm}$). The gate pulse was delayed for 0 – 3.3 ns in a delay line (in 20 fs steps between 0 and 5 ps and in logarithmic steps at longer delay times), attenuated by a neutral density filter to $\leq 500\text{ nJ}$

(12500 cm⁻¹ (800 nm)) and then focused by a lens ($f = 200$ mm) onto the anisotropic crystal with a vector phase matching angle of $\sim 11^\circ$. After passing through the crystal, the fluorescence and the gate beams were blocked by an iris whereas the sum frequency signal (29200 cm⁻¹ (340 nm)) was focused onto the entrance slit of a double monochromator. The upconverted signal intensity was measured by a photomultiplier tube (PMT). A linear polarisation of the pump and gate beams was ensured by wire grid polarisers (Thorlabs). The polarisation direction of the pump beam was set parallel and perpendicular to that of the gate beam by a $\lambda/2$ wave-plate leading to the intensities I_{\parallel} and I_{\perp} of the sum frequency signal, respectively. The IRF was measured by stray light or Raman signals of the pure solvents. Its fwhm was estimated to ~ 770 fs for PhCN.

The obtained data were fitted globally by a self-written procedure based on MATLAB (see Appendix 3). During the fitting process the self-written procedure constructs a decay curve for I_{\parallel} and I_{\perp} , compares it to the respective measured curve and changes its parameters if the match is insufficient. The basic equations to construct such curves are equation 55 and 56 (see polarisation/anisotropy section). However, these have to be extended to equation 32 due to the fact that the pure decays are convoluted by the instrument response function (IRF) of the measurement setup.^{84,85}

$$\begin{pmatrix} I_{\parallel}(t) \\ I_{\perp}(t) \end{pmatrix} = \begin{bmatrix} S(t) & (1 + 2r(t)) \\ S(t) & (1 - r(t)) \end{bmatrix} \otimes \text{IRF} \quad (32)$$

The IRF was assumed to be Gaussian and $r(t)$ and $S(t)$ both to be a sum of exponential functions (equation 33).

$$\text{IRF} = \frac{1}{\sigma\sqrt{2\pi}} \exp\left(-\frac{(x-x_0)^2}{2\sigma^2}\right) \quad \text{with} \quad \text{fwhm} = 2\sqrt{2\ln 2} \cdot \sigma$$

$$r(t) \text{ and } S(t) = \sum_{i=1}^b a_i \exp\left(-\frac{x}{\tau_i}\right) \quad (33)$$

Thereby σ is the standard deviation and x_0 the mean of the Gaussian distribution. The former can be related to the fwhm and the latter can be understood as the point of time with maximal pump pulse intensity. The i -th exponential function is described by the amplitude a_i and the decay time constant τ_i . The advantage of this treatment is that the convolution of a Gaussian and an exponential function has an analytical solution (equation 34) and can therefore be calculated easily.

$$a_i \exp\left(-\frac{x}{\tau_i}\right) \otimes IRF = \frac{a_i}{2} \exp\left(-\frac{x-x_0}{\tau_i}\right) \exp\left(-\frac{\sigma^2}{2\tau_i^2}\right) \left[1 + \operatorname{erf}\left(\frac{x-x_0 - \frac{\sigma^2}{\tau_i}}{\sqrt{2}\sigma}\right) \right] \quad (34)$$

If equations 32-34 are combined a trial function with any number of exponential decays can be obtained to reproduce the measured data.⁸⁵ The data of I_{\parallel} and I_{\perp} were fitted globally, which means that all decay time constants and amplitudes as well as the fwhm and the zero time delay of the IRF was assumed to be equal for both decay curves. This was done to reduce the impact of the signal-to-noise ratio and to minimise the impact of fluctuations introduced by the environment (e.g., temperature) during the sequential measurement of I_{\parallel} and I_{\perp} . In addition, due to the $\lambda/2$ wave-plate the intensities of the pump pulse polarised parallel and perpendicular to the gate pulse differed slightly in intensity, which was accounted for in the fitting routine. This was possible as I_{\parallel} and I_{\perp} should be equal in the absence of anisotropy according to equation 32. Thus, the two decay curves could be normalised at very long delay times (after 3 ns) when rotational depolarisation has already taken place.

3.3.1.2 Transient absorption

In the ultrafast transient absorption measurements the sample is excited by a pump pulse and the absorption characteristics of the sample is probed by a weak WLC pulse.⁸⁶ As described for fluorescence upconversion the time dependency is introduced by the time delay between the two pulses. Due to the broadband probe pulse entire spectra are recorded for every WLC pulse with a spectral width depending on the WLC characteristics. The transient absorption is presented by absorbance difference spectra in ΔOD . Thus, two absorption measurements are performed for every given time delay. The intensity of the WLC is monitored when passing through the sample which was in one case pumped and in the other case unpumped to obtain $I(\lambda)_{\text{pumped}}$ and $I(\lambda)_{\text{unpumped}}$, respectively. This is achieved by blocking every other pump pulse by a chopper. The absorbance difference spectra are then calculated by equation 35.

$$\Delta OD(\lambda) = -\log\left(\frac{I(\lambda)_{\text{pumped}}}{I(\lambda)_{\text{unpumped}}}\right) \quad (35)$$

The change in optical density ΔOD is linear proportional to the number of molecules in the excited state and in the case of one-photon processes also linear proportional to the pump pulse intensity.

The sensitivity of the measurement can be increased by monitoring the intensity of the WLC pulse in a reference channel for every laser shot. Hence, fluctuations in the WLC spectrum can be accounted for (equation 36). Accordingly, parts of the WLC pulse are separated before reaching the sample by a semitransparent mirror and guided directly to a detector to obtain $I(\lambda)_{\text{ref}}$.

$$\Delta OD(\lambda) = -\log\left(\frac{I_1(\lambda)_{\text{pumped}}}{I_2(\lambda)_{\text{unpumped}}}\frac{I_2(\lambda)_{\text{ref}}}{I_1(\lambda)_{\text{ref}}}\right) \quad (36)$$

There are three possible contributions to the transient absorption signal (Figure 15):

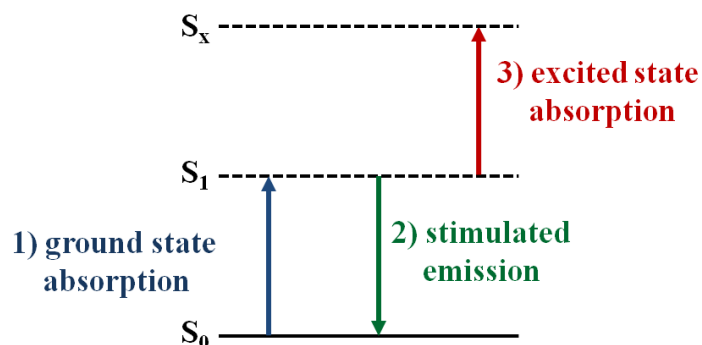


Figure 15 Energy diagram of the processes observed in the transient absorption.

1) When the pump pulse passes the sample volume, some molecules are excited to higher energy states and therewith the number of molecules in the ground state is decreased. Consequently, the probe pulse experiences a stronger ground state absorption in the unpumped case ($I(\lambda)_{\text{pumped}} > I(\lambda)_{\text{unpumped}}$), which leads to a negative signal in the spectral range of the ground state absorption. The signal intensity is linear proportional to the number of molecules which are not in the ground state. The possibility to monitor the dynamics of the ground state bleaching allows in some cases to indirectly investigate dark states. These are states that do not absorb or emit light.

2) The probe pulse can trigger stimulated emission from the pumped sample. That is, a photon of the probe pulse induces an excited molecule to relax to the ground state by emitting a photon in coherence with the probing photon. Stimulated emission can only be observed when the transition between the excited state and the ground state is allowed. This process amplifies $I(\lambda)_{\text{pumped}}$ so that a negative signal is monitored in the spectral range of the molecules fluorescence. The stimulated emission in transient absorption experiments however differs from the spontaneous emission in fluorescence experiments in band shape due to the difference in the Einstein coefficients.

3) The molecules excited by the pump pulse can absorb a photon of the probe pulse if transitions to higher energy states are allowed. Due to this absorption process $I(\lambda)_{\text{pumped}}$ is reduced and thus a positive signal can be observed. The band form of the excited state absorption can be used to characterise the excited state. For example, charge transfer states can be identified if the excited state absorption can be reproduced by the absorption spectra of the respective oxidised and reduced redox centres.

The observed transient absorption spectra are the sum of these three contributions so that the investigation of a specific process is, if at all possible, limited to a spectral region one contribution is dominating or the characteristics of the other contributions are known.

Anisotropic transient absorption data is obtained by monitoring $\Delta OD_{\parallel}(t)$, with the probe pulse polarised parallel to the pump pulse, and $\Delta OD_{\perp}(t)$, with a perpendicular polarisation direction of the two pulses. The anisotropy is then calculated by equation 37.

$$r(t) = \frac{\Delta OD_{\parallel}(t) - \Delta OD_{\perp}(t)}{\Delta OD_{\parallel}(t) + 2\Delta OD_{\perp}(t)} \quad (37)$$

However, the superposition of the ground state bleaching, stimulated emission and excited state absorption makes it nearly impossible to interpret the anisotropy values.^{87,88} This is because the weights of the contributions and the exact directions of the transition moments of all involved components are in general not known. Moreover, the law of addition (equation 59, see polarisation/anisotropy section) does not strictly hold true in the transient absorption as the signal can have both positive and negative $\Delta OD(t)$ values. Hence, the total intensity of the transient absorption, $\Delta OD_{\parallel}(t) + 2\Delta OD_{\perp}(t)$, can be zero when the involved contributions cancel each other out. It follows that the anisotropy can have infinitely high or low values when the denominator in equation 37 approaches zero and is not defined in the case the denominator equals zero.

Due to the spectral broadness of the probe pulse, group velocity dispersion is observed. As high energy light of the probe pulse travels slower through a medium (e.g. filters, the CaF₂ plate and the sample) compared to low energy light, the probe pulse gets temporally broadened with high energy light in the rear part of the pulse and low energy light at the leading part. This phenomenon is called *chirp*. Hence, the pump pulse overlaps at different time delays with differing spectral regions of the probe pulse. The chirp of the probe pulse distorts therewith the transient absorption data by shifting the zero time delay with the energy of the probe pulse. This shift can be accounted for by a polynomial fit (see Figure 16).

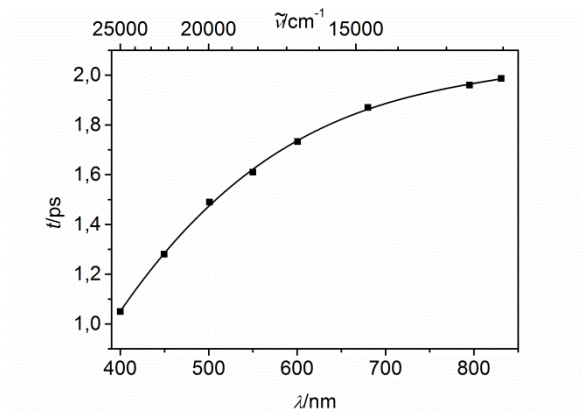


Figure 16 Polynomial fit (line) of the probe pulse chirp (points) observed in DCM.

When the probe and the pump pulse pass at the same time through the sample at zero time delay, cross-phase modulation can be observed (see the third order nonlinear effects section). The weaker probe pulse experiences the nonlinear refractive index changes generated by the high intensity pump pulse. It follows that the phase of the WLC is modulated and therewith its spectrum changed. This spectral change leads to an oscillatory patterned signal in the transient absorption spectra at zero time delay called *coherent artifact* (Figure 17).⁸⁶

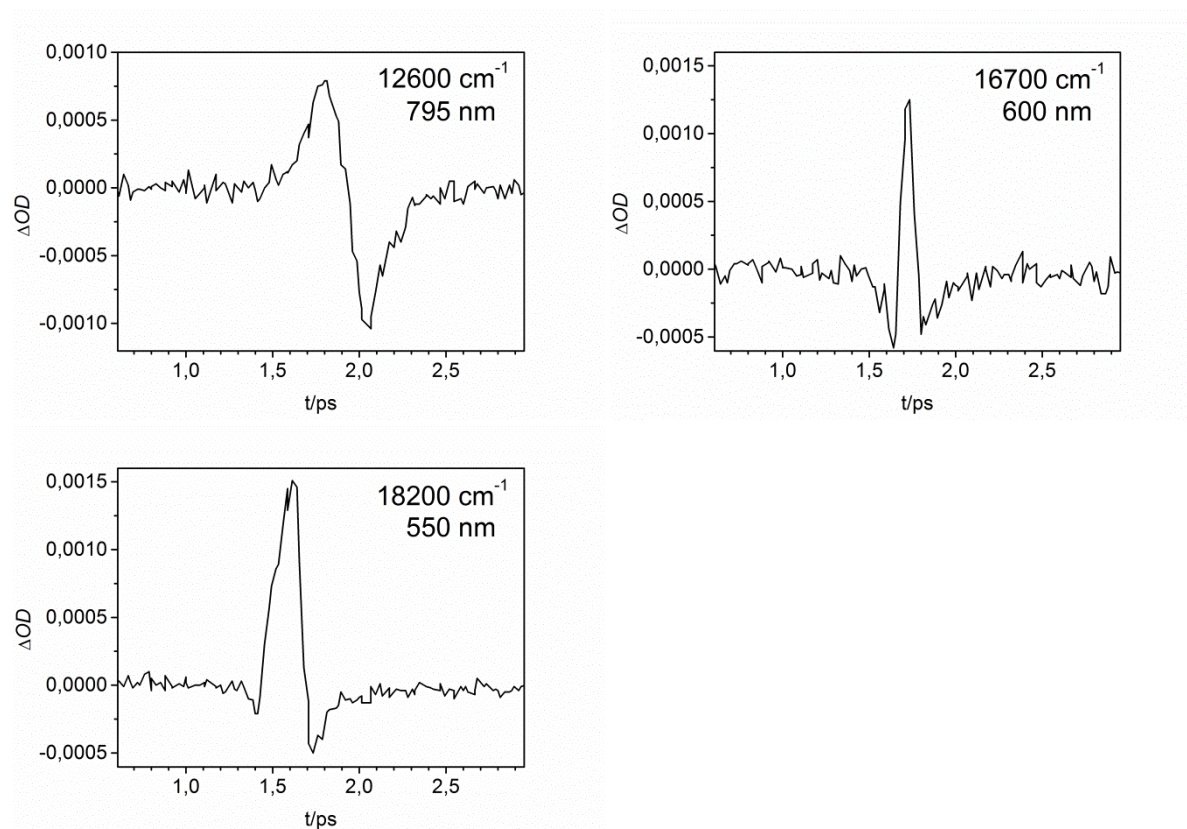


Figure 17 Coherent artifacts experienced in DCM at probe energies of 12600 cm^{-1} (795 nm), 16700 cm^{-1} (600 nm) and 18200 cm^{-1} (550 nm). The pump pulse had a central wavenumber of 15200 cm^{-1} (660 nm)

The observed positive and negative $\Delta OD(t)$ values are due to two competing effects. On the one hand, light of the monitored wavenumber is converted to higher or lower energy light due to the cross phase modulation which leads to a decrease in $I(\lambda)_{\text{pumped}}$ and consequently to positive $\Delta OD(t)$ values. On the other hand, light of higher or lower energy is converted to the monitored wavenumber such that $I(\lambda)_{\text{pumped}}$ increases and $\Delta OD(t)$ has negative values. The energy conversion is moreover time dependent as the pump and the probe energies pass the sample with a different speed due to the differing energy. When the probe pulse experiences the trailing (leading) part of the pump pulse the energy of the probe light is converted to higher (lower) energies following the concepts discussed for

self-phase modulation (see third order nonlinear effects section). The coherent artifact can have the shape of the first derivative of a Gaussian function in the case the chirp in the probe light is negligible. This holds true for the probe wavenumber of 12600 cm^{-1} in Figure 17. If the probe spectrum is considerably chirped the coherent artifact can take the shape of the second derivative of a Gaussian function. This is observed at probe energies of 16700 cm^{-1} and 18200 cm^{-1} in Figure 17. However, the longer the sample volume and the higher the pump pulse intensity the more complex the coherent artifact signals can get.⁸⁹ The intensity of the coherent artifact is dependent on the polarisation directions of the pump and gate beams,⁹⁰ the intensity of the pump and probe pulses,⁹⁰ the nonlinear refractive index n_2 of the medium and the length of the sample cuvette.⁸⁹ The coherent artifact can be used to estimate the chirp of the probe pulse and temporal width of the IRF.

The ultrafast transient absorption measurement setup is depicted in Figure 18.

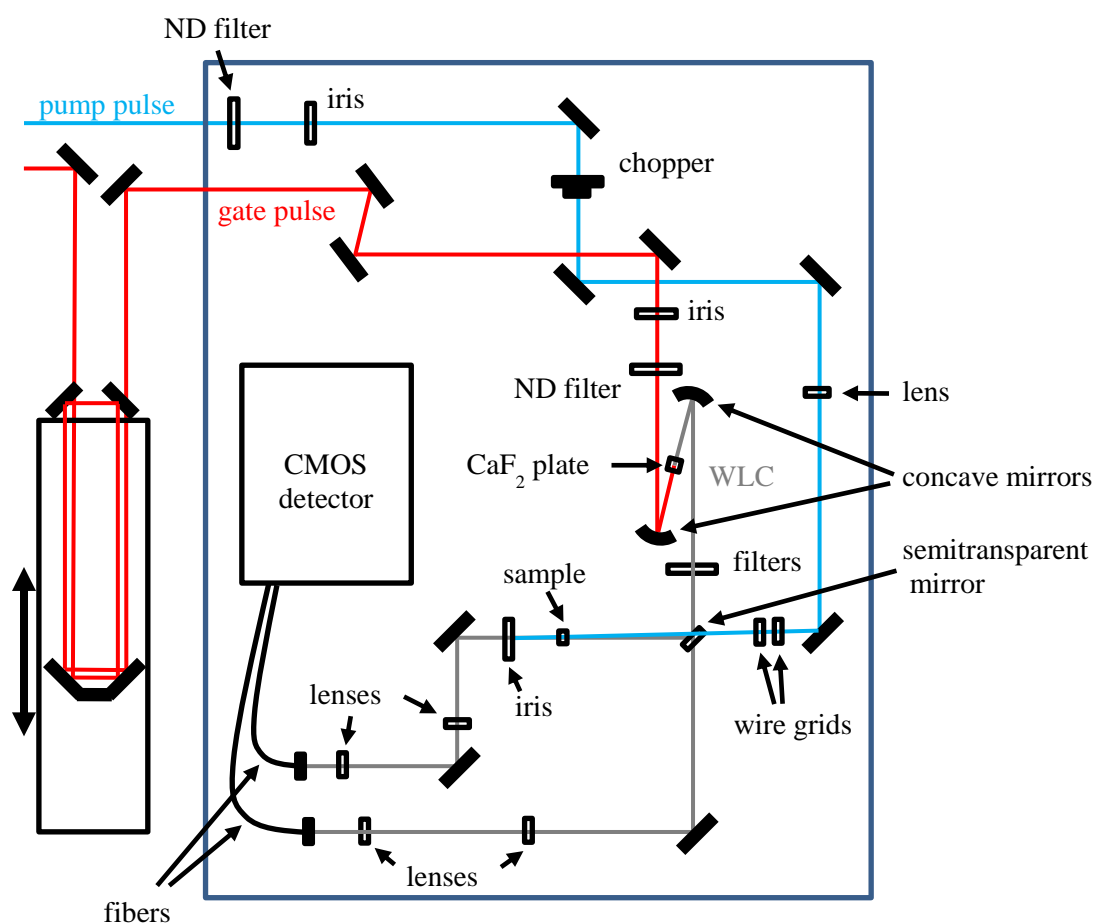


Figure 18 Layout of the transient absorption measurement setup. ND filter stands for neutral density filter.

In accordance to the fluorescence upconversion, the used pulses were generated in a “Solstice” Ti:Sapphire amplifier (Newport-Spectra-Physics) with a pulse length of 100 fs at 12500 cm^{-1} (800 nm) and a repetition rate of 1 kHz. The remaining part of the setup was a “Helios” transient spectrometer from Ultrafast Systems. One part of the amplifier output was used to seed an optical parametric

amplifier (Newport-Spectra-Physics, TOPAS) to obtain pump pulses with a pulse length of 140 fs at energies of 13800cm^{-1} (723 nm) and 15200cm^{-1} (660 nm). The pump pulse intensity was adjusted to ~ 800 nJ by a neutral density filter. The other part of the amplifier output was focused onto a moving calcium fluoride plate to generate the probe white light continuum between 23400cm^{-1} (410 nm) and 12100cm^{-1} (830 nm) which was polarised horizontally. The generation of the WLC could be influenced by the adjusting the gate pulse intensity by a neutral density filter and by adjusting the focus with concave mirrors. Subsequently, the WLC passed two coloured glass filters (BG 38 (Schott) and SP775 (Edmund Optics)) to block the gate pulse. Part of the probe pulse was cut off by a semitransparent mirror before the sample and monitored in a reference channel. The polarisation axis of the pump pulse was adjusted by two wire grids directly in front of the sample. The first wire grid was used to rotate the polarisation axis by 45° and with the second wire grid the polarisation axis of the pump was regulated between parallel, perpendicular and magic angle relative to the probe polarisation axis. The pump pulses at the different polarisation adjustments had intensities of $I_{\perp} = I_{\parallel} = 200$ nJ and $I_{\text{magic angle}} = 390$ nJ which were checked by a photo diode prior to the measurement. The pump and probe pulses overlapped in a 2 mm quartz cuvette equipped with a micro-stirrer with the pump pulse having at least a two times larger diameter than the probe pulse. Every second pump pulse was blocked by a mechanical chopper and the probe pulse was monitored (spectrograph with a CMOS sensor) after passing alternately the pumped and unpumped sample. From these two measurements absorbance difference spectra in ΔOD were calculated. The time delay between pump and probe pulses were altered to a maximum of 40 ps with a motorised, computer-controlled linear stage. The samples were dissolved in spectroscopic grade DCM with concentrations of $1 \cdot 10^{-4}$ - $2 \cdot 10^{-3}$ M and filtered prior measurement. To ensure sample stability, absorption spectra were recorded before and after the measurement. Furthermore, the probe spectral intensity maintained linearity when varying the pump pulse energy in the range of 50-400 nJ. Accordingly, simultaneous and sequential two-photon processes can be excluded in this energy range.

The analysis of the isotropic time resolved spectra was performed by a global fit with GLOTARAN.⁸⁵ Thereby, the unbranched unidirectional model was used to model the instrument response function, the white light dispersion (chirp) and the coherent artifact at time zero. Evolution associated difference spectra (EADS) and their respective time constants were obtained by this procedure. The number of independent components and the goodness of the fits were estimated by singular value decomposition.

The anisotropic data were analysed in a similar fashion described for the fluorescence upconversion by a self-written procedure based on MATLAB.⁹¹ The difference in optical density $\Delta OD_{\parallel}(t)$, $\Delta OD_{\perp}(t)$ and $\Delta OD_{\text{mag}}(t)$ were fitted globally at specific energies. The magic angle trace $\Delta OD_{\text{mag}}(t)$ was integrated into the fitting process to minimise measurement inaccuracies. These traces are related by equation 38.⁸⁴

$$\begin{pmatrix} \Delta OD_{\text{mag}}(t) \\ \Delta OD_{\parallel}(t) \\ \Delta OD_{\perp}(t) \end{pmatrix} = \begin{bmatrix} S(t) & 1 \\ S(t) & 1+2r(t) \\ S(t) & 1-r(t) \end{bmatrix} \otimes \text{IRF} \quad (38)$$

The fit was only possible at energies with small interference of the coherent artefact which was then tried to be represented by exponential functions likewise. However, the temporal window of the coherent artifact (<400 fs) is not interpretable as this signal distorts the anisotropy.⁹⁰

3.3.2. Nonlinear optical processes

Both TA and FUC are based on nonlinear optical processes that will be explained in the following. More specifically, the generation of a white light continuum in the TA measurements can be explained by the third order nonlinear effects of *self focusing*, *self-phase modulation*, *self-steepening*, *four wave mixing* and *stimulated Raman scattering*. The coherent artefact arises due to *cross-phase modulation*. Regarding FUC, the upconversion process is based on the second order nonlinear process of *sum frequency generation*. The description will refrain from a complete mathematical derivation but rather concentrate on the physical observations. For a more detailed overview about nonlinear optical processes the reader is referred to the following references.⁹²⁻⁹⁶

The interaction of light with a non-conducting medium, a dielectric, is the basis of all the discussed phenomena. In doing so, electromagnetic waves excite oscillations of electrons in the medium which lead to a separation of charges and thus induce a dipole moment. In other words the medium gets polarised. This polarisation P depends linearly on the strength of the electric field vector E of the electromagnetic wave at low intensity of radiation, e.g. by conventional lamps. However, laser radiation is so intense that the polarisation is a complicated nonlinear function of E . This complex dependency can be physically described by a power (Taylor) series of E as shown in equation 39.

$$P(E) = \chi^{(1)}E + \chi^{(2)}E^2 + \chi^{(3)}E^3 + \dots \quad (39)$$

The constant $\chi^{(1)}$ is the linear dielectric susceptibility and $\chi^{(2)}$, $\chi^{(3)}$ are the nonlinear dielectric susceptibilities of the second and third order, respectively. These constants are medium specific and describe the interaction strength between the radiation and the specific dielectric. In addition, the values of the constants decrease considerably with increasing order: $\chi^{(1)} \gg \chi^{(2)} \gg \chi^{(3)}$. Consequently, nonlinear effects are observed only at high light intensities as mentioned above. Furthermore, in materials with a symmetry center (in isotropic crystals) $\chi^{(2)}$ is zero, whereas $\chi^{(3)}$ exists in all materials. The susceptibilities are mathematically treated as tensors. These are matrices that describe the overall conversion of E^n to the polarisation P dependent on the space coordinates x , y and z . For example, the tensor of $\chi^{(1)}$ is a 3 x 3 matrix (equation 40) with the polarisation in x , y , and z direction P_x , P_y and P_z

(representing the rows) being constructed by interaction of the electronic field vectors E_x , E_y and E_z (representing the columns) with the medium dependent susceptibilities $\chi_{ij}^{(1)}$ ($i,j=1-3$).

$$\chi^{(1)} = \begin{pmatrix} E_x & E_y & E_z \\ \chi_{11}^{(1)} & \chi_{12}^{(1)} & \chi_{13}^{(1)} \\ \chi_{21}^{(1)} & \chi_{22}^{(1)} & \chi_{23}^{(1)} \\ \chi_{31}^{(1)} & \chi_{32}^{(1)} & \chi_{33}^{(1)} \end{pmatrix} \begin{pmatrix} P_x \\ P_y \\ P_z \end{pmatrix} \quad (40)$$

In case of an isotropic medium only the diagonal elements $\chi_{11}^{(1)}$, $\chi_{22}^{(1)}$ and $\chi_{33}^{(1)}$ are nonzero. For anisotropic media the susceptibilities deviate for the different space coordinates. The tensor of $\chi^{(2)}$ is consequently a 3 x 3 x 3 matrix for the interaction of $E_{x,y,z}^1$ and $E_{x,y,z}^2$ to yield $P_{x,y,z}$.

The refractive index of the medium, describing the speed of light in vacuum compared to the speed of light in that medium, is likewise dependent on the strength of the electric field vector E of the electromagnetic wave. This is expressed physically, as shown for P , by a power series of E (equation 41),

$$n(E) = n_0 + n_1 E + n_2 E^2 + \dots \quad (41)$$

with n_0 being the refractive index in the absence of the electric field used in conventional linear optics and n_1 and n_2 are higher coefficients of this series expansion of $n(E)$. It follows that in a medium the speed of light is dependent on the intensity of the electromagnetic wave. This is an important aspect of nonlinear optics and will be discussed in more detail later.

The refractive index can be related to the dielectric susceptibility by equation 42.

$$\chi^{(1)} = \frac{1}{4\pi} (n_0^2 - 1); \chi^{(2)} \cong \frac{1}{2\pi} n_0 n_1; \chi^{(3)} \cong \frac{1}{2\pi} n_0 n_2 \quad (42)$$

Consequently, the induced nonlinear polarisation can be described by the intensity dependent refraction index in that medium.

3.3.2.1 Second order nonlinear effects

As stated above, light can induce polarisation in a medium. Each component of this polarisation can be rationalised by characteristically oscillating dipoles which will in turn radiate and generate new electromagnetic waves depending on the induced polarisation. To describe this process, first off all the inducing electromagnetic wave and its electric field vector E have to be considered. In the case of a monochromatic plane wave the time dependency of E can be expressed as a cosine function (see equation 43),

$$E = E_n \cos(\omega_n t) \quad (43)$$

with the amplitude E_n and the frequency ω_n of the n-th electromagnetic wave. Equation 43 can now be inserted into equation 39 to describe the overall induced polarisation. In the following only the result for the linear and second order nonlinear polarisation shall be discussed. In addition, two light rays with varying frequencies ω_1 and ω_2 shall simultaneously polarise the medium. By doing so and with the help of trigonometric transformations equation 44 is obtained.

$$\begin{aligned}
 P(E) = & \underbrace{\chi^{(1)} E_1 \cos(\omega_1 t) + \chi^{(1)} E_2 \cos(\omega_2 t)}_{\text{linear polarisation}} + \underbrace{\frac{1}{2} \chi^{(2)} (E_1^2 + E_2^2)}_{\text{optical rectification}} + \underbrace{\frac{1}{2} \chi^{(2)} E_1 \cos(2\omega_1 t) + \frac{1}{2} \chi^{(2)} E_2 \cos(2\omega_2 t)}_{\text{SHG}} \\
 & + \underbrace{\frac{1}{2} \chi^{(2)} E_1 \cos(\omega_1 t + \omega_2 t)}_{\text{SFG}} + \underbrace{\frac{1}{2} \chi^{(2)} E_2 \cos(\omega_1 t - \omega_2 t)}_{\text{DFG}}
 \end{aligned} \quad (44)$$

The first two terms of equation 44 are linear polarisation components with the frequencies ω_1 and ω_2 of the inducing light beams. Accordingly, these polarisation components emit light of the same frequencies as the inducing electromagnetic waves. Second order nonlinear effects are expressed by the remaining terms. The third term describes an induced constant polarisation named “optical rectification” that will not be further discussed here. The last four terms are crucial for the following discussion. In these, the frequencies of the two electromagnetic waves ω_1 and ω_2 are altered. According to the fourth and fifth term, a nonlinear polarisation is induced and from this radiation is emitted that has twice the frequency of the inducing light rays $2\omega_1$ and $2\omega_2$. This process is called second harmonic generation (SHG). In addition, terms six and seven describe an oscillation of dipoles with the frequencies $\omega_1 + \omega_2$ and $\omega_1 - \omega_2$. Hence, these polarisation components are responsible for the radiation of electromagnetic waves with the sum and difference frequencies, respectively. The former is named sum frequency generation (SFG) and the latter difference frequency generation (DFG). It has therefore been shown that the frequency of high intensity electromagnetic waves can be changed by passing through media with nonlinear characteristics (see Figure 19).

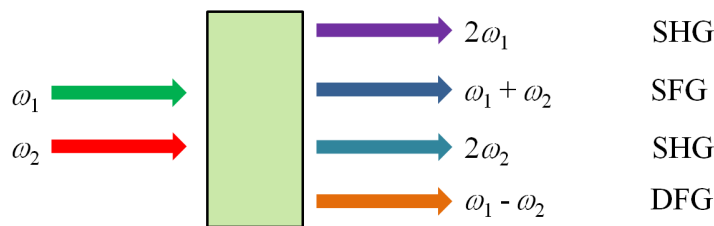


Figure 19 Frequency conversion of the incident beams with frequency ω_1 and ω_2 ($\omega_1 > \omega_2$) by second order nonlinear processes in a transparent medium.

This is utilised in the FUC setup, where the sum frequency of the fluorescence and the laser output (800 nm) is generated in a nonlinear crystal. The energy of the fluorescence is so to say “upconverted”. In equation 44 the condition of energy preservation is already included, which says that the emitted light, with frequency ω_3 , has to have the same energy as the light inducing the polarisation (equation 45).

$$\omega_3 = \omega_n \pm \omega_n \quad \text{with } n=1,2 \quad (45)$$

This holds true for all the above mentioned nonlinear processes. In addition, to prevent destructive interactions of the involved electromagnetic waves their momentum has to be preserved. The physical meaning is illustrated in the following. In the case of SFG, two light waves induce simultaneously a nonlinear polarisation with the frequency $\omega_1 + \omega_2$. The polarisation then relaxes immediately by radiating. When the inducing light waves travel collinear along the nonlinear medium, polarisation is induced that seemingly moves with the same speed and in the same direction as these two light waves. To observe a constructive amplification of the nonlinear effect, the emitted sum frequency light wave has to move with the same speed and in the same direction as the polarisation that emits it. This is expressed by the mutual relationship of the wave vectors k_i corresponding to the waves with frequencies ω_i . For the collinear case of SFG described above, equation 46 can be formulated,

$$k_3 = k_1 + k_2 \quad \text{or alternatively } \omega_3 n_3 = \omega_1 n_1 + \omega_2 n_2 \quad (46)$$

with n_i being the refractive index at the frequency ω_i .

This is called scalar phase matching, when the electromagnetic waves are collinear, and vector phase matching in the case of non-collinearity. Both are illustrated in Figure 20.

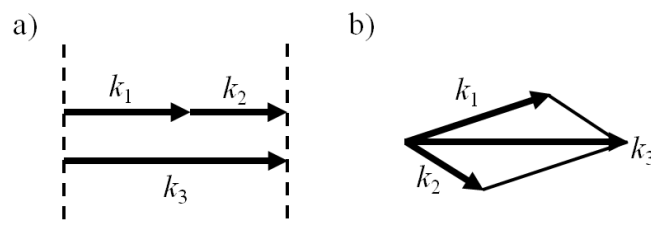


Figure 20 a) scalar and b) vector phase matching in the case of SFG.

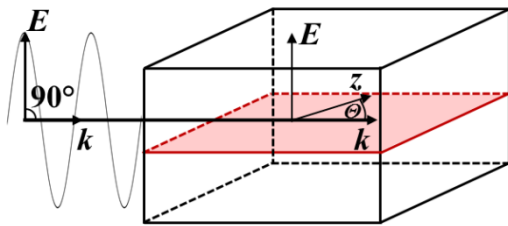
Equation 46 is hardly fulfilled in isotropic media as the refractive index is changing with the frequency of the light. This phenomenon is called dispersion and in general the higher the energy of the light the slower its propagation speed in a medium. Hence, to fulfill the phase matching condition a medium has to be chosen that counteracts the dispersion. This is realised in anisotropic crystals in which the refractive index of the trespassing light is as well dependent on its polarisation axis. A distinction is made between uniaxial and biaxial crystals. For the sake of simplicity only the former shall be

overviewed in the next section. Consistently, biaxial crystals are not used in the measurement setups discussed below.

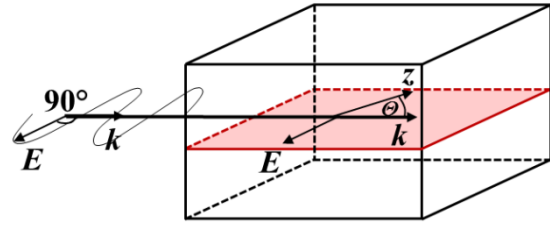
3.3.2.2 Uniaxial crystals

Uniaxial crystals (e.g. potassium dihydrogen phosphate (KDP) or beta-barium borate (BBO)) are birefringent (or birefractive) and possess one specific optical axis z . The wave vector k of the trespassing light and the axis z define the so called principal plane (red) (see Figure 21).

a) ordinary beam



b) extraordinary beam



c)

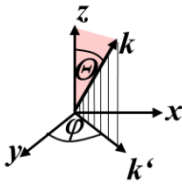
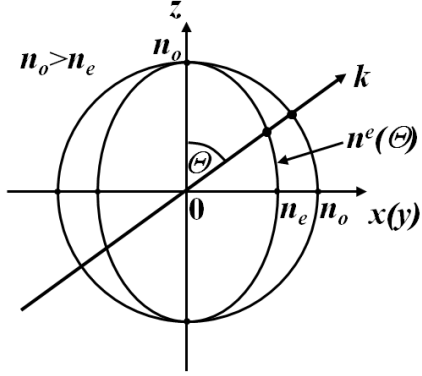


Figure 21 Principal plane (red) of an anisotropic crystal and a) ordinary beam and b) extraordinary beam. In c) the polar coordinate system, described by θ and φ is depicted. The vector k is the wave vector, z the optic axis and k' the projection of k onto the x,y -plane.

The specification of this type of crystal is that electromagnetic waves that are polarised perpendicular to the principal plane, called ordinary or o-beams, experience a constant refractive index n_o . Whereas those polarised parallel to the principal plane, called extraordinary or e-beams, feature a refractive index $n^e(\theta)$ dependent on the angle θ between k and z . The birefringence is quantified by the difference in the refractive index Δn between n_o and $n^e(\theta)$. The extrema of the extraordinary refractive index are $n^e(0^\circ) = n_o$ and $n^e(90^\circ) = n_e$. The values n_o and n_e are called the principal values of the refractive index. The crystal is positive uniaxial if $n_o < n_e$ and negative uniaxial if $n_o > n_e$. The azimuthal angle φ , defined as the angle between the x axis and the projection of k on the x,y -plane, describes the three dimensional position of the principal plane in the crystal. The refractive index of a light wave is independent of φ . In summary, in a birefringent crystal the refractive index of an electromagnetic wave can be adjusted by its propagation direction and the polarisation axis. This can

be illustrated geometrically by plotting the refractive indices of the o-beam and e-beam as a function of Θ (Figure 22).

a) negative uniaxial crystal



b) positive uniaxial crystal

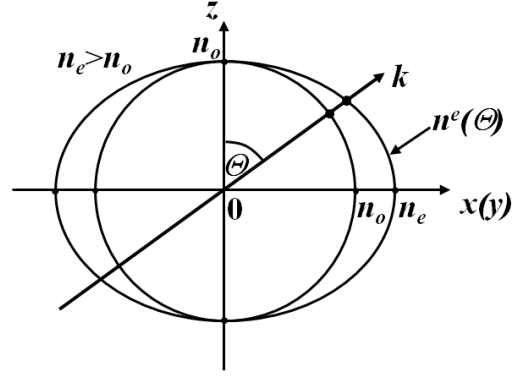


Figure 22 Dependence of the refractive index of the ordinary and extraordinary beam on the propagation direction in a) negative and b) positive uniaxial crystals.

In doing so the o-beam has the electric field vector E pointing normal to the plane of drawing. Its refractive index is independent of Θ , in which case a circle with radius n_o is obtained. In contrast, E of the e-beam is located in the plane of drawing and as the refractive index is dependent on the angle between the wave vector k and the optical axis z an ellipse is obtained. Its maximum (for a positive crystal) or respectively minimum (for a negative crystal) values n_e are observed at $\Theta = 90^\circ$. With the help of these diagrams it is therefore possible to determine the refractive indices of the o- and e-beam at various values of Θ .

To obtain phase matching for the SFG the two mixing and the resulting upconverted signals have consequently to be polarised differently. There are several possibilities to do so in uniaxial crystals which are shown in Table 1. To explain the notation, the phase matching condition as given in equation 47 is named “ooe” phase matching, the first letter describing the polarisation direction of the wave with the lowest frequency and the third letter that of the wave with the highest frequency.

$$k_{o1} + k_{o2} = k_3^e(\Theta) \quad \text{with } \omega_1 < \omega_2 < \omega_3 \quad (47)$$

In this situation the mixing light rays are o-beams polarised normal to the principal plane. In contrast, the upconverted signal is an e-beam polarised parallel to the principal plane with its refractive index depending on Θ . The different possibilities are categorised by type I and II depending on the polarisation of the mixing light rays and by (+) and (-) if the phase match conditions hold true for positive or negative uniaxial crystals.

Table 1. Phase matching conditions of type I and II for positive (+) and negative (-) uniaxial crystals.

crystal type	type I	type II
positive uniaxial	eeo	oeo, eoo
negative uniaxial	ooe	oeo, eoe

These phase matching conditions deviate in the efficiency of the nonlinear process at various light frequencies and in Θ which is both discussed below. It is possible to determine the angle Θ for these phase matching conditions mathematically⁹² or geometrically. This is shown for scalar and vector “ooe” / Type I⁽⁻⁾ phase matching in Figure 23. However, instead of the refractive indices as in Figure 22 the wave factors (see equation 47) for all involved light waves are illustrated in dependence of angle Θ with both the ordinary and extraordinary polarisation. The interception of the respective circles and ellipses mark the wave factor with optimal phase matching.

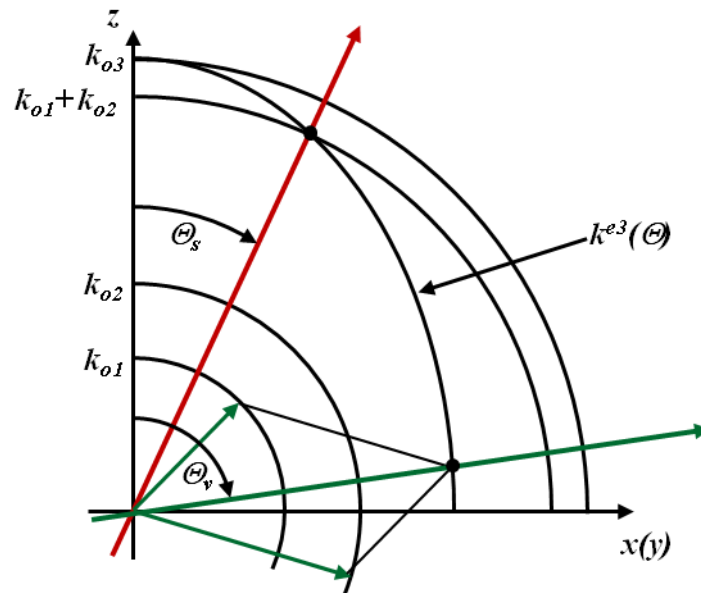


Figure 23 Scalar (red) and vector (green) phase matching of type I in a negative uniaxial crystal with phase matching angles Θ_s and Θ_v , respectively. The coordinates are given in wave vectors k .

Hitherto, one effect of birefringence was disregarded in determining the phase matching. That is, the propagation direction of an extraordinary beam in an anisotropic crystal is generally not parallel to that of an ordinary beam although their wave vectors k are pointing in the same direction before immersing into the medium. The difference in direction is quantified by the so called “walk-off” angle $\rho(\Theta)$. It is an often demonstrated characteristic of birefringent crystals to divide a light ray into two parts (see Figure 24), the o- and the e-beam.

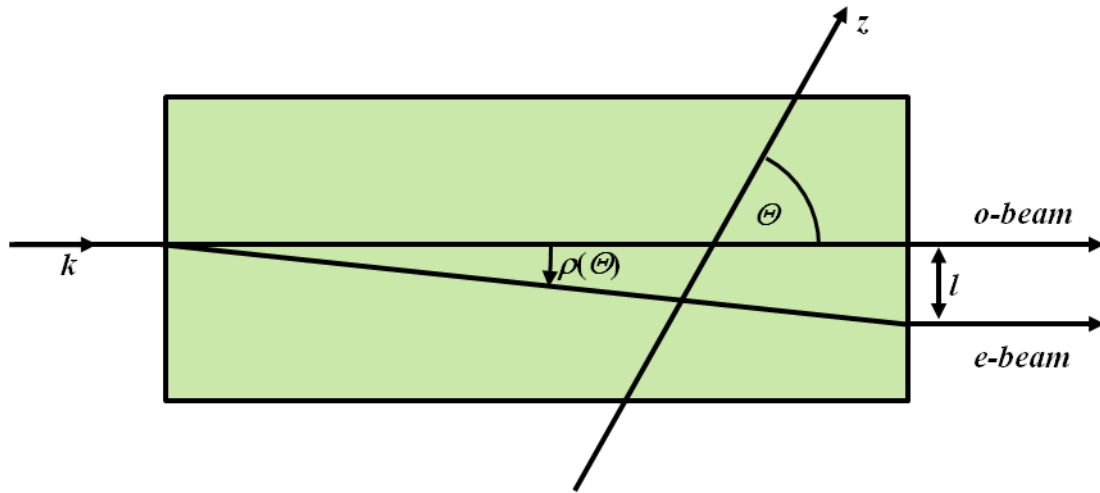


Figure 24 Birefringence in an anisotropic crystal. The quantity $\rho(\Theta)$ is called the “walk-off” angle.

These two light rays leave the medium after all with parallel propagation directions, however with a distance l . This distance as well as the “walk-off” angle are depending on the angle Θ which can therefore be determined experimentally by measuring l of an anisotropic crystal. The “walk-off” is strongest in the region of Θ , where small changes of Θ lead to great changes in the refractive index $n^e(\Theta)$. The described effect can be explained by the induced linear polarisation. In the case of the ordinary beam, the refractive index is independent on the entrance angle. The medium can therefore be treated as isotropic so that the tensor of $\chi^{(1)}$ describing the linear polarisation becomes diagonal. Accordingly, the polarisation has a vector parallel to the inducing light wave and the o-beam does not change the propagation direction in the medium. In contrast, the tensor of the linear susceptibility $\chi^{(1)}$ for an e-beam has off-diagonal elements in this anisotropic environment. The result is that the induced polarisation vector and with that the emitted wave need not have the same direction as the inducing wave. In general, the e-beam is deflected so that $n^e(\Theta)$ is decreasing and the speed of the light wave is increasing. The propagation directions of the e-beam can be geometrically determined by the normal to the tangent drawn at the intersection point of k with the $n^e(\Theta)$ ellipse (see Figure 25).

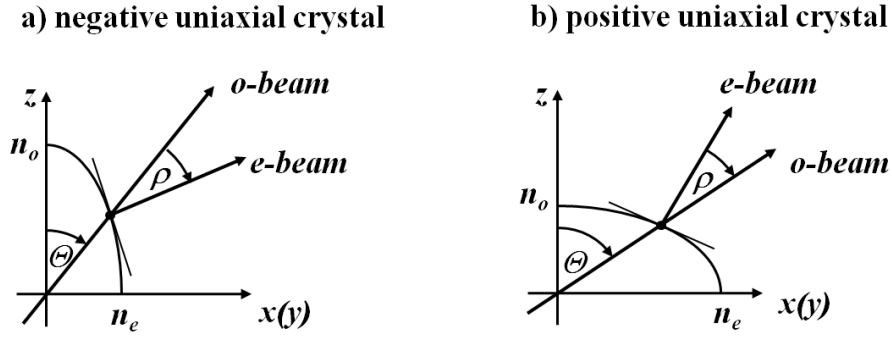


Figure 25 “Walk-off” angle ρ between the ordinary and the extraordinary beam in a negative and a positive uniaxial crystal.

The described “walk-off” effect complicates the phase-matching considerations discussed above. A more accurate description of phase matching goes however beyond the scope of this discussion.

The quantity that describes the efficiency of an anisotropic crystal to induce second order-nonlinear effects is d_{eff} . It is derived from the susceptibility tensor $\chi^{(2)}$ first by reducing the number of tensor elements needed due to symmetry considerations of the involved anisotropic crystals space group. The mathematically transformed tensor d_{il} is obtained with $i = 1, 2, 3$ corresponding to x, y, z , respectively, and $l = 1-6$ to the “planes” $XX, YY, ZZ, YZ, XZ,$ and XY , respectively. In the second step d_{il} is adapted to the polarisation conditions of phase matching given above and by conversion to the polar coordinate system with angles θ and ϕ (see Figure 21), d_{eff} is yielded. See Table 2 for the d_{eff} expressions of two space groups $I42d$ and $R3c$ of two widely used anisotropic materials, namely potassium dihydrogen phosphate (KDP) and beta-barium borate (BBO), respectively.

Table 2. Expressions for d_{eff} in uniaxial anisotropic crystals with the listed point group and phase matching conditions.

space group	$d_{\text{eff}}(\text{ooe}, \text{oeo}, \text{eoo})$	$d_{\text{eff}}(\text{eoo}, \text{eoe}, \text{oeo})$
$I42d$ (KDP)	$d_{36} \sin \theta \sin 2\phi$	$d_{36} \sin 2\theta \cos 2\phi$
$R3c$ (BBO)	$d_{31} \sin \theta - d_{22} \cos \theta \sin 3\phi$	$d_{31} \cos^2 \theta \cos 3\phi$

It can be seen that d_{eff} is dependent in all cases on up to two tensor elements d_{il} , which can be determined experimentally and are listed in the literature.⁹² In addition, both angles θ and ϕ are relevant for the effective nonlinearity of the crystal. To minimise reflection and diffraction at the crystal surface the commercially available anisotropic crystals are manufactured in such a way that for the respective SFG process both angles θ and ϕ have optimum values when correctly polarised laser pulses advance into the crystal normal to the surface plane.

The overall conversion efficiency of the sum-frequency generation is given in equation 48. This equation is valid only in the plane-wave fixed-field approximation. This means that it holds true only if the effects of diffraction, anisotropy, dispersion, heat, linear and nonlinear absorption and group-velocity mismatch to the SFG process are neglected.

$$\frac{P_3}{P_1} = \frac{2^3 \pi^2 d_{\text{eff}}^2 L^2 P_2}{\varepsilon_0 c n_1 n_2 n_3 \lambda_3^2 A} \cdot \frac{\sin^2(|\Delta k|L/2)}{(|\Delta k|L/2)^2} \quad \text{with } \Delta k = k_1 + k_2 - k_3 \quad (48)$$

In the case of fluorescence upconversion the conversion efficiency is defined as the ratio of the pulse powers of the produced, upconverted light P_3 to that of the fluorescence P_1 . It is dependent on the pulse power of the laser output P_2 , on the square of the effective linearity of the medium d_{eff} , the square of the crystal length L , the refractive indices of the involved pulses n_{1-3} , the square of the wavelength of the upconverted signal λ_3 and the cross sectional area of the combined laser beams A . Furthermore, the second term in equation 48 describes the effect of phase mismatch. With this formula it is possible to estimate the performance of different crystals in the fluorescence upconversion as well as to identify medium independent quantities that can be used to adjust the conversion efficiency. Crystal dependent quantities are d_{eff} and n_{1-3} and can only be varied by exchanging the crystal. In contrast, the quantities P_2 and A are dependent on the measurement setup and can be adjusted easily by controlling the power and focus of the laser pulses. It has to be kept in mind that by increasing the intensity of the pulses nonlinearities of higher order can be induced in the medium which can damage the crystal or corrupt the experiment. From equation 48 it follows furthermore that an increasing conversion efficiency is observed when increasing the crystal length. This is however misleading as with very short pulses the group velocity mismatch becomes relevant. This effect describes a temporal “walk-off” of pulses with different frequencies or polarisation directions in a transparent medium. To circumvent this group-velocity mismatch, the crystals have to be thinner the shorter the used pulses.

3.3.2.3 Third order nonlinear effects

In the following chapter nonlinear effects of the third-order shall be discussed, which are relevant for the ultrafast transient absorption measurement. In order to describe these phenomena a brief introduction to the characteristics of ultrafast light pulses is given.

An ultrafast laser pulse can be described as a superposition of electromagnetic waves with a slightly different frequency (see Figure 26). These waves have a strict phase relation which means that at one point all waves are interacting constructively- are in phase- describing the centre of the intensity envelope of the pulse. The latter is assumed to be Gaussian. The more waves with different frequencies are present, the temporally shorter the pulse can be. There are two important velocities to be explained. The phase velocity v_p is the speed of a single wave with frequency ω along the propagation direction. The group velocity is the speed of the intensity envelope of the pulse.

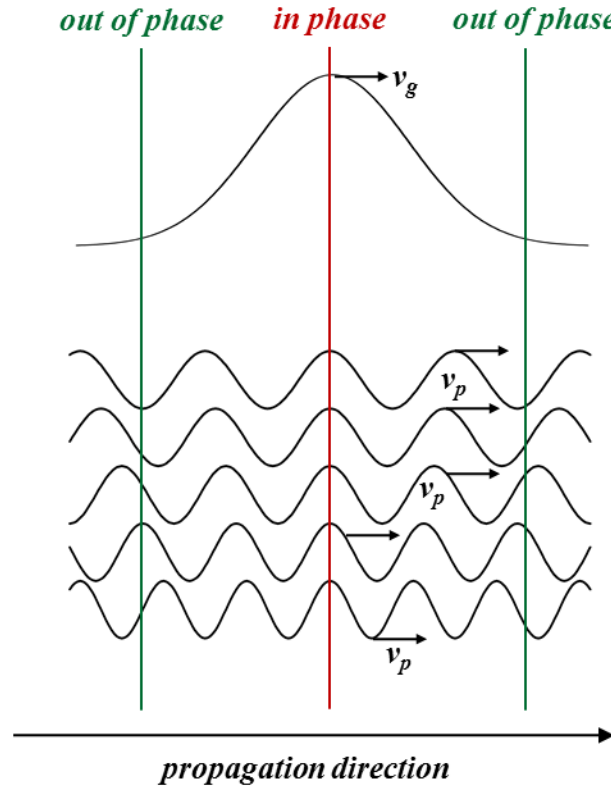


Figure 26 Group velocity v_g of the Gaussian intensity envelope of a modeled ultrafast light pulse and phase velocities v_p of several light waves constituting the pulse.

These two velocities are equal when the pulse travels through vacuum but in general deviate in a medium. The phase velocity v_p of a single wave with frequency ω_i depends on the refractive index in the medium following equation 49.

$$v_p = \frac{c}{n_0(\omega_i) + n_2 E} \quad (49)$$

In an isotropic medium the refractive index consists of a linear term $n_0(\omega_i)$, that is frequency dependent, and a third-order nonlinear term, that is intensity dependent $n_2 E$ (see equation 41). Due to the linear term, waves with higher frequencies have a different propagation speed v_p as those with lower frequencies, which is called dispersion. Consequently, the intensity envelope of the pulse broadens when traveling through a medium. Regarding the nonlinear term of the refractive index, two domains have to be considered: time and space.

Self-focusing (space domain)

The spatial intensity distribution of the pulse normal to the propagation direction can be described by a Gaussian similarly to the temporal intensity distribution shown in Figure 26. The spatial impact of nonlinearity is shown in Figure 27. Thereby it is assumed that the waves respond instantaneously to changes of the refractive index.

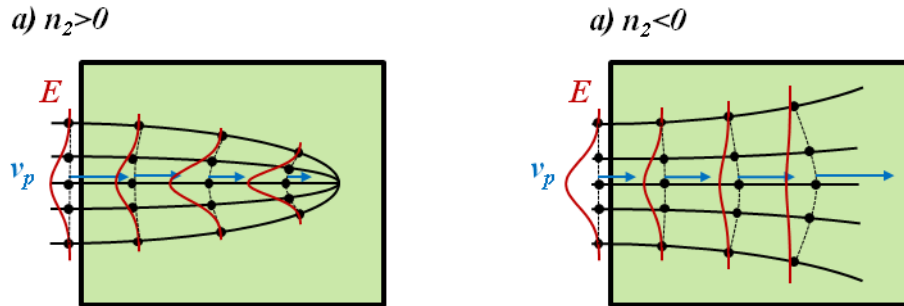


Figure 27 The intensity dependent phase velocity leads to self-focusing for $n_2 > 0$ and to self-defocusing for $n_2 < 0$. In the former case v_p is decreasing, in the latter case v_p is increasing strongest in the pulse centre what causes the intensity envelope to contradict or disperse, respectively. In the case of self-focusing the theoretical beam collapse is shown in the absence of diffraction or other nonlinear effects.

The wave front gets distorted because the phase velocity of the waves in the centre of the pulse deviates from that at the edges due to the difference in intensity. As a consequence, the propagation direction of the waves is altered. This can be compared to the effect of a positive or negative lens, depending on the sign of n_2 . In the former case, $n_2 > 0$, the spatial pulse width is decreasing which is named *self-focusing*. For $n_2 < 0$, *self-defocusing* is observed. There exists a threshold E_{sf} for the light intensity below which self-focusing cannot be observed due to diffraction. Accordingly, only high intensity ultrafast light pulses experience self-focusing. The pulse should collapse theoretically in a single point (Figure 27) because this effect is cumulative. However, with increasing intensity more nonlinear effects, like stimulated Raman scattering or multi-photon absorption, can be observed which decrease the intensity of the pulse and thus counteract the self-focusing. These phenomena are discussed below.

Self/cross-phase modulation and self-steepening (time domain)

The effects in the time domain are similar to those described for the space domain. Intensity localisation, like self-focusing in the space domain, is thus also detected in the time domain. The temporal width of the pulse is thus decreasing ($n_2 > 0$) or increasing ($n_2 < 0$) due to the third-order nonlinearity. In the same way self-focusing is counterbalanced by diffraction, the intensity localisation in time is impeded by dispersion. In addition, the effect of *self-phase modulation* is observed in the time domain. This is demonstrated in Figure 28 for $n_2 > 0$.

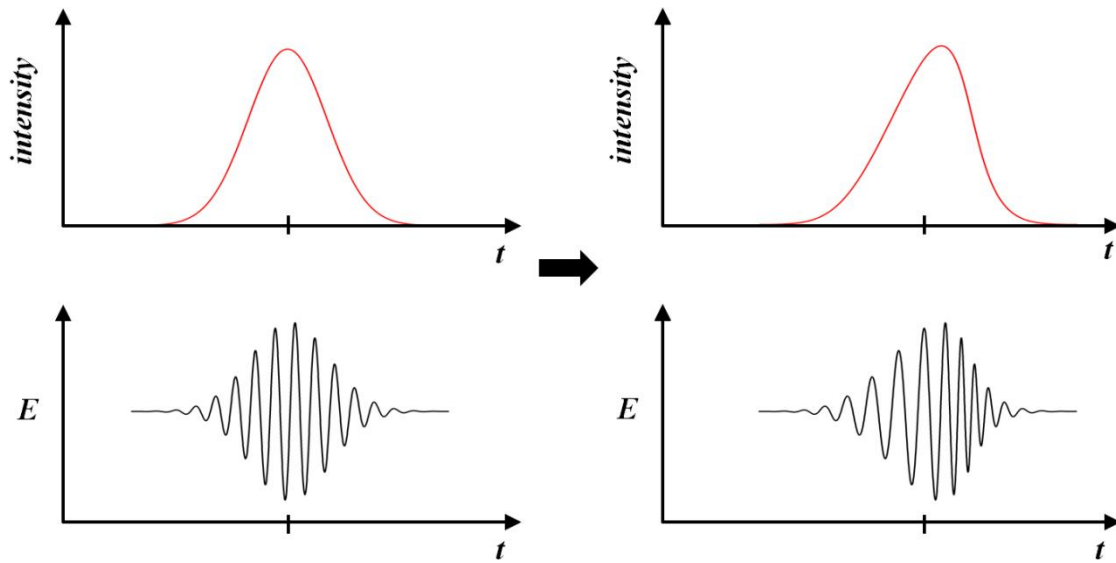


Figure 28 The sketch indicates the impact of the intensity dependent phase velocity ($n_2 > 0$) onto the temporal intensity envelope of the pulse (red) and the frequency of the wave.

The wave is compressed in the rear part of the pulse and stretched in the leading part of the pulse by reducing the phase velocity more strongly in the centre of the pulse. Therefore, higher energy light is produced in the rear part and lower energy light in the leading part as this is equivalent to a frequency change. Consequently, the frequency spectrum of the pulse is broadened. The self-phase modulation is more pronounced for steeper intensity changes. Thus, the spectral broadening is generally stronger for shorter pulses. Moreover, due to the intensity dependent phase velocity the intensity envelope of the pulse can be distorted. This leads to a steeper front in the trailing part of the pulse whereas the leading edge is flattened for $n_2 > 0$. This is called *self-steepening* and induces a frequency change which is more pronounced to higher energies (Figure 29).



Figure 29 The Sketch indicates the frequency changes of an ultrafast light pulse experiencing self-phase modulation in combination with self-steepening with $n_2 > 0$.

As stated above, the self-focusing process can be regulated by multi-photon absorption processes. That is, several photons will simultaneously excite the medium so that electrons can be transferred from the valence band of the medium to its conduction band. These electrons are then essentially free and will

oscillate with the laser field. With that a new term to the nonlinear change of the refractive index is induced and will enhance the self-phase modulation.⁹⁷ The spectrally broadened pulse retains the directional properties of the inducing pulse.^{97,98}

The concept of self-phase modulation can further on be applied to a second pulse that temporally and spatial crosses the high intensity pulse. This is called *cross-phase modulation*. The second pulse will experience the same change in the refractive index as the high intensity pulse and a similar change in the frequencies in the second pulse will occur.

In summary, self-focusing in combination with self-phase modulation can cause a spectral broadening of a high intense, ultrafast light pulse when passing through a transparent medium. The observed broadened spectrum can range between 400 – 1500 nm, covering the whole visible spectrum, and is called in this case white-light continuum (WLC). A WLC is an important element of the ultrafast transient absorption setup.

Four wave mixing and stimulated *Raman* scattering

Besides the self-phase modulation, *four wave mixing* in combination with *stimulated Raman scattering* can be likewise responsible for WLC generation.⁹⁹ We have seen for the second order susceptibility that two light pulses can be mixed to obtain a third pulse with added or subtracted frequency. By similar reasoning the third order susceptibility can be responsible for an interaction of four electromagnetic waves, also called *four wave mixing*. Again, the criteria for a constructive interaction are energy and momentum conservation. It can be thought of a huge amount of possible mixing conditions with valid criteria, but the following discussion will focus on those responsible for the WLC generation. Before these are presented a further effect has to be considered. Until now, it was assumed that only electronic dipoles are contributing to the polarisation. It has been neglected that atomic motions can affect electron motion, too. Accordingly, nuclear vibrations with specific symmetry can alter the induced polarisation. In this case, the dielectric susceptibilities have to be corrected by a term characterising these nuclear modes.¹⁰⁰ This is done for $\chi^{(1)}$ in equation 50, the first term being the linear dielectric susceptibility in the hypothetical absence of nuclear modes and the second term describing the coupling between electronic and nuclear (Q) coordinates. The shown correction term is the first term of a Taylor series.

$$\chi^{(1)}(t) = \chi_0^{(1)} + \left(\frac{\delta\chi^{(1)}}{\delta Q} \right)_0 Q(t) + \dots \quad (50)$$

According to this correction the frequency of the polarisation and therewith that of the emitted light can be up ($\omega_{as} = \omega_p + \omega_v$) or down shifted ($\omega_s = \omega_p - \omega_v$) by the frequency of vibrations of the medium (ω_v) in comparison to that of the inducing light wave (ω_p) (see Figure 30). This is called *Raman*

scattering. The down shifted frequencies are called *Stokes* and up shifted *anti-Stokes* ω_s and ω_{as} , respectively.

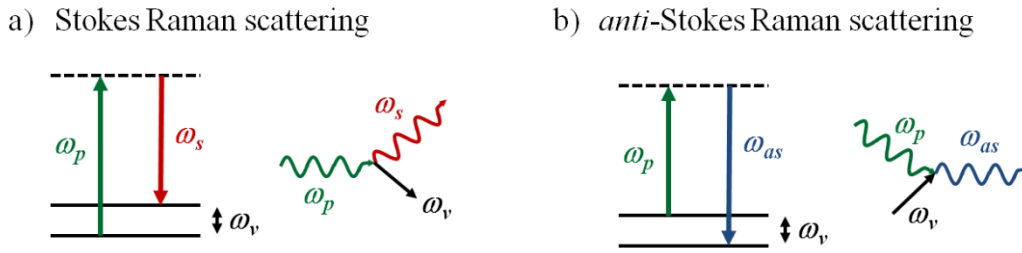


Figure 30 Energy diagrams for spontaneous Stokes and anti-Stokes Raman scattering.

In the linear case, this process is spontaneous which means that the vibration in the medium and electromagnetic wave inducing the polarisation are generally not in phase. Hence, the Raman signal is likewise not in phase with the light wave generating the polarisation and is emitted in all three space directions. This is the starting point for the generation of a WLC. If this spontaneous Raman signal generated by a high intensity light pulse is incidentally in phase with the latter, stimulated Raman processes can be observed. These are in general four wave mixing interactions in the third-order nonlinear regime with the condition that the energies of the four light waves differ by multiples of ω_v . In Figure 31 energy diagrams are depicted which characterise the stimulated Raman scattering.

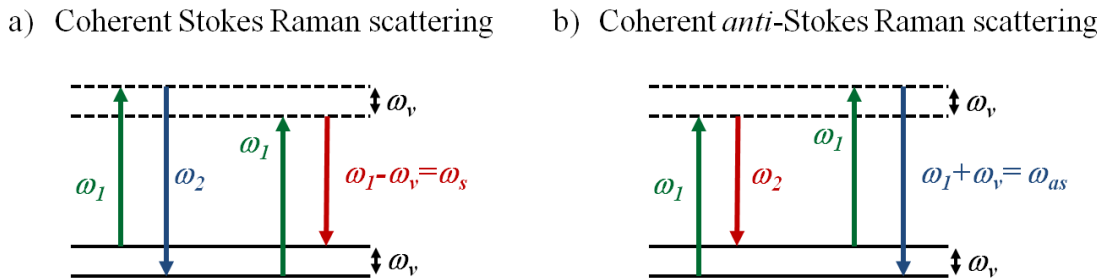
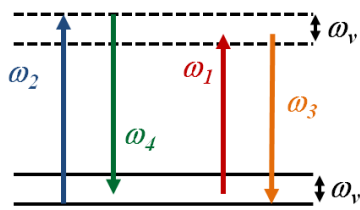


Figure 31 Energy diagrams for the coherent Stokes Raman scattering (CSRS) and the coherent *anti*-Stokes Raman scattering (CARS).

The difference between the spontaneous and stimulated case is that in the latter formally two light waves with frequencies ω_1 and ω_2 can induce a nonlinear electron motion with a different frequency ($\omega_1 - \omega_2 = \omega_v$), which in turn can drive the nuclear mode with the same frequency ω_v . In this case the nuclear mode, the induced polarisation and the inducing light waves are all in phase. A third light wave interacts with this induced polarisation which can yield a coherent (having a strict phase relation) Stokes Raman scattering (CSRS) signal or a coherent *anti*-Stokes Raman scattering (CARS) signal, depending on the selection of the wave frequencies. By traversing through the medium the Stokes and anti-Stokes signals will rise in intensity so that they in turn produce second order Stokes and anti-Stokes signals and so on. As a result, the stimulated Raman scattering can be responsible for the

appearance of a series of peaks with fixed frequency intervals in the spectrum of the ultrashort light pulse (see Figure 33). The intermediate frequencies are generated by conventional four-wave mixing without the involvement of nuclear modes so that a WLC is obtained. The energy conservation condition of this four-wave mixing is of the form $\omega_1 + \omega_2 = \omega_3 + \omega_4$ with ω_1 and ω_2 being the frequencies of two adjacent Raman signals and $\omega_3 + \omega_4$ frequencies between the Raman signals ($\omega_1 < \omega_3 < \omega_4 < \omega_2$). This is depicted in Figure 32.

a) energy diagram



b) wave vector diagram

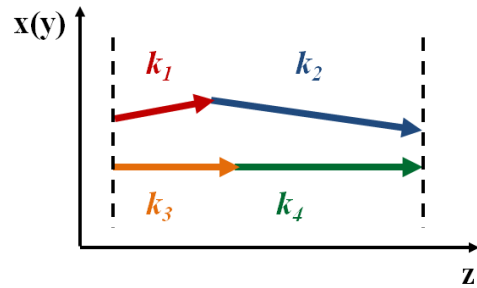


Figure 32 a) Energy and b) wave vector diagrams of four-wave-mixing with the following conditions: $\omega_1 + \omega_2 = \omega_3 + \omega_4$ and $\omega_1 < \omega_3 < \omega_4 < \omega_2$

The Raman signals are in general more intense as signals generated by conventional four wave mixing. This can be reasoned by the dielectric susceptibility increasing in magnitude when nuclear motions are participating. Accordingly, in these WLC spectra intensity peaks can be observed at fixed frequencies besides the central frequency of the pulse (see Figure 33).

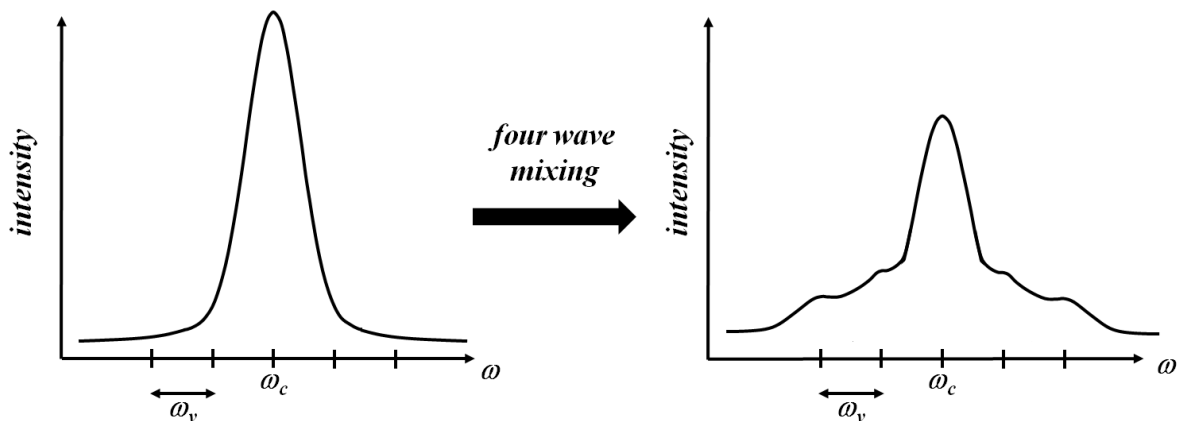


Figure 33 The Sketch indicates the frequency changes of an ultrafast light pulse experiencing four-wave mixing in combination with stimulated Raman scattering with $n_2 > 0$.

To this point only energy conservation was regarded, however as could be seen in the SFG chapter, momentum considerations are vital. The four wave mixing is a constructive interaction when equation 51 is valid.

$$k_1 + k_2 = k_3 + k_4 \quad \text{or alternatively} \quad \omega_1 n_1 + \omega_2 n_2 = \omega_3 n_3 + \omega_4 n_4 \quad (51)$$

This can be discussed geometrically with vectors (Figure 32). In general it is not possible to conserve momentum in a completely collinear setup. Nonetheless, these interactions are observed for WLC generation because self-focusing of the pulse relaxes the phase matching conditions. In this case, the refractive indices are adjusted by the intensity of the participating waves and phase matching must be strictly adhered to only longitudinal (in the z-direction), whereas a certain phase mismatch in the transverse direction (in x and y direction) is allowed.⁹⁹ As a consequence, self-focusing is the fundament of this type of WLC generation. Furthermore, only waves within a narrow frequency range can interact constructively to satisfy the transverse phase mismatch limit. Accordingly, the WLC is built up from the centre gradually to the edges. In addition, the spectrally broadened pulse shows an enlarged spatial divergence in respect to the inducing pulse.

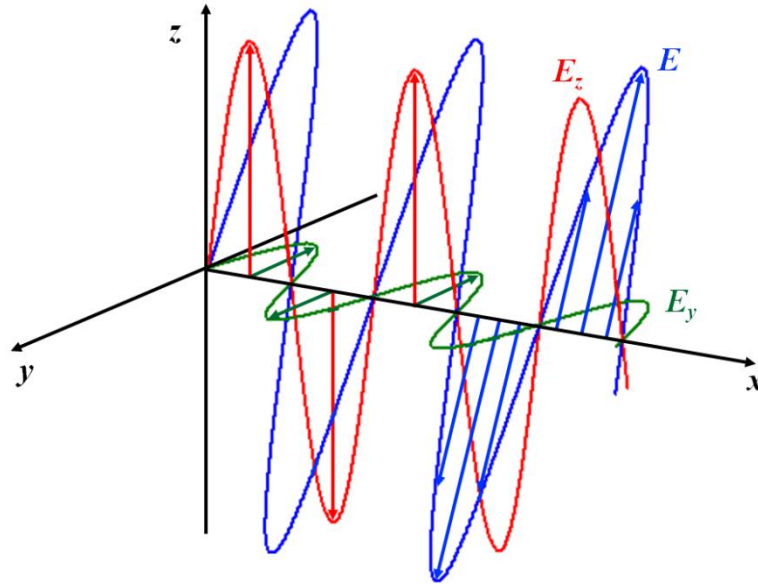
A white light continuum can be experienced only when the intensity of the inducing pulse E exceeds a threshold E_{th} and only in materials with a bandgap E_{gap} larger than E_{th} .⁹⁷ The threshold E_{th} is consistent with the intensity needed to observe self-focusing E_{sf} . Hence, it is assumed that in all cases self-focusing triggers the generation of the continuum. The exact mechanism for the white light generation is difficult to identify. It is however assumed that self-phase modulation is the dominating interaction for femtosecond pulses with intensities near E_{th} , whereas stimulated Raman scattering and four-wave mixing can be important at higher pulse intensities and for picosecond and nanosecond pulses. The width of the white-light continuum increases with increasing E_{gap} . At high values of E ($E \gg E_{th}$) complex nonlinear effects can be observed so that small fluctuations in the inducing pulse lead to strongly varying WLC properties. Consequently, E has to be adjusted experimentally so that a WLC can indeed be generated but destabilising effects are avoided. It was reported, that the polarisation direction of the inducing pulse should be virtually retained in condensed matter despite spectral broadening.^{101,102} However, it has been shown that the polarisation directions of the WLC and the inducing pulse are increasingly deviating with rising pulse intensities due to nonlinear effects like plasma formation.¹⁰³ Moreover, for isotropic crystals with cubic structure, e.g. CaF_2 or LiF , nonlinear birefringence was observed which altered the polarisation direction of the WLC depending on the inducing pulses angle of incidence into the medium.¹⁰²

3.3.3. Polarisation/Anisotropy

To characterise the mutual orientation of the electric field of multiple light waves the concepts of polarisation and anisotropy are introduced.¹⁰⁴ This is of importance as energy transfer processes in molecules can change the orientation of the exciting electric field. The term polarisation is used in this thesis only for the description of beams and anisotropy for samples. This is to avoid confusion about the meaning of the term polarisation with that discussed in the prior chapter. To describe the

orientation of E a coordinate system is introduced with the x axis being the propagation direction of a light wave and the z and y axes being perpendicular to each other and to the x axis (see Figure 34).

a) linear polarisation



b) circular polarisation

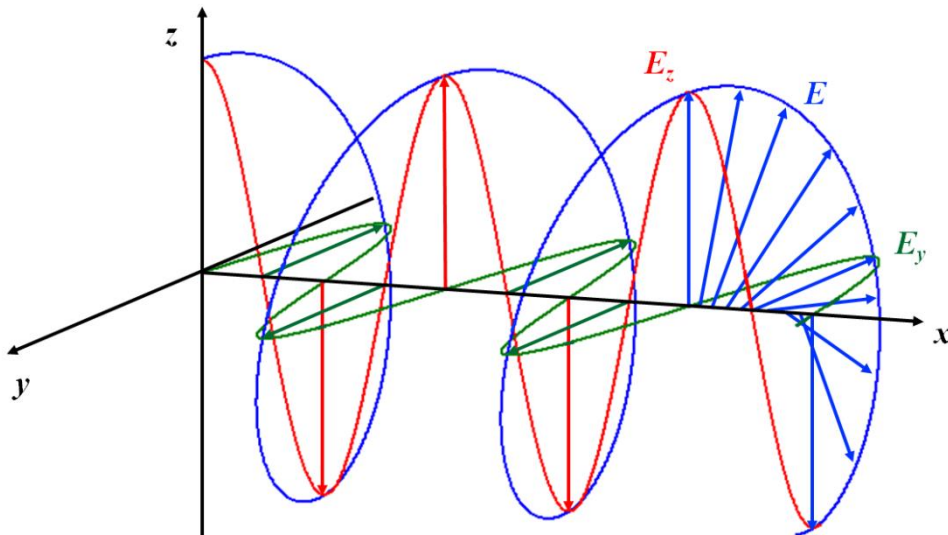


Figure 34 a) linear polarised light with E_z and E_y in phase and b) circular polarized light with E_z and E_y out of phase.

The wave factor E is then projected onto the z and y axes to obtain E_z and E_y . If these two formed waves are in phase the electromagnetic wave is said to be linear polarised, else wise elliptic or as a special case circular polarisation is observed (see Figure 34). The following discussion is focused on linear polarisation because it is generally used to test for energy transfer processes. Until now only a single light wave was considered, however a light beam consists of innumerable light waves. In this context, linear polarised means that E of every light wave is furthermore oriented in the same direction. A measure thereof is the polarisation P which is defined as the intensity of the polarised component in z direction $I_z - I_y$ divided by the total intensity of E perpendicular to the propagation direction $I_z + I_y$ (see Figure 35 and equation 52). When the polarisation of a light beam is referenced to a beam polarised linearly along the z -direction, the intensities I_z and I_y can be classified into being oriented parallel or perpendicular to the reference beam polarisation direction. It follows that $I_z = I_{\parallel}$ and $I_y = I_{\perp}$.

$$P = \frac{I_z - I_y}{I_z + I_y} = \frac{I_{\parallel} - I_{\perp}}{I_{\parallel} + I_{\perp}} \quad (52)$$

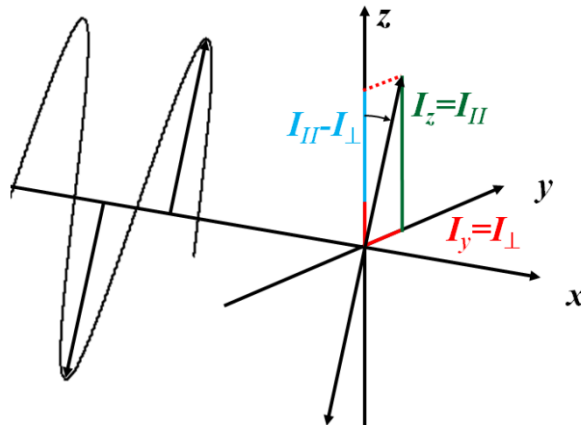


Figure 35 Projection of the intensity of a linear polarized light wave onto the z and y axes. The x axis is the propagation direction of the light wave.

By definition P has a range of values between 1 and -1, the maxima representing the case of strictly linear polarised light along the z and y axes, respectively (see Table 3). A random orientation of the electric field vectors yields a value of $P = 0$.

In contrast to the polarisation, the anisotropy considers furthermore the third dimension and is usually monitored time dependently. Here again the z axis is the reference orientation. The time dependent anisotropy $r(t)$ is defined as the time dependent intensity of the polarised component in z direction $I_z(t) - I_y(t)$ divided by the total intensity of E . The total intensity is the intensity sum along all three axis

$I_z(t) + I_y(t) + I_x(t)$. The characteristic values of the anisotropy and their interpretation shall be explained by examining the common measurement setup. As stated before, the anisotropy shall describe processes in samples (see Figure 36). In this thesis anisotropic transient absorption measurements of the PCTM containing compounds **HAB-S**, **HAB-A**, **HAB-Model**, **Star** and **Star-Model** are presented. In case of the TAB containing compounds **B1**, **B2** and **B3** anisotropic fluorescence upconversion was monitored. All measurements were performed in solution.

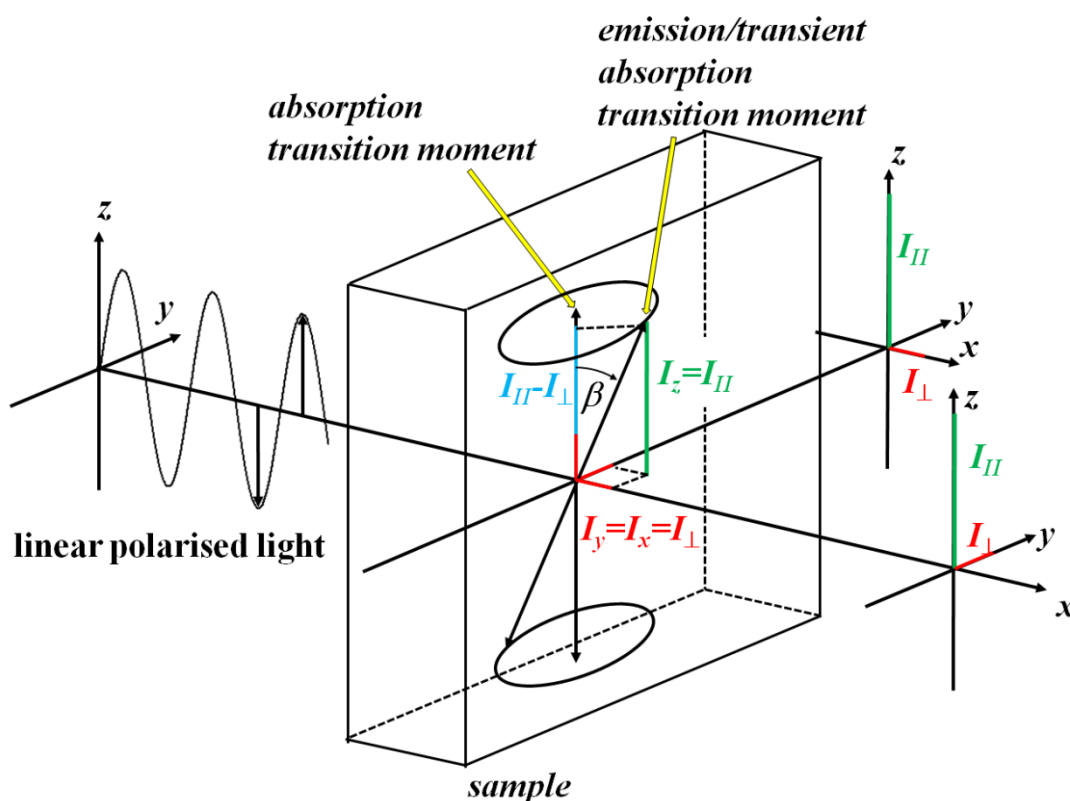


Figure 36 Projection of the emission/transient absorption intensity onto the x, y and z axes. The exciting light wave is linear polarised along the z axis.

The sample is generally excited with linear polarised light oriented along the z-axis making this the reference orientation. Then the polarisation direction of the transient absorption or of the fluorescence of the excited sample is measured by monitoring the respective intensities parallel ($I_z(t)$) and perpendicular ($I_y(t)$ or $I_x(t)$) to the z axis with time. As the excitation is symmetrically to the z axis, the absorption or emission characteristics of the excited molecules are equal along the y and x axis, so that the anisotropy formula simplifies with $I_y(t) = I_x(t) = I_{\perp}(t)$ and $I_z(t) = I_{\parallel}(t)$ to equation 53.

$$r(t) = \frac{I_z(t) - I_y(t)}{I_z(t) + I_y(t) + I_x(t)} = \frac{I_{\parallel}(t) - I_{\perp}(t)}{I_{\parallel}(t) + 2I_{\perp}(t)} \quad (53)$$

The anisotropy values are accordingly a measure for the change of the transition moment directions of the absorption and of the transient absorption/fluorescence represented by the likewise time dependent

angle $\beta(t)$ between these two directions. The correlation between $r(t)$ and $\beta(t)$ is expressed in equation 54.

$$r(t) = \frac{2}{5} \frac{3 \cos^2 \beta(t) - 1}{2} \quad (54)$$

Equation 53 and 54 are equivalent with the exception of the prefactor of $2/5$ in equation 54, which accounts for the phenomenon called *photoselection*.¹⁰⁵ That is, not only those transitions can be excited which transition moments are strictly oriented parallel to the wave factor E of the exciting light beam. In fact, the probability of excitation depends on the size of the transition moment projected onto the z -axis. Accordingly, the excitation probability is indeed maximal when the absorption transition moment is parallel to the polarisation direction of the exciting light beam. However, it is only zero when these two directions are perpendicular to each other and increases steadily with decreasing angle between them. By plotting the absorption probability dependent on the absorption transition moment direction a dumb bell shape is obtained (see Figure 37).

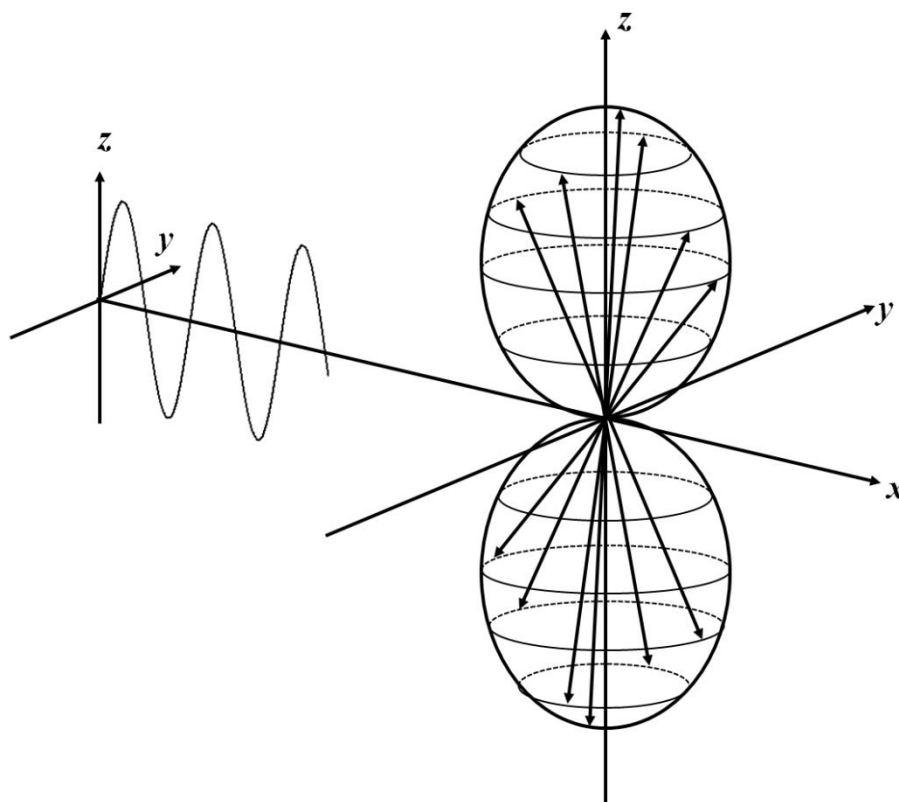


Figure 37 Absorption probability (length of the arrows) in dependency on the absorption transition moment direction (direction of the arrows). The exciting light wave is linear polarized along the z axis.

Hence, due to the photoselection the excited molecules are distributed around the z -axis and the overall anisotropy is therefore reduced. This is mathematically expressed by the prefactor. This is done

only in equation 54 as $\beta(t)$ does not account for this phenomenon. In contrast, equation 53 is used to calculate the anisotropy with the measured intensities $I_{\perp}(t)$ and $I_{\parallel}(t)$ which already include the photoselection. In the case of multi-photon excitation processes, the photoselection has to be accounted for each participating photon so that the prefactor changes for example to 4/7 in two-photon processes.¹⁰⁵

By rearranging equation 53 expressions for $I_{\perp}(t)$ and $I_{\parallel}(t)$ can be obtained (equation 55-57)

$$I_{\parallel}(t) = \frac{I_{\parallel}(t) + 2I_{\perp}(t)}{3} (1 + 2r) = S(t)(1 + 2r) \quad (55)$$

$$I_{\perp}(t) = \frac{I_{\parallel}(t) + 2I_{\perp}(t)}{3} (1 - r) = S(t)(1 - r) \quad (56)$$

$$I_{mag}(t) = \frac{I_{\parallel}(t) + 2I_{\perp}(t)}{3} = S(t) \quad (57)$$

The pure population decay of the excited state $S(t)$ is defined as the mean value of the intensity decays along the three axis (equation 57). In other words $S(t)$ represents the fluorescence/transient absorption decay under isotropic conditions. $I_{\parallel}(t)$ equals $S(t)$ plus twice the anisotropic part $S(t) \cdot r(t)$ (equation 55) and $I_{\perp}(t)$ equals $S(t)$ minus the anisotropic part $S(t) \cdot r(t)$ (equation 56). This fixed intensity relationship between $S(t)$, $I_{\perp}(t)$ and $I_{\parallel}(t)$ can be used to check the correctness of the measured data set. Furthermore, the pure population decay $S(t)$ can be directly obtained by monitoring $I_{\perp}(t)$ and $I_{\parallel}(t)$ in the ratio described in equation 57. This is done by measuring the intensity of the transient absorption/fluorescence polarised with an angle of $\sim 54.7^{\circ}$ relative to the z axis. This angle is called *magic angle* and the measured intensity accordingly $I_{mag}(t)$.

If the transient absorption/fluorescence transition moment is oriented parallel to the polarisation direction of the exciting light beam, the anisotropy has a value of $r = 0.4$. When they are perpendicular to each other, $r = -0.2$ (see Table 3). There are several reasons for the angle β to be nonzero:¹⁰⁴ (i) in the time interval between absorption and transient absorption/fluorescence the molecules may be able to rotate. As a result the transition moment of the transient absorption/fluorescence gets randomly oriented in space. It follows that $I_y = I_x = I_z$ and thus $r = 0$. Hence, information about the position of transition moments can only be obtained when rotational depolarisation does not take effect. This is achieved when measuring the sample in solvents of very high viscosity, e.g. embedded into a glass matrix of sucrose octaacetate at RT or in conventional solvents at low temperatures. In addition rotational depolarisation is negligible when monitoring the anisotropy in a time domain in which rotation is so slow that the sample is assumed to be stationary. Rotational motions of small to medium sized compounds ($M = 600\text{-}3000$ g/mol) are starting to take effect at around 100 ps – 1 ns after

excitation varying with the volume of the respective molecule V and the viscosity of the solvent η .^{67,106} In the case of only rotational Brownian motion of spherical molecules the temporal evolution of the anisotropy $r(t)$ can be described by a mono exponential decay of the anisotropy at zero time delay r_0 (equation 58).¹⁰⁵

$$r(t) = r_0 e^{-6Dt} \quad \text{with } 6D = \frac{kT}{V\eta} \quad (58)$$



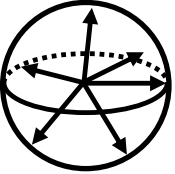

Multiple decay times can be observed for non-spherical molecules.

(ii) the angle β is nonzero if the state excited by the linear polarised light is not the same as that monitored by the fluorescence/transient absorption signals and both states differ in the orientation of their transition moments. In anisotropic fluorescence measurements this behaviour is experienced when internal conversion between excited states has occurred prior to the emission of light. In the transient absorption the case is more complex and therefore the reader is referred to the transient absorption section for a detailed description. (iii) geometric reorganisation of the chromophores within the excited state can be the reason for the change of the transition moment direction. (iv) the energy of the excited state can be transferred between several parts of the molecule each with a different transition moment direction. This is mathematically treated by the law of addition (equation 59).

$$r(t) = \sum_{i=1}^6 r_i(t) w_i(t) \quad \text{with } w_i(t) = \frac{P_i(t)}{\sum_{k=1}^6 P_k(t)} \quad (59)$$

According to this law, the measured anisotropy $r(t)$ is the sum of the individual anisotropies $r_i(t)$ of each state i , weighted by the probability $P_i(t)$ state i is in the excited state. It is therefore possible to calculate the mean value of the anisotropy in systems in which the excitation energy is rapidly transferred between several chromophores with known transition moment directions. In the special case of a two dimensional energy delocalisation the anisotropy has a value of $r = 0.1$.

Table 3. Values for the anisotropy and the polarisation in various constellations of polarisation directions.

polarisation directions		anisotropy	polarisation
parallel		0.4	1
2-D depolarised		0.1	-
3-D depolarised		0	0
perpendicular		-0.2	-1

If the eigenstates of two identically chromophores are coherently excited the initial anisotropy can have a value of up to 0.7 depending on the angle between the absorption transition moments of the two eigenstates.^{107,108} As the coherence dephases in general very rapidly (within a few hundreds of femtoseconds) the anisotropy drops contemporarily to the before mentioned maximum value of $r = 0.4$. This effect is accordingly seen only in ultrafast anisotropic spectroscopy.

3.3.4. Devices to change the polarisation characteristics of light beams

In this chapter several devices are presented which are used to generate linear polarised light beams or to change the polarisation direction of these light beams.

Glan-Thompson polarisers

In the anisotropic steady state fluorescence measurements Glan-Thompson polarisers were used to generate linear polarised light. Their layout is depicted in Figure 38.

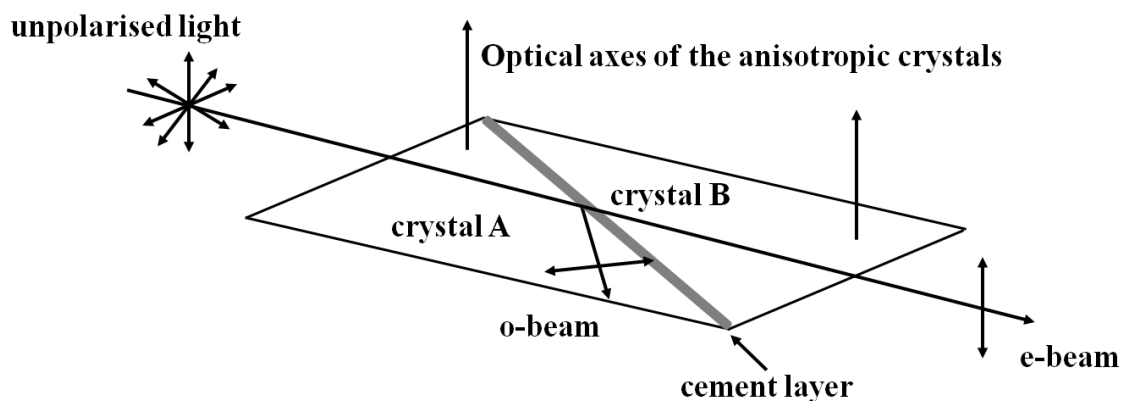


Figure 38 Layout of a Glan-Thompson polariser consisting of two prisms cemented together. The plane of reflection is shown which is held by the incident and reflected light beams.

These polarisers consist of two prisms (A and B) cemented together. The concept to generate polarised light is based on total internal reflection (TIR) at the surface of an anisotropic medium. The existence of TIR is dependent on the angle of incidence and on the refractive indices of the two involved materials, in this case the cement and the anisotropic medium. The prisms are made of calcite glass, a negative uniaxial crystal, whose optical axes are oriented perpendicular to the plane of reflection. The incident, unpolarised light beam can be described by two light waves with the electric wave vector E perpendicular and parallel to the optical axis, the o- and e-beams, respectively (see the uniaxial crystal section). In calcite, the o-beam experiences a higher refractive index as the e-beam so that when they reach the glass-cement interface, the o-beam is totally reflected and the e-beam is transmitted. The o-beam is absorbed at the blacked side face and the e-beam represents the demanded, linear polarised light beam which is isolated. The second prism serves to compensate beam deflections. Glan-Thompson polarisers are commonly used as they are cheap (due to the usage of the cement) and have a high transmittance (>90 %) of the e-beam. However, high intensity laser radiation should be avoided as the cement layer degrades under these conditions. In Glan-Taylor and Glan-Laser polarisers the cement layer is substituted by an air gap to circumvent this drawback and the optical

axes are placed in the plane of refraction. The principle of generating linear polarised light is still TIR as described above, but the production costs are considerable increased.^{109,110}

Wire grids

An alternative to the polarisers of the Glan family are wire grids. These consist of parallel aligned metal wires (e.g., aluminium or silver) spaced by a dielectric medium (e.g., air or glas) (see Figure 39).

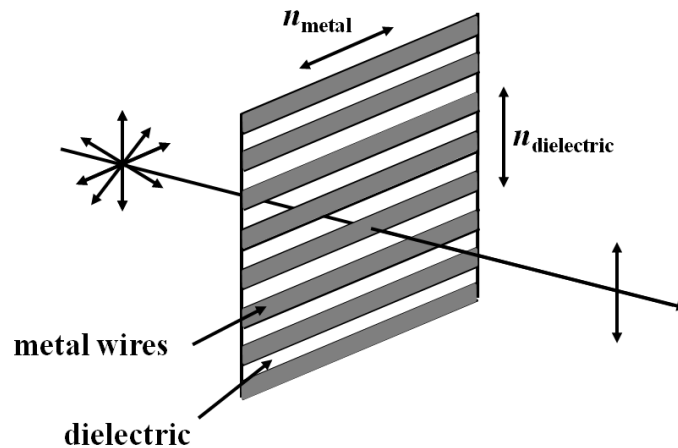


Figure 39 Layout of a wire grid. Electromagnetic light waves with their polarisation axis parallel to the wires experience the complex refractive index of the metal and are mostly reflected. Light waves with their polarisation axis perpendicular to the wires are transmitted due to the refractive index of the dielectric.

In the metal light induces motion of free electrons of the conduction band which leads to a complex refractive index. Its high imaginary part is responsible for a strong absorption of visible and infrared light within the metal and furthermore for a strong reflection of this light at the surface. If the distance between neighbouring wires is less than or equal to half the wavelength of the incident light then the whole structure behaves like a homogeneous birefringent medium. Accordingly, light waves polarised parallel to the wires experience the refractive index of the metal and thus get reflected (~90 %) or absorbed by the metal. Whereas those light waves, that are polarised perpendicular to the wires, experience the refractive index of the dielectric medium and are transmitted. The induced motion of free electrons in the metal is possible along the wires but not perpendicular to the wires.^{111,112}

$\lambda/2$ wave plates

To change the polarisation direction of a light beam $\lambda/2$ wave plates and Fresnel double rhombs were used. The wave plates are made of an anisotropic uniaxial crystal with the optical axis parallel to the face of the crystal (see Figure 40).

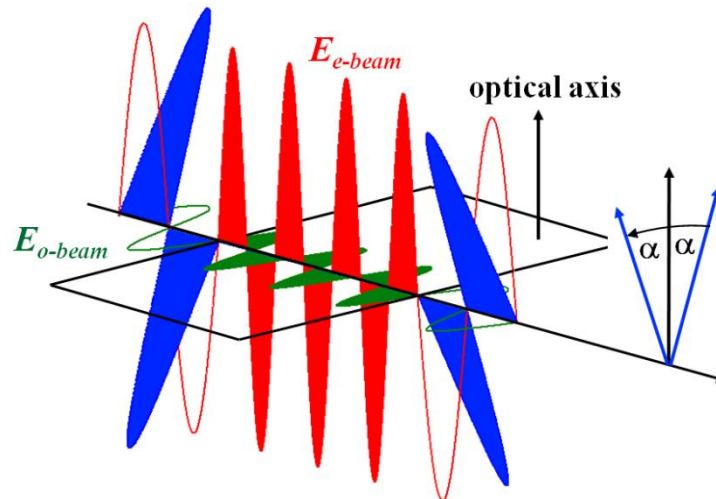


Figure 40 Layout of a $\lambda/2$ wave plate. A phase shift of $\lambda/2$ between the o- and e-beam is induced in an anisotropic crystal. The polarisation axis is rotated by twice the angle α between the polarisation axis of the incident light beam and the optical axis.

As discussed before an incident light wave can then be described by the o- and the e-beam with differing refractive index. This leads to a phase shift between the two beams as they travel at different speeds through the birefringent medium. If the length of the crystal is chosen so that by traveling through the whole crystal the phase shift between o- and e-beam is half the wavelength, the outgoing wave is still linear polarised but the polarisation orientation is rotated. The rotation angle equals twice the angle between the incident light and the optical axis. The phase shift at a specific wavelength is dependent on the refractive indices of the anisotropic crystal n_o and n_e and the length of the plate. When the phase shift is slightly deviating from half the wavelength, elliptically polarised light is produced. Hence, this device can be used only in a defined wavelength range.¹¹³

Fresnel double rhombs

The dependency of the phase shift on the wavelength is much less pronounced in a *Fresnel* double rhomb. Its layout is depicted in Figure 41 and consists of two prisms made from isotropic glass.

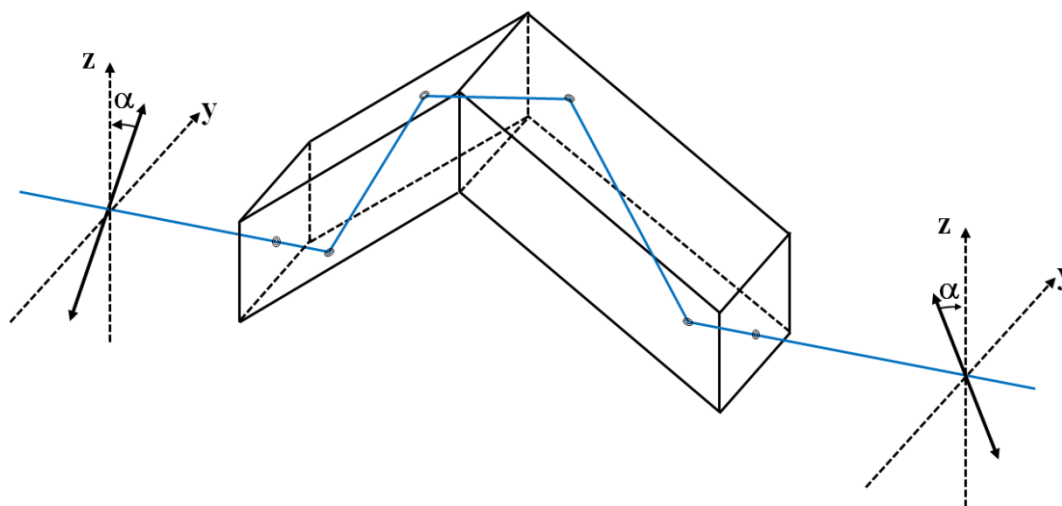


Figure 41 Layout of a *Fresnel* double rhomb. The z-axis is parallel and the y-axis perpendicular to the plane of reflection.

The prisms are cut in such a way that the incident light beams reflect totally at the tilted glass/air surfaces. When undergoing TIR the phase of light polarised perpendicular and parallel to the plane of reflection is shifted differently, depending on the difference between the refractive indices of the glass and the air and the angle of reflection. This angle can be adjusted so that by experiencing four times TIR the phase difference of the two light beams is half the wavelength. The result is as explained for the $\lambda/2$ wave plates the rotation of the polarisation axis of the incident light beam. With a constant angle of reflection the phase shift is only dependent on the refractive indices and not on the length of the material. Hence, the wavelength range of *Fresnel* double Rhombs is much broader in comparison to $\lambda/2$ wave plates.¹¹⁴

3.3.5. Measurement issues

3.3.5.1 Fluorescence upconversion

The analysis of the fluorescence upconversion measurements proved to be difficult as the signal-to-noise ratio of the obtained data was poor. This was probably due to the exceptional long lifetime of the examined molecules **B1**, **B2** and **B3** (>60 ns). It was shown that as a result the fluorescence transition moment of these molecules is small.¹⁹ In Figure 42 the relation of the fluorescence transition moment and the lifetime to the fluorescence intensity is illustrated.

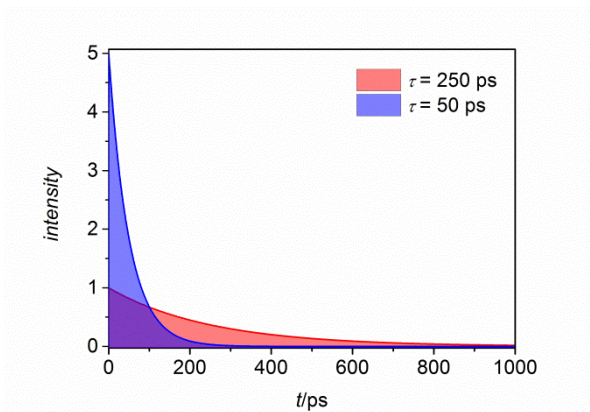


Figure 42 Fluorescence intensity in relation to the fluorescence lifetime. The fluorescence quantum yield and fluorescence band shape is considered to be equal for both decays.

Under the assumption that two kinds of molecules show the same fluorescence quantum yield and fluorescence band shape, the overall emitted number of photons (the integral of the time dependent fluorescence) has to be equal for both cases. This leads to a lower fluorescence transition moment and fluorescence intensity at shorter delay times in the case of the molecules with a longer fluorescence lifetime and consequently to a lower signal-to-noise ratio. It has to be stressed that the fluorescence transition moment can change due to internal conversion or relaxation processes. This change is indeed apparent in the molecules **B1**, **B2** and **B3**. However, these effects seem to be less important at the monitored wavelength as the amplitudes of the fastest resolved decays are small compared to that of the lowest energy state.

To increase the signal-to-noise ratio two approaches were pursued. Firstly, it was attempted to optimise the sum frequency generation according to equation 48. In general the intensity of the fluorescence P_1 , regulated by the pump pulse intensity, was limited by the stability of the molecules. The intensity of the gate pulse P_2 could not be increased due to the appearance of non-linear effects in the BBO crystal, e.g. WLC generation. Focusing the gate beam more strongly into the BBO crystal led to the same effects. When simultaneously decreasing the gate intensity P_2 , the efficiency nevertheless decreased although the beam area A decreased. That is because with a smaller A also P_1 decreased, as the fluorescence beam and the gate beam overlapped now only partially. For spectroscopic reasons the change of the fluorescence wavelength was not possible. At last, the anisotropic crystal could be changed as d_{eff} and the refractive indices n_1 , n_2 and n_3 are medium dependent values. However, BBO proved to be most suitable for the usage in the described routine fluorescence upconversion measurement system due to the high damage threshold, large d_{eff} and wide spectral transparency.¹¹⁵ LiIO₃ crystals, for example, do have indeed an even higher d_{eff} value, which could theoretically lead to a 2-4 fold higher nonlinear conversion efficiency. However, these crystals are highly hygroscopic and therefore unusable in this context. Besides the type I BBO crystals a type II BBO crystal was tested for the sum frequency generation. The type II crystal should have theoretically a fourfold lower

conversion efficiency as the type I counterpart, but the signal-to-noise ratio should be better due to the better SHG suppression of the gate pulse.¹¹⁶ The test measurements could confirm the lower conversion efficiency, at the same time, however, a threefold lower signal-to-noise ratio was observed (see Figure 43).

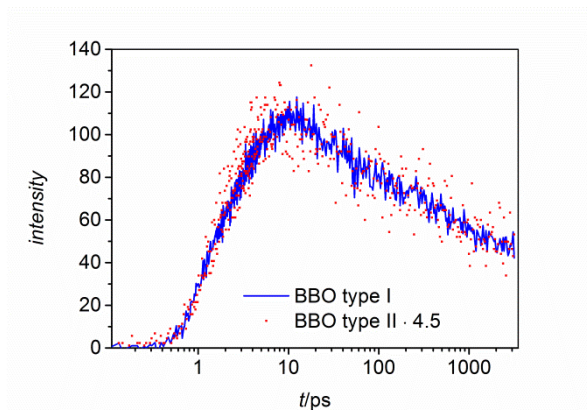


Figure 43 The magic angle fluorescence upconversion traces of **B3** in PhCN excited at 25000 cm^{-1} with the SFG performed in BBO type I and type II crystals. The signal generated in the BBO type II crystal was multiplied by 4.5.

The second approach was to use the seed laser output prior amplification instead of the amplified output of the Solstice system. The seed laser was a Ti:Sapphire oscillator (MaiTai BB) generating pulses with a central wavenumber of 12500 cm^{-1} (800 nm), a length of 80 fs at a repetition rate of 80 MHz. As described before the output pulse was divided into the pump and gate pulses. The wavelength of the pump pulse was converted to 25000 cm^{-1} (400 nm) by SHG generation (Ultrafast Systems) before exciting the sample. All other measurement settings remained unchanged. The pulse energies of the pump and gate beams were in this case $<5\text{ nJ}$, considerable lower in comparison to the setup using the amplified laser output (pump: $\leq 250\text{ nJ}$, gate: $\leq 500\text{ nJ}$). This should however be overcompensated by the 80000 fold higher repetition rate of the MaiTai output and therewith a significant higher number of measurements per time interval. Moreover, with the low pump pulse energy sample degradation should be less likely, so that the measurement could be prolonged. However, the long life time of the investigated molecules **1 - 3** ($\sim 60\text{ ns}$) and the time interval of 12.5 ns between two consecutive pump pulses, provided by the high repetition rate (80 MHz), resulted in a superposition of the fluorescence decays. Hence, most of the excited molecules could not relax to the ground state before the next pump pulse arrived the sample. This effect was observed as an “offset” in the measurement data (see Figure 44).

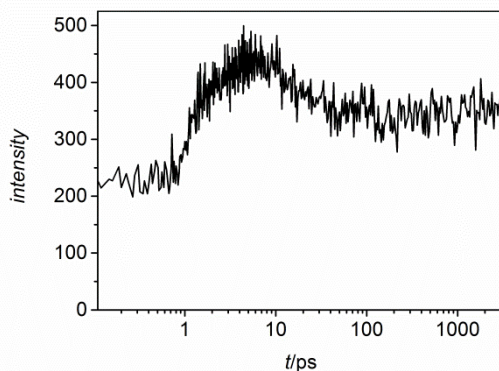


Figure 44 The magic angle fluorescence upconversion trace of **3** in PhCN excited at 25000 cm^{-1} (400 nm) with the seed laser (MaiTai BB) output.

The “offset” should decrease exponentially with a decay constant similar to the lifetime of the molecules. Although multiple excitations of a molecule should be very unlikely due to the low pump pulse energy,⁶⁷ the analysis of the data was nevertheless complicated by the temporal superposition of the fluorescence signals. In the end the fluorescence upconversion was measured with the amplified solstice output as the signal-to-noise ratio was not considerably increased when using the seed laser output.

3.3.5.2 Transient absorption

Before measuring the transient absorption the WLC generation was calibrated to produce a stable probe pulse. Hence, transient absorption spectra of **HAB-S** in DCM were recorded with varying intensities of the gate pulse producing the WLC (Figure 45).

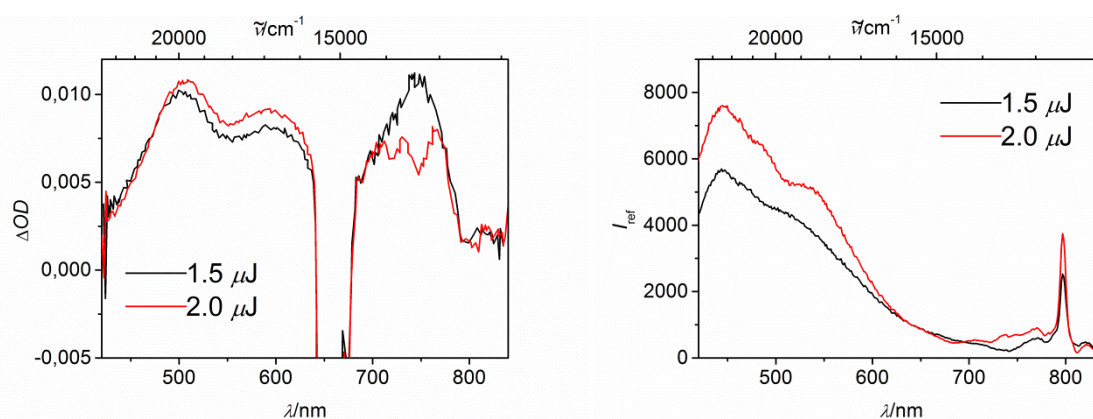


Figure 45 Transient absorption ΔOD spectra of **HAB-S** in DCM pumped at 15200 cm^{-1} (660 nm) (left) and the respective I_{ref} trace (right). The probe pulse was generated by the gate pulse (at 12500 cm^{-1} (800 nm)) with an intensity of $1.5\text{ }\mu\text{J}$ and $2.0\text{ }\mu\text{J}$.

At gate pulse intensities below $1.5\text{ }\mu\text{J}$ no WLC could be observed marking this the P_{th} . In the intensity region between $1.5\text{ }\mu\text{J}$ and $2.0\text{ }\mu\text{J}$ a WLC was generated with a very low I_{ref} in the spectral region

between $13000 - 14300 \text{ cm}^{-1}$ (700 - 760 nm) after passing the coloured glass filters. If the gate pulse intensity is further increased the whole WLC spectrum increases in intensity. Additionally, in the range between $13000 - 14300 \text{ cm}^{-1}$ (700 - 760 nm) the band form is changed both in the WLC and in the transient absorption spectra. Sharp spikes are observed at $2.0 \mu\text{J}$ gate intensity in the before mentioned spectral region, while at $1.5 \mu\text{J}$ gate intensity the transient absorption has a band structure. As it is known that the WLC generation can get destabilised with increasing pulse intensity (see third order nonlinear effects section), all transient absorption measurements were performed with a WLC shown for the $1.5 \mu\text{J}$ gate pulse intensity.

In the case of **Star**, **Star-Model**, **HAB-A**, **HAB-S** and **HAB-Model** anisotropic transient absorption measurements were performed. From equation 38 the measured values of $\Delta OD_{\parallel}(t)$, $\Delta OD_{\perp}(t)$ and $\Delta OD_{\text{mag}}(t)$ need to have a strict intensity correlation: $\Delta OD_{\text{mag}}(t) = (\Delta OD_{\parallel}(t) + \Delta OD_{\perp}(t))/3$. This defined ratio serves as a measure for the accuracy of the measurement setup.⁸⁴ In all cases the measured data differed from the defined ratio and due to the short molecules lifetime ($<10 \text{ ps}$) the anisotropic data could not be normalised as explained for the fluorescence upconversion. During the error search, intensity fluctuations of the amplified laser output, molecule degradation and temperature effects were proved to be negligible. It could be thought of two further, obvious sources of error. Either the intensity of the pump pulse was not equal for the three polarisation directions or the pulses were not strictly linearly polarised. To test the intensity of the pump pulse the thermal sensor provided by Newport-Spectra-Physics was replaced by a much more sensitive photodiode. Whenever the polarisation direction of the pump pulse was changed the photodiode was placed just in front of the sample and the intensity of the pump pulse set to a defined value. However, the polarised transient absorption signals were not in accordance to the before mentioned ratio, although an equal pump intensity ($\pm 1 \%$) was ensured. To guarantee a linear polarisation of the pulses, two different setups were tested (Figure 46).

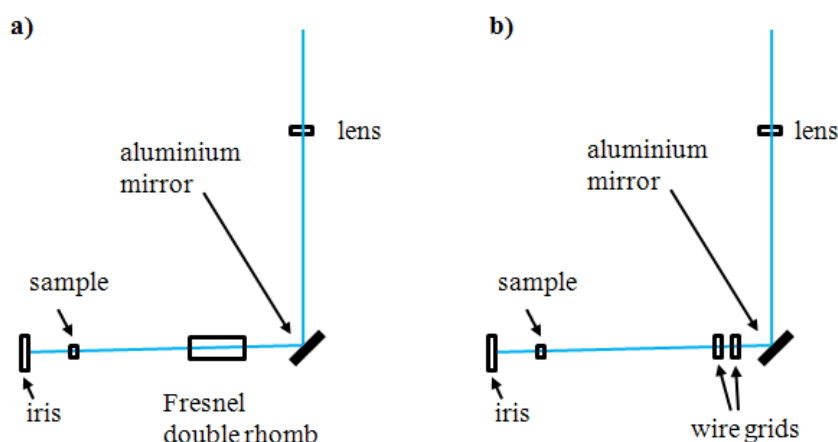


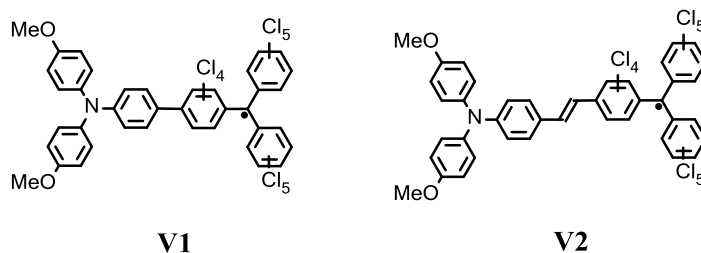
Figure 46 Schematic illustration of the optically setups a) and b) to tune the polarisation characteristics of the pump pulse. (part of Figure 18)

Thereby, the focus was on the pump pulse, as the WLC was ensured to be linear polarised by light extinction when reaching a perpendicular oriented wire grid. The $\lambda/2$ wave plate provided by Ultrafast Systems did not retain the linear polarisation when changing the polarisation direction of the pump pulse. Obviously, the used pump energies were beyond the wavelength range of the wave plate resulting in elliptically polarised light (see polarisation section). It was replaced by either a *Fresnel* double rhomb a) or wire grids b), which both ensured a polarisation of the pump pulses of P_{\parallel} , P_{\perp} and $P_{\text{mag}} > 0.99$. Moreover, it was found that the change of the polarisation direction had to be performed after the last aluminum mirror directing the pump pulse into the sample, because the aluminium mirror considerably decreased the polarisation at magic angle to $P_{\text{mag}} < 0.58$. It is assumed that the reflection at the mirror induces a phase shift between the parallel and perpendicular polarised pulse components leading to elliptically polarised light. In setup a) the transient absorption showed irregular intensity fluctuations when rotating the Fresnel double rhomb. This might be explained by the long optical path length of the double rhomb resulting in a beam offset when rotated.¹¹⁷ Accordingly, the overlap between the pump and probe pulses might change slightly resulting in an increased or decreased transient absorption signal. The arrangement of the wire grids in setup b) was explained before. With this setup both a linear polarisation and a defined intensity relationship of the pump pulses were ensured and a beam offset avoided. However, the demanded ratio for $\Delta OD_{\parallel}(t)$, $\Delta OD_{\perp}(t)$ and $\Delta OD_{\text{mag}}(t)$ was still not observed. In the case of **HAB-Model**, **HAB-A** and **HAB-S** the measured data differed from the defined ratio by 2-6% and in the case of **Star-Model** and **Star** by 9-13%. This implies that the magic angle measurement has in each case too low intensity and/or the parallel and/or the perpendicular measurements have too high intensity by up to the mentioned values. We cannot ascertain if all or individual traces are inaccurate but the error is always in the same direction so that we assume it to be systematic. As a consequence the obtained anisotropy values can be inaccurate up to the same amount of error. However, the temporal evolution of the anisotropy should be unaffected and as we are assuming a systematic error in all the measurements the obtained data for the different compounds is comparable.

4. Multidimensional chromophores containing PCTMs*

4.1. Introduction

Polychlorinated triphenylmethyl radicals (PCTM) are open shell, electron poor systems¹¹⁸ which belong to the class of inert carbon free radicals.¹¹⁹⁻¹²¹ The two chlorine atoms in *ortho*-position to the radical centre prevent typical radical reactions due to sterical shielding.¹¹⁹ On the basis of their electronic and magnetic properties PCTMs are applied in neutral mixed-valence (MV) compounds,^{31,122-128} in redoxactive switches,¹²⁹⁻¹³² in purely organic radical open frameworks (POROFs)^{133,134} and as sensors.¹³⁵⁻¹³⁸ The concept of the star-like framework is based on the charge transfer investigations of MV compounds **V1** and **V2** synthesised by Heckmann *et al.*¹²⁴ Accordingly, these serve as reference for **Star-Model**.



In contrast to **V1** and **V2**, the PCTMs utilised in this work are not substituted by chlorine atoms in *meta*-position to the radical centre. This has no influence on the stability of the redox centre¹²¹ but shifts the reduction potential by 450 mV to lower potentials.¹³⁸

4.2. Synthesis

The compounds **HAB-S** and **HAB-A** were synthesised by dicobaltoctacarbonyl catalysed cyclotrimerisation of the tolan derivative **P6** (Figure 47).

*Parts of this section have already been published in M. Steeger, S. Griesbeck, A. Schmiedel, M. Holzapfel, I. Krummenacher, C. Lambert and H. Braunschweig, *Phys. Chem. Chem. Phys.*, **2015**, submitted.

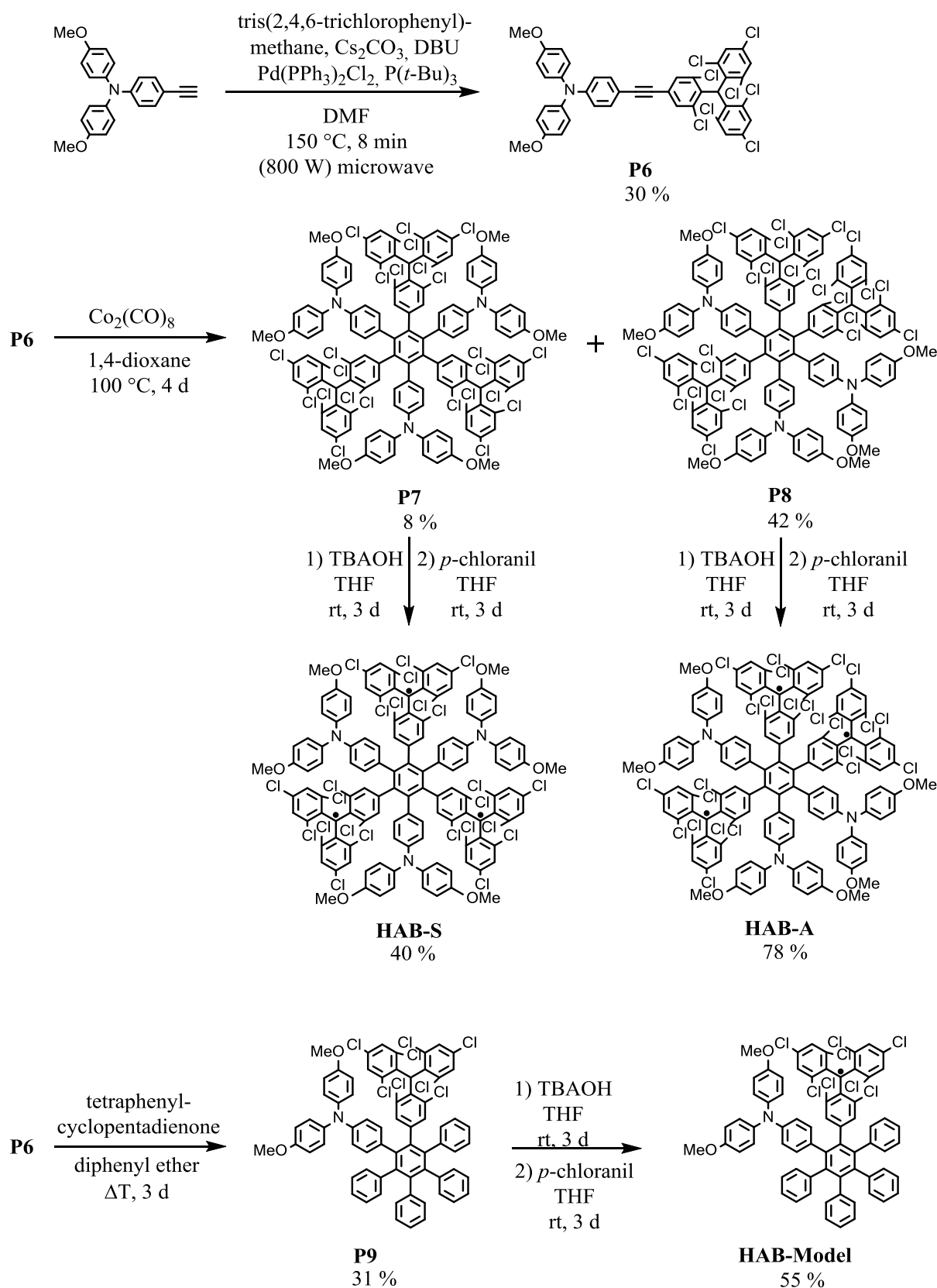
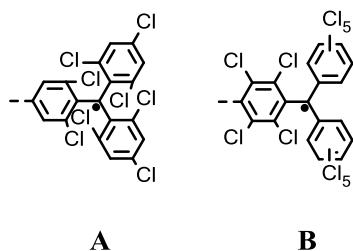


Figure 47 Synthesis of **HAB-S**, **HAB-A** and **HAB-Model**.

The cyclotrimerisation reaction is sensible to the steric demands of the arene substituents in *ortho*-position to the acetylene group. Therefore we chose the polychlorinated triarylmethane radical **A** as

electron poor redox centre.¹³⁹ Cyclotrimerisation attempts of structurally similar molecules with the fully perchlorinated acceptor centre **B**¹²⁴ with $\text{Co}_2(\text{CO})_8$ and $\text{CpCo}(\text{CO})_2$ were not successful.



The cyclotrimerisation of tolan **6** yielded a symmetric (**HAB-S**) and an asymmetric isomer (**HAB-A**) in a ratio of 1:5.3. The isomer ratio obtained differs considerably from the expected statistical value of 1:3.¹³⁹ This can be explained by a distinct difference in the sterical demand of the two acetylene substituents in tolan **P6** which favours an asymmetrical oxidative coupling within the catalytic cycle.¹³⁹ The tolan derivative **P6** was obtained by *Sonogashira* coupling of the known tris(2,4,6-trichlorophenyl)methane and *N,N*-di(4-methoxyphenyl)-*N*(4-(ethynyl)phenyl)amine. Although several very reactive catalysts for coupling of chlorinated arenes are described in literature the difficulty of the present synthesis was the required selectivity. It turned out that the catalytic systems either were not reactive enough (e.g. $\text{Pd}(\text{PPh}_3)_2\text{Cl}_2$, CuI)¹⁴⁰ or too reactive (e.g. $\text{Pd}(\text{PPh}_3)_4$, $\text{P}(t\text{-Bu})_3$, CsCO_3 , DBU)¹⁴¹ or $\text{Pd}(\text{MeCN})_2\text{Cl}_2$, *x*-Phos, CuI)¹⁴² as multiple reactions and side reactions presumably at the chloro substituents in *ortho*-position to the methane centre could be observed. The latter by-products could only be separated by size exclusion gel permeation chromatography as solubility and polarity of the isomers are very similar. For the synthesis of **P6** the optimised reaction conditions proved to be stirring *N,N*-di(4-methoxyphenyl)-*N*(4-(ethynyl)phenyl)amine (2 equiv.), tris(2,4,6-trichlorophenyl)methane (1 equiv.), Cs_2CO_3 , DBU , $\text{Pd}(\text{PPh}_3)_2\text{Cl}_2$, and $\text{P}(t\text{-Bu})_3$ in DMF at 150 °C (800 W) in a microwave oven for 8 min according to the procedure by *Huang et al.* which gave **P6** in 30% yield.¹⁴¹

The model compound **P9** was synthesised by a Diels-Alder reaction of the tolan derivative **P6** with tetraphenylcyclopentadienone. All α -H compounds of this series (**P7**, **P8** and **P9**) showed complex NMR spectra. Although the overall peak integrals were matching to the different type of atoms the assignment of the signals was impossible due to an excessive number of signals and complex splitting patterns. We assume that the steric demand induced by the HAB framework to the pyramidal polychlorinated triarylmethane centres generates stereoisomers that cannot interconvert rapidly on the NMR time scale at rt. In order to provoke rapid equilibration of all these isomers and, thus, to simplify the NMR spectra, temperature dependent NMR measurements were performed in dimethylsulfoxide- d_6 , 1,1,2,2-tetrachloroethane- d_2 , 1,2-dichlorobenzene- d_4 and acetone- d_6 from rt up to 353 K. With increasing temperature some signals coalesced but the coalescence point could not

be exceeded in the used solvents. Although we could not obtain simplified NMR spectra, the observed coalescence indicates that the origin of the complex NMR spectra are most likely stereoisomers.

The last step in the synthetic approach to **HAB-S**, **HAB-A** and **HAB-Model** is the radicalisation of the α -H compounds **P7**, **P8** and **P9**. In this process, the α -H compounds were first deprotonated by TBAOH and then oxidised by *p*-chloranil. In each case a reaction time of 2 days was crucial to ensure maximum conversion. NMR analysis of **HAB-S**, **HAB-A** and **HAB-Model** was prevented by the paramagnetic character of the PCTM centres, resulting in line-broadening. The presence of stereoisomers could therefore not be clarified in case of the radicals. However, as the geometry of the polychlorinated triarylmethane centres changed from pyramidal to trigonal planar upon radicalisation, the sterical demand of neighbouring centres should thereby be decreased disfavours the formation of stereoisomers. The degree of radicalisation was determined to be ≥ 95 % by comparison of the oxidation and reduction peaks in the square-wave voltammograms.

The star-like oligomere **P10** was synthesised by *Sonogashira* coupling of *tris*(2,4,6-trichlorophenyl)methane and *N,N*-di(4-methoxyphenyl)-*N*(4-(ethynyl)phenyl)amine similar to the synthesis of the tolan derivative **P6** (Figure 48).

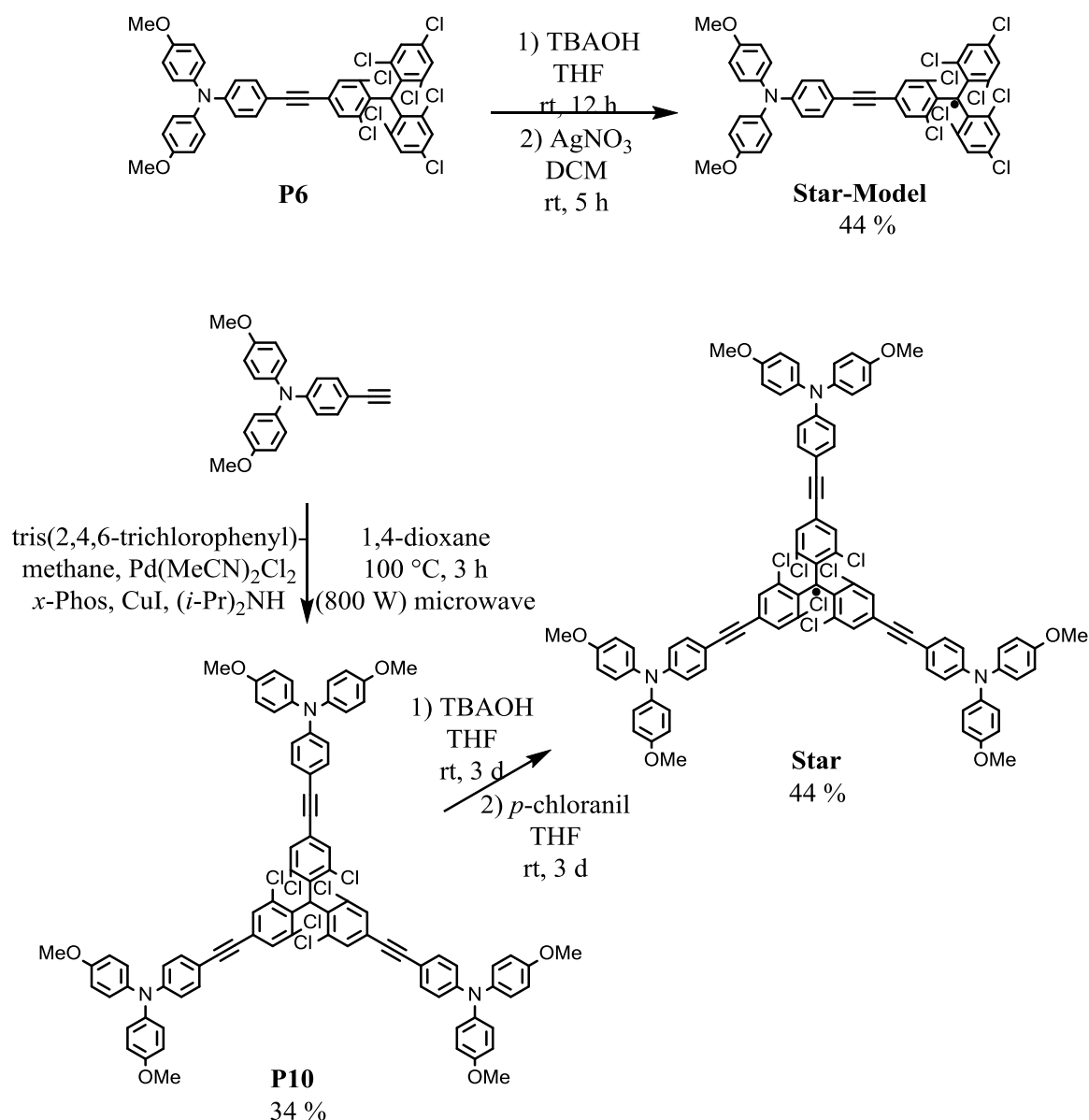


Figure 48 Synthesis of **Star-Model** and **Star**.

Thereby, the addition of *N,N*-di(4-methoxyphenyl)-*N*-(4-(ethynyl)phenyl)amine was carried out in three consecutive steps each with at most four equivalents. The best reaction conditions gave yields of 34 % and consist of $\text{Pd}(\text{MeCN})_2\text{Cl}_2$, *x*-Phos and CuI as described by *Langer et al.*¹⁴² Radicalisation of **P10** was performed in the same manner as described above. The degree of radicalisation in case of **Star** was determined to be 90 %. However, the remaining starting material in the sample should not affect the spectroscopic evaluation of the charge transfer properties. The latter exhibits no absorption in the range of the IV-CT transition of **Star** (see below) and thus can be neglected in the following investigations. **Star-Model** was synthesised by deprotonating **P6** with TBAOH and oxidation with AgNO_3 to achieve a 97 % degree of radicalisation.

4.3. Electrochemistry

Electrochemical measurements of the target compounds were performed to estimate the donor and acceptor redox potentials as well as interactions between these centres. The oxidation and reduction potentials were determined by CV (see Figure 49) and are given in Table 4. For a clearer representation of the electrochemical processes the square wave voltammetry (SWV) measurements are depicted in Figure 50. The potentials determined by SWV agree with those of the CV measurements.

Table 4 Redox potentials of **Star-Model**, **Star**, **HAB-Model**, **HAB-A** and **HAB-S** ($\sim 3\text{-}7 \cdot 10^{-4}$ M) versus Fc/Fc^+ determined by CV^a. The measurements were performed in 0.2 M DCM/[Bu₄N][PF₆] at a scan rate of 250 mV s⁻¹.

	Star-Model	Star	HAB-Model	HAB-A	HAB-S
E_{red}/mV	-960	-950	-1050	-1010, -1040, -1170	-1020, -1080, -1130
E_{ox}/mV	330	250, 320, 350	240	210, 260, 290	230, 280, 290

^a multiple processes were fitted with DigiSim¹⁴³.

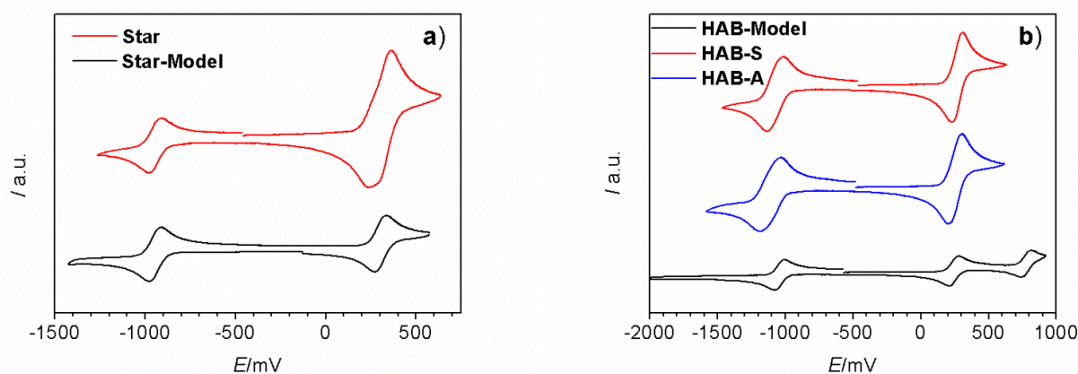


Figure 49 a) CVs of **Star**, **Star-Model** and b) **HAB-S**, **HAB-A** and **HAB-Model** in 0.2 M DCM/[Bu₄N][PF₆] measured at a scan rate of 250mV/s. The second oxidation process of **HAB-Model** is attributed to the second oxidation of the TAA moiety.³²

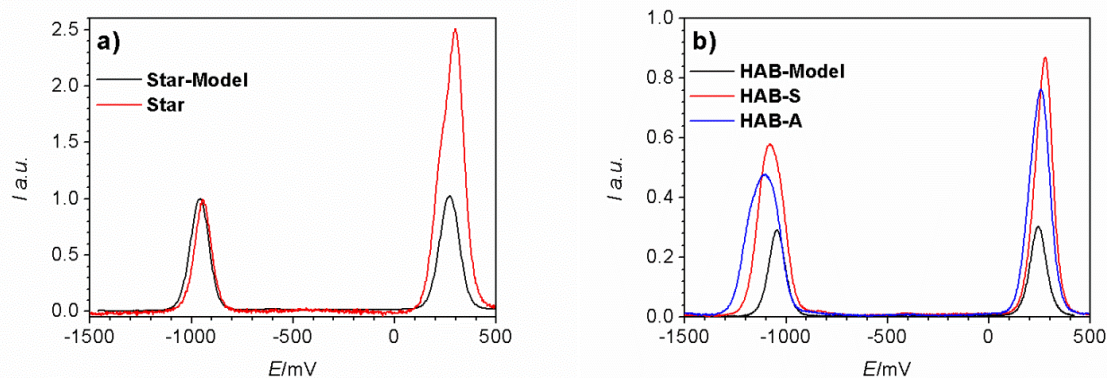


Figure 50 a) SWV of **Star** and **Star-Model** in 0.2 M DCM/[Bu₄N][PF₆] normalised to the signal maximum of the reduction. b) SWV of **HAB-S**, **HAB-A** and **HAB-Model** in 0.2 M DCM/[Bu₄N][PF₆] normalised to the integral of the oxidation including the number of amine redox centres.

The oxidation processes at 210-350 mV are assigned to the first oxidation of the TAA centres. Typical values for TAAs are in the range of 250-400 mV^{19,124} depending on the substitution pattern. Furthermore, the reduction signals at -950-(-1130) mV are typical of the PCTM units.^{144,145} Both electrochemical processes were proved to be chemically fully reversible by thin-layer CV measurements and spectroelectrochemistry (SEC). The redox potentials of the model compounds **HAB-Model** and **Star-Model** have nearly the same potential difference of 1300 mV even though they are shifted by 100 mV to higher potentials in **Star-Model**. This reflects an equal free energy difference ΔG^{00} between ground and possible IV-CT states (see absorption section). The shift is most likely induced by the differing substitution pattern of the redox centres, which in case of **Star-Model** provides a more electron rich environment for both redox centres. In addition, their redox potentials are in good agreement with the potentials of their corresponding multi-chromophore compounds **HAB-S**, **HAB-A** and **Star**. In the latter multiple oxidation states from -3 to +3 can be reached according to the number of the redox centres present. But the accessibility of oxidation states between -3 and 3 is limited as the redox processes show no distinct potential separation but a single broadened wave in the SWV.

The potential separation in **HAB-S**, **HAB-A** and **Star** is indicative of electronic communication. Compared to **HAB-Model** with only one amine redox centre, the width at half-maximum of the oxidation signal is increased in **HAB-S** and to a greater extent in **HAB-A**, both containing three amine chromophores. In the multi-chromophore compounds, the width at half-maximum can be assessed by the difference of the two outermost potentials, increasing from 60 mV in **HAB-S** to 80 mV in **HAB-A**. The different potential splitting is correlated to the different substitution pattern of the HABs. Whereas in the symmetric **HAB-S** the amines are interconnected strictly by *meta*-substitution and separated by 1.2 nm (measured centre to centre from MM2 optimised^{146,147} structures), this is not the case in the asymmetric HAB. There, the centres are linked in *meta*-, *para*- and *ortho*-position with a minimum

distance of 0.8 nm in the last case, resulting in a stronger electrostatic interaction upon oxidation, and, therefore, a larger potential separation. The same effects can be found in case of the reduction potentials albeit more pronounced. As redox potential splittings of multi-redox-chromophores are highly dependent on the solvent and supporting electrolyte,^{19,148} their magnitude can differ in oxidation and reduction. The width at half-maximum of the SWV oxidation signal of **Star** is with 100 mV the largest compared to **HAB-S** and **HAB-A** although in **Star** the amines are separated by the largest distance (2.5 nm, measured centre to centre from MM2 optimised^{146,147} structures). We explain this by a better electronic communication between the redox centres.

4.4. Electron paramagnetic resonance

Electron paramagnetic resonance (EPR) measurements were performed to characterise the PCTM centres in all radicals. Furthermore, the interactions between the three PCTM radical centres in **HAB-S** and **HAB-A** as well as between the TAA⁺ and PCTM radical centres in the oxidised **HAB-Model** and **Star-Model** were investigated.

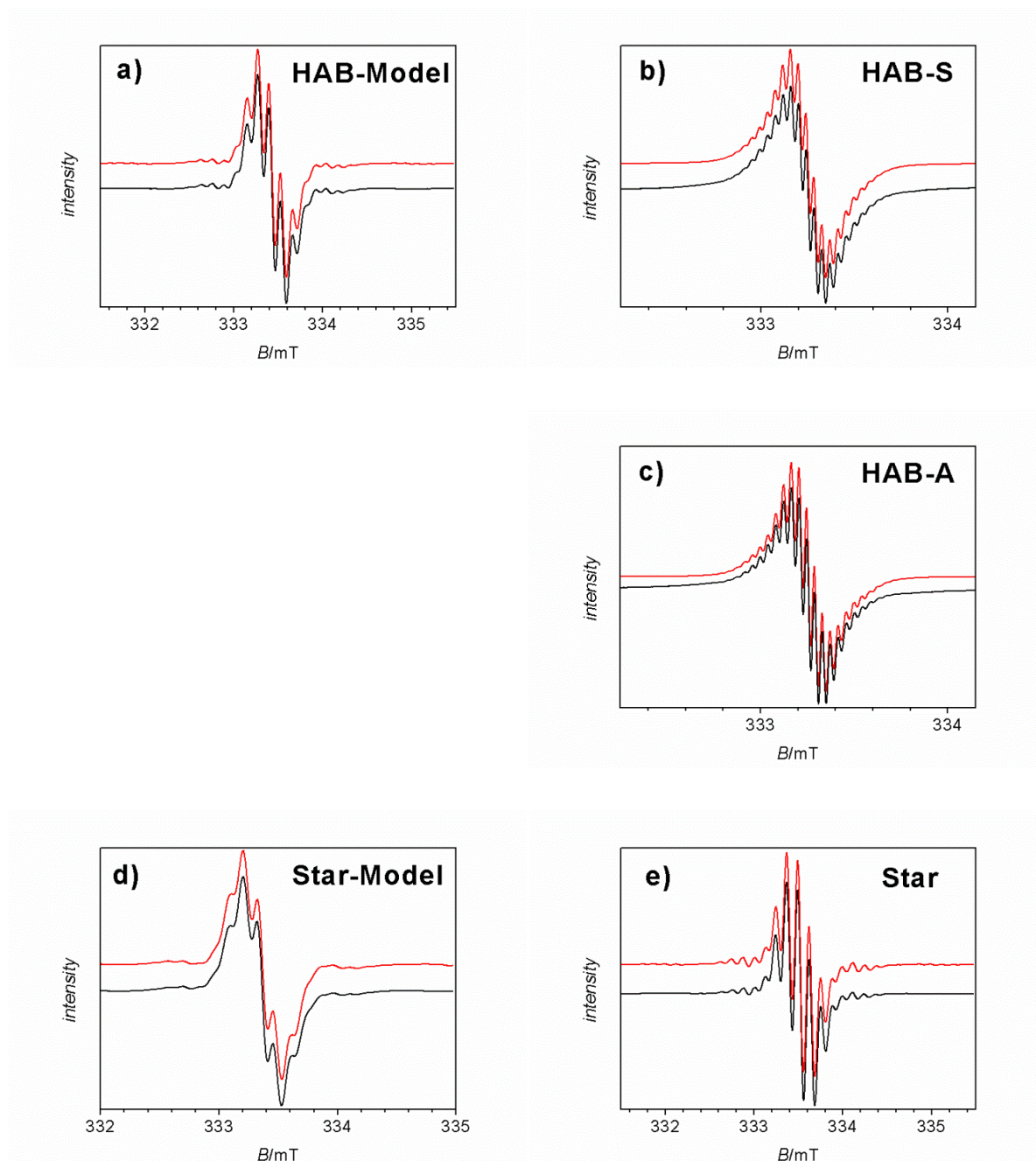


Figure 51 Simulated (red) and experimental (black) CW EPR spectra of a) **HAB-Model**, b) **HAB-S** and c) **HAB-A** in DCM at rt, 250 K and 230 K, respectively, and of d) **Star-Model** and e) **Star** in DCM at rt.

Table 5 Electronic g factor and hyperfine coupling constants $|a|$ from simulated EPR spectra of all radicals in DCM. The EPR spectra of **HAB-S** and **HAB-A** were measured at 250 K and 230 K, respectively, those of **Star**, **Star-Model** and **HAB-Model** at rt. Radical cations were generated by oxidation with *tris*(bromophenyl)amminium hexachloroantimonate(V).

	g	$ a_N /\text{mT}$	$ a_H /\text{mT}$	$ a_C /\text{mT}$
Star-Model	2.003	-	0.116 (4 H), 0.121 (2 H)	3.1, 1.31, 0.97
Star-Model ⁺	-	-	-	-
Star	2.003	-	0.12 (6 H)	3.0, 1.3, 0.95
HAB-Model	2.003	-	0.12 (4 H), 0.13 (2 H)	3.1, 1.3, 1.0
HAB-Model ⁺	2.003	~0.4	-	-
HAB-A	2.003	-	0.040 (12 H), 0.041 (6 H)	0.41, 0.35
HAB-S	2.003	-	0.041 (12 H), 0.042 (6 H)	0.42, 0.34

The EPR spectra were measured in DCM at rt with the exception of **HAB-A** and **HAB-S** which were measured at 230 K and 250 K, respectively, for a better hyperfine splitting resolution (see Figure 51). The obtained spectra were simulated to obtain the electronic g -factor and the isotropic hyperfine coupling constants hfc $|a|$ to nuclei with nonzero magnetic moments (see Table 5). For **Star-Model**, **Star** and **HAB-Model** EPR signals were observed which are characteristic for this type of PCTM, namely a g factor close to the value for the free electron ($g_{\text{iso}} = 2.003$), and hfc to the *meta* hydrogen atoms of $|a_H| = 0.12$ mT, to the α -carbon atom of $|a_C| = 3.0$ mT and to neighbouring aromatic carbon atoms of $|a_C| = 1.29$ mT and $|a_C| = 1.05$ mT.¹²¹ In agreement with the substitution pattern of the PCTM, the proton hfc of **Star-Model** and **HAB-Model** were found to be asymmetric showing two different hfc constants and that of **Star** to be symmetric with only one hfc constant. The signals of the multidimensional systems **HAB-A** and **HAB-S** are centered around the same characteristic g factor but all hfc constants are by a factor of ca. one third smaller. For multiradicals¹⁴⁹⁻¹⁵² if each of the unpaired electrons has spin density on the other radical centres a hfc pattern results for all these radical centres with apparent hfc constants divided by the number of involved radical centres.^{153,154} More precisely, this is observed when the electron exchange interaction J is much greater than the hfc constant $|a|$ but the dipolar spin-spin interaction between the unpaired spins is weak. The same effect is found for the triradical compounds **HAB-A** and **HAB-S**. In these multiradicals the energy difference between states of differing spin multiplicity is negligible.

Both model compounds **HAB-Model** and **Star-Model** were oxidised to verify the necessity to consider diverse spin states regarding charge transfer. The EPR spectra of oxidised **HAB-Model** and **Star-Model** show basic differences (see Figure 52).

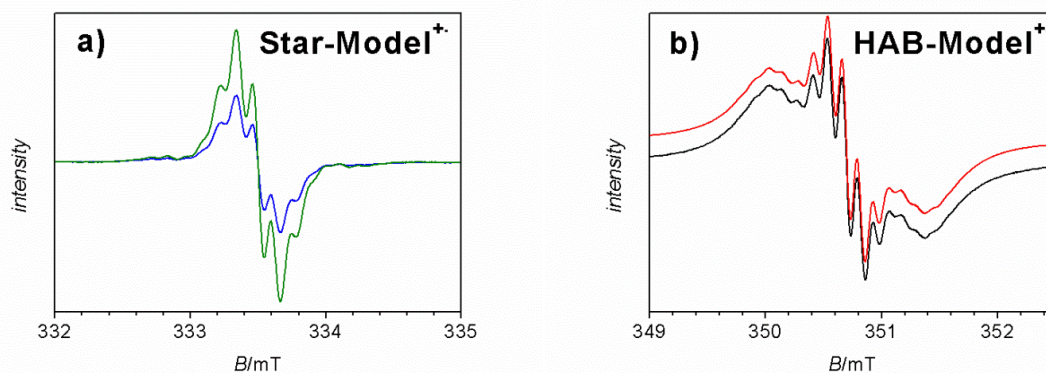


Figure 52 EPR spectra of oxidised a) **Star-Model** and b) **HAB-Model** by *tris*(bromophenyl)amminium hexachloroantimonate(V) at rt in DCM. **HAB-Model** was oxidised by ~35 % (green) and ~70 % (blue) maintaining the overall concentration of the radical centre. **Star-Model** was oxidised by 80 % (black) with the simulated signal in red.

Whereas the signal intensity of **Star-Model** gradually decreased upon stewise oxidation, in case of **HAB-Model** a new broad signal is formed in addition to the characteristic PCTM signal. In principle, three possible scenarios have to be considered: 1) In diradicals, in which the two radical sites do not interact with each other, the electron exchange interaction constant J is smaller than the hfc constants $|a|$ and thus only the spectra of the individual radical centres are observed. 2) If J is larger than $|a|$ but smaller than the zero-field splitting parameter D the two centres are weakly interacting. In this case a “biradical” is observed with the typical changes to the hfc as explained above for the spectra of **HAB-A** and **HAB-S**. In the last case 3) J is considerably larger than D , meaning the two radical centres are strongly interacting. If so, singlet (EPR silent) and triplet states (only observable at low temperatures) are formed which differ in energy depending on the magnitude of J .¹⁵⁵ In case of **HAB-Model** the characteristic PCTM signal is assigned to the remaining neutral radical species and the new broad signal belongs to the “biradical” = weak interacting case. The simulation indicated a g factor of 2.003 and although no hfc was directly observable due to the broadness of the signal a nitrogen hfc of ~0.41 mT was estimated. This hfc constant is roughly half the value of TAA⁺ centres (~0.82 - 0.89 mT).^{156,157} Following the explanation above J has to be much greater than the hfc constant $|a| = 0.004 \text{ cm}^{-1}$ but has to be lower or to be in the range of D with typical values of $|D| = 0.05\text{-}0.20 \text{ cm}^{-1}$ ¹⁵⁸ for biradical molecules.¹⁵⁵ Regarding **Star-Model**, only a decrease of the PCTM signal is observed so that the formed cation has to be ESR silent. This implies a strong electron exchange interaction constant J and the formation of either a singlet or triplet species or both. To distinguish between these cases, EPR spectra were measured at 80 K but no change in the signal nor a half-field signal, typical of a triplet electronic state, could be observed. We therefore assume that **Star-Model**⁺ is in a singlet state, consistent with the antiferromagnetic coupling pathway between the radical centres.

4.5. Absorption spectroscopy

Absorption spectra were recorded to analyse possible charge transfer transitions with the aim to get information on the electronic coupling between the electron donor and acceptor centres. The absorption spectra of **HAB-S**, **HAB-A** and **HAB-Model** resemble each other strongly in band structure (Figure 53) and intensity if the lower number of chromophore units in **HAB-Model** is taken into account.

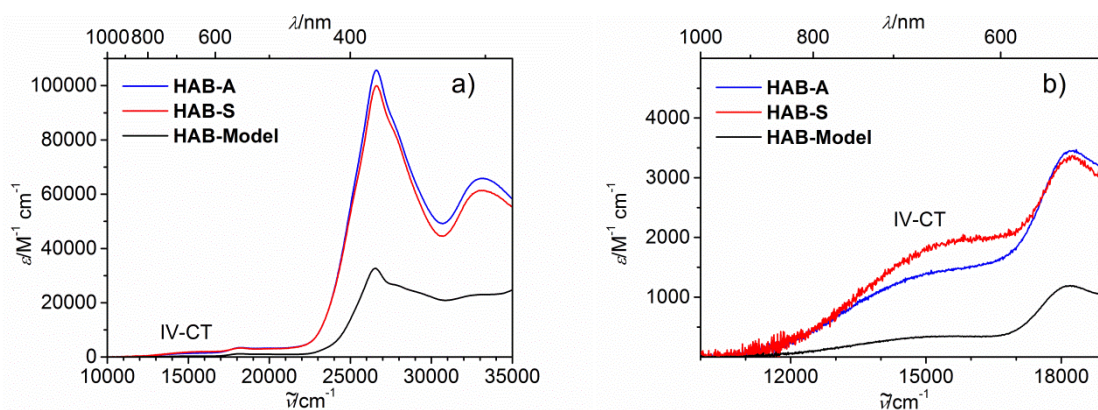


Figure 53 a) Absorption spectra of **HAB-S**, **HAB-A** and **HAB-Model** in DCM. b) Absorption spectra of **HAB-S**, **HAB-A** and **HAB-Model** in DCM in the range of 10000 cm⁻¹ to 19000 cm⁻¹

All three HABs show two striking absorption features at 26500 cm⁻¹ and 33200 cm⁻¹. The former, with its shoulders at ca. 27700 and 24900 cm⁻¹, consists of overlapping π - π^* transitions located at the TAA (expected at ~24900 cm⁻¹)^{32,122,124} and the PCTM centres (SOMO-LUMO transitions are expected at 27200 cm⁻¹).¹²⁰⁻¹²⁴ In addition, two weak absorption bands at 18200 and 19700 cm⁻¹ can be observed originating from HOMO-SOMO transitions located at the radical centres.^{120,121} The observation of two bands for this transition results probably from the asymmetric substitution of the radical chromophore and therefore from the loss of degeneracy of the HOMO. This was shown before for the isoelectronic triarylamine radical cation.³² The lowest energy absorption band at 15700 cm⁻¹ is in each case attributed to an intervalence charge transfer band (IV-CT) associated with the optically induced charge transfer from an electron rich triarylamine centre to an electron poor radical centre.¹²³ The intensity decreases in the series **HAB-S** ($\epsilon_{\max} \leq 2000$ M⁻¹ cm⁻¹), **HAB-A** ($\epsilon_{\max} \leq 1500$ M⁻¹ cm⁻¹) and **HAB-Model** ($\epsilon_{\max} \leq 300$ M⁻¹ cm⁻¹). This observation is in good agreement with the number of possible charge transfer pathways in the respective HABs which decreases likewise in the series **HAB-S** (six), **HAB-A** (four) and **HAB-Model** (one).¹⁹

To characterise the charge transfer properties in **HAB-Model** a *Mulliken-Hush* analysis was performed.^{57,159-163} According to this theory the electronic coupling V between the diabatic ground and IV-CT excited states can be calculated by equation 13 with the transition moment μ_{ab} (obtained by

equation 14), the energy $\tilde{\nu}_{\max}$ of the measured IV-CT band maximum and the diabatic dipole moment difference $\Delta\mu_{12}$ of the ground state (with its diabatic dipole moment μ_{11}) and excited state (μ_{22}). As these diabatic dipole moments are not available by experiment this $\Delta\mu_{12}$ difference has to be evaluated by the adiabatic dipole moment difference $\Delta\mu_{ab}$ of the ground state (with its adiabatic dipole moment μ_{aa}) and excited states (μ_{bb}) by equation 15. The two adiabatic quantities were obtained by TDDFT calculations with a custom hybrid functional using the procedure developed by *Kaup et al.*¹⁶⁴ The calculations are in good agreement with the measured absorption spectra (see Table 6 for the comparison and Table 7 for the calculated IV-CT parameters).

$$V = \frac{\mu_{ab} \tilde{\nu}_{\max}}{\Delta\mu_{12}} \quad \text{with} \quad \tilde{\nu}_{\max} = \Delta G^{00} + \lambda_o + \lambda_v \quad (13)$$

$$\mu_{ab}^2 = \frac{3hc\varepsilon_0 \ln 10}{2000\pi^2 N} \frac{9n}{(n^2 + 2)^2} \int \frac{\varepsilon}{\tilde{\nu}} d\tilde{\nu} \quad (14)$$

$$\Delta\mu_{12} = \mu_{22} - \mu_{11} = \sqrt{(\Delta\mu_{ab})^2 + 4\mu_{ab}} \quad (15)$$

An electronic coupling of $V = 340 \text{ cm}^{-1}$ between the ground state and the IV-CT state was obtained for **HAB-Model** which can be safely attributed to the weak regime. This small interaction between the redox centres is due to a mostly through space coupling in the HAB framework.¹⁹

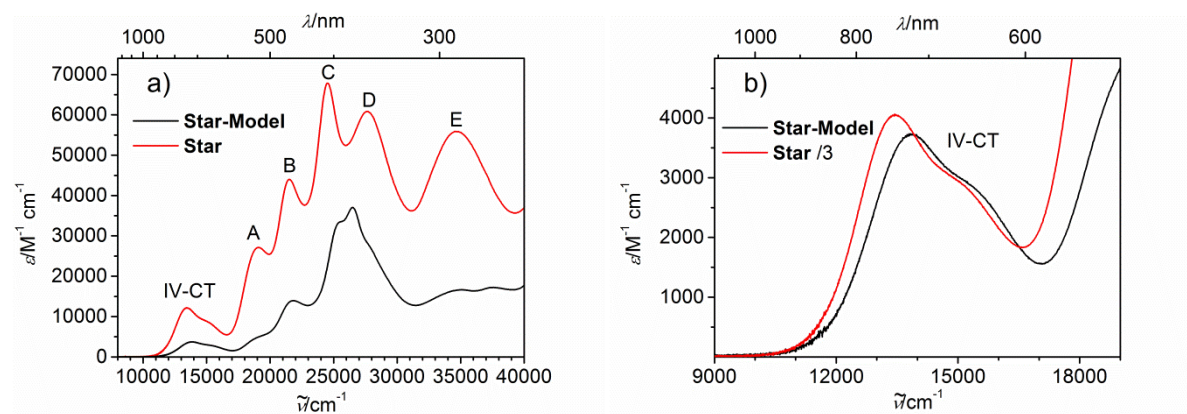


Figure 54 a) Absorption spectra of **Star** and **Star-Model** in DCM. b) Absorption spectra of **Star** and **Star-Model** in DCM in the range of 9000 cm^{-1} to 19000 cm^{-1} . The IV-CT band intensity of **Star** was divided by three for better comparison.

The UV/vis/NIR spectrum of **Star** shows six distinct absorption bands (see Figure 54). The two bands at 27700 cm^{-1} (D) and 34700 cm^{-1} (E) are attributed to $\pi\text{-}\pi^*$ transitions of the TAA.^{122,124} The sharp, intensive band at 24500 cm^{-1} (C) is assigned to $\pi\text{-}\pi^*$ transitions of the radical subunit.^{120-122,124} Furthermore, two absorption bands at 19100 cm^{-1} (A) and 21500 cm^{-1} (B) can be observed which are

common for this kind of electron donor-acceptor compound.¹²⁴ The lowest energy, asymmetric absorption band at 13500 cm^{-1} can be understood as an IV-CT transition from the amine donor to the radical acceptor. However, in contrast to the HABs the IV-CT band in **Star** and **Star-Model** is less overlapped by other transitions and much more intense.¹²³ An analogous spectrum is obtained from the model compound **Star-Model** with differences in band intensities, as the number of TAA chromophores has changed. Furthermore, the radical influenced transitions are changed because their electronic environment is altered, but only to a minor degree. In agreement with that, the extinction coefficient of the transition (E) located at the amine is lower by the factor of around three for **Star-Model**. The two $\pi\text{-}\pi^*$ transitions (C) and (D) are shifted and are overlapping in the range of 23000 cm^{-1} to 30000 cm^{-1} . Therefore, an accurate assignment of band positions and intensities for **Star-Model** is not possible. The absorption bands (A) and (B) show decreased oscillator strengths by a factor of around five and three, respectively, whereas their positions remain virtually unaltered. In addition, the IV-CT band maximum is shifted by 400 cm^{-1} to higher energies and the intensity is reduced by a factor of around three (Figure 54) as the number of possible IV-CT pathways is reduced from three in **Star** to one in **Star-Model**.¹⁶⁵

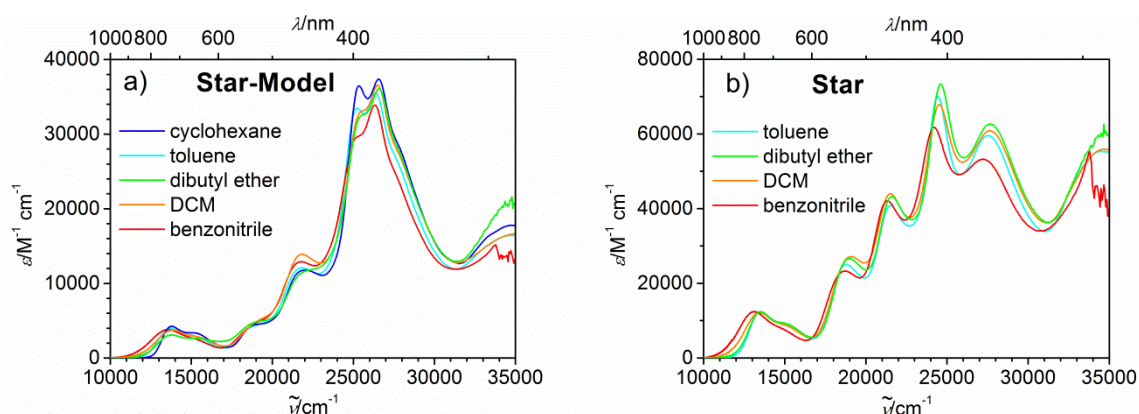


Figure 55 a) Absorption spectra of **Star-Model** in solvents of different polarity. b) Absorption spectra of **Star** in solvents of different polarity.

Solvatochromism studies of **Star** and **Star-Model** shall give information about the IV-CT processes involved. The spectra of both compounds in solvents ranging from totally apolar (cyclohexane) to highly polar (acetonitrile) in general show little systematic variation with exception of the IV-CT band (see Figure 55). Their band shapes were analysed using equation 9 based on *Jortner's* theory.^{53,124,166,167}

$$\varepsilon/\tilde{\nu} = \frac{2000N\pi^2}{3\varepsilon_0 \cdot \ln 10} \frac{(n^2 + 2)^2}{9n} \mu_{\text{eg}}^2 \sum_{j=0}^{\infty} \frac{e^{-S} S^j}{j!} \sqrt{\frac{1}{4\pi hc \lambda_0 kT}} \exp\left[-\frac{hc(j\tilde{\nu}_v + \lambda_0 - \tilde{\nu} + \Delta G^{00})^2}{4\lambda_0 kT}\right] \quad (9)$$

with the Huang Rhys factor $S = \frac{\lambda_v}{\tilde{\nu}_v}$

With this semiclassical treatment absorption bands can be fitted by four parameters.^{124,166,168,169} These are the inner and outer reorganization energies λ_v and λ_o associated with bond length and bond angle changes and solvent reorientations, respectively. In addition, the free energy difference ΔG^{00} between the diabatic ground and IV-CT states and the quantum chemically treated high-temperature averaged molecular vibration mode $\tilde{\nu}_v$ are obtained. The *Huang-Rhys* factor S determines the IV-CT band shape. If this value is too high the IV-CT band has a *Gaussian* form and can no longer be treated by Jortner's theory due to ambiguous dependency of the fit parameters as observed in the case of the HABs. In the latter compounds $\tilde{\nu}_v$ is likely to be very small as was assumed in the biaryl compound **V1** because a vinyl or alkyne bridging unit is missing and the biaryl torsions should have low frequencies.¹²⁴ In contrast, in **Star-Model** the *Huang-Rhys* factor is small so that the IV-CT band is asymmetric based on a *Poisson* distribution of vibrational transitions, each *Gaussian*-broadened by solvent interactions. The fits are depicted in Figure 56 and the fitted parameters are summarised in Table 6.

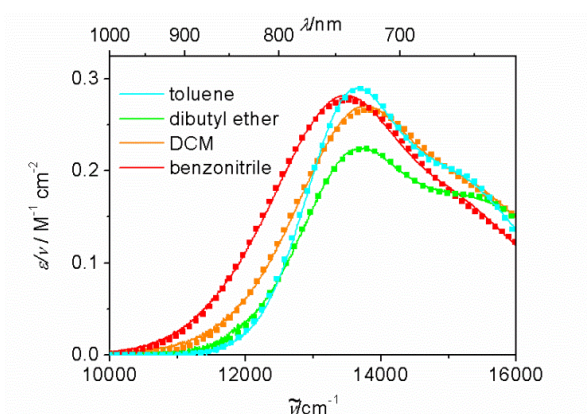


Figure 56 Least-squares fits (squares) of equation 9 to the reduced IV-CT bands (lines) of **Star-Model** in solvents of different polarity.¹⁷⁰

Table 6 ET parameters λ_v , λ_o , $\tilde{\nu}_v$ and ΔG^{00} , the calculated and measured reduced absorption maxima $\tilde{\nu}_{\max}$ and transition dipole moments μ_{ab} of the IV-CT bands of **Star-Model** and of **HAB-Model**.

	$\tilde{\nu}_{\max, \text{meas}}$	$\tilde{\nu}_{\max, \text{calc}}$	$\mu_{ab, \text{meas}}$	$\mu_{ab, \text{calc}}$	λ_v^a	λ_o^b	$\tilde{\nu}_v^b$	ΔG^{00b}
	/cm ⁻¹	/cm ⁻¹	/D	/D	/cm ⁻¹	/cm ⁻¹	/cm ⁻¹	/cm ⁻¹
Star-Model								
cyclohexane	13760		2.63		c	c	c	c
toluene	13680		2.53		1050	1300	1700	12300
dibutyl ether	13720		2.56		1380	1660	1930	11970
DCM	13770	15200	2.70	5.38	1100	2330	2040	11330
benzonitrile	13470		2.59		950	2710	2190	10660
acetonitrile	13950		- ^d		1240	2780	2140	11000
HAB-Model								
DCM	14900	15400	0.81	0.90				

^a maximum error of ± 50 cm⁻¹. ^b maximum error of ± 150 cm⁻¹. ^c the maximum error was too large for a reliable fit. ^d could not be measured due to low solubility.

The absorption maxima of the IV-CT bands show no obvious trend in solvents of varying polarity but appear to be randomly distributed around 13700 cm⁻¹. As shown for **V2**¹²⁴ this is due to opposing solvatochromic behaviours of the ET parameters (see Figure 57).

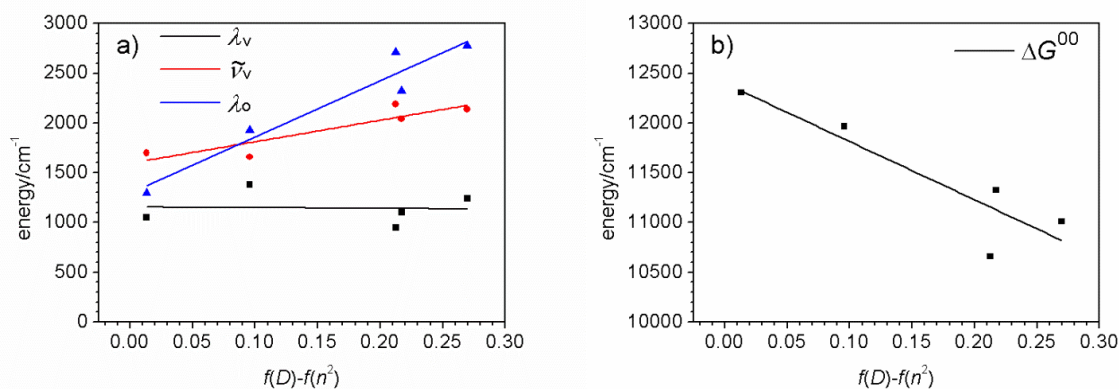


Figure 57 a) Linear regression of λ_v , $\tilde{\nu}_v$ and λ_o vs. solvent polarity function $f(D) - f(n^2)$, with $f(D) = (D - 1)/(2D + 1)$ and $f(n^2) = (n^2 - 1)/(2n^2 + 1)$ for **Star-Model**. b) Linear regression of ΔG^{00} vs. solvent polarity function $f(D) - f(n^2)$ for **Star-Model**.

Whereas ΔG^{00} decreases with increasing solvent polarity as the excited state is much better stabilised in polar solvents than the ground state, λ_o increases in the same ratio. Both λ_v and $\tilde{\nu}_v$ are only minor influenced by the solvent polarity. When comparing the ET parameters of **V2** with those of **Star-**

Model, the ΔG^{00} values are by 1500-3000 cm^{-1} higher in the latter. This is reasonable as **Star-Model** has the weaker electron acceptor centre, the polychlorinated triphenylmethyl radical ($E_{\text{red}} = -1000$ mV), compared to its per-chlorinated counterpart in **V2** ($E_{\text{red}} = -600$ mV). The value of λ_v is nearly doubled from around 650 cm^{-1} in **V2** to around 1200 cm^{-1} in **Star-Model** whereas λ_o and $\tilde{\nu}_v$ have similar values in solvents of low polarity but show a distinctly higher solvatochromism in **V2**.

To calculate the electronic coupling of the two redox centres in **Star-Model** by equation 13 only the adiabatic dipole moment difference $\Delta\mu_{12}$ remains to be determined. A value of $\Delta\mu_{\text{ab}} = 32.9$ D was obtained by TDDFT calculations (see Table 7) which is nearly twice as high as the value given for **V2** ($\Delta\mu_{\text{ab}} = 17.9$ D).¹²⁴ The latter was determined by electro-optical absorption (EOA) measurements which agrees with estimates by the *Lippert* and *Mataga* model. With $\Delta\mu_{\text{ab}} = 32.9$ D the electronic coupling yields $V = 1190$ cm^{-1} in **Star-Model** which is about half the coupling of **V2** ($V = 2630$ cm^{-1}). This finding is somewhat unexpected as the decreased steric hindrance of the bridge in **Star-Model** should facilitate the electronic communication between the two redox centres in comparison to **V2** and not hamper it. To assess the accuracy of the high $\Delta\mu_{\text{ab}}$ value obtained by the TDDFT calculations we determined this quantity by a second approach. As demonstrated before for **V2** in ref.¹²⁴ $\Delta\mu_{\text{ab}}$ can also be calculated by correlating the total reorganization energy $\lambda_v + \lambda_o$ with the *Onsager* solvent parameter $f(D) - f(n^2)$ (equation 60) as shown by *Lippert* and *Mataga* (see Figure 58).^{171,172}

$$2(\lambda_v + \lambda_o) = \frac{(\Delta\mu_{\text{ab}})^2}{2\pi\epsilon_0 hca_0^3} (f(D) - f(n^2)) + (\tilde{\nu}_{\text{abs}}^{\text{gas}} - \tilde{\nu}_{\text{fl}}^{\text{gas}}) \quad (60)$$

$$\text{with } f(D) = \frac{D-1}{2D+1} \text{ and } f(n^2) = \frac{n^2-1}{2n^2+1}$$

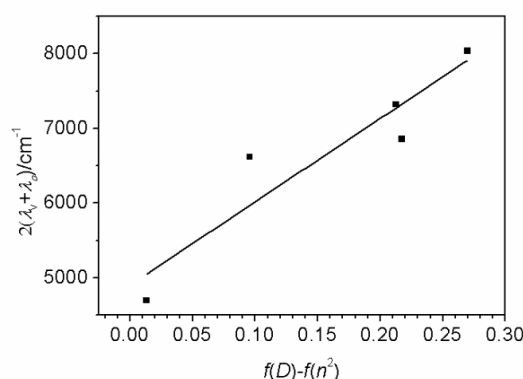


Figure 58 Linear regression of $2(\lambda_v + \lambda_o)$ vs. solvent polarity function $f(D) - f(n^2)$ for **Star-Model**.

Table 7. The *Connolly* solvent excluded volume a_0 , the adiabatic dipole moment difference $\Delta\mu_{ab}$, the measured transition dipole moments $\mu_{ab,meas}$ and electronic coupling V calculated according to *Lippert* and *Mataga* (index LM) and calculated from TDDFT data (index TDDFT)

	a_0 /Å	$\Delta\mu_{ab,LM}$ /D	$\Delta\mu_{ab,TDDFT}$ /D	$\mu_{ab,meas}$ /D	V_{LM} /cm ⁻¹	V_{TDDFT} /cm ⁻¹
Star-Model	5.31	12.9 ± 1.4	32.9	2.70 ^b	2940 ± 280	1190
HAB-Model	-		35.7	0.81 ^b		340
V2^a	5.54	17.9 ± 1.4		4.1 ^c	2630 ± 240	

^a data taken from Lit.¹²⁴, ^b in DCM, ^c in *n*-Hexane

From the slope of Figure 58 the adiabatic dipole moment difference $\Delta\mu_{ab}$ can then be evaluated. Therefore, the radius a_0 of **Star-Model** is needed which was calculated from its *Connolly* solvent excluded volume¹⁴⁷ assuming the molecule to be spherical (see Table 7). The adiabatic dipole moment difference obtained in this way is $\Delta\mu_{ab} = 12.9$ D which appears more reasonable and is by far smaller than the value obtained by TDDFT calculations. Calculating the electronic coupling with $\Delta\mu_{ab} = 12.9$ D for **Star-Model** by equation 13 yields $V_{LM} = 2940$ cm⁻¹ which indicates a much stronger electronic communication of the two redox centres as the one calculated by using dipole moment differences from TDDFT¹⁷³, see Table 7. However, the electronic couplings calculated for **Star-Model** and **V2** are in good agreement when applying the methodology according to *Lippert* and *Mataga*. Consequently, the electronic communication between the redox centres in **Star-Model** and **V2** is marginally influenced by the differing structure of the PCTM centres. In any case, the electronic coupling V of **Star-Model** is distinctly larger than that of **HAB-Model**. Hence, the alkyne bridge provides a much better electronic linkage as the HAB framework.

4.6. Spectroelectrochemistry

In order to investigate the spectral changes that undergo the radicals upon oxidation of the TAA moieties or reduction of the PCTM groups we performed spectroelectrochemistry experiments in DCM/electrolyte solution. The spectra of the oxidised and reduced species will also be helpful for the interpretation of transient absorption spectra.

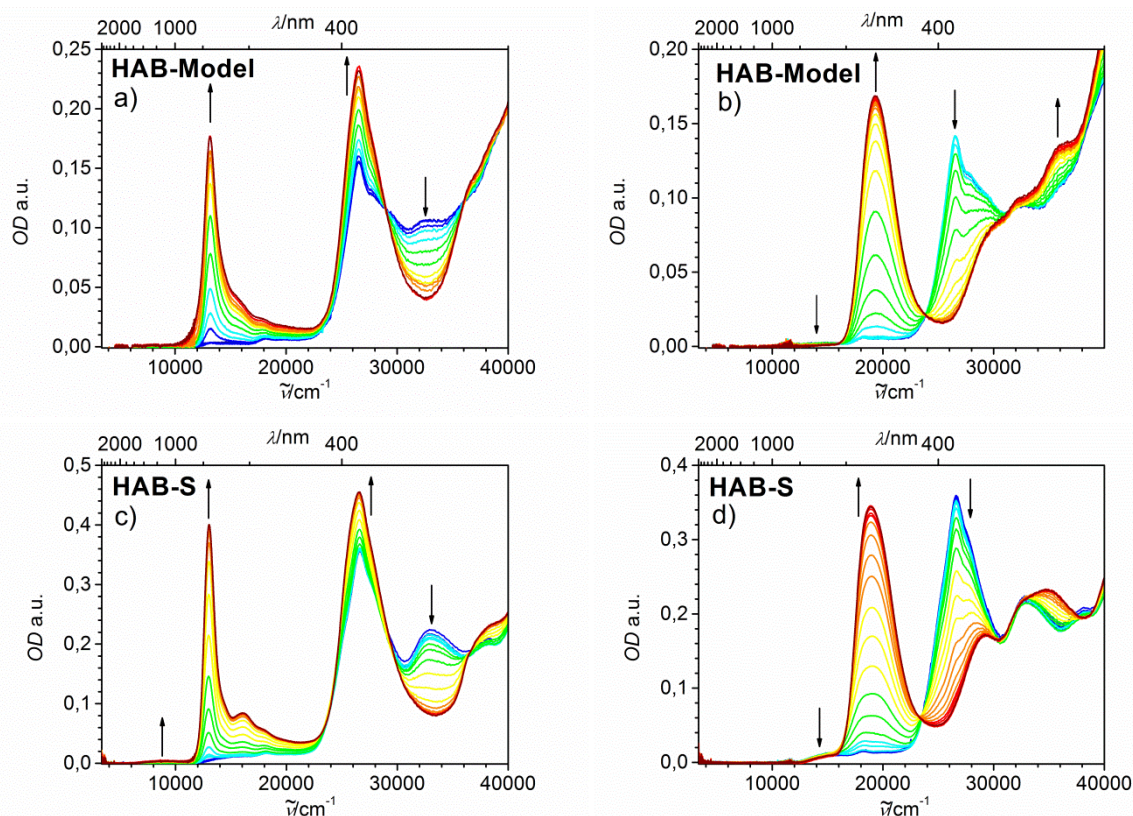


Figure 59 SEC of a) the first oxidation and b) the first reduction of **HAB-Model**. SEC of c) the first oxidation and d) the first reduction and **HAB-S**. The neutral species are given in blue, the fully electrolysed species in brown. The applied potential was varied in 20 mV steps.

Radical **HAB-A** showed considerable irregularities in band intensity during the measurements possibly caused by deposition at the platinum working electrode rendering a discussion impossible. The spectroelectrochemistry of **HAB-Model** and **HAB-S** (Figure 59) are very similar and will be discussed together. This is reasonable as the single electron redox steps in **HAB-S** are spectroscopically indiscernible. By reduction both compounds show the formation of an intensive absorption band at 18900-19300 cm^{-1} which is attributed to π - π^* transitions of the PCTM anion centre. These are expected at 20000 cm^{-1} for a single PCTM¹²¹ but might be bathochromically shifted in mixed-valence compounds.¹²⁴ Furthermore, the radical centred transitions at 26600 cm^{-1} as well the CT transitions at 15000-15600 cm^{-1} decrease in intensity upon reduction.

During the oxidation process an intensive and narrow absorption band emerges at 13000-13100 cm^{-1} with a shoulder at 15900-16100 cm^{-1} characteristic for π - π^* transitions in TAA radical cations.³² In addition, the absorption bands at 26600 cm^{-1} are increasingly overlapped by a second transition which is also attributed to the TAA radical cation.³² In contrast, transitions localised at the neutral TAA centres in the range of 32500-33000 cm^{-1} decrease. In the SEC of **HAB-S** one can clearly observe the appearance of a very weak absorption band at 8900 cm^{-1} . It is attributed to a charge transfer reversed from that of the neutral species, that is, from the PCTM radical to the electron poorer cationic TAA centre.¹²⁴ In **HAB-Model**⁺ this band is not observed possibly due to an insufficient signal to noise

ratio. The CT band in **HAB-S⁺⁺** is very weak and that in **HAB-Model⁺⁺** is expected to be one third as intensive.

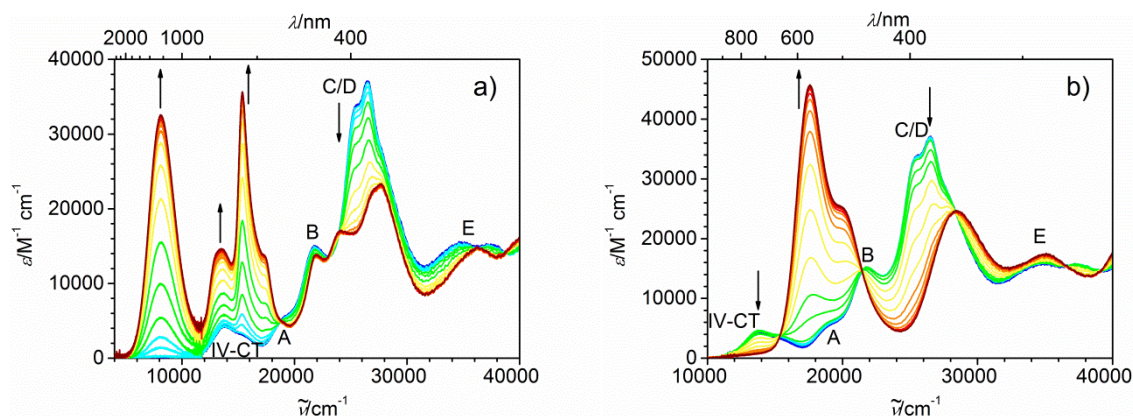


Figure 60 SEC of a) the first oxidation and b) the first reduction of **Star-Model**. The neutral species is given in blue, the fully electrolysed species in brown. The applied potential was varied by 20 mV per step until no further change in the spectrum was observed.

By reducing **Star-Model**, the IV-CT absorption band (13500 cm^{-1}), band B (21500 cm^{-1}) and the bands between 24000 cm^{-1} and 30000 cm^{-1} , all featuring transitions involving the radical centre (see Figure 60), vanish. Furthermore, the reduced species shows a strong absorption band at 17600 cm^{-1} with a shoulder band at 19900 cm^{-1} . These are caused by $\pi\text{-}\pi^*$ transitions at the anion centre.

During oxidation of **Star-Model** (Figure 60) the absorption bands at 26000 cm^{-1} and 34500 cm^{-1} decrease as expected for transitions located at the amine. Two intense absorption bands at 15400 cm^{-1} and 13500 cm^{-1} rise. The former asymmetric band is attributed to $\pi\text{-}\pi^*$ transitions of the radical cation, the latter is presumably a bridge-to-radical cation CT. This has been observed before in molecules in which an oxidised TAA is connected via a conjugated bridge to an acceptor.^{35,59,156} Even more interesting is an intense absorption band at 8100 cm^{-1} ($\epsilon_{\text{max}}=32400\text{ M}^{-1}\text{ cm}^{-1}$), attributed to a charge transfer from the PCTM radical to the TAA centre that is likewise present in the **HAB-S**.¹²⁴ The increased oscillator strength of this band in contrast to the IV-CT band in the neutral species is remarkable and cannot be explained by the bathochromic shift exclusively but must be caused by an increase in electronic coupling. For comparison, it is about five times as intensive as in **V2**.

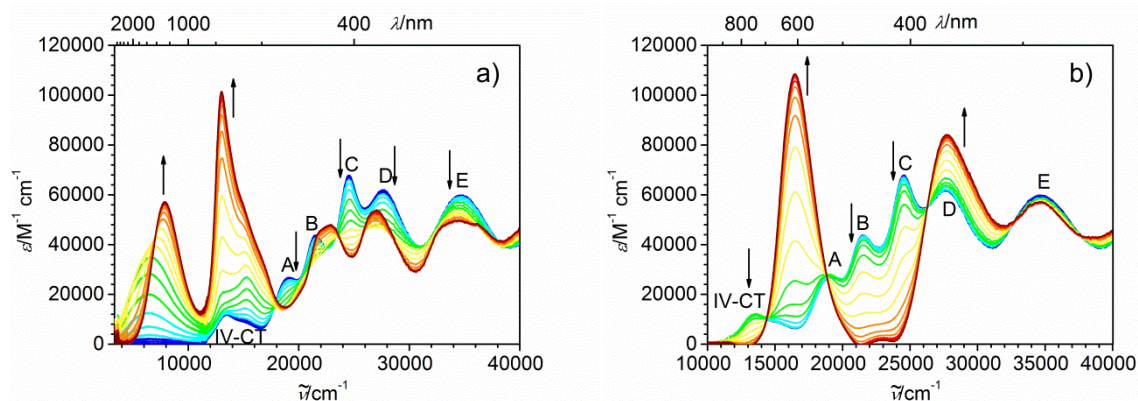


Figure 61 SEC of a) the first oxidation and b) the first reduction of **Star**. The neutral species is given in blue, the fully electrolysed species in brown. The applied potential was varied by 20 mV per step until no further change in the spectrum was observed.

The reduction of **Star** (Figure 61) induces spectral changes very similar to that of the model compound **Star-Model**. With the exception of the absorption bands D and E originating from π - π^* transitions located at the TAAs, all bands vanish including band A. As observed before, an intense absorption band originating from π - π^* transitions at the anion centre is forming at 16500 cm^{-1} . Its asymmetry is much less pronounced compared to that of **Star-Model**. This is most likely a result of the symmetric substitution pattern of the PCTM and thus a smaller splitting of the formally degenerate LUMO orbitals.

By oxidising **Star** (Figure 61) to the trication we observed a continuous change of spectra. To get absorption spectra related to the individual oxidation steps the SEC data were deconvoluted by a global fitting routine implemented in the SpecFit software package (Figure 62).¹⁷⁴

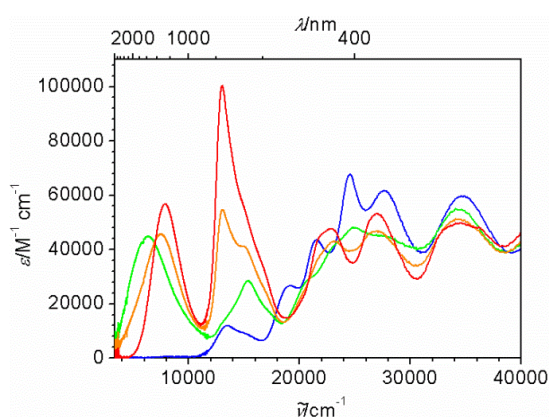


Figure 62 Deconvoluted spectra of a global fit of the SEC. The absorption spectra of the oxidation states 0 (blue), +1 (green), +2 (orange) and +3 (red) are shown.

The quality of the fit was ascertained by comparison of the potential splitting calculated by the global fitting software to that measured by CV. These values are in good agreement (measured:

$\Delta E_{\text{ox1-2}} = 70$ mV, $\Delta E_{\text{ox2-3}} = 30$ mV, calculated: $\Delta E_{\text{ox1-2}} = 69$ mV, $\Delta E_{\text{ox2-3}} = 38$ mV). However, it has to be stressed that the measured potential splitting for the three oxidation processes is very small (100 mV), so substantial deviations in the fitted absorption spectra arise by altering the splitting by a few millivolts. Nevertheless, several trends in the SEC spectra can be observed. Starting from the low energy part of the spectra, an intense absorption rises in **Star**⁺ with a maximum at 6300 cm⁻¹, getting narrower and showing higher energetic maxima at 7400 cm⁻¹ for **Star**²⁽⁺⁾ and at 8000 cm⁻¹ for **Star**³⁽⁺⁾. The absorption band of the trication is very similar to the low energy transition in the model compound **Star-Model**⁺ and is likewise explained by a charge transfer from the radical centre to the oxidised TAA moieties. The illustrated changes in the SEC can be interpreted by the IV-CT transition depending on the oxidation state of the multidimensional chromophore. Due to oxidation of the second (in **Star**²⁽⁺⁾) and third TAA centre (in **Star**³⁽⁺⁾) the electron donor ability of the central PCTM is reduced in comparison to **Star**⁺ (see Table 8). This can be seen in the charge transfer parameters extracted by fitting the IV-CT absorptions bands of the cations by the *Bixon-Jortner* expression (equation 9)(see Figure 63).

Table 8 Charge transfer parameters $\tilde{\nu}_v$, λ_o , λ_v and ΔG^{00} and transition dipole moments μ of the low energy IV-CT bands of **Star**⁺, **Star**³⁽⁺⁾ and **Star-Model**⁺.

	μ / D	$\tilde{\nu}_v / \text{cm}^{-1}$	$\lambda_o / \text{cm}^{-1}$	$\lambda_v / \text{cm}^{-1}$	$\Delta G^{00} / \text{cm}^{-1}$
Star ⁺	15.5	1770	3300	1230	1875
Star ²⁽⁺⁾	14.4	a	a	a	a
Star ³⁽⁺⁾	12.9	1470	2310	580	5140
Star-Model ⁺	9.2	1400	2120	410	5710

^a could not be determined due to ambiguous fitting.

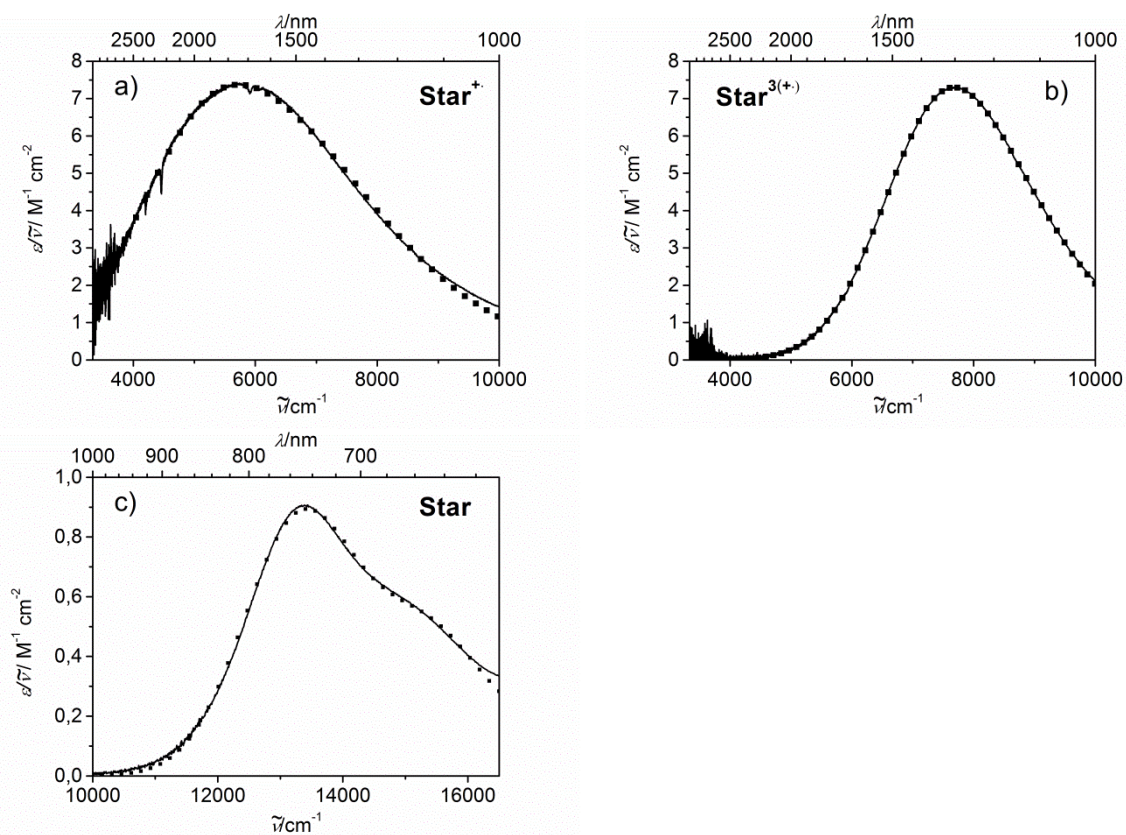


Figure 63 Least-squares fits (squares) of the reduced IV-CT bands (line) of a) **Star**⁺, b) **Star**³⁽⁺⁾ and c) **Star** in DCM.

The free energy ΔG^{00} is substantially lower in **Star**⁺ in comparison to **Star-Model**⁺ indicating that the electron rich TAA moieties strengthen the donor ability of the radical centre in **Star**⁺. At the same time both reorganization energies λ_v and λ_o are increased (see Table 8), whereas $\tilde{\nu}_v$ remains nearly unaltered. The IV-CT absorption band of **Star**²⁽⁺⁾ obtained by SpecFit could not be fitted by the *Bixon-Jortner* expression as it is too symmetric to get reliable values for the parameters.³¹ The obtained set of parameters for **Star**³⁽⁺⁾ confirms the resemblance of its IV-CT bands to that of **Star-Model**⁺ in spite of the different molecular structures.

Remarkably, the transition dipole moments (Table 8) of the IV-CT bands of **Star**⁺, **Star**²⁽⁺⁾ and **Star**³⁽⁺⁾ are slightly decreasing in this sequence. Although the number of possible charge transfer pathways increases equally with the oxidation state and thus an increase in band intensity is expected. In addition, the square of the transition dipole moment of the IV-CT band of **Star**³⁽⁺⁾ is about two times higher than that of **Star-Model**⁺. A factor of three would be expected if the three possible CT pathways **Star**³⁽⁺⁾ are accounted for. Both phenomena can be attributed to a varying electronic environment of the IV-CT states in question with changing the redox centres either by altering substitution or oxidation of their substituents.

4.7. Transient absorption spectra

fs-Transient absorption spectra of all radical compounds were measured in DCM to investigate the evolution and decay of the excited IV-CT states. Therefore, the molecules were excited at the centre of their respective IV-CT absorption band to exclude dynamics of localised transitions and the excitation of the contaminating α -H precursors (see synthesis). Thus, **HAB-Model**, **HAB-A** and **HAB-S** were excited at 15200 cm^{-1} , **Star-Model** and **Star** at 13800 cm^{-1} , that is, directly into the IV-CT band. The pump pulses had a temporal width of 140 fs and the probe white light continuum ranged from 12900 cm^{-1} to 23500 cm^{-1} (in the case of **HAB-Model** from 12100 cm^{-1}). The transient data (see appendix 1) were deconvoluted by a global fitting routine (see experimental section) to get evolution associated difference spectra (EADS) and their respective time constants of formation and decay. All EADS are rising with the decay time constant of the previous EADS and are decaying with the time constants given in the Figure 64 and 68 and Tables 9 and 10, with the exception of the respective first EADS which is formed in the time regime of the instrument response (180-200 fs in DCM).

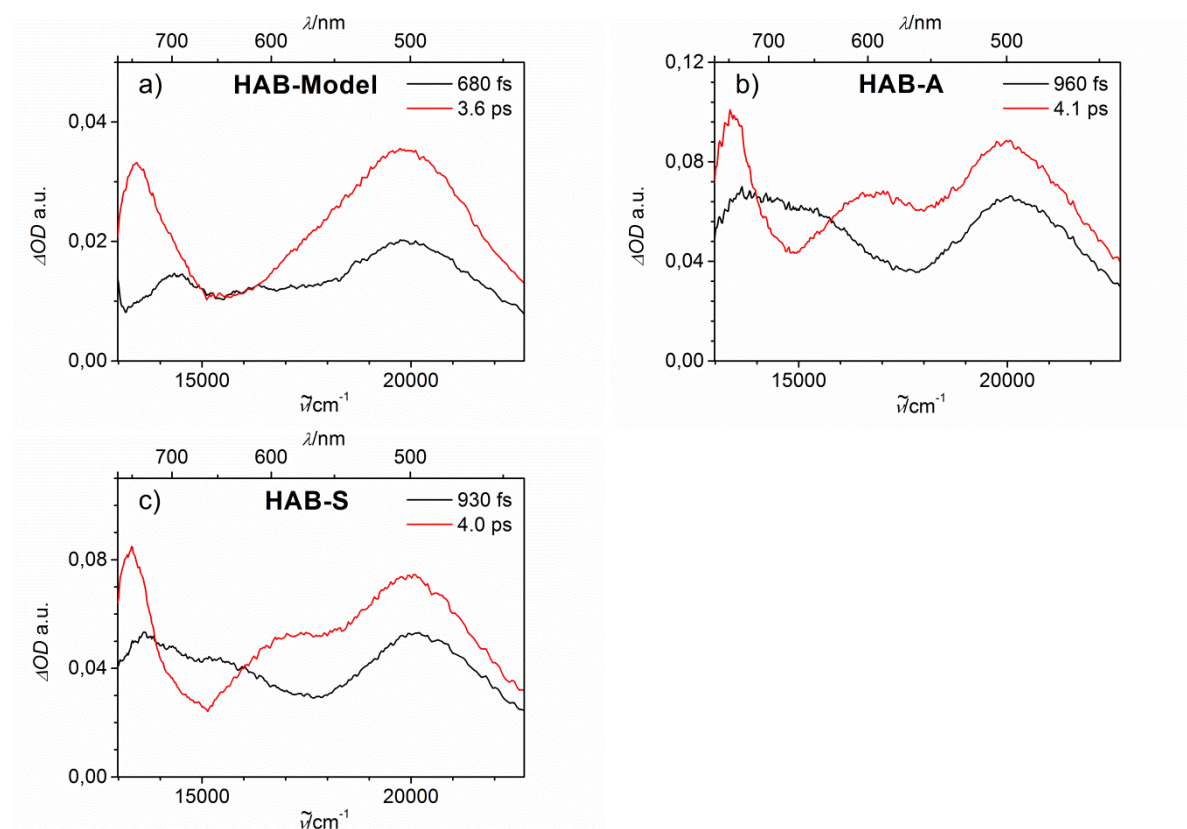


Figure 64 Evolution associated difference spectra of a) **HAB-Model**, b) **HAB-A** and c) **HAB-S** in DCM with the associated decay times. Pump energy = 15200 cm^{-1} .

The global fit of the transient maps of **HAB-Model**, **HAB-A** and **HAB-S** resulted in all cases in two EADS (EADS1 and EADS2) with time constants of $\tau_1 = 0.7\text{-}1.0\text{ ps}$ for the first and $\tau_2 = 3.6\text{-}4.1\text{ ps}$ for the second. In all the EAS a maximum at 20000 cm^{-1} and a maximum in the range of $13300\text{-}14500\text{ cm}^{-1}$

¹ is observed. Regarding the evolution from EADS1 to EADS2 the former band is only increasing in intensity whereas the latter is additionally narrowing and especially in the case of **HAB-Model** shifting to lower energies. Furthermore, in the EADS2 of **HAB-A** and **HAB-S** a band at around 17000 cm⁻¹ is observed. To verify the possible involvement of excited charge transfer states, the EADS2 were compared to the sum of the cation and anion spectra obtained by SEC, corrected for the ground state bleaching by subtracting the absorption spectra in DCM (Figure 65). In this way, we model the excited IV-CT state where a PCTM moiety is reduced and a TAA is oxidised.

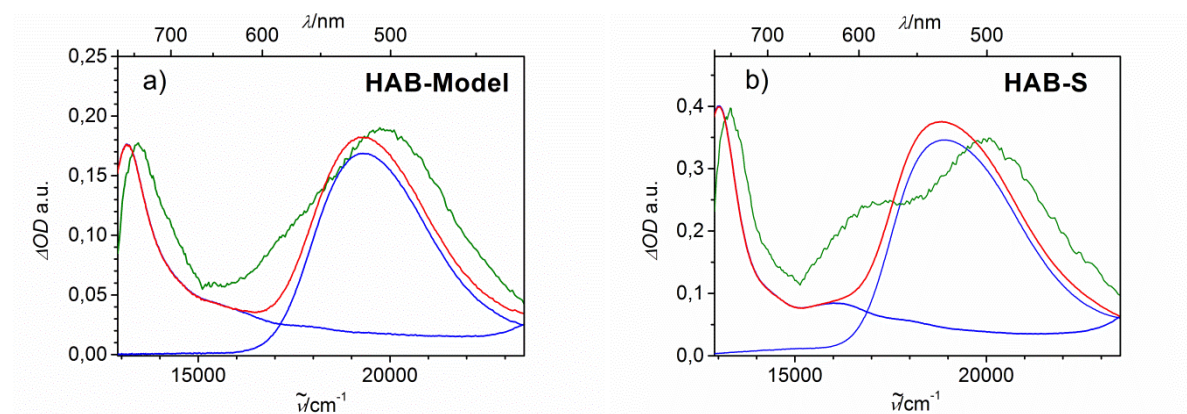


Figure 65 EADS2 (green) and the sum (red, corrected for the ground state bleaching) of the individual SEC spectra of oxidation and reduction (blue) for a) **HAB-Model** and b) **HAB-S** in DCM.

From Figure 65 a good agreement of EADS2 with the SEC spectra is obtained if accounting for a shift of the SEC data of around 350-750 cm⁻¹ to lower energies¹²⁸ and for an increased transient absorption in the region around 16900 cm⁻¹. Thus, the transient absorption at 13300 cm⁻¹ is assigned to the TAA radical cation and the transient absorption at 20000 cm⁻¹ to the PCTM anion verifying the state to be the lowest excited state. The band at 16900 cm⁻¹ is more prominent for **HAB-A** and **HAB-S** than for **HAB-Model**.¹⁷⁵ However, no specific assignment of this absorption is obvious. A similar transition was observed also in the fs-transient absorption spectra of **V1** in toluene and MTBE.¹⁷⁵ This band might be caused by a strong electronic communication between the two redox centres, an effect which is not considered in the spectra obtained by SEC. On the other hand, the low intensity of the IV-CT band and the good agreement of the TAA⁺ absorption band profile obtained by SEC with that of the transient absorption indicate a weak electronic coupling between the two redox centres.

Because we pumped the radical samples directly into the IV-CT band and all EADS1 present maxima in the same region as the respective EADS2, the former are attributed to the partially unrelaxed IV-CT states.^{67,106,176-181} These are the first states observed after excitation and their molecular geometry and/or solvation are similar to the ground state (see Figure 66).

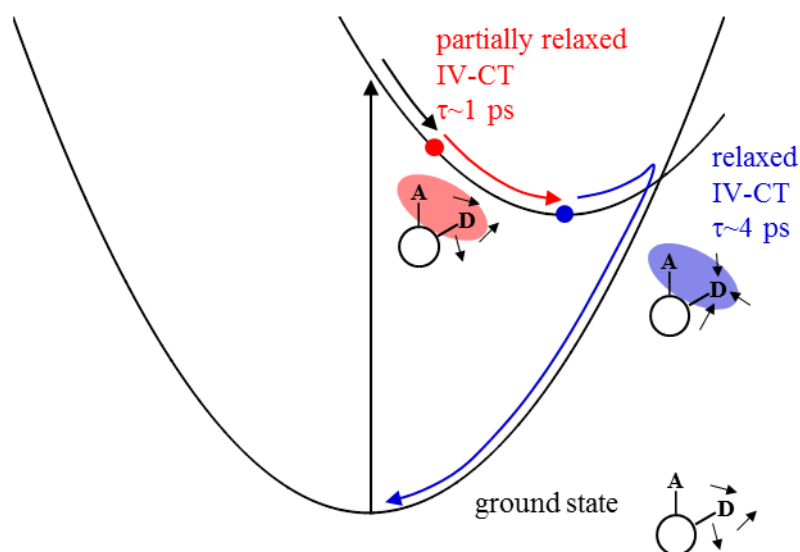


Figure 66. Potential energy diagram for the relaxation processes in the excited state of **HAB-Model**. The molecule is sketched besides the relevant states. The small black arrows represent solvent molecules.

After excitation, these unrelaxed IV-CT states relax to the thermally equilibrated IV-CT states observed as EADS2. While the global fit assumes discrete species associated with EADS1 (partially relaxed IV-CT state) and EADS2 (relaxed IV-CT state) such a relaxation process may well be described by a continuous shift along an excited state potential energy surface.^{177,180,182,183} The dynamics of this relaxation may give information about its mechanism. Therefore, we analysed the time-dependent shift of the absorption maximum of the low energy band at ca 13500 cm⁻¹, which is least affected by overlapping ground state bleaching. Then, the spectral response function $S_{\tilde{\nu}}(t)$ was calculated by equation 61.⁵¹

$$S_{\tilde{\nu}}(t) = \frac{\tilde{\nu}_{\max}(t) - \tilde{\nu}_{\max}(\infty)}{\tilde{\nu}_{\max}(0) - \tilde{\nu}_{\max}(\infty)} \quad (61)$$

The maxima of the transient absorption bands $\tilde{\nu}_{\max}(t)$ at t after time zero were determined from the chirp corrected and smoothed raw spectra. The value of the longest measured time delay of 4 ps served as $\tilde{\nu}_{\max}(\infty)$, the maximum of the transient spectra at infinite time. The energy $\tilde{\nu}_{\max}(0)$ corresponds to the maximum of the transient spectra at time zero, which we define as the time of the instrument response maximum. The signal-to-noise ratio as well as the coherent artefact cause severe errors for time constants < 400 fs. The fastest processes observable have time constants of ~ 100 fs.

Consequently, very fast shifts of the maxima, which are expected for solvent controlled processes, are possibly not resolved.⁵¹ The fitted spectral response functions of **HAB-S**, **HAB-A** and **HAB-Model** are depicted in Figure 67 (see appendix 1 for the chirp corrected transient maps) and the time constants are given in Table 9.

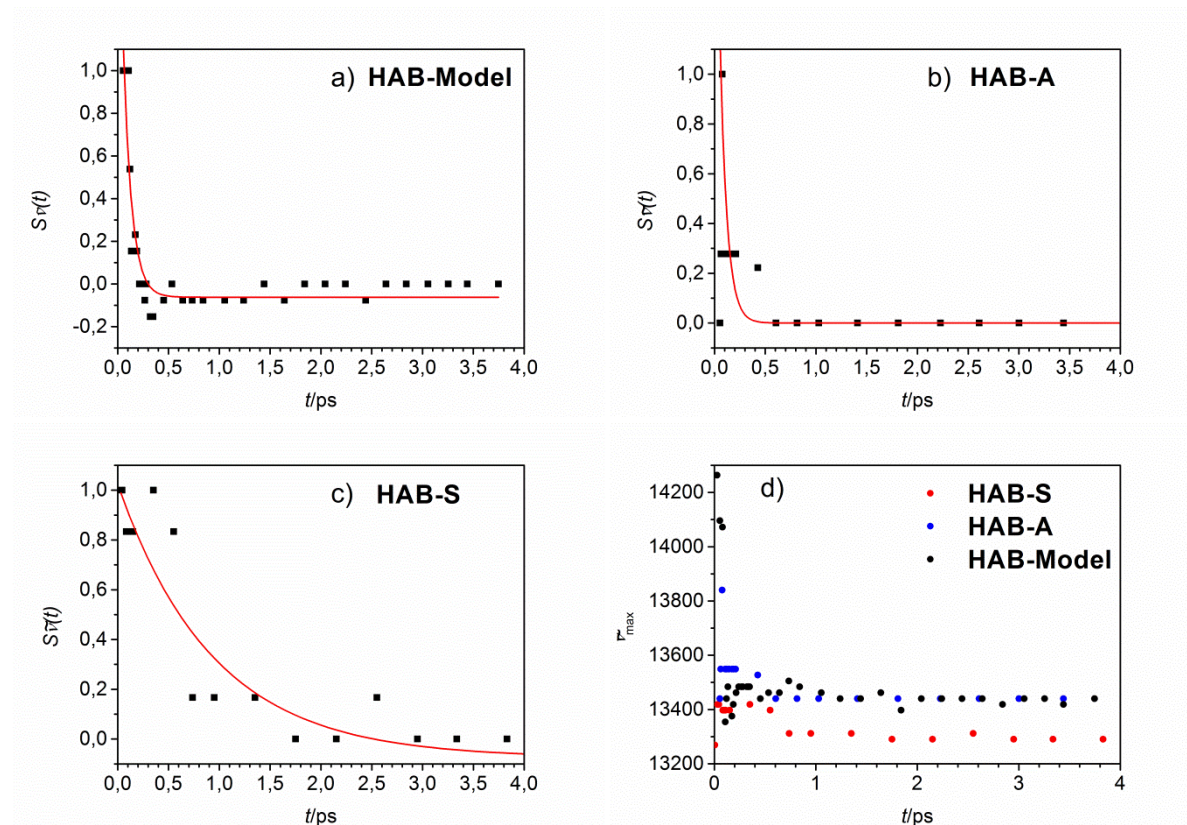


Figure 67 Spectral response function $S_{\tilde{\nu}}(t)$ (black) and its exponential fit (red) of a) **HAB-Model**, b) **HAB-A** and c) **HAB-S**. d) Shift of the absorption maxima of **HAB-Model**, **HAB-A** and **HAB-S** in wavenumbers.

Table 9 Decay time constants τ_1 and τ_2 of the evolution associated spectra EADS1 and EADS2, respectively, and the mono-exponential time constants τ_s for the spectral response function $S_{\tilde{\nu}}(t)$ of **HAB-S**, **HAB-A** and **HAB-Model** in DCM.

	τ_1 / ps	τ_2 / ps	τ_s / ps
HAB-Model	0.68	3.6	0.08 ± 0.1
HAB-A	0.96	4.1	0.07 ± 0.1
HAB-S	0.93	4.0	0.94

In the case of **HAB-Model** and **HAB-A** a very short time constant of $S_{\tilde{\nu}}(t)$ was obtained, whereas for **HAB-S** a time constant of $\tau_s = 0.94$ ps was obtained. The latter time constant could be ascribed to solvation processes. *Maroncelli et al.* found a multiexponential decay with time constants of

$\tau_a = 0.144$ ps and $\tau_b = 1.02$ ps and an average time constant of $\langle \tau \rangle = 0.56$ ps in DCM for the time dependent solvation of coumarin 153.⁵¹ On the other hand, intramolecular vibrational redistribution contributes to the deactivation of the partially unrelaxed IV-CT state with time constants of typically ≤ 100 fs¹⁸⁴. Thus, in the case of **HAB-Model** and **HAB-A** the shift of the maxima is governed essentially by the very fast inertial motion of the solvent molecules and/or intramolecular relaxation processes both with time constants ~ 100 fs. In contrast, the narrowing of the TAA⁺ absorption bands of **HAB-Model** and **HAB-A** (see appendix 1) can be attributed to low frequency dynamics of the solvent with time constants τ_1 in good agreement with the time constants $\langle \tau \rangle$ or τ_b of coumarin 153 in DCM. In **HAB-S** the very fast 100 fs processes are not resolved. Only a weak shift of 100 cm^{-1} and the narrowing process is attributed to the slow solvent relaxation time τ_b (see appendix 1). Thus, the relaxation process seems to be influenced by the solvent viscosity. It follows that most likely a large amplitude motion is involved in this process, e.g. the twist of two or more aryl rings within the HAB framework.^{77,176,177} A time dependent shift of the absorption band of the PCTM is not observed so both anion localised states responsible for this transition have similar potentials regarding solvent and intramolecular relaxation. In the case of the TAA⁺ transient absorption band ascribed to localised π - π^* transitions, the potential of the lower state (State₁) has to be flattened in comparison to the high energy state (State_x). This leads to a red shift and a sharpening of the absorption band.¹⁷⁵

The time constant τ_2 represents the back electron transfer from the relaxed excited IV-CT state to the ground state. A theoretical investigation of this time constant is not possible here. Because of the Gaussian shaped IV-CT absorption band the necessary IV-CT parameters, e.g. λ_o and λ_v , are not known and could not be determined by the *Hush* analysis performed above. It has to be noted though that these back electron transfer time constants ($\tau_2 \sim 4$ ps for all HABs) are in the range of the solvation time constant obtained for DCM ($\tau_b = 1.02$ ps).⁵¹ For similar molecules it was found that the back electron transfer can be influenced by the solvation processes as well.¹⁷⁵

The analysis of the transient spectra of **Star** and **Star-Model** yielded in each case three EADS (see Figure 68 and Table 10) with time constants of $\tau_1 = 0.9$ ps for EADS1, $\tau_2 = 0.9$ -1.1 ps for EADS2 and $\tau_3 = 2.8$ -4.5 ps for EADS3. The excited state time constants τ_1 and τ_2 are in good agreement to the measured values for **V1** in MTBE¹⁷⁵ and for linear oligomers consisting of alternating TAA and PCTM centres.¹⁸⁵

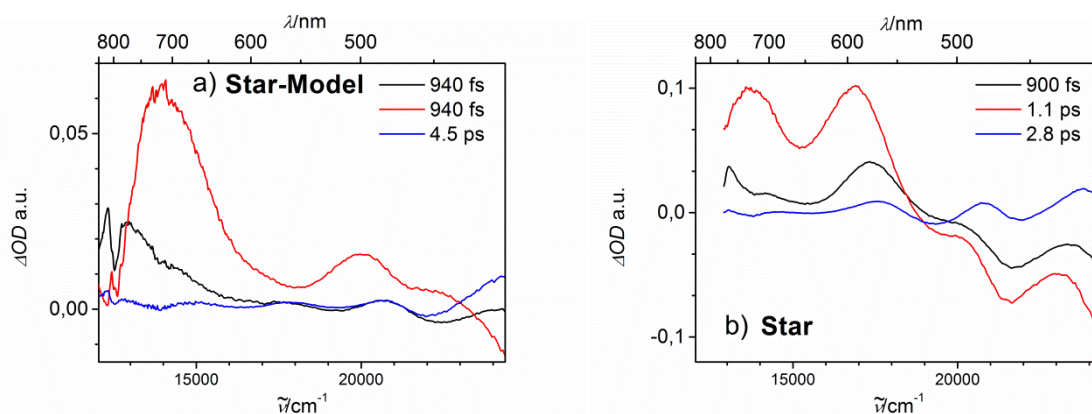


Figure 68 Evolution associated difference spectra of a) **Star-Model** and b) **Star** in DCM. Pump energy = 13800 cm^{-1} .

Table 10. Decay time constants τ_1 , τ_2 and τ_3 of the evolution associated spectra EADS1, EADS2 and EADS3, respectively, and time constants τ_{s1} and τ_{s2} for the biexponential decay of the spectral response function $S_{\tilde{\nu}}(t)$ of **Star** and **Star-Model** in DCM.

	τ_1/ps	τ_2/ps	τ_3/ps	τ_{s1}/ps	τ_{s2}/ps
Star-Model	0.94	0.94	4.5	0.08 ± 0.1	0.78
Star	0.90	1.1	2.8	-	-

The EADS1 of **Star** and **Star-Model** show a transient absorption at the far red side of the measured spectrum with a maximum lying around 12500 cm^{-1} . This maximum is superimposed with an artefact caused by the fundamental amplifier output at 800 nm. At higher energies in the EADS1 of **Star** an absorption band at 17300 cm^{-1} is observed which is absent in the spectra of **Star-Model**. At 19300 cm^{-1} and in the range of $21600\text{--}22300\text{ cm}^{-1}$ minima are observed in the spectra of both compounds caused by ground state bleaching. The EADS2 of both molecules consist of two transient absorption bands, one with a band maximum at $13700\text{--}13900\text{ cm}^{-1}$ and another one at higher energies with a transition energy of 20000 cm^{-1} for **Star-Model** and of 16900 cm^{-1} for **Star**. EADS3 is in both cases characterised by a negative transient absorption in the ranges of the absorption band maxima of the neutral compounds and a positive transient absorption red-shifted to the former. This band structure and the respective decay times in the range of a few picoseconds are known for a superposition of a ground state bleaching with a red-shifted hot ground state absorption.^{176,184} EADS2 is in both cases attributed to the relaxed IV-CT state and τ_2 to the back electron transfer process. A reconstruction of the transient absorption profile is no longer possible by the sum of SEC spectra as expected for a strongly coupled system. The low energy absorption band can nevertheless be assigned to the TAA^+ centre, in spite of the hypsochromic shift of around 1000 cm^{-1} compared to the much more decoupled HABs. The high energy PCTM⁻ absorption band is in the case of **Star-Model** very weak, possibly due to strong superposition with the comparably strong ground state bleaching (see absorption section). In

contrast, in the EADS2 of **Star** this band is strongly shifted to lower energies by about 2300 cm^{-1} . A red-shift is also observed in the SEC measurements (see Figure 60 and 61) and a maximum up to 16900 cm^{-1} for this kind of redox centre was observed in the transient absorption before.¹⁸⁶ EADS1 represents the partially unrelaxed IV-CT state as observed in the HABs (see above). The missing absorption of the PCTM⁻ in the transient spectrum of **Star-Model** is consistent with the weak signal in the relaxed IV-CT states and is explained by a strong overlap with the ground state bleaching. In **Star**, the excited state transition of the PCTM⁻ centre is at 17200 cm^{-1} . We assume that in both cases the partially unrelaxed IV-CT state is observed as the behaviour of the TAA⁺ transient absorption is very similar, that is, an absorption maximum at the very red side of the spectrum shifting to higher energies with time. The PCTM⁻ absorption band in the spectrum of **Star** is superimposed by a varying intensity of ground state bleaching and for this reason no spectral evolution can be identified.

The relaxation process of the partially unrelaxed IV-CT states of **Star-Model** was analysed by the spectral response function $S_{\tilde{\nu}}(t)$ (equation 61) of the TAA⁺ absorption maximum (Figure 69 and Table 10). The analysis was only possible in case of **Star-Model** as a measurement artefact distorted this low energy absorption signal of **Star** more strongly. Therefore, the chirp corrected and smoothed transient data of **Star-Model** were fitted by a polynomial (see Figure 70) whose temporal shift of the absorption maximum was analysed by equation 61.

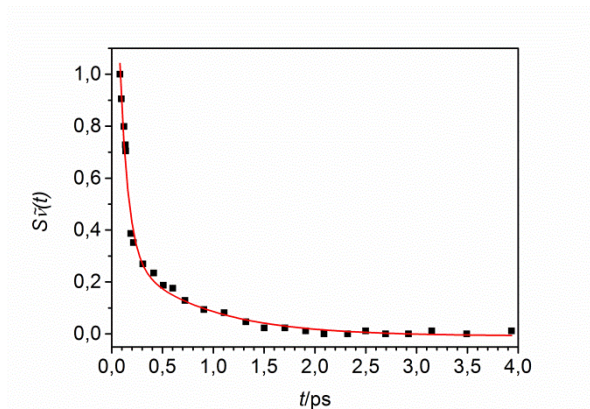


Figure 69 Spectral response function $S_{\tilde{\nu}}(t)$ (black) and its biexponential fit (red) of the transient spectra of **Star-Model**.

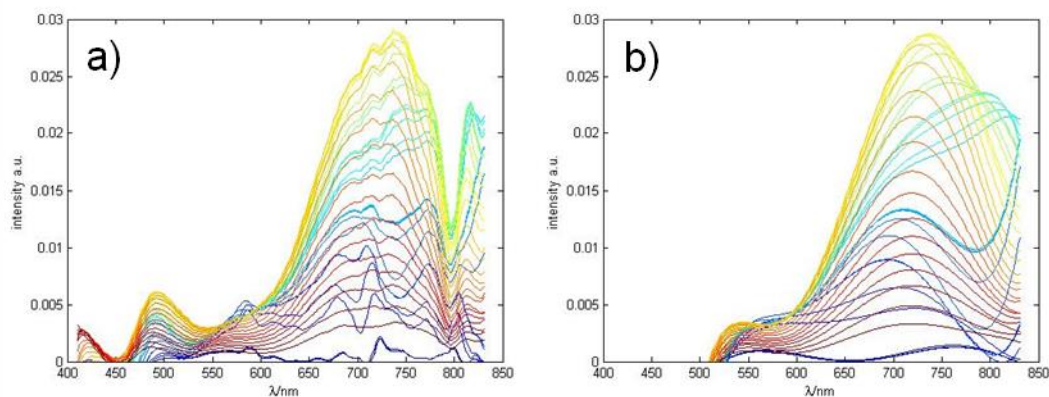


Figure 70 a) Raw data of the fs-transient absorption corrected for chirp and scattered light of **Star-Model** in DCM excited at 13800 cm^{-1} and b) a six degree polynomial fit to this data set. Data points around 12500 cm^{-1} (800 nm) were ignored for the fit because the spectra are in this range distorted by a measurement artefact from the fundamental amplifier output at 800 nm. The spectra are coloured from blue to red.

The spectral response function $S_{\nu}(t)$ revealed two time constants, a very short one $\tau_{s1} \sim 0.1\text{ ps}$ and a second with $\tau_{s2} = 0.78\text{ ps}$. As discussed before, the former time constant describes the relaxation by inertial solvent motion and intramolecular, high frequency vibrational equilibration. The latter time constant points to a relaxation caused by low frequency dynamics of the solvent as it is in the same time regime as the solvent relaxation time constant $\tau_b = 1.02\text{ ps}$ and the average solvent relaxation time constant $\langle\tau\rangle = 0.56\text{ ps}$ measured for DCM by *Maroncelli et al.*⁵¹ As discussed above, this suggests that a large amplitude motion is involved in this process. We assume that especially the aryl rings next to the acetylene bridge are twisting relative to the central atom of their respective redox centre (C or N) influencing therewith the electronic coupling between the donor and acceptor.

The described relaxation process causes a band shift to higher energies. This is in contrast to the observations made for the HABs discussed above where the shift of the radical cation transient absorption is to lower energies. This shift is caused by the differences in the potential energy surfaces of the involved State_1 and State_x , which in turn are greatly influenced by the degree of charge localisation at the respective TAA centres. The electronic coupling V between the TAA and PCTM moieties has a great impact on the charge localisation and may therewith cause the diverging shapes of the potential energy surfaces between the more delocalised states in **Star** and **Star-Model** and the more localised states in **HAB-S**, **HAB-A** and **HAB-Model**.

The back electron transfer rate constants k_{ET} can be interpreted using *Bixon-Jortner* theory (equation 7).^{187,188} This equation allows calculating k_{ET} with the IV-CT parameters ($\tilde{\nu}_v$, λ_o , λ_v and ΔG^{00}) obtained above (see Table 6) and to compare k_{ET} with experimental values.

$$k_{-ET} = 4\pi^2 hc^2 V^2 \sum_{j=0}^{\infty} \frac{e^{-S} S^j}{j!} \sqrt{\frac{1}{4\pi\hbar c \lambda_o kT}} \exp \left[-\frac{hc(j\tilde{\nu}_v + \lambda_o + \Delta G^{00})^2}{4\lambda_o kT} \right] \quad (7)$$

Table 11. Measured (τ_2) and calculated back electron transfer lifetime without ($1/k_{-ET}$) and with inclusion of the solvent relaxation time ($1/k_{-ET\text{solv}}$) for **Star-Model** in DCM.

	τ_2/ps	τ_{-ET}/ps	$\tau_{-ET\text{solv}}/\text{ps}$
Star-Model	0.94	0.85 ^a /0.14 ^b	2.3 ^a /1.3 ^b

^a calculated with $V_{\text{TDDFT}} = 1190 \text{ cm}^{-1}$. ^b calculated with $V_{\text{LM}} = 2940 \text{ cm}^{-1}$.

The rate constants and lifetimes were determined for both electronic couplings V calculated above (Table 11). With $V_{\text{TDDFT}} = 1190 \text{ cm}^{-1}$ the obtained lifetime of $\tau_{-ET} = 0.85 \text{ ps}$ is in good agreement with the measured $\tau_2 = 0.94 \text{ ps}$. In contrast, with $V_{\text{LM}} = 2940 \text{ cm}^{-1}$ the lifetime $\tau_{-ET} = 0.14 \text{ ps}$ is an order of magnitude shorter than the measured value of τ_2 .

The solvent relaxation time of DCM ($\langle \tau \rangle = 0.56 \text{ ps}$)⁵¹ is in the range of the experimental back electron transfer lifetimes. Because solvation can limit the back electron transfer in adiabatic processes⁴⁴ the solvation process has to be accounted for in the theory.^{175,176} Therefore, equation 7 which holds true in the non-adiabatic limit has to be transformed to the solvent-controlled adiabatic limit⁵² yielding equation 8:

$$k_{-ET} = 4\pi^2 hc^2 V^2 \sum_{j=0}^{\infty} \frac{e^{-S} S^j}{j!} \sqrt{\frac{1}{4\pi\hbar c \lambda_o kT}} \exp \left[-\frac{hc(j\tilde{\nu}_v + \lambda_o + \Delta G^{00})^2}{4\lambda_o kT} \right] \frac{1}{1 + H_A \frac{e^{-S} S^j}{j!}} \quad (8)$$

$$\text{with } H_A = \frac{8\pi^2 c V^2 \tau_1}{\lambda_o}$$

where τ_1 is the longitudinal relaxation time of the solvent. In our calculations τ_1 was represented by the average solvent relaxation time constant measured for DCM $\langle \tau \rangle = 0.56 \text{ ps}$.⁵¹ With this, back electron transfer lifetimes of $\tau_{-ET\text{solv}} = 2.3$ and 1.3 ps were obtained for V_{TDDFT} and V_{LM} , respectively. From these results the conclusion is drawn, that the solvation processes are indeed limiting the back electron transfer in **Star-Model** since the lifetimes are prolonged in the solvent-controlled adiabatic limit. Thus, further considerations are restricted to the adiabatic approach.

4.8. Transient absorption anisotropy measurement

In the following the possibility of energy redistributions within the IV-CT states of the multichromophoric systems will be discussed. Therefore, polarised transient absorption measurements were performed. Transient maps were recorded with the polarisation of the pump and probe pulses parallel (I_{\parallel}), perpendicular (I_{\perp}) and in the magic angle (I_{magic}) to each other. For several probe energies these three traces were fitted globally by a fitting routine which also considers the convolution of the individual traces by the instrument response.^{91,189} With this procedure the amplitudes and time constants of the anisotropy decay were directly obtained. The anisotropy r is thereby defined by equation (53 and 54):

$$r(t) = \frac{I_{\parallel}(t) - I_{\perp}(t)}{I_{\parallel}(t) + 2I_{\perp}(t)} = \frac{2}{5} \left(\frac{3 \cos^2 \beta(t) - 1}{2} \right) \quad (53 \text{ and } 54)$$

with $\beta(t)$ being the angle between the transition moment directions of the pumped and probed transitions. The magic angle trace was integrated into the fitting process to minimise measurement inaccuracies. Besides that, the intensities of the three traces have to follow a defined ratio $I_{\text{magic}} = (I_{\parallel} + 2I_{\perp})/3$ which is a measure for the accuracy of the measurement setup.⁸⁴ A small deviation from this defined ratio was experienced and attributed to a systematic error in the measurement setup (see 1.3.4.1 for a discussion). We chose probe energies of 13000 cm⁻¹, 13900 cm⁻¹ and 19600 cm⁻¹ for several reasons. First, the coherent artefact could be well fitted at all energies. Second, 13000 cm⁻¹ and 13900 cm⁻¹ were chosen because the underlying TAA⁺ absorption band is least superimposed by ground state bleaching and we get more information about the relaxation processes of the partially unrelaxed IV-CT states. Third, probing at the maximum of the PCTM⁻ band at 19600 cm⁻¹ served to exclude coincidences in the anisotropic behaviour at the other two probe energies. The time-dependent transient absorption anisotropy curves of **HAB-Model**, **HAB-A** and **HAB-S** at various energies are depicted in Figure 71 (for the fits of the respective traces see the appendix 1).

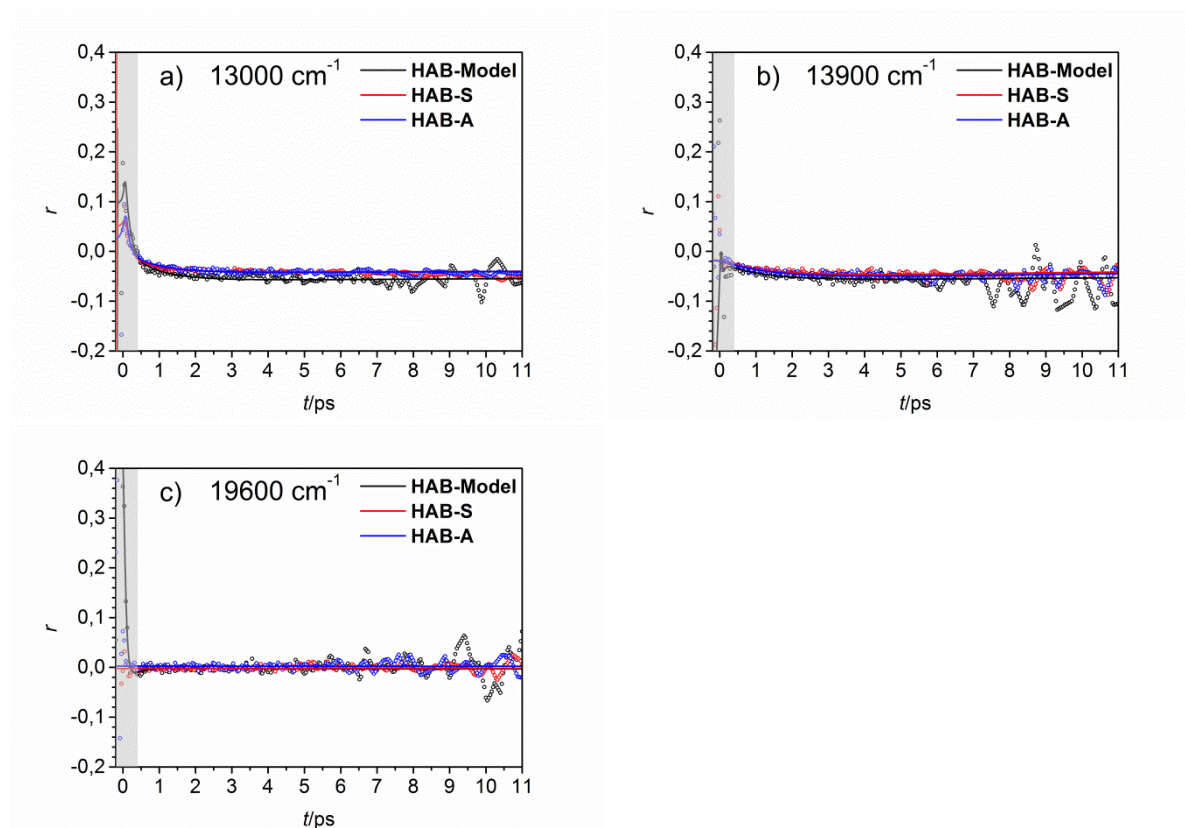


Figure 71 Time-dependent transient absorption anisotropy curves (circles) and the associated fits (lines) convoluted with the instrument response of **HAB-Model**, **HAB-A** and **HAB-S** pumped at 15200 cm^{-1} and probed at (a) 13000 cm^{-1} , (b) 13900 cm^{-1} and (c) 19600 cm^{-1} . We consider the grey shaded as unreliable because of strong overlap with the coherent artifact.

The obtained time constants for the anisotropy decays as well as their amplitudes are given in Table 12. We refrain from the interpretation of the time range < 0.4 ps (grey shaded in Figure 71 and 73) as the signal and the anisotropy is distorted by the coherent artefact in this region.⁸⁴

Table 12. Amplitudes a and decay time constants τ of the time dependent transient absorption anisotropy curves of **HAB-Model**, **HAB-A** and **HAB-S** pumped at 15200 cm^{-1} and probed at $\tilde{\nu}_{\text{probe}}$.

$\tilde{\nu}_{\text{probe}}/\text{cm}^{-1}$		a_1	τ_1/ps	a_2	τ_2/ps	a_3	τ_3/ps
13000	HAB-Model	0.26	<0.4	0.06	0.90	-0.06	>40
	HAB-A	0.22	<0.4	0.04	0.91	-0.04	>40
	HAB-S	0.11	<0.4	0.03	1.04	-0.04	>40
13900	HAB-Model	0.04	1.15	-0.06	>40		
	HAB-A	0.04	1.37	-0.06	>40		
	HAB-S	0.03	1.28	-0.05	>40		
19600	HAB-Model	-0.04	<0.4	0.001	>40		
	HAB-A	0.002	>40				
	HAB-S	-0.002	>40				

Remarkably, the time dependent transient absorption anisotropy curves of the three compounds at the respective probe energies match each other. At a probe energy of 19600 cm^{-1} the anisotropy curves have a constant value of nearly zero. The associated fitting parameters reflect that the time constants are either too long or too short to be fitted reasonably. At probe energies of 13000 cm^{-1} and 13900 cm^{-1} the anisotropy drops with small amplitudes of ≤ 0.06 and time constants of 0.9-1.4 ps to a value of around -0.05 and depolarises with a time constant that is too long to be determined within the short lifetime of the excited state. At 13000 cm^{-1} probe energy a third time dependent process can be observed which is very fast ($< 0.4\text{ ps}$) and has high amplitudes of > 0.1 . The latter cannot be interpreted because the coherent artefact also is anisotropic⁹⁰ and influences the anisotropy curve in just that time region. The longer time constants of around 1 ps are in agreement with the relaxation phenomena observed in the isotropic measurements and will be discussed later. The obtained anisotropy value of $r_1 = -0.05$ refers to an angle of 60° between the transition moments of pump and probe excitation. This is in good agreement with the situation given in Figure 72. However, we stress that in transient absorption spectroscopy, unlike in fluorescence spectroscopy, the observed anisotropies are the weighted average of ground state bleaching, excited state absorption and, if present, stimulated emission, and is therefore in general difficult to assign to specific angles.^{87,88} In the present case, at 13000 cm^{-1} there is only excited state absorption of TAA^+ which makes the evaluation of an angle more useful.

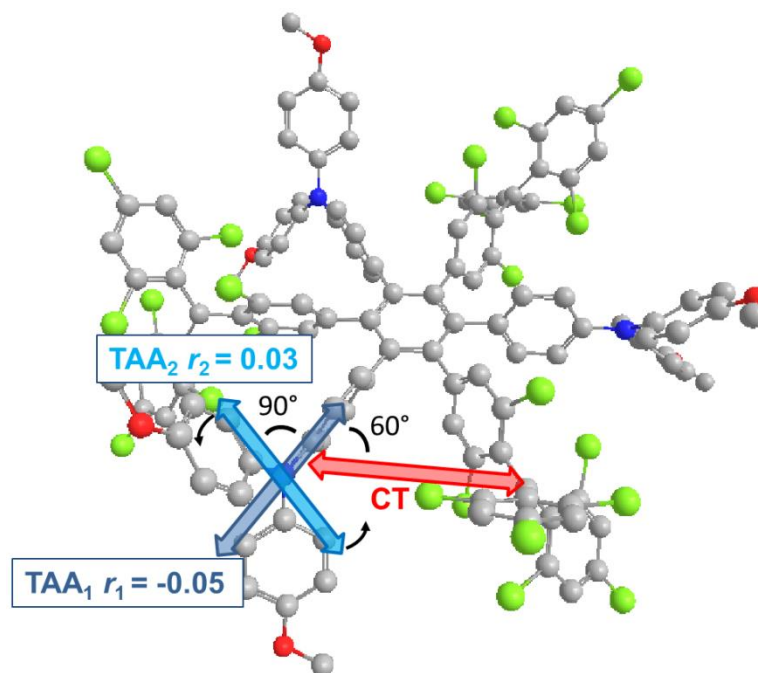


Figure 72 Structural model of **HAB-S**.¹⁹⁰ The transition moment direction of the IV-CT transition (red) and localised transitions at the TAA⁺ (blue) are represented by arrows. The given anisotropy values are calculated for pumping the IV-CT state and probing the respective TAA⁺ transition.

The transition moment direction of the IV-CT states is approximately oriented along the line between the centres of the TAA and PCTM units. In contrast, the localised transitions of the TAA⁺ centre consist of two non-degenerate transitions (see spectroelectrochemistry section) whose transition moments point in one case to the central benzene ring while the other lies perpendicular to this axis.⁶⁰ The first forms an angle of 60° to the IV-CT transition moment in accordance to the measured data. For the second transition moment direction an anisotropy value of $r_2 = 0.03$ is calculated if accounting for the unrestricted rotation of the TAA⁺ unit. Recalling the systematic errors mentioned above both transitions are most likely observed with focus on the former which therefore dominates the anisotropy value according to equation 59.

$$r = \sum_i w_i r_i \quad (59)$$

The experimental anisotropy r is a sum of all anisotropy contributions r_i multiplied by their weighing factor w_i . The anisotropy loss with a time constant of 1 ps can be explained in two ways. First, we can assume that while the partially unrelaxed IV-CT state is relaxing the transition moment of the probed localised transitions at the TAA⁺ are also reorienting due to the twisting motion described above.⁷⁸ The extent of reorientation can be calculated by equation 54 to be of no more than 6°. Second, due to the band shifting in the transient absorption the ratio between the two localised excited state transitions of the TAA⁺ centres is changing with time at the static probe energy. The anisotropy values observed

when probing the PCTM⁻ band at 19600 cm⁻¹ are slightly higher than those at lower probe energy. This finding can be explained by an increased superposition of the transient absorption signal by ground state bleaching which contributes to the anisotropy with a value of 0.4 when energy transfer is absent. Besides, the rotation of the PCTM⁻ can be considered to be restricted because of the sterical demand introduced by the chlorine atoms. This can be likewise a reason for the altered anisotropy values. For two reasons we conclude that there is no energy transfer between the six and four IV-CT states in **HAB-S** and **HAB-A**, respectively. The strongest argument is that the anisotropy shows no differences between **HAB-Model**, where energy transfer is not possible, and **HAB-A** and **HAB-S**, where several energy transfer pathways are conceivable. The second argument is that, in case of probing the TAA⁺ a higher anisotropy value of around 0.1 is expected for the delocalization of the transition moments predominantly located on the axis to the central benzene ring. This value differs too much from the observed -0.05 value. **In other words, the excited state remains localised within one donor-acceptor pair within the lifetime of the excited IV-CT state.**

The time-dependent, polarised transient absorption curves of **Star-Model** and **Star** pumped at 13800 cm⁻¹ and probed at 13300 cm⁻¹ and 14300 cm⁻¹ are shown in Figure 73. The pump and probe energies were chosen as stated for the HABs with the exception that the PCTM⁻ band was not analysed because of strong superposition with the hot ground state bleaching (see above). The latter distorts anisotropy curves especially at long delay times. This behaviour could not be fitted by the used routine.

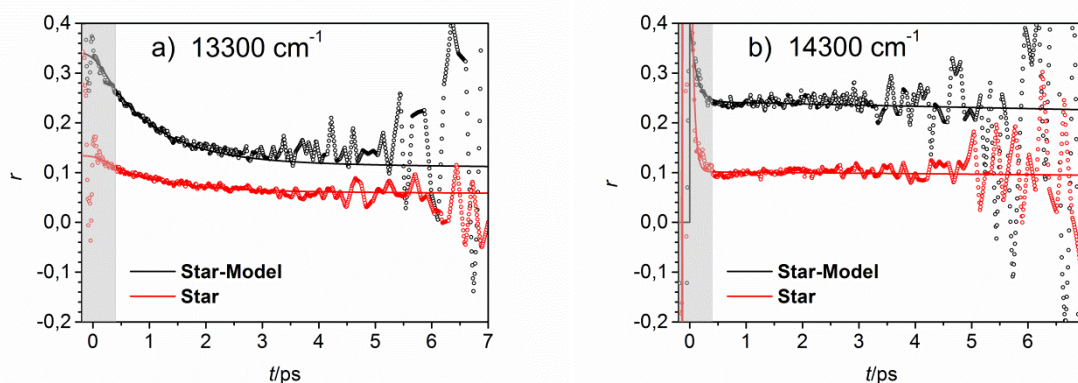


Figure 73 Time-dependent transient absorption anisotropy curves (circles) and the associated fits (lines) convoluted with the instrument response of **Star-Model** and **Star** pumped at 13800 cm⁻¹ and probed at (a) 13300 cm⁻¹ and (b) 14300 cm⁻¹. We consider the grey shaded as unreliable because of strong overlap with the coherent artifact.

All anisotropy decay curves were fitted with a biexponential anisotropy function (see Table 13 for fit parameters). In contrast to the HABs, the model compound **Star-Model** shows at all time delays a higher anisotropy than the multidimensional **Star**.

Table 13 Amplitudes a and decay time constants τ of the time dependent transient absorption anisotropy curves of **Star-Model** and **Star** pumped at 13800 cm^{-1} and probed at $\tilde{\nu}_{\text{probe}}$. The sum of the amplitudes yields the initial anisotropy.

$\tilde{\nu}_{\text{probe}}/\text{cm}^{-1}$		a_1	τ_1/ps	a_2	τ_2/ps
13300	Star-Model	0.22	0.97	0.12	>40
	Star	0.07	0.97	0.06	>40
14300	Star-Model	0.16	<0.4	0.24	>40
	Star	0.9	<0.4	0.10	>40

By probing close to the band maximum of the partially unrelaxed IV-CT state at 13300 cm^{-1} in both molecules **Star-Model** and **Star** a decrease of anisotropy with a time constant of around 1 ps is observed followed by depolarisation with an indefinite long time constant. Thereby the anisotropy decreases from a value of $r = 0.34$ and $r = 0.13$ at time zero to $r = 0.12$ and $r = 0.06$ within 10 ps for **Star-Model** and **Star**, respectively. The anisotropy curve of **Star-Model** tends at longer delay times to higher values which could not be represented by the fit. As mentioned above, this is due to the hot ground state bleaching. Both the ground state bleaching and the hot ground state bleaching should have high anisotropy values of $r = 0.4$ as their transition moments are matching that of the pumped IV-CT transition with small deviations for the hot ground state bleaching. This explains the rise of anisotropy observed at long delay times where the hot ground state bleaching is starting to dominate the transient absorption signal. The above mentioned anisotropy values are difficult to interpret because of the high error in the measurement setup of >10% and because several superimposed probed transitions are involved. In Figure 74 the relevant transition moments are depicted.

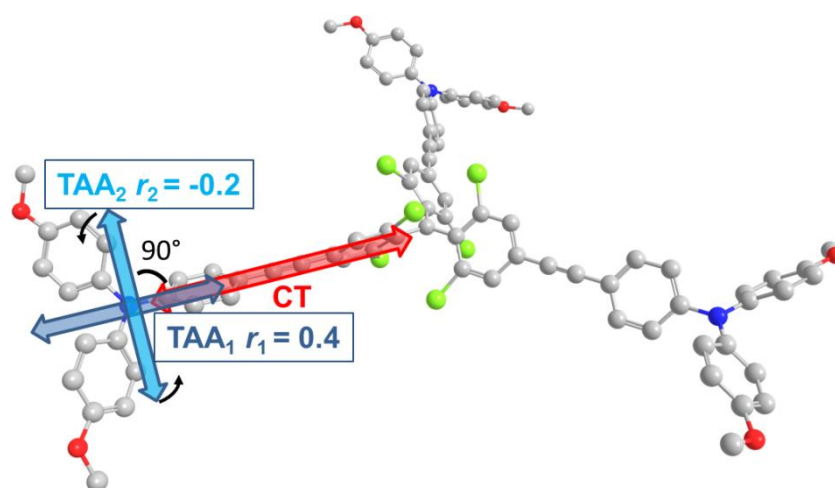


Figure 74 Structural model of **Star**.¹⁹⁰ The transition moment direction of the IV-CT transition (red) and localised transitions at the TAA^+ (blue) are represented by arrows. The given anisotropy values are calculated for pumping the IV-CT state and probing the respective TAA^+ transition.

As discussed above the localised absorption of the TAA⁺ moieties consist of two transitions of non-degenerate states with transition moment directions perpendicular to each other which gives rise to anisotropy values of $r_1 = 0.4$ and $r_2 = -0.2$ when excluding energy transfer. This is true for both the partially relaxed and the relaxed IV-CT states. Therefore, the observed anisotropy values are a sum of two transitions for each state superimposing each other with differing weighing factors. The time dependency of the anisotropy has the same time dependency as the isotropic relaxation process of the partially unrelaxed IV-CT state. This is explained by the following scenario: at the fixed probe energy the amplitude ratio of the two non-degenerate TAA⁺ transitions are differing for the partially unrelaxed and the relaxed IV-CT state. With solvent relaxation the two IV-CT states interconvert as well as the amplitude ratios of the TAA⁺ states. A distinct assignment of the observed anisotropy values to this ratio is not possible. In contrast to the probe energy of 13300 cm⁻¹, the anisotropy curve probed at 14300 cm⁻¹ is independent of time in the observable window possibly due to the relaxed IV-CT state dominating the transient absorption signal. If accounting for energy transfer in **Star** the theoretical anisotropy values tend to the average values of $r_1 = 0.1$ and $r_2 = -0.05$. So the lower anisotropy values observed for **Star** can be explained by a very fast ($\ll 0.4$ ps), unresolved energy transfer between the IV-CT states located at the different branches.

4.9. Conclusion

The absence of energy transfer in the HABs can be explained as follows. The dipole-dipole interaction formulated by Förster¹⁹¹ is dependent on the electronic coupling V_{pq} of the transition moments μ_p and μ_q of two weakly coupled subchromophores p and q. This coupling can be calculated using the point-dipole-point-dipole approximation (equation 25).

$$V_{pq} = \kappa \mu_p \mu_q r^{-3} \quad (25)$$

with $\kappa = (\mathbf{e}_p \cdot \mathbf{e}_q) - 3(\mathbf{e}_p \cdot \mathbf{e}_{pq})(\mathbf{e}_q \cdot \mathbf{e}_{pq})$

The interacting distance r is estimated by the distance between the middle points of the C-N separation (~ 6.8 Å was obtained from MM2 optimised structures).¹⁴⁶ The factor κ describes the orientation of the transition moments to each other with the unit vectors \mathbf{e}_p , \mathbf{e}_q and \mathbf{e}_{pq} of μ_p , μ_q and r , respectively, and is determined to be 1.75. A value of $V_{pq} = 20$ cm⁻¹ is obtained with $\mu_p = \mu_q = 0.81$ D (see Table 6). With this small electronic coupling V_{pq} the energy transfer process is bound to be very slow (>100 ps) compared to other non-radiative deactivation processes. In contrast, energy transfer described by Dexter is based on electronic communication between the chromophores exchanging concerted two electrons.⁸⁰ The classical theory of exchange energy transfer can be pictured by the orbital diagram shown in Figure 75 where we considered that we deal with radicals, that is, in the

excited IV-CT state the SOMO of the PCTM moiety is doubly occupied while the HOMO of the TAA is singly occupied. The ET process thus involves six electrons.

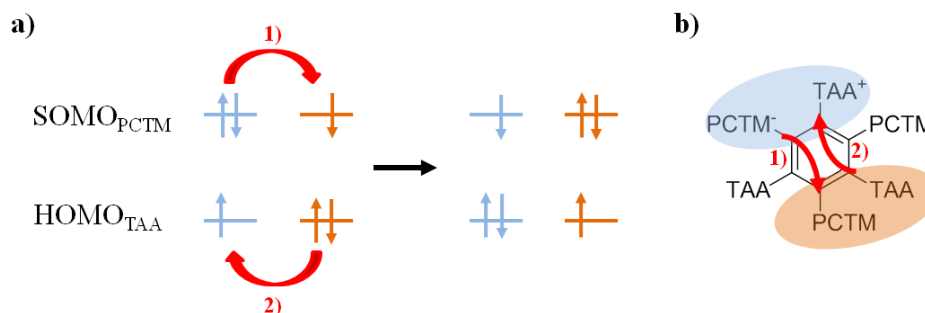


Figure 75 a) Orbital diagram of the “through bond” exchange energy transfer. b) The corresponding states in **HAB-S**.

This concept of electron migration holds true if we look at the energy transfer between IV-CT states which have no redox centres in common e.g. IV-CT states at opposite sides of **HAB-S** (see Figure 75). The rate constant of this process is governed therefore, amongst others, by the electronic communication between two redox centres *meta*-linked to the central benzene ring. When considering neighbouring IV-CT states in **HAB-S** or IV-CT states in **Star** as shown in Figure 76 the number of molecular orbitals necessary to describe the energy transfer is reduced to three and the number of electrons to five as one redox centre remains formally unaltered in this process. Here we consider the process $\text{TAA}^+ \text{-PCTM}^- \text{-TAA} \rightarrow \text{TAA} \text{-PCTM}^- \text{-TAA}^+$ for **HAB-S**. In analogy, $\text{PCTM}^- \text{-TAA}^+ \text{-PCTM} \rightarrow \text{PCTM} \text{-TAA}^+ \text{-PCTM}^-$ would also be conceivable.

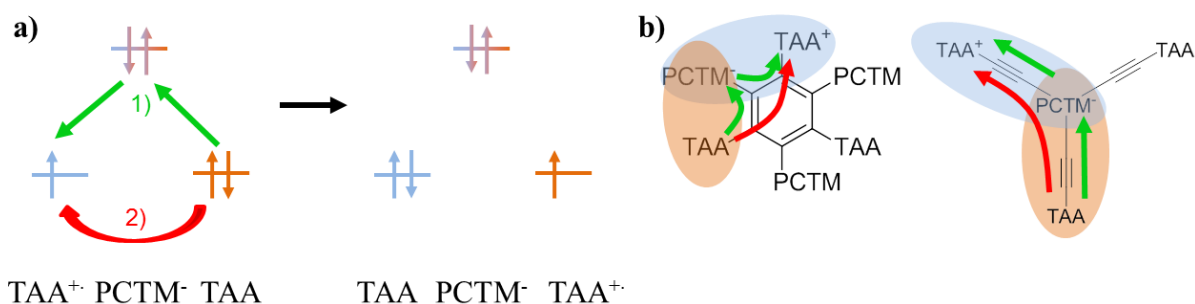
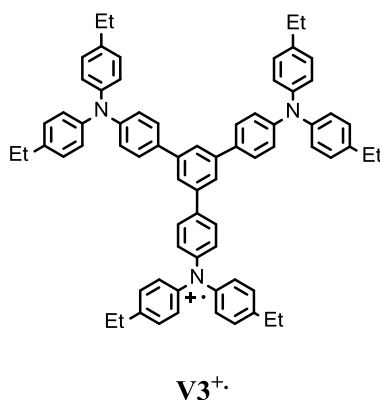


Figure 76 a) Orbital diagram of the exchange energy transfer. b) The corresponding states in **HAB-S** and **Star** in case of neighbouring states with a PCTM^- as the centre.

Figure 76 makes the identity between energy transfer and electron transfer in the specific situation apparent. The energy transfer is in fact a single charge transfer between *meta*-linked redox centres. This process has to compete with the back electron transfer to the ground state with a time constant of ~ 4 ps. *Bonvoisin et al* investigated molecule **V3⁺** with *meta*-linked TAA-TAA⁺ redox centres, very similar to the situation depicted for **HAB-S** in Figure 76.



From their data a IV-CT time constant of several hundreds of picoseconds can be calculated.¹⁹² Thus we assume that the direct electronic coupling of *meta*-linked redox centres in **HAB-S** (pathway 2 in Figure 76) is so weak that the energy transfer between neighbouring IV-CT states is too slow to be observed within the excited state lifetime. However, electron transfer can be facilitated by the presence of bridge states in the case of a small direct electronic coupling between donor and acceptor.^{31,61} In fact, in **HAB-S** and **Star** such a bridge state can be formulated which is absent in **V3**. This state corresponds to the ground state and is lower in energy than the initial and final IV-CT states (pathway 1 in Figure 76). Following the description by *Bixon and Jortner*⁶¹ a sequential mechanism has to be considered in this case with two time constants for the charge transfer from the initial to the bridge (ground) state and from the bridge (ground) to the final state. The former corresponds to the relaxation of the excited state to the ground state and the latter to the thermally induced charge transfer from a TAA to a PCTM centre, which is energetically unfavourable and thus slow. Hence, the formulated bridge state will never lead to an energy transfer rate that is faster than the excited state relaxation in the described system.

In the case of the star-shaped compound **Star** complete energy delocalisation takes place within the first 400 fs. Very fast, (< 200 fs) coherent energy delocalisation may occur in multichromophoric systems^{184,193,194} and in conjugated polymers.^{195,196} In these cases, the chromophores have to be coupled strongly otherwise energy is transferred via the slower hopping mechanism.^{68,197} To discriminate between coherent and hopping cases the homogeneous line width Γ of the excited IV-CT band is compared to the coupling element V_{energy} of the chromophores.⁶⁶⁻⁶⁸ Γ is a measure for the loss of coherence due to interaction with phonons and an upper limit is estimated by equation 18.

$$\Gamma = \frac{\sqrt{4\pi\lambda_0 k_b T}}{\pi} \quad (18)$$

For the reorganisation energy λ_0 a value of 1960 cm⁻¹ was obtained by fitting the IV-CT band of **Star** using equation 9 (see Figure 63). Accordingly, the upper limit of Γ is 720 cm⁻¹. As a first approximation V_{energy} is described by the dipole-dipole coupling element V_{pq} which can be calculated by equation 25. A value of $V_{\text{pq}} = 50$ cm⁻¹ is obtained when using the data of **Star-Model**

($\mu_p = \mu_q = 2.8$ D, $r = 11$ Å, $\kappa = 1.75$, see above). As V_{pq} is by more than one order of magnitude smaller than Γ , the dipole-dipole coupling seems not to be responsible for this ultrafast energy transfer alone. It has to be pointed out that the point-dipole approximation used in equation 25 is not accurate when the interchromophore-distance is in the range of the chromophore size.⁴ This is certainly the case in **Star** as the IV-CT states exceed 12 Å (distance between the centre of the donor and acceptor obtained from the DFT calculations of **Star-Model**). Other reasons for the breakdown of the dipole approximation could be the neglect of dielectric screening. In all these cases, an explicit calculation of the transition densities at the individual chromophores and their mutual interaction yields improved electronic couplings.^{65,73,74} The absorption band of **Star** is shifted to lower energies by 400 cm⁻¹ compared to **Star-Model**. If D_3 symmetry is assumed for **Star**, this difference in energy should be three times the Coulomb coupling of the three IV-CT states.^{81,168} Accordingly, a value of 130 cm⁻¹ is derived which is still much smaller than Γ .

Furthermore, electron exchange interactions were neglected hitherto. Regarding **Star** only the special case of neighbouring redox centres is present as shown in Figure 76. In the simplest case the energy transfer can be described by the charge transfer between TAA and TAA⁺ redox centres. For this process a discrete IV-CT band is expected in the NIR-spectra of **Star**⁺ which we do not observe because it is either too weak due to the long distance between two TAA redox centres (>20 Å) or possibly hidden by other bands.³¹ In addition, this charge transfer should be limited by the dielectric relaxation of the solvent as shown for the adiabatic back electron transfer.⁴⁴ It is therefore implausible to obtain ultrafast charge transfer rates (< 400 fs) with the charges being localised at the respective redox centres. Consequently, to explain the findings by the “through bond” exchange mechanism, charge delocalisation over the three chromophore branches in **Star** has to be considered. However, we do not have direct spectroscopic data that would support strong electronic communication. On the one hand that is due to the fact that the presumably delocalised state relaxes so rapidly to the localised IV-CT states that it cannot be monitored. On the other hand the low energy absorption characteristics of **Star** and **Star-Model** are very similar (Figure 54), which does not support a strong electronic coupling between the IV-CT states in **Star**.

Although the reason for the very fast energy delocalisation could not be identified the excited state processes in **Star** can be summarised as follows (see Figure 77):

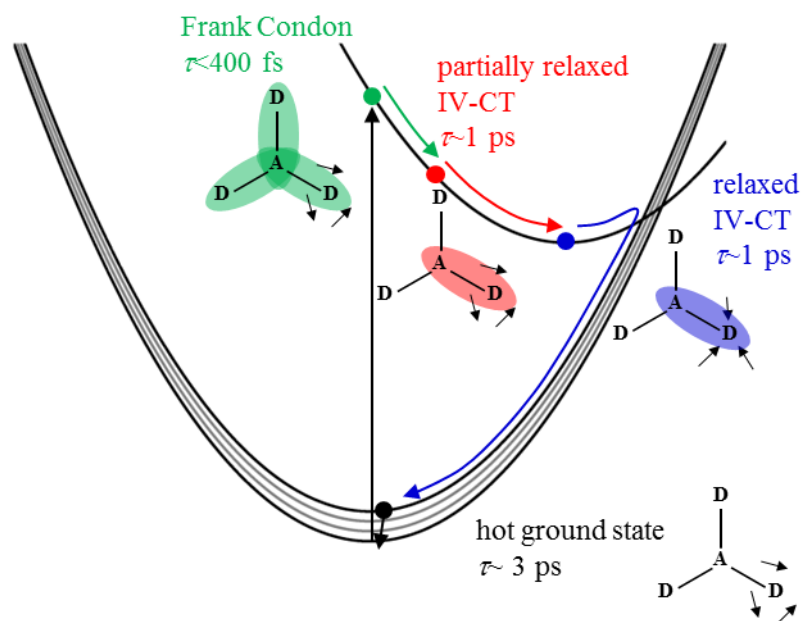


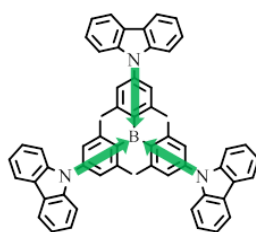
Figure 77 Potential energy diagram for the relaxation processes in the excited state of **Star**. The molecule is sketched besides the relevant states, the small black arrows represent solvent molecules and the coloured ellipses highlight the spatial extent of the excited states.

Upon excitation the Frank-Condon excited state is formed with the molecular and solvent geometry equal to the ground state.¹⁷⁹ In case of **Star** the branches are in this state strongly coupled so that the energy is distributed coherently between all three branches with $\tau < 400$ fs.¹⁷⁹ In **HAB-S** and **HAB-A** the coupling between the branches is too small for ultrafast energy distribution. Very fast molecular relaxation processes and inertial solvent reorientations ($\tau < 400$ fs) lead to localisation of the energy on a single branch. The partially relaxed IV-CT state is obtained which is observed for all radical compounds. Presumably, low frequency dynamics of the solvent ($\tau \sim 1$ ps) induce further a twisting motion of the aryl systems reducing the electronic communication between donor and acceptor. The relaxed IV-CT state is formed which is characterised by a stronger charge localisation in comparison to the partially unrelaxed IV-CT state and can therefore be better stabilised by the solvent. In this time range energy hopping between the IV-CT states is also not observed for **HAB-A** and **HAB-S** due to the small electronic and dipole-dipole coupling of the involved states. In case of **Star** incoherent energy hopping cannot be ruled out completely. However, anisotropy measurements indicate complete energy distribution between the three chromophore branches by a coherent process followed by localisation of energy in one branch. As soon as the relaxed IV-CT state is formed, all radical compounds relax to the ground state ($\tau \sim 1$ -4 ps) limited by the dielectric relaxation of the solvent. In case of **Star** and **Star-Model** a hot ground state is observed which relaxes to the ground state with a time constant of $\tau \sim 3$ -5 ps.

5. Hexaarylbenzenes containing TABs*

5.1. Introduction

Owing to the unoccupied boron p_z -orbital the acceptor properties of the triarylboranes have been used in optoelectronic devices as electron transporting and/or emitting layer,¹⁹⁸⁻²⁰² but also in studies about their linear^{168,203-214} and nonlinear optical properties,^{208,210,215-225} and in sensor systems for fluoride^{213,226-230} and cyanide anions.²³¹⁻²³⁵ Because of these favourable characteristics *Lambert et al.* incorporated triarylboranes into polymeric structures²⁰⁷ and a multidimensional chromophore **C**,^{168,236,237} in both cases in combination with carbazole as the electron donating redox centre. In case of the multidimensional chromophore **C** the excitation energy of optically induced CT states is redistributed between the different chromophore branches of the molecule which initiated the EN investigations presented in this work.



C

Because of general susceptibility towards hydrolysis, the boron centres have to be kinetically shielded by sterically demanding methyl groups in *ortho*-position of the aryl rings.^{220,238-240} However, due to the very small size of fluoride and cyanide these anions can selectively form a complex with the trivalent boron which thus can be used for ion sensing by colorimetric, fluorescence or electrochemical responses.²²⁷ In general, binding constants of triorganoboranes though depend on the Lewis acidity of the boron centre and the steric hindrance of the substituents. It was shown that the Lewis acidity can be amplified by linking multiple trivalent boron centres²¹². Therewith the binding constant of the first complexation is enhanced whereas further binding constants are characterised by a negative binding cooperativity which is explained by a gradual loss of Lewis acidity. The question arises if the triarylborane moieties in the HAB **B1** and **B2** are subject to the same effects which shall be investigated by fluoride titration experiments.

*Parts of this section have already been published in M. Steeger and C. Lambert, *Chem. Eur. J.*, **2012**, *18*, 11937-11948.

5.2. Synthesis

HABs **B1** and **B2** can easily be synthesised by cobalt catalysed cyclotrimerisation of the appropriate tolan precursor **B4** (Figure 78).²⁴¹ Although complexes of other metals are also known to catalyse this type of reaction, cobalt complexes rank among the most effective.¹³⁹ The tolan derivative **B4** was synthesised by lithiation of the known triarylamine derivative **B5**³³ followed by reaction with Mes_2BF .

The cyclotrimerisation was carried out with $\text{Co}_2(\text{CO})_8$ as the catalyst which yields a symmetric (**B1**) and an asymmetric isomer (**B2**). Because of the reaction mechanism that leads over metallacyclopentadiene intermediates²⁴² the two different isomers with chromophore substituents in 1,3,5- and 1,2,4-position result. The yields of 17 % (for **B1**) and 62 % (for **B2**), respectively, are in agreement with the statistically expected product ratio of 1:3.¹³⁹ Since the product ratio of such reactions are influenced by substituents that differ strongly in size, the **steric** hindrance of the two different chromophores can be assumed to be nearly identical.¹³⁹

The synthesis of model compound **B3** is again based on the triarylamine derivative **B5** (Figure 79), which is transformed by a Diels-Alder reaction with tetraphenylcyclopentadienone to HAB **B6**. The boron acceptor centre is built up in the last step by the same procedure as mentioned above, as it decomposes under high temperature Diels-Alder reaction conditions.

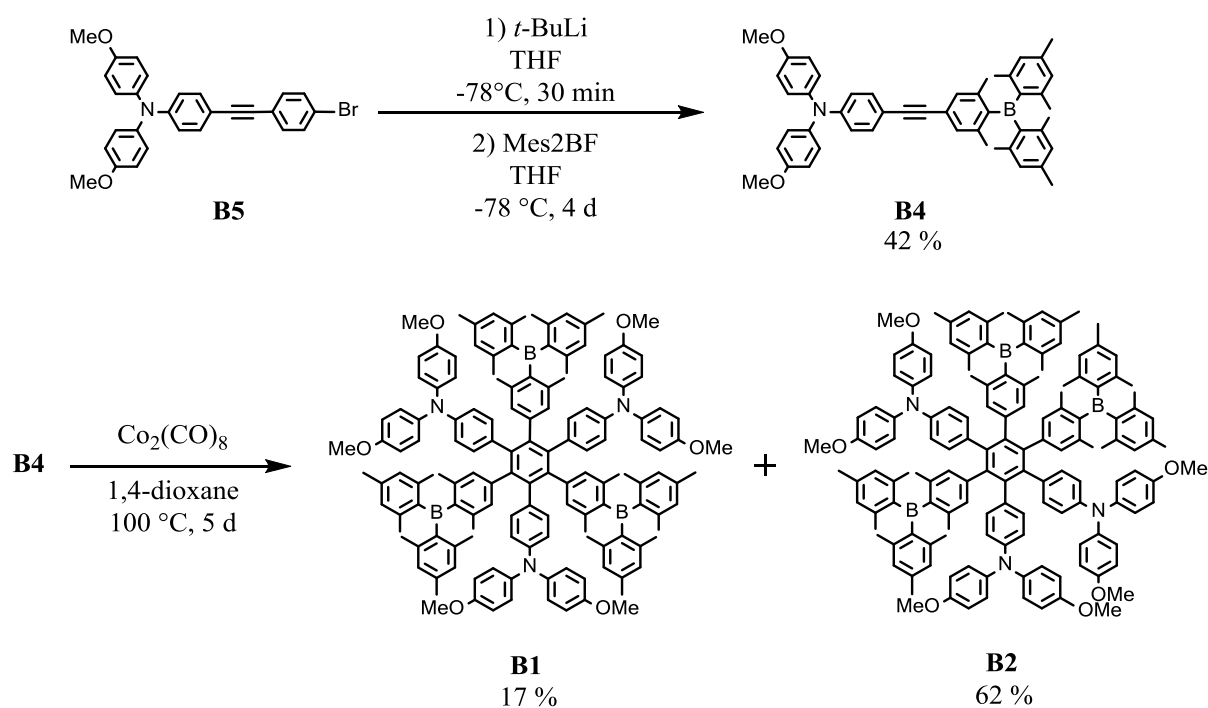
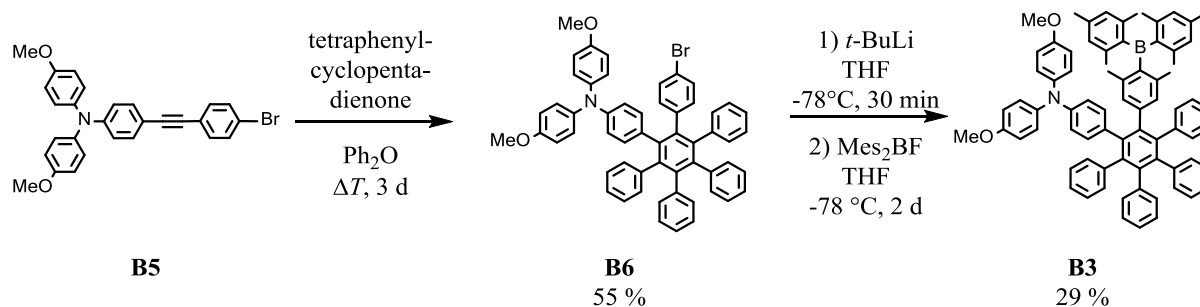


Figure 78 Synthesis of HABs **B1** and **B2**.

Figure 79 Synthesis of model HAB **B3**.

5.3. Electrochemistry

HABs **B1** and **B2** each possess three electron acceptors and three electron donors which should lead to in total seven accessible redox states: -3, -2, -1, 0, +1, +2, and +3. HAB **B1** unfortunately proved to be not soluble enough for electrochemical measurements but we were able to measure the oxidation and reduction potentials of HABs **B2** and **B3** by cyclic voltammetry (CV) which are listed in Table 14.

Table 14 Redox potentials of HABs **B2** and **B3** (vs Fc/Fc⁺).^c

	B2 ^a	B3 ^b
E_{ox}/mV	316	300 ^d
E_{red}^1/mV	-2453	-2517
E_{red}^2/mV	-2586	-
E_{red}^3/mV	-2726	-

^a 0.65 M THF/[Bu₄N][ClO₄]. ^b 0.5 M THF/[Bu₄N][ClO₄]. ^c Compound **B1** is insufficient soluble in THF for electrochemical measurements. ^d Determined by differential pulse voltammetry (DPV).

To measure the very negative reduction potentials of the boron redox centres our conventional electrochemical cell had to be upgraded by an intrinsic aluminiumoxide column for further drying of the electrolyte as recommended by *Kiesele*.²⁴³ The measureable potential window could thereby be expanded from -3.1 V to -3.4 V in THF. The best results were obtained when the electrolyte together with the added substance was dried over the aluminiumoxide column until all peaks were well separated from the accessible solvent potential limit. This procedure requires substances which do not degrade on the column. Unfortunately compound **B3** is not stable under these conditions and particularly the oxidation was not well resolved in the CV. Thus, we applied differential pulse techniques (DPV), which compensate better for electrochemical processes of the solvent. By this way, a one electron oxidation of the triarylamine and a reversible one electron reduction of the triarylborane moiety of model compound **3** could be observed at 300 mV and -2517 mV, respectively (Table 14).

These values lie in the typical range for this type of donor-acceptor compounds.^{124,244} The CV of compound **B2** shows three reversible reduction and one reversible oxidation processes (Figure 80) at around the same potential as model compound **B3**. As mentioned above the solubility of **B1** in THF is unfortunately insufficient for electrochemical studies.

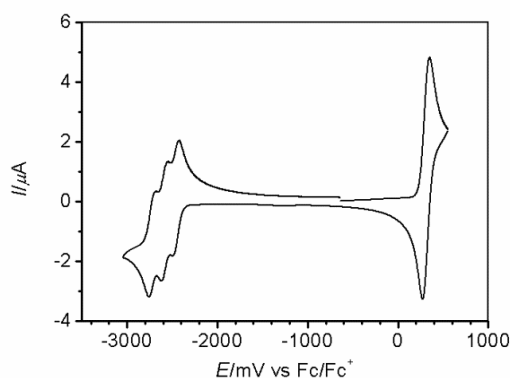


Figure 80 CV of **B2** in 0.65 M THF/[Bu₄N][ClO₄], $\nu = 100 \text{ mV s}^{-1}$.

Each reduction wave in the CV of **B2** corresponds to the reduction of one boron centre, whereas the oxidation of the three nitrogen centres occurs at almost the same potential. Since the triarylamine and triarylborane centres have nearly the same linkage and distance relative to each other the different redox behaviour of amine and borane centres has to be ascribed mainly to effects of the electrolyte. *Geiger et al.* showed that the donor/acceptor number and polarity of the solvent and the ion-pairing ability of the conducting salt may have a strong influence on the separation of the potentials of multi-step redox processes.¹⁴⁸ In order to investigate these effects in HAB **B2**, we replaced the tetrabutylammonium perchlorate conducting salt by [Bu₄N][B(C₆F₅)₄] which has a very poorly coordinating anion. Indeed, the use of the non-coordinating anion leads to a small shift of the reduction potentials of **B2** to less negative and of the oxidation potentials to less positive values. Even more remarkable is a change of the redox potential splittings within the oxidation and reduction signals as can be seen in the differential pulse voltammetry (DPV) in Figure 81: those of the reduction are closer together in [Bu₄N][B(C₆F₅)₄] while those of the oxidation are now split (visible shoulder) in contrast to THF/[Bu₄N][ClO₄].

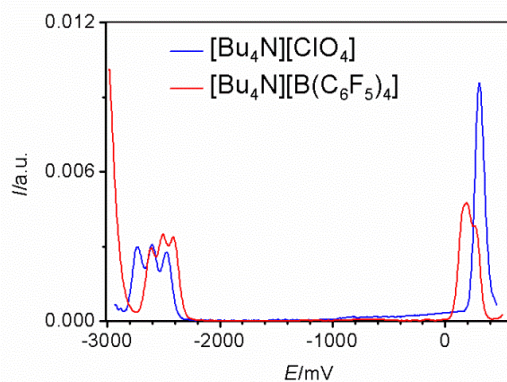


Figure 81 Differential pulse voltammogram of **B2** in 0.46 M THF/[Bu₄N][ClO₄] (blue) and in 0.36 M THF/[Bu₄N][B(C₆F₅)₄] (red) normalised to the integral of the reduction.

For better comparison all redox peaks in the DPV were fitted by Voigt functions, with the exception of the oxidation peak in THF/[Bu₄N][ClO₄]. Here, the potentials are too close to get a stable fit. In this case using three Voigt functions yields the two outermost oxidation processes being separated by maximal 60 mV while the third in-between is fitted equally well for variable potential values. In contrast, the two outermost oxidation processes are separated by 135 mV in THF/[Bu₄N][B(C₆F₅)₄]. For both electrolyte salts, three reduction peaks are visible in the DPVs with a somewhat larger outermost peak difference of 264 mV in THF/[Bu₄N][ClO₄] than in THF/[Bu₄N][B(C₆F₅)₄] (196 mV). Both phenomena are consistent with a decreased donor strength of the borate counteranion compared to the perchlorate anion, which leads to reduced ion-pair formation with and reduced shielding of the oxidised triarylamine moieties. As a result the electrostatic repulsion of a given oxidised amine to other positive charges within the molecule is increased and consequently the next oxidation hampered. Furthermore, ion-pair formation of the borate and the tetrabutylammonium cation is decreased as well, resulting in increased acceptor strength of the tetrabutylammonium cation. Following the same train of thought as stated above, the second and third reduction is facilitated and hence the peak separation is reduced. Two further remarks have to be made: first, the redox potentials of the DPVs differ from those of the CVs by up to 20 mV which can be ascribed to slow interfacial electron transfer kinetics in the DPV.²⁴⁵ However, as all potentials are shifted in the same direction the above mentioned differences in the peak separations are not perturbed. Second, by using the [Bu₄N][B(C₆F₅)₄] conducting salt, the reductions of the borane moieties become chemically irreversible for unknown reasons.

The above stated results nicely demonstrate that the redox potential splitting of multi-redox-chromophores depend on the type of electrolyte salt in the electrochemical experiment and no definite conclusions about possible mixed valence interactions in the differently charged species can be drawn from the redox potential splitting. On the other hand, the observation of discrete reduction waves and

at least partially resolved oxidation waves of **B2** in THF/[Bu₄N][B(C₆F₅)₄] shows that a series of mixed valence states **B2**²⁻, **B2**⁻, **B2**⁺, and **B2**²⁺ can selectively be generated.

5.4. Absorption and emission spectroscopy

The UV/vis spectra of compounds **B1**, **B2** and **B3** are characterised by intense absorption bands at 32000, 31700 and 31900 cm⁻¹, respectively, in DCM (Figure 82). These bands can be attributed to overlapping π - π^* excitations localised at the triarylamine and triarylborane centres.²⁰⁶ As expected the extinction coefficient of this band in the model compound **B3** (43000 M⁻¹ cm⁻¹) is around three times weaker as that of **B1** (116000 M⁻¹ cm⁻¹) and of **B2** (129000 M⁻¹ cm⁻¹), since there is only one donor-acceptor pair instead of three. Furthermore, in all three spectra the lowest energy absorption band is visible as a weak shoulder at around 27000 cm⁻¹. This band can be attributed to CT transitions whose intensity varies with the number of possible CT transitions. In the symmetric HAB **B1** there are in total six possible CT interactions (see Figure 2), in the asymmetric trimer **B2** there are four and in the model compound **B3** only one. Accordingly, the CT absorption band of **B1** is most intense, that of **B3** least.

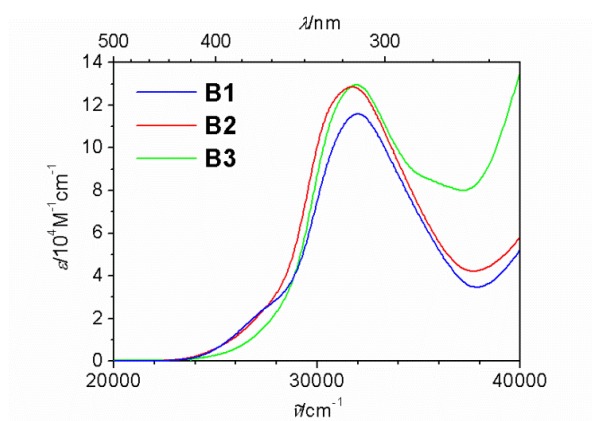


Figure 82. Absorption spectra of **B1** (blue), **B2** (red) and **B3** (green) in DCM. The absorption spectrum of **B3** is multiplied by 3.

The fluorescence spectra of all compounds show a large positive solvatochromism which supports the lowest excited state being a CT state (Figure 83 and 84 and Table 14). From this observation we conclude that the molecules have a small or vanishing (for the symmetric **B1**) dipole moment in the ground state and a high dipole moment in the dipolar excited CT.¹⁶⁸ As the fluorescence solvatochromism of all HABs is remarkably similar, it follows that the lowest excited state of the multichromophore systems **B1** and **B2** must be localised within one donor-acceptor pair of the molecule resembling the situation in the model compound **B3**. While this would be no surprise for the asymmetric **B2**, there has to be symmetry breaking in the first excited state of the formally symmetric HAB **B1**.

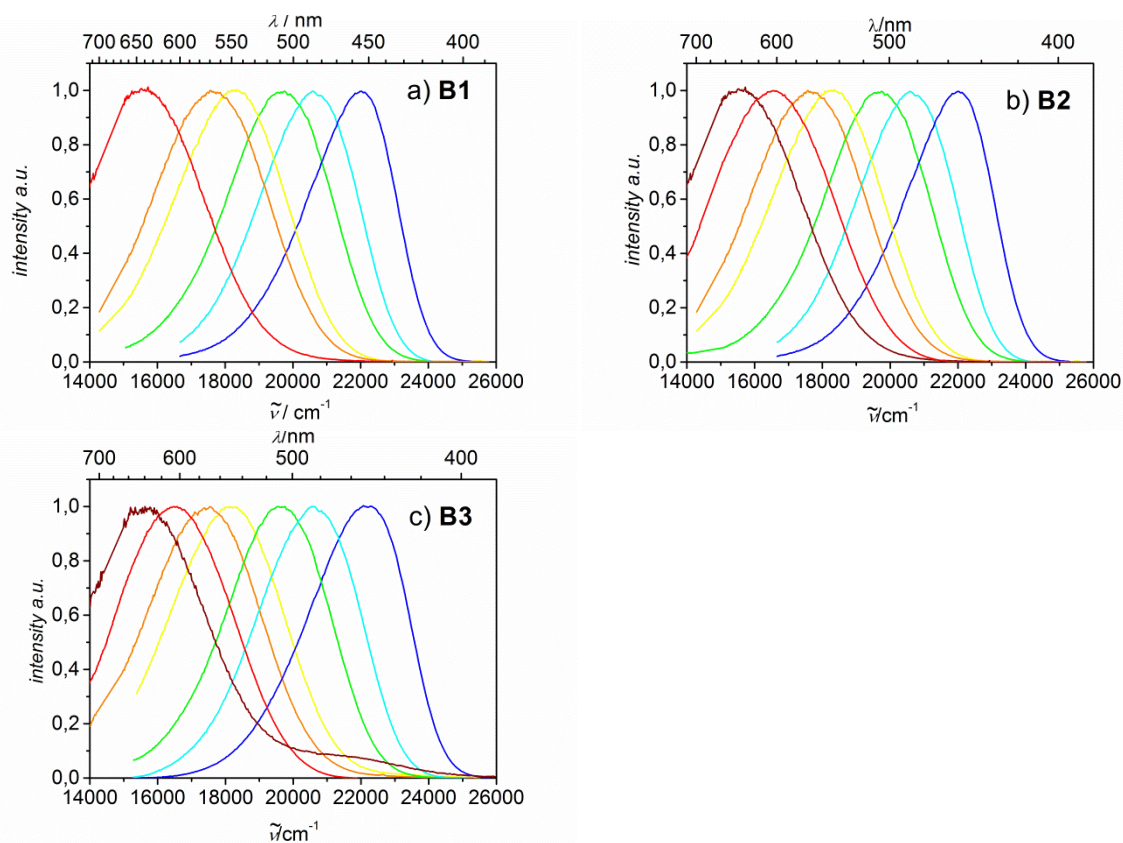


Figure 83 Fluorescence spectra of a) **B1**, b) **B2** and c) **B3** in solvents of different polarity (from right to left: C_6H_{12} , nBu_2O , MTBE, THF, DCM, PhCN, MeCN). A spectrum of **B1** in acetonitrile could not be measured due to low solubility and the spectrum of **B3** in acetonitrile shows a weak high energy fluorescence band which is due to complexation of the solvent to the boron centre.²⁰⁶

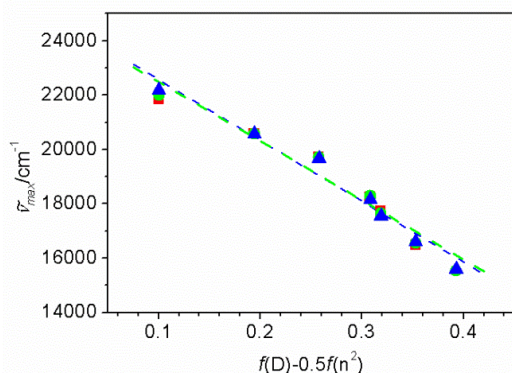


Figure 84 Emission maxima of HABs **B1** (red squares), **B2** (green circles) and **B3** (blue triangles) in solvents of different polarity (from left to right: C_6H_{12} , nBu_2O , MTBE, THF, DCM, PhCN, MeCN). $f(D)-0.5f(n^2)$ is the solvent polarity function with $f(D)=(D-1)/(2D+1)$ and $f(n^2)=(n^2-1)/(2n^2+1)$. The molecules were excited at 29400 cm^{-1} .

Table 15 Extinction coefficients, absorption- and emission maxima of HABs **B1** - **B3** in solvents of different polarity.

solvent	$\tilde{\nu}_{\text{abs}} / \text{cm}^{-1}$ ($\epsilon/10^4 / \text{M}^{-1} \text{cm}^{-1}$)			$\tilde{\nu}_{\text{fl}} / \text{cm}^{-1}$		
	B1	B2	B3	B1	B2	B3
MeCN	- ^a	32000 (12.7)	32300 (4.4)	- ^a	15600	15600
PhCN	31700 (11.0)	31300 (11.9)	31600 (4.4)	16500	16600	16600
DCM	32000 (11.6)	31700 (12.9)	31900 (4.3)	17800	17600	17500
THF	32100 (-) ^[a]	31800 (12.5)	32000 (4.8)	18300	18300	18200
MTBE	32200 (-) ^[a]	31800 (12.3)	31900 (4.6)	19700	19700	19600
<i>n</i> Bu ₂ O	32200 (-) ^[a]	31800 (12.4)	31900 (4.8)	20500	20600	20600
C ₆ H ₁₂	32100 (-) ^[a]	31700 (13.2)	31700 (4.5)	22200	22000	22200

^a insufficient solubility

The fluorescence excitation spectra of compounds **B1** - **B3** agree very well with the absorption spectra in these solvents, indicating a complete energy transfer from higher excited to the lowest excited states. Fluorescence quantum yields of the three compounds were determined in benzonitrile (Table 16) and are in the expected range for this type of donor-acceptor systems.²⁰⁶

5.5. Time-resolved fluorescence spectroscopy

Fluorescence lifetimes of **B1** - **B3** were obtained by measuring the fluorescence decays in benzonitrile using time gated technique (Table 16). The decays proved to be single exponential in all cases. With the quantum yields ϕ_f and fluorescence lifetimes τ_f the rate constants for the fluorescent k_f and non-radiative deactivation processes k_{nr} were calculated using the following equations (equation 62 and 63):

$$k_f = \frac{\Phi_f}{\tau_f} \quad (62)$$

$$k_{nr} = \frac{1 - \Phi_f}{\tau_f} \quad (63)$$

Table 16 Fluorescence quantum yields ϕ_f , fluorescence lifetimes τ_f , rate constants for the fluorescent and non-radiative deactivation processes, k_f and k_{nr} , and transition moments of the fluorescence μ_{fl} of HABs **B1** - **B3** in PhCN. Excitation at 29400 cm^{-1} (340 nm).

	ϕ_f	τ_f/ns	$k_f/10^6 \text{ s}^{-1}$	$k_{nr}/10^7 \text{ s}^{-1}$	μ_{fl}/D
B1	0.30	58	5.2	1.2	1.11
B2	0.36	59	6.1	1.1	1.25
B3	0.35	63	5.6	1.0	1.18

It is noticeable that the measured fluorescence lifetimes and quantum yields of the compounds **B1**, **B2** and **B3** are very similar. This again supports that the photophysically active unit is in all cases a single donor-acceptor pair which requires symmetry breaking in **B1**.

The lifetimes of around 60 ns for all HABs are considerable longer (by a factor of 3 to 20) than those of other known triarylamine-triarylborane donor-acceptor compounds.^{168,210,246} Consequently, both the rate constants k_f and k_{nr} are significantly lower in the HABs **B1** - **B3**. The relatively small k_f can be explained by the small fluorescence transition moment (which should be equal to the absorption transition moment in the absence of structural changes in the excited state) which was estimated by the *Strickler-Berg* equation²⁴⁷ (equation 64) and which is due to the essentially through-space character of the CT process. The latter is affirmed by structure optimisations of **B1**, which show very small molecular orbital coefficients at the central benzene ring in the three HOMOs of highest energy and in the three LUMOs of lowest energy.

$$\mu_{fl}^2 = \frac{3h\epsilon_0}{16 \times 10^6 \pi^3} \frac{9}{n(n^2 + 2)^2} \frac{g_e}{g_g} \frac{\int \tilde{\nu}^{-3} I_f d\tilde{\nu}}{\int I_f d\tilde{\nu}} k_f \quad (64)$$

Here, g_e and g_g are the degree of degeneracy of the excited and ground state, n is the refractive index of the solvent and I_f is the fluorescence intensity at the given wavenumber.

5.6. Transient absorption spectroscopy

Transient absorption spectra in the ns-time regime were recorded for HABs **B1** - **B3** in benzonitrile (Figure 88) in order to characterise the excited state in more detail. Generally the transient absorption signal rises immediately with the 24000 cm^{-1} (416 nm) laser light excitation (instrument response function 8 ns) and decay to the ground state with the same time constants (58 ns for **B1** and 59 ns for **B2** and **B3**, measured at the low energy transient absorption band maximum) as the fluorescence lifetimes (see Figure 85-87).

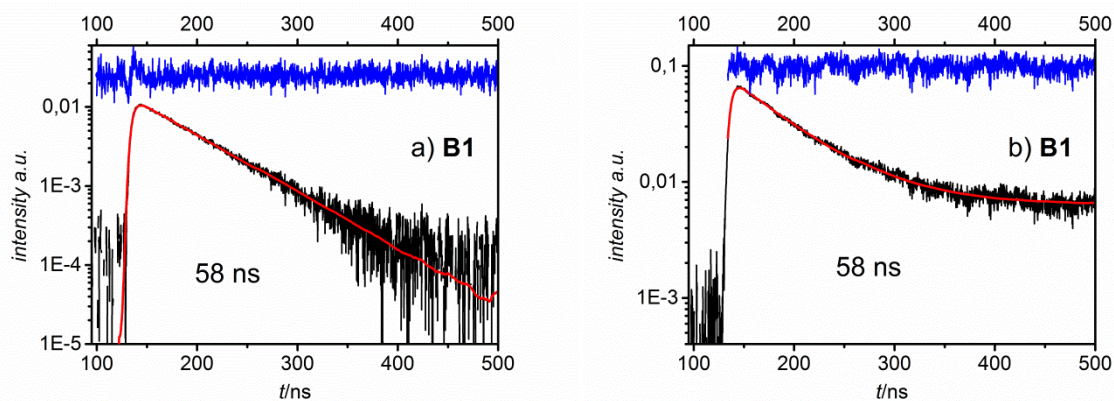


Figure 85 a) Fluorescence decay at 14300 cm⁻¹ (700 nm) (black) and b) transient absorption decay at 13500 cm⁻¹ (742 nm) (black) of **B1**, mono-exponential fits (red) and residuals of the fits (blue).

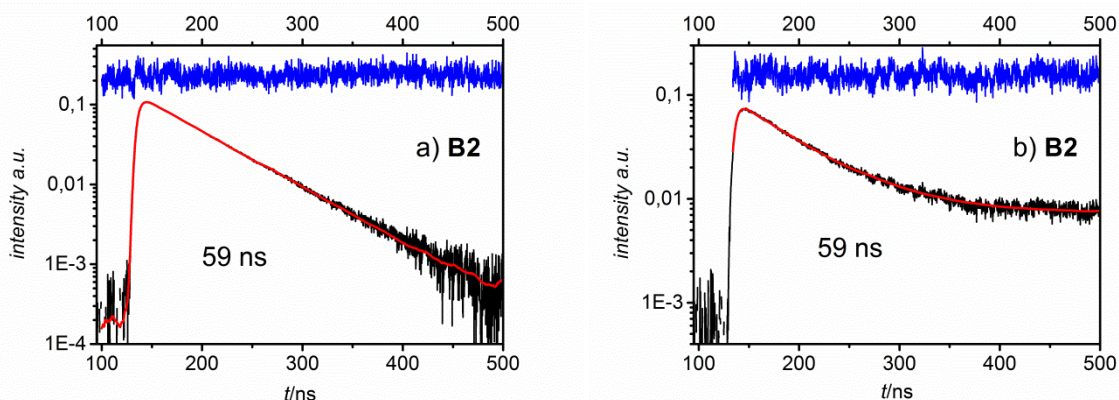


Figure 86 a) Fluorescence decay at 16100 cm⁻¹ (620 nm) (black) and b) transient absorption decay at 13500 cm⁻¹ (739 nm) (black) of **B2**, mono-exponential fits (red) and residuals of the fits (blue).

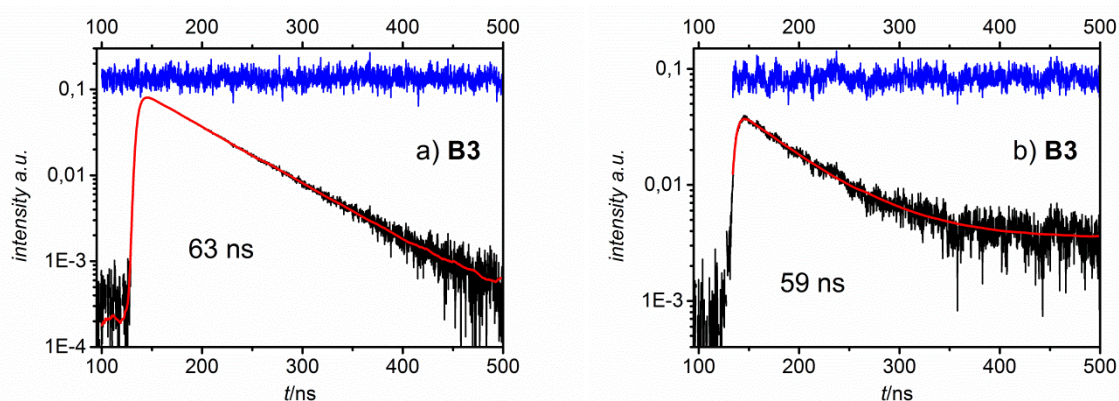


Figure 87 a) Fluorescence decay at 16100 cm⁻¹ (620 nm) (black) and b) transient absorption decay at 13400 cm⁻¹ (745 nm) (black) of **B3**, mono-exponential fits (red) and residuals of the fits (blue).

Consequently, all transient signals originate from the first excited singlet state and no intersystem crossing to any triplet states can be observed. The transient spectra of compounds **B1**, **B2** and **B3** all

feature an absorption band at 13400, 13500 and 13400 cm^{-1} . These can be assigned to an overlap of SOMO-LUMO transitions of the triarylborane radical anion (absorption maximum is expected at 14500 cm^{-1})²⁴⁸ and of the triarylamine radical cation moieties (absorption maximum is typically located at 13000 cm^{-1}).³² Furthermore, in all the transient spectra a broad absorption band can be observed at the high energy end of the spectra at around 26000 cm^{-1} , accompanied by a shoulder at 22800-23400 cm^{-1} . The exact maxima of these bands cannot be determined, but they can be attributed to HOMO-SOMO transitions of the boron radical anion and the nitrogen radical cation. The assignments are based on the spectroelectrochemical studies on the 4,4'-bis(dimesitylboryl)biphenyl radical anion compared to the isoelectronic tetramethylbenzidinium radical cation by the group of *Kaim*.²⁴⁸ The UV/vis spectra of both species show exceptionally similar band structures albeit slightly shifted. Although the maxima of HOMO-SOMO transitions of triarylboranes are expected to be in the near-UV region, they can be shifted to lower energies (up to 23500 cm^{-1}) by conjugation with π -acceptor centres. Likewise this effect can be observed in triarylamines.²⁴⁸ All the information supports the formation of a CT state between the triarylamine and triarylborane moieties with pronounced radical cation and radical anion character in the first excited state of **B1**, **B2** and **B3**.

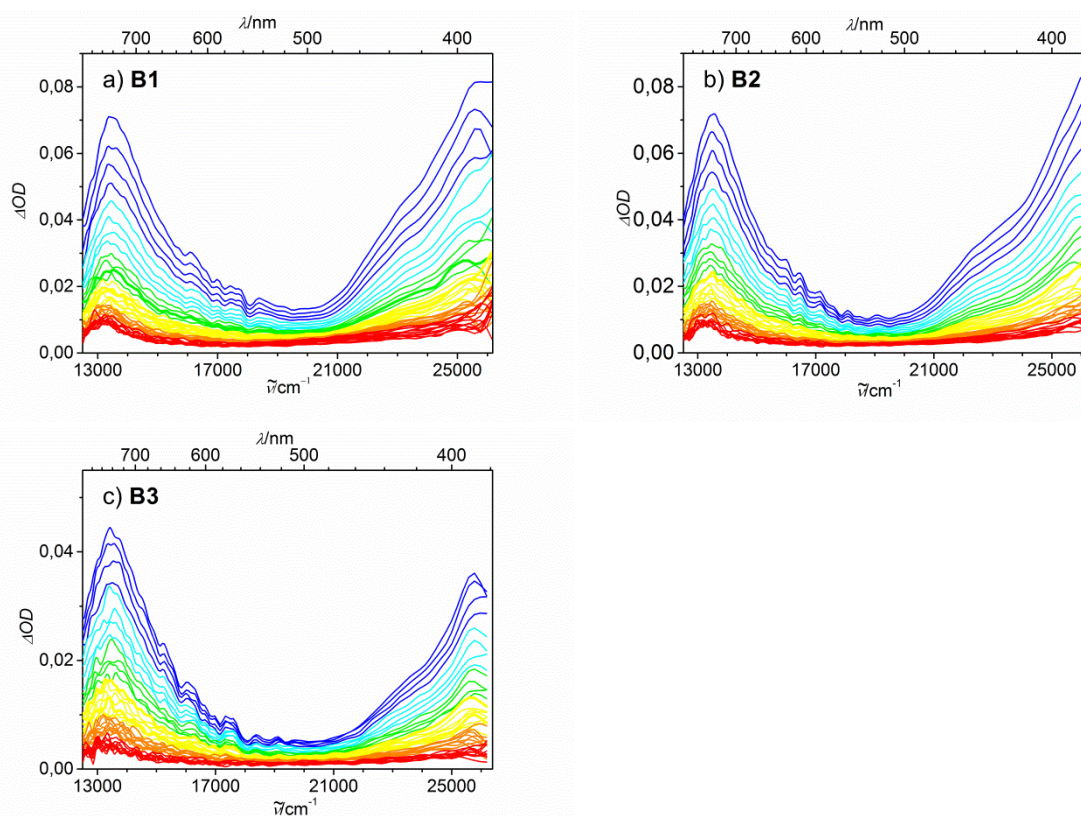


Figure 88 Transient absorption spectra of HABs **B1** - **B3** in benzonitrile. Excitation at 24000 cm^{-1} (see Figure 85-87 for the transient absorption decay curves and their fits). The spectra are displayed in 7 ns steps (from blue to orange) and 33 ns to 66 ns (for red).

5.7. Steady-state fluorescence anisotropy spectroscopy

In order to gain further insight into the symmetry breaking effects in **B1** and **B2** we performed steady-state fluorescence anisotropy measurements at rt in sucrose octaacetate. The latter forms a rigid glass matrix upon heating and subsequent cooling to rt, which is necessary to avoid rotation of the chromophores during fluorescence lifetime. By measuring the fluorescence anisotropy r as defined by equation 54 the relative orientation r of the excitation and fluorescence transition dipole moments can be studied.

$$r = \frac{2}{5} \left(\frac{3 \cos^2 \beta - 1}{2} \right) \quad (54)$$

With parallel orientation ($r = 0^\circ$) of the transition dipole moments a maximum anisotropy $r = 0.4$ should be observed, with perpendicular orientation ($r = 90^\circ$) a minimum value of -0.2 should be obtained. In the special cases of three- and two-dimensional depolarisation of the fluorescence light, anisotropy values of 0 and 0.1, respectively, are expected.^{104,249} Particularly the anisotropy for three- and two-dimensional depolarisation is of great significance in **B1** and **B2**, because excitation into one donor-acceptor CT state of the molecule could be followed by energy redistribution within all possible donor-acceptor CT combinations of the chromophore, thus leading to depolarisation within two (or three) dimensions. The topology of the HAB framework and the CT nature of the transition are ideal for this kind of study because excitation and fluorescence transition moments of the CT processes should be parallel and oriented in the plane of the central benzene ring whereby the analysis of the polarised steady-state fluorescence data is simplified. The anisotropy curves for the excitation spectra of compounds **B1**, **B2** and **B3** are depicted in Figure 89.

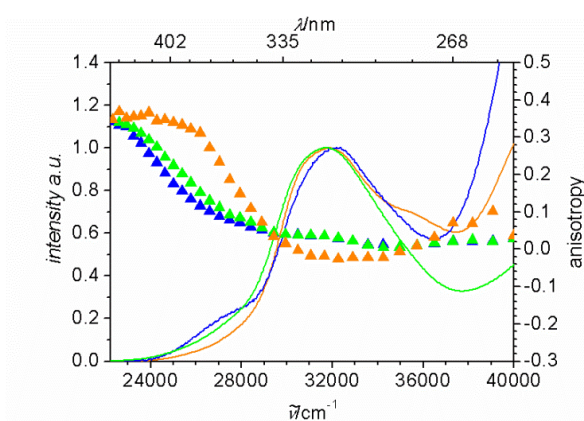


Figure 89 Excitation anisotropy spectra in sucrose octaacetate (triangles) and normalised absorption spectra in $n\text{Bu}_2\text{O}$ (solid lines) of HABs **B1** (blue), **B2** (green) and **B3** (orange).

The excitation anisotropy of model compound **B3** has a high value of 0.34 in the energy range of the lowest absorption band, the CT-transition. This is somewhat lower than the expected $r = 0.4$ for parallel transition moments and may be due to residual molecular motion in the sucrose octaacetate matrix at rt. To higher energies the anisotropy decreases and has a rather constant value of -0.02 in the range of the second absorption band, which is attributed to localised π - π^* -transitions mentioned above. The interpretation of this value is difficult as several absorption bands are overlapping and their transition moments are not precisely known. In comparison, the lower anisotropy of compounds **1** and **2** in the range of the CT transitions is remarkable and can be explained by the “red-edge excitation effect”.^{250,251} This effect can be observed in symmetry broken or asymmetric chromophores in which energy transfer between chromophoric branches occurs.¹⁶⁸ Owing to symmetry breaking in **B1** induced by the inhomogeneous environment (solvent or matrix) and to the inherently asymmetric **B2** the six and four possible CT transitions in compound **B1** and **B2**, respectively, differ among each other slightly in energy. Following Kasha’s rule fluorescence will be emitted from the lowest energy CT state only. On the low energy side of the CT absorption bands only the lowest energy CT state will be excited and the transition moments for absorption and fluorescence are parallel, resulting in a high anisotropy value of ideally 0.4. Excitation at the high energy side of the CT bands leads to energy transfer to the lowest energy CT state followed by fluorescence emission. Thus, the transition moments for absorption and fluorescence are no longer parallel which leads to lower anisotropies. Because of the additivity of anisotropies, one should ideally observe an anisotropy of 0.1 if there is rapid energy transfer between all CT states in two dimensions. Overlap of the CT bands with the more intense π - π^* -transitions may in fact lead to the observed complete depolarisation ($r \sim 0$) in that spectral range. The different anisotropy behaviour of the CT band of **B1** and **B2** on the one hand and of **B3** on the other hand nicely demonstrates that energy transfer between the different CT states occurs in **B1** and **B2** within the fluorescence lifetime.

5.8. Titration with fluoride

Fluoride sensing is an important issue in detection of chemical weapons based on phosphorous fluorides.^{252,253} In order to probe the applicability of **B2** and **B3** (**B1** is not soluble enough in THF) for fluoride sensing, fluoride titration experiments were performed in THF using tetra-*n*-butylammonium fluoride as the anion source. Complexation of the triarylborane centres with fluoride anion was observed both by UV/Vis and by fluorescence spectroscopy. By fluoride complexation of the unoccupied p_z -orbital the boron centre loses its acceptor character²²⁷ and the CT states and the associated transitions vanish in the absorption and fluorescence spectra. As can be seen in the absorption spectra of **B2** and **B3** in Figure 90 fluoride titration leads to a decrease of the π - π^* transitions at ca. 33000 cm^{-1} and the CT shoulder at 27000 cm^{-1} . Likewise, upon the addition of fluoride to HABs **B2** and **B3** the charge transfer fluorescence at ca. 18000 cm^{-1} decreases and a new band rises at ca. 23000 cm^{-1} .

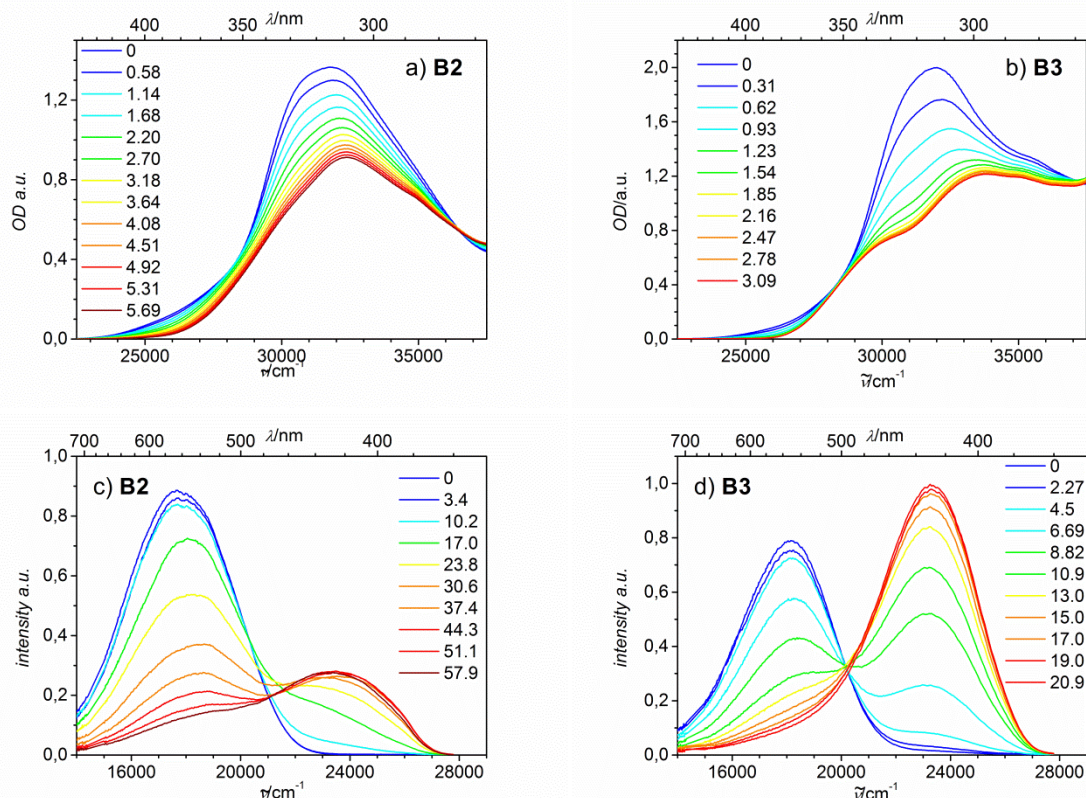


Figure 90 UV/Vis of a) **B2** and b) **B3** and fluorescence spectra of c) **B2** and d) **B3** in THF upon titration with TBAF under ambient conditions. The equivalents of added TBAF are given in the graphs. The UV/Vis spectra were measured at concentrations of $1 \cdot 10^{-5}$ M (**B2**) and $4 \cdot 10^{-5}$ M (**B3**), fluorescence spectra at a concentration of $5 \cdot 10^{-7}$ M (**B2** and **B3**).

The latter band at 23000 cm^{-1} is due to localised fluorescence from the TAA chromophores. This high energy fluorescence is more intense than the CT fluorescence in the model HAB **B3**, whereas in HAB **B2** it is much weaker. For a quantitative analysis of the spectral changes it is important to account for the decreasing absorption in the range of the CT and the $\pi\text{-}\pi^*$ transitions from 23000 cm^{-1} to 37000 cm^{-1} where the chromophores were excited ($\lambda_{\text{ex}}=340 \text{ nm}$). However, the quantitative analysis of the fluorescence titration experiments in THF at ambient conditions is further complicated by instability of the complexed species noticeable by a slow decrease of its fluorescence in the time range of hours. This is possibly due to rearrangement reactions known for four-coordinated organoboron compounds.²⁵⁴ Furthermore, there is another process which competes with the complexation of the fluoride by the boron centre. In case of the model compound **B3** with only one TAB moiety this competing process can be seen in the fluoride binding curve from fluorescence (absorption) spectra at very low chromophore concentrations ($\sim 10^{-7}$ M) which does not rise (fall) instantaneously with a finite slope while adding fluoride as expected for a 1:1 ratio of binding sites to ligands, but is sigmoidal, indicating that the added fluoride is “deactivated” partially prior to boron complexation (see Figure 91).

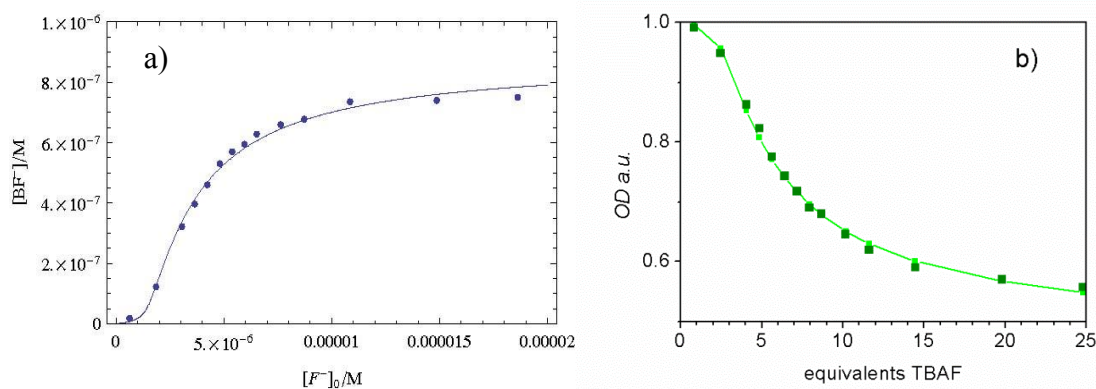


Figure 91 a) Fit (line) of the fluoride binding curve (dots) of **B3** ($7.5 \cdot 10^{-7}$ M) at 23900 cm^{-1} fluorescence in THF under ambient conditions by adding incremental amounts of TBAF ($1.3 \cdot 10^{-4}$ M) using coupled chemical equilibria (see below) and a Mathematica script.²⁵⁵ The “deactivating” substrate was fitted with a concentration of $1.5 \cdot 10^{-6}$ M and a binding constant of $1.4 \cdot 10^7$. b) Fit (pale green line) of the fluoride binding curve (dark green squares) of **B3** ($7.5 \cdot 10^{-7}$ M) at 31900 cm^{-1} absorption in THF under ambient conditions by adding incremental amounts of TBAF ($1.3 \cdot 10^{-5}$ M) using the HypSpec software package.²⁵⁶

Absorption measurements at much higher chromophore concentrations of $\sim 10^{-5}$ M are affected much less. Thus, this fluoride “deactivation” can neither be caused by impurities present in the analyte nor in the chromophore. However, it is possible that residual moisture in the THF solvent affects the measurements by hydrogen bonding to the fluoride anions. By analysing the absorption measurements using the global fit routine of the HypSpec software package (Figure 92) the complexation constant of **B3** was determined to be $1.5 \cdot 10^5$. The fluorescence titration could be both fitted by HypSpec software (Figure 91) and by a simple mathematical treatment using coupled chemical equilibria (Figure 91 and equations 65-68), from which complexation constants of $3.6 \cdot 10^5$ and $5 \cdot 10^5$, respectively, could be obtained. The deactivation process is thereby described by a 1:1 complex of fluoride with a second unknown substrate. Both the substrate and the “deactivating” complex do not interact with light in the given range of the spectrum.

$$K_b = \frac{[\text{BF}^-]}{[\text{B}] \cdot [\text{F}^-]} \quad (65)$$

$$K_d = \frac{[\text{DF}^-]}{[\text{D}] \cdot [\text{F}^-]} \quad (66)$$

$$[\text{B}]_0 = [\text{B}] + [\text{BF}^-] \quad (67)$$

$$[\text{F}]_0 = [\text{F}] + [\text{BF}^-] + [\text{DF}^-] \quad (68)$$

with K_b being the binding constant of fluoride to the boron centre, K_d the binding constant to the “deactivating” substrate, $[B]$ concentration of the borane, $[D]$ concentration of the deactivating” substrate, $[F^-]$ concentration of uncomplexed fluoride, $[BF^-]$ concentration of the complexed borane, $[DF^-]$ concentration of the complexed “deactivating” substrate, $[B_0]$ the overall concentration of the borane and $[D_0]$ the overall concentration of the “deactivating” substrate. The complexation constants obtained in this way are similar to those found in the literature for other triarylboranes connected to a donor centre.²⁰⁶ For further investigation of the “deactivation” process, compound **B3** ($4.4 \cdot 10^{-5}$ M) was titrated under inert gas conditions in dry THF (water content < 0.03 %) monitored by UV/Vis spectroscopy. In this experiment fluoride “deactivation” could no longer be detected and the complexation constant increases so strongly that it could not be determined by a fit of the data (see Figure 92) and only an upper limit of $K > 1 \cdot 10^7$ could be estimated. From this observation we conclude that by choosing moisture free conditions the reactivity of the fluoride is no longer reduced by hydrogen bonding to water which thus leads to a higher complexation constant.

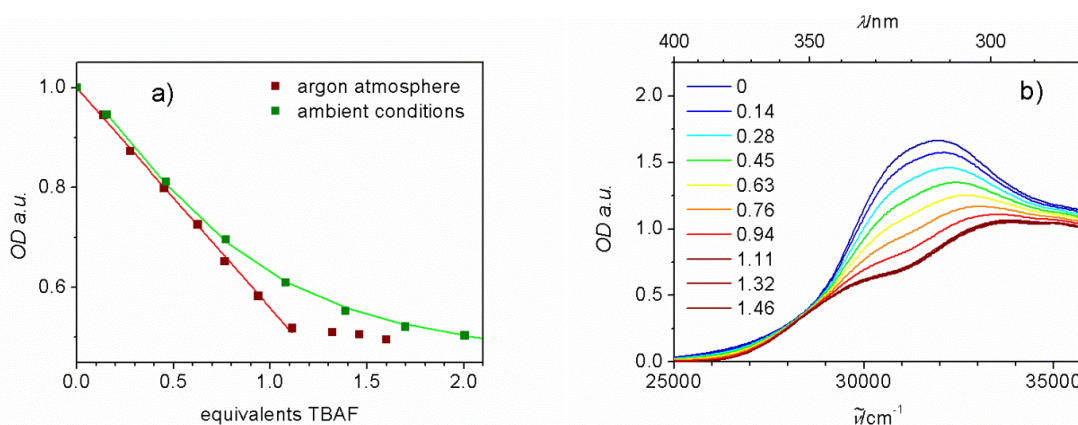


Figure 92 a) Normalised fluoride binding curve of **B3** at 31900 cm^{-1} absorption under an argon atmosphere (dark red squares) in dry THF and at 31800 cm^{-1} in THF under ambient conditions (dark green squares) upon adding incremental amounts of TBAF. The linear fit of the former is shown in red and the fit of the latter by the HypSpec software is shown in bright green. b) UV/Vis absorption spectra of the titration of **B3** ($4.4 \cdot 10^{-5}$ M) with TBAF (equivalents given in the graph) in abs. THF under an argon atmosphere.

In case of **B2** - a substrate with three binding sites - the fitting of the binding curve from absorption spectra in THF at ambient conditions is a much more demanding task, which is due to the fact, that the extinction coefficients of the involved complex species are unknown and the binding constants are too similar to get well defined complexation steps. For this reason the automatic global fitting routine of HypSpec was not able to yield physically reasonable results from the absorption spectra. However, with manual optimisation the arguable best fit is obtained with binding constants of $6 \cdot 10^5$, $2 \cdot 10^5$ and $0.7 \cdot 10^5$ for the first, the second and the third complexation, respectively (see Figure 93).

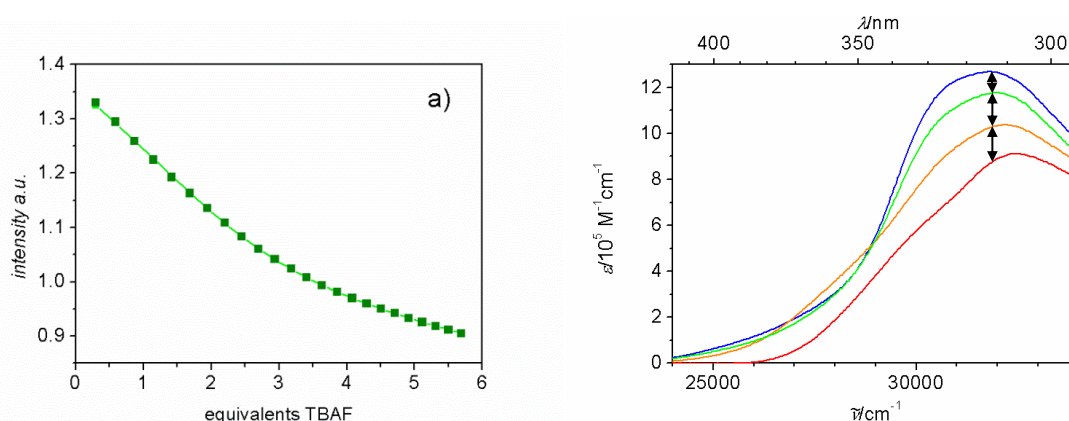


Figure 93 a) Fit (pale green line) of the fluoride binding curve (dark green squares) of **B2** at 32100 cm^{-1} absorption (311.5 nm) in THF under ambient conditions by adding incremental amounts of TBAF using the HypSpec software package. b) Absorption spectra of **B2** (blue) and the complex species BF^- (green), BF_2^{2-} (orange) and BF_3^{3-} (red), manually calculated by global fit with the HypSpec software package.

The goodness of the fit was determined by the curve progressions. Thereby it is assumed that the absorption in the range of the CT and the π - π^* transitions located at the boron centres decreases by the same amount for every complexation step (black arrows in Figure 93 b). The absorption band of the complexed triarylborane chromophore should be at much higher energy.²¹² The absorption spectra of the complexed species reflect that assumption reasonable well in the range of the π - π^* transitions but not at lower energies for unknown reasons. The binding constants of $6 \cdot 10^5$, $2 \cdot 10^5$ and $0.7 \cdot 10^5$ agree with the statistical ratio of $3:1:\frac{1}{3}$ for the subsequent complexation of the analyte with three noninteracting ligands. However, these findings disagree with the negative binding cooperativity found in many systems with more than one boron centre.^{227,230} A reason for this disagreement could be the poor electronic coupling of the neighbouring redox centres in **B2**. This is also supported by the complexation constants of **B2** being in good agreement with that of the model compound **B3**. Thus, the greater sterical hindrance provided by the HAB framework in **B2** does not affect the binding ability of the triarylboranes to the small fluoride anion. Under moisture-free conditions a binding curve with a linear decrease was observed (see Figure 94), which was impossible to be fitted with the given procedures.

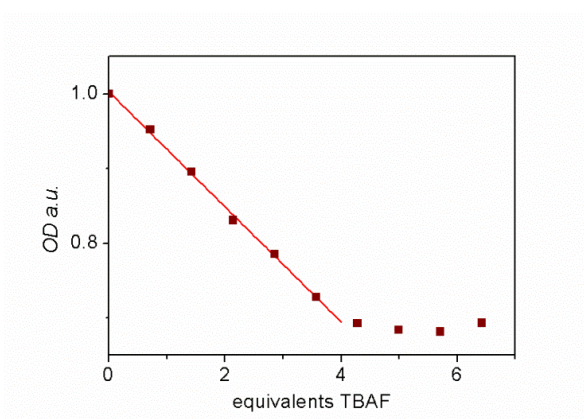


Figure 94 Linear fit (red line) of the binding curve (dark red squares) of **B2** at 31800 cm^{-1} (314 nm) absorption in dry THF under an argon atmosphere adding incremental amounts of TBAF.

Full complexation is reached after adding four equivalents of TBAF. At this point we stress that the commercially available TBAF solution contains around 5 wt. % water which definitely hampers its *Lewis*-base reactivity. Nevertheless, both observations indicate binding constants exceeding those measured under ambient conditions, which agrees with the findings in HAB **B3**. Fluorescence titration experiments at concentrations of $7 \cdot 10^{-7}\text{ M}$ under ambient conditions gave no definite fit of the binding curves with all parameters optimised due to the increased complexity of the system and the significant fluoride “deactivation” process at these low concentrations. However, with some constraint parameters a fit was possible (see below). It is remarkable that the fluoride binding curve at 31800 cm^{-1} absorption decreases almost immediately after addition of fluoride, whereas the CT fluorescence at 17600 cm^{-1} has a constant high intensity until 10 equivalents of fluoride are added (Figure 95). This observation shows that as long as there is one unblocked CT state present in the molecule fluorescence will be emitted from this unblocked state at constant intensity. This requires energy transfer in-between the chromophore branches to take place before emission.

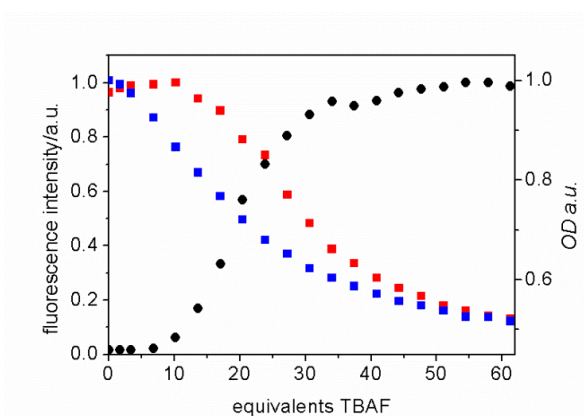


Figure 95 Normalised fluoride binding curves of **B2** at 17600 cm^{-1} fluorescence in red and at 23100 cm^{-1} fluorescence in black and at 31800 cm^{-1} absorption in blue in THF under ambient conditions upon adding incremental amounts of TBAF.

With the assumption of energy transfer and no cooperativity effects the binding curve at 23100 cm^{-1} fluorescence could be fitted with binding constants of $K = 1.8 \cdot 10^6$, $6 \cdot 10^5$ and $2 \cdot 10^5$ for the first, the second and the third complexation, respectively (see Figure 96).

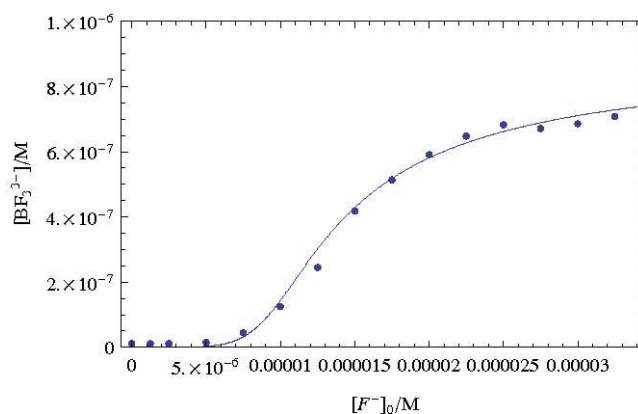


Figure 96 Fit (line) of the fluoride binding curve (dots) of **B2** ($7.3 \cdot 10^{-7}$ M) at 23900 cm^{-1} fluorescence in THF under ambient conditions by adding incremental amounts of TBAF ($2.5 \cdot 10^{-4}$ M) using coupled chemical equilibria (see below) and a Mathematica script. The “deactivating” substrate was fitted with a concentration of $7.2 \cdot 10^{-6}$ M and a binding constant of $5 \cdot 10^6$.

The fit is based on the coupled chemical equilibria described in equations 69-74:

$$K_{b1} = \frac{[\text{BF}^-]}{[\text{B}] \cdot [\text{F}^-]} \quad (69)$$

$$K_{b2} = \frac{[\text{BF}_2^{2-}]}{[\text{BF}^-] \cdot [\text{F}^-]} \quad (70)$$

$$K_{b3} = \frac{[\text{BF}_3^{3-}]}{[\text{BF}_2^{2-}] \cdot [\text{F}^-]} \quad (71)$$

$$K_d = \frac{[\text{DF}^-]}{[\text{D}] \cdot [\text{F}^-]} \quad (72)$$

$$[\text{B}]_0 = [\text{B}] + [\text{BF}^-] + [\text{BF}_2^{2-}] + [\text{BF}_3^{3-}] \quad (73)$$

$$[\text{F}]_0 = [\text{F}] + [\text{BF}^-] + [\text{BF}_2^{2-}] + [\text{BF}_3^{3-}] + [\text{DF}^-] \quad (74)$$

with K_{b1} to K_{b3} being the stepwise binding constants of fluoride to the boron centre, K_d the binding constant to the “deactivating” substrate, $[\text{B}]$ concentration of the borane, $[\text{D}]$ concentration of the deactivating” substrate, $[\text{F}]$ concentration of uncomplexed fluoride, $[\text{BF}^-]$, $[\text{BF}_2^{2-}]$ and $[\text{BF}_3^{3-}]$

concentrations of the complexed borane species, $[DF^-]$ concentration of the complexed “deactivating” substrate, $[B_0]$ the overall concentration of the borane and $[D_0]$ the overall concentration of the “deactivating” substrate. The fitted binding constants are very similar to those obtained by the UV measurements at higher substrate concentrations.

5.9. Ultrafast TA and FUC measurements

5.9.1. Model compound B3

Pump-probe transient absorption spectra in the fs to ns time regime were measured for compound **B3** in DCM and PhCN to monitor the temporal evolution of the CT transfer state. Therefore, the molecule was pumped at 26700 cm^{-1} (375 nm) and probed with a white light continuum in the wavelength range between 25000 cm^{-1} (400 nm) and 12500 cm^{-1} (800 nm) (the chirp corrected transient absorption raw data can be found in the appendix 2). This pump energy excites not only the charge transfer state, but furthermore states localised at the borane and amine centres. However, at smaller pump energies the signal-to-noise ratio of the transient absorption measurement is drastically decreased due to a lower extinction coefficient. Furthermore, the internal conversion from the localised states to the energy lowest CT state is so fast that it cannot be traced by the measurement setup (see below for justification) and thus does not complicate the analysis. By a global fit routine evolution associated difference spectra (EADS) and their respective decay time constants were obtained (Figure 97 and Table 17).

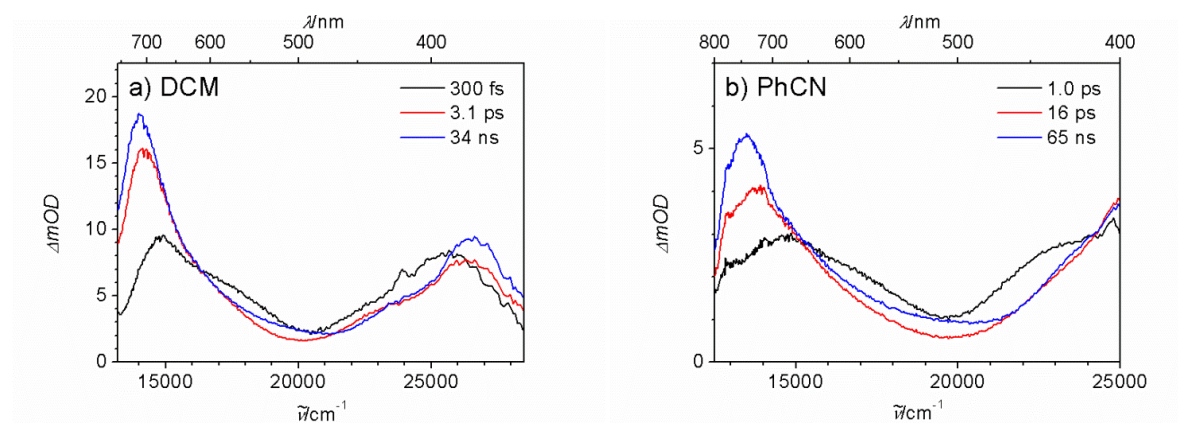


Figure 97 Evolution associated fs-transient absorption spectra of **B3** in a) DCM and b) PhCN. The decay times of the respective EADS are given in the legend. The compounds were pumped at 26700 cm^{-1} .

Table 17 Decay time constants $\tau_1 - \tau_3$ of the evolution associated spectra EADS1 – EADS3 and time constants τ_s for the spectral response function $S_{\tilde{\nu}}(t)$ of **B3** in DCM and PhCN.

	τ_1	τ_2	τ_3	τ_s
	/ps	/ps	/ns	/ps
DCM	0.3	3.1	34	1.4
PhCN	1.0	16.0	65	9.8

EADS1 rises with the instrument response function (~ 300 fs in DCM and ~ 500 fs in PhCN) and all further EADS rise with the decay time constant of the preceding EADS. The transient absorption data could be fitted for both solvents with three EADS. All these EADS show an absorption band rising to the high energy end of the spectrum at ca 26500 cm^{-1} (380 nm) in PhCN and above 25000 cm^{-1} (400 nm) in DCM and an absorption band in the range between 14700 cm^{-1} (680 nm) and 13500 cm^{-1} (740 nm). The maxima of the low energy band shift from EADS1 to EADS3 to lower energies by 1100 cm^{-1} and 800 cm^{-1} in PhCN and DCM, respectively, and the intensity increases in the same order. The bandshape of EADS3 measured in PhCN and DCM and the decay time constant in PhCN are in good agreement with the transient absorption data of **B3** measured in the ns time regime ($\tau = 59$ ns) in PhCN (see Figure 88).¹⁹ Accordingly, EADS3 represents in both solvents the charge transfer state between the amine donor and boron acceptor centres as discussed in the previous transient absorption spectroscopy section.¹⁹ The low energy transient absorption band can be ascribed to the SOMO-LUMO transition and the high energy band to the HOMO-SOMO transition of the amine radical cation superimposed by that of the boron radical anion centre.^{19,32,248} EADS1-EADS2 can be rationalised by a relaxation process of the charge transfer state as a continuous shift along an excited state potential energy surface.^{177,180,182,183,185,257} The temporal evolution of this process was monitored by calculating the spectral response function $S_{\tilde{\nu}}(t)$ of the time-dependent shift of the low energy transient absorption band (equation 61).⁵¹

$$S_{\tilde{\nu}}(t) = \frac{\tilde{\nu}_{\max}(t) - \tilde{\nu}_{\max}(\infty)}{\tilde{\nu}_{\max}(0) - \tilde{\nu}_{\max}(\infty)} \quad (61)$$

The maxima of the transient absorption bands $\tilde{\nu}_{\max}(t)$ were determined from polynomial fits of the chirp corrected raw spectra. The value $\tilde{\nu}_{\max}(\infty)$ corresponds to the maximum of the transient spectra at infinite time represented in this case by the value of the longest measured time delay of 1-3 ns. Although we are aware of the inaccuracy this value seems reasonable as the shift is restricted to the first 200 ps. The maximum of the transient spectra at zero time delay corresponds to $\tilde{\nu}_{\max}(0)$. The signal to noise ratio, the presence of the coherent artefact as well as the broadness of the TA band

complicate an analysis before 300 fs (DCM) to 400 fs (PhCN) after excitation. Hence, very fast shifts of the maxima, which are expected for solvent controlled and intramolecular vibrational redistribution processes,^{51,184} might not be resolved. By fitting the spectral response function of **B3** in PhCN a monoexponential time constant of $\tau_s = 9.3$ ps was obtained (Figure 98, Table 17).

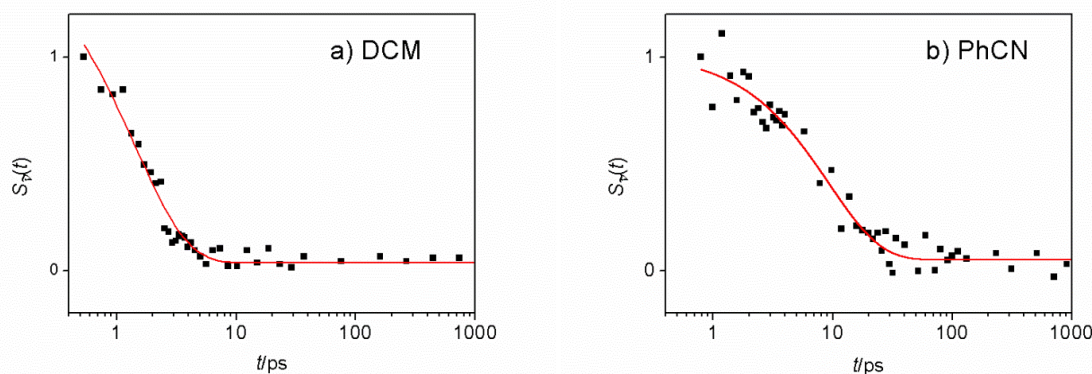


Figure 98 Spectral response function of the transient absorption of **B3** in a) DCM and in b) PhCN.

For comparison, *Maroncelli et al.* probed the time dependent solvation of coumarin 153 in a wide range of solvents.⁵¹ They found a multiexponential decay with time constants of $\tau_a=0.35$ ps (amplitude $a_a=0.38$), $\tau_b=5.27$ ps ($a_b=0.530$) and $\tau_c=25$ ps ($a_c=0.088$) in PhCN. The first time constant τ_a is presumably too fast to be resolved with the used instrumentation but the other two time constants should be detectable for a solvent controlled process. As can be seen in Figure 98, the signal to noise ratio of the spectral response function is very low. It could therefore be possible that the fitted time constant $\tau_s = 9.3$ ps may represent an average value of the solvation dynamics. Accordingly, the correlation time $\langle \tau \rangle$ of the two longer time constants τ_b and τ_c for the solvation of coumarin 153 in PhCN was calculated by equation 75.⁵¹

$$\langle \tau \rangle = \sum_i a_i \tau_i \quad (75)$$

The obtained value of $\langle \tau \rangle = 8.1$ ps is in good agreement to the fitted time constant of $\tau_s = 9.3$ ps. From the fit of the spectral response function of **B3** in DCM (Figure 98, Table 17) a time constant of $\tau_s = 1.4$ ps is obtained. *Maroncelli et al.* reported two solvation time constants in DCM, $\tau_a=0.144$ ps and $\tau_b=1.02$ ps.⁵¹ The solvation time constant τ_a is presumably too fast to be resolved and τ_b is in good agreement with τ_s obtained for **B3**. Thus, it can be concluded that the relaxation process of the CT state is influenced by the viscosity of the solvent. Furthermore, as the transient absorption maxima shifts to lower energies the potential energy surfaces of the lower energy states (State₁) is flattened in comparison to that of the high energy states (State_x) involved in these localised SOMO-LUMO transitions at the amine and borane centres.

To support the findings obtained by the transient absorption measurements fluorescence upconversion experiments were performed in PhCN. HAB **B3** was therefore excited with a 140 fs pulse at either 26700 cm^{-1} (375 nm) or 24700 cm^{-1} (405 nm) and the induced fluorescence signal at 16700 cm^{-1} (600 nm) was upconverted by a gate pulse (12500 cm^{-1} , 800 nm) in a 0.5 mm BBO type 1 crystal and the upconverted signal monitored. The measurements were performed with the polarisation axis of the exciting pulse and the gate pulse being perpendicular (I_{\perp}) as well as parallel (I_{\parallel}) to each other. These two anisotropic decay traces were then fitted globally by a fitting routine^{91,189} to obtain the isotropic and anisotropic time constants of the fluorescence decay. For this fitting process the instrument response function was assumed to be *Gaussian*. The two excitation energies were chosen to investigate the influence of electronically higher excited states on the temporal evolution of the CT transfer state. The fluorescence at 16700 cm^{-1} was upconverted to minimise interferences with fluorescence from **B3** which might partly be complexed by the solvent and is expected at higher energies.^{19,206} On the other hand, the signal-to-noise ratio at lower fluorescence energies was too poor for reliable fits of the measured data. This is due to a lower fluorescence intensity as well as a poorer upconversion efficiency of the BBO crystal. For both excitation wavelengths three isotropic as well as one anisotropic time constant were obtained (see Table 18, and Figure 99 for the fits).

Table 18 Isotropic (index i) and anisotropic (index a) time constants τ and amplitudes a of the fluorescence upconversion measurements of **B3** in PhCN excited at the given energies $\tilde{\nu}_{\text{exc}}$.

$\tilde{\nu}_{\text{exc}}$ / cm^{-1}	a_{i1}	τ_{i1} /ps	a_{i2}	τ_{i2} /ps	a_{i3}	τ_{i3} /ns	a_a	τ_a /ps
26700	-118	2.57	52	29.8	113	25	0.19	475
24700	-109	1.96	63	27.3	110	32	0.32	561

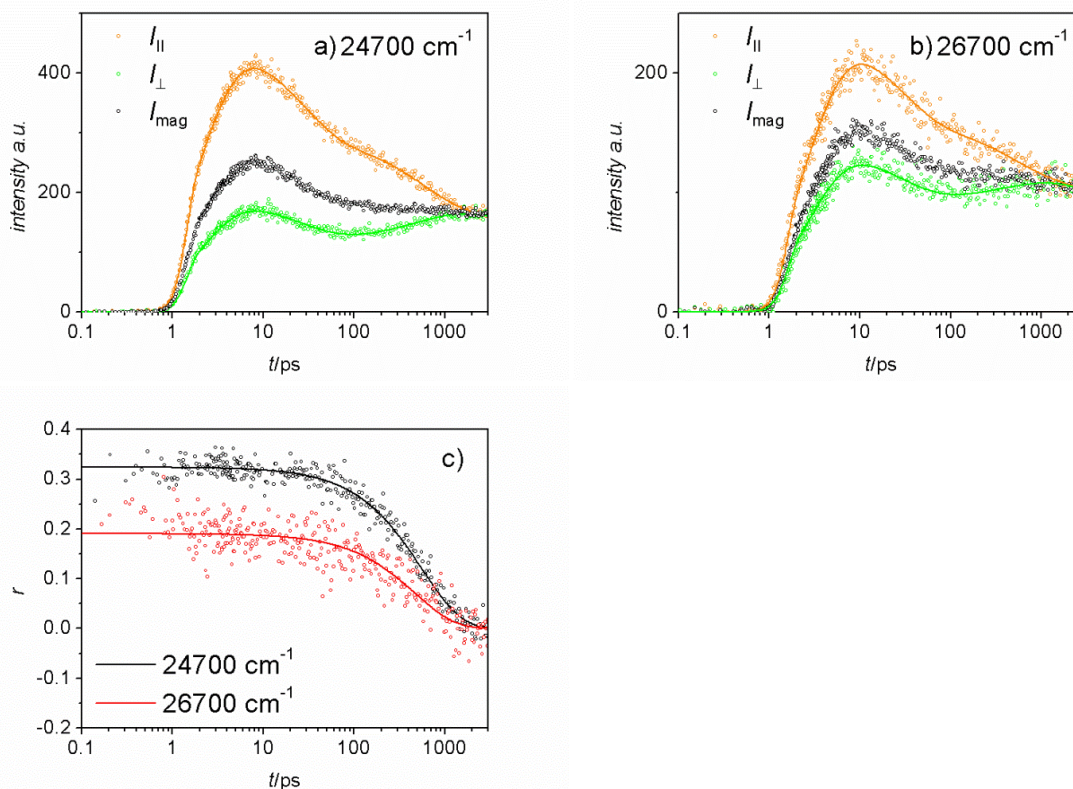


Figure 99 The fluorescence upconversion traces (circles) $I_{||}$, I_{\perp} and the reconstructed I_{mag} excited at a) 24700 cm^{-1} (405 nm) and b) 26700 cm^{-1} (375 nm) in PhCN and c) the respective convoluted anisotropy decay curves of **B3**. The global fits are shown in all cases as solid lines. In the case of the anisotropy the fit curve is deconvoluted.

The time constants and the ratio of the amplitudes are nearly independent of the excitation energy, with the exception of the anisotropic amplitudes. This indicates that although higher energy electronic states are excited the internal conversion processes are too fast to be resolved by this measurement setup and thus only the CT state can be monitored. The reduced amplitude of the anisotropic decay when exciting at higher energies can be explained as follows. When only the CT state is excited, the fluorescence, originating from the same state, should theoretically have anisotropic amplitude of 0.4. Values below 0.4 are indicating that higher energy electronic states are as well excited with transition moment directions deviating from that of the CT state. The lower the anisotropic amplitude the more are the higher energy electronic states excited. From the absorption spectra it can be clearly seen that at 26700 cm^{-1} (375 nm) transitions localised at the borane and amine centres are significantly excited whereas at 24700 cm^{-1} (405 nm) the excitation is mainly restricted to the CT state.

The isotropic time constants are in the same order of magnitude as those obtained by the transient absorption measurements (see Table 17 and 18). This implies that the evolution of the CT state is also observable in the fluorescence. To monitor this evolution a fluorescence map was constructed by a series of fluorescence upconversion traces recorded at fluorescence wavelengths between 21700 cm^{-1}

(460 nm) and 13900 cm^{-1} (720 nm) in steps of 10 nm. The map was corrected for the chirp in the fluorescence signal. Furthermore, the fluorescence intensity was corrected by comparing the fluorescence spectrum at the longest delay time with the steady-state fluorescence spectrum measured in PhCN. In addition, the spectra were divided by $\tilde{\nu}^3$ to correct for the ν^3 dependency of the spontaneous emission according to Einstein. The corrected map was then sliced at several delay times and the obtained fluorescence spectra fitted in each case by a log-normal function (see Figure 100 and appendix 2).

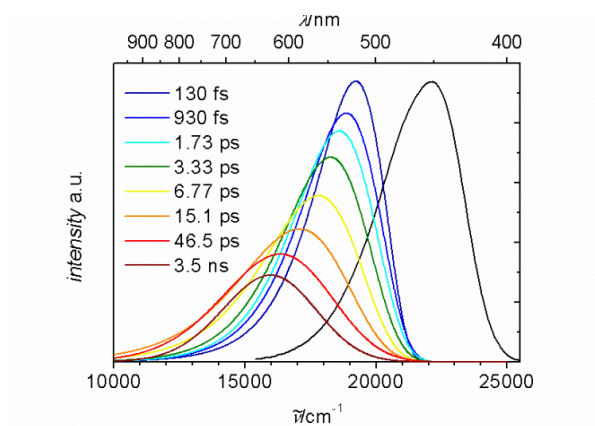


Figure 100 Log-normal functions fitted to the fluorescence upconversion map of **B3** in PhCN at various delay times (colour given in the legend) and the steady state emission spectra of **B3** in cyclohexane (black).

The maxima of the log-normal functions were used to calculate the spectral response function $S_{\nu}(t)$ by equation 61 (Figure 101). A biexponential decay was obtained with time constants of $\tau_{s1} = 3.09\text{ ps}$ and $\tau_{s1} = 23.4\text{ ps}$. These are in good agreement to the solvation time constants $\tau_b = 5.27\text{ ps}$ and $\tau_c = 25\text{ ps}$ of Coumarin 153 in PhCN.⁵¹ Accordingly, the fluorescence of **B3** displays the same solvation dynamic that could be observed in the transient absorption. In addition, the integrals of the reduced fluorescence spectra decreased linearly with the shift of the fluorescence maxima (Figure 101), indicating that both observations have the same cause.

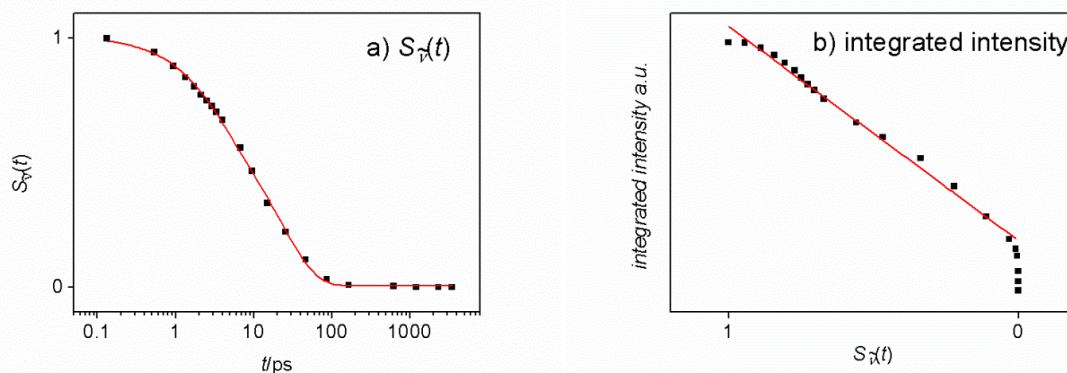


Figure 101 a) Spectral response function and b) integrated intensity of the log-normal functions fitted to the fluorescence upconversion map of **B3** in PhCN

This fluorescence intensity drop was observed before in electron donor-acceptor compounds.⁷⁷ In accordance with the transient absorption band shifts discussed above, this may be explained by the change of the electronic properties of the charge transfer state by large amplitude motions,²⁵⁸ e.g. a twist of the phenyl rings between the donor and acceptor centres. This twisting motion is influenced by the solvent viscosity and presumably changes the electronic coupling of the two redox centres from a more delocalised situation directly after the excitation to a localised, less radiative system at longer delay times.

The time dependent anisotropy measured for **B3** can be described by a mono-exponential decay (Figure 99c, Table 18) with the amplitudes depending on the excitation wavelength as described above. The anisotropy drop to a value of zero with a time constant of around 500 ps can be ascribed to rotational diffusion of the molecules.⁶⁷ Hence, no energy transfer or internal conversion can be observed within the time resolution of the measurement setup. Furthermore, the solvent relaxation processes observed in the emission and transient absorption do not change the transition moment direction of the charge transfer state because an anisotropy decay was not observed in this time domain.

In conclusion, the evolution of the CT state observed for **B3** is very similar to that of **Star-Model** and **HAB-Model** and can presumably be ascribed to the framework connecting the redox centres in all these cases. That is, the flexibility of the bridging unit to respond to two competing driving forces to stabilise the excited state. On the one hand, planarisation of the π -system provides ideal conjugation between the redox centres leading to a lower energy, delocalised state. On the other hand, when the conjugation is disturbed by e.g. twisting motions localised charges can be effectively stabilised by polar solvent molecules.²⁵⁸ Apparently, as soon as the DCM or PhCN solvent molecules are able to adjust to the electronic properties of the CT states by rotation, the latter solvent stabilisation seems to be dominating.

5.9.2. HABs **B1** and **B2**

To test for the same CT dynamics as observed for **B3**, fs-transient absorption measurements were performed for the multidimensional HABs **B1** and **B2** in DCM. It turned out that **B1** (not shown) and **B2** decomposed by pumping with an energy of 26700 cm^{-1} (375 nm , see the intensity drop at longer delay times in Figure 102 (right)), which could however be avoided by exciting the molecules at 24700 cm^{-1} (405 nm). Remarkably, the recorded transient spectra of **B2** pumping at these two wavelengths resemble each other in the time interval from time zero to 1 ps and show furthermore the same time dependent behaviour as **B1** pumped at 24700 cm^{-1} (405 nm) and **B3** pumped at 26700 cm^{-1} (375 nm) (see Figure 102).

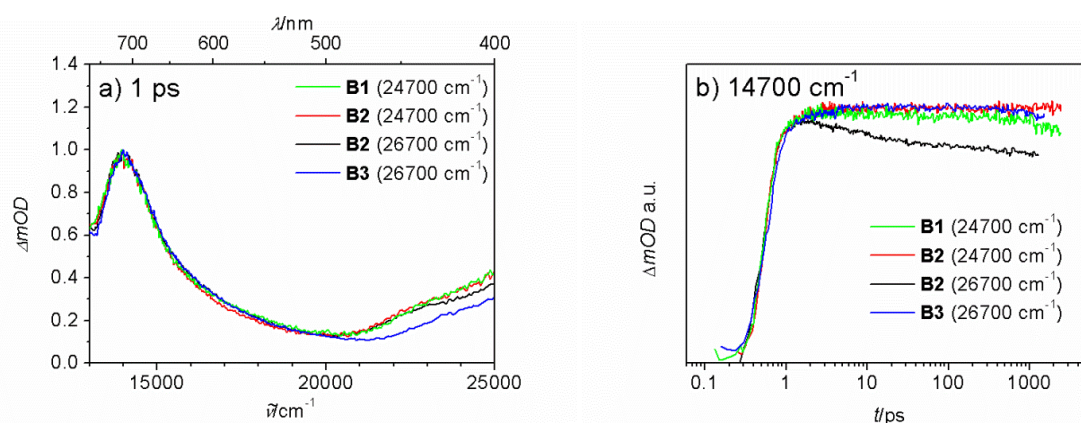


Figure 102 a) Normalised transient absorption spectra after 1 ps and b) decay curves at 14700 cm^{-1} (680 nm , right) of **B1** - **B3** excited at 24700 cm^{-1} (405 nm) and 26700 cm^{-1} (375 nm).

From this it follows that on the one hand, higher energy electronic states, which are excited to a greater extent at 26700 cm^{-1} (375 nm), cannot be observed with the measurement setup used due to ultrafast internal conversion. On the other hand, the temporal evolution of the CT state is similar for all presented HABs showing the same shift of the low energy transient absorption maximum and similar time constants for the three evolution associated difference spectra (Figure 103 and Table 19) fitted to the data.

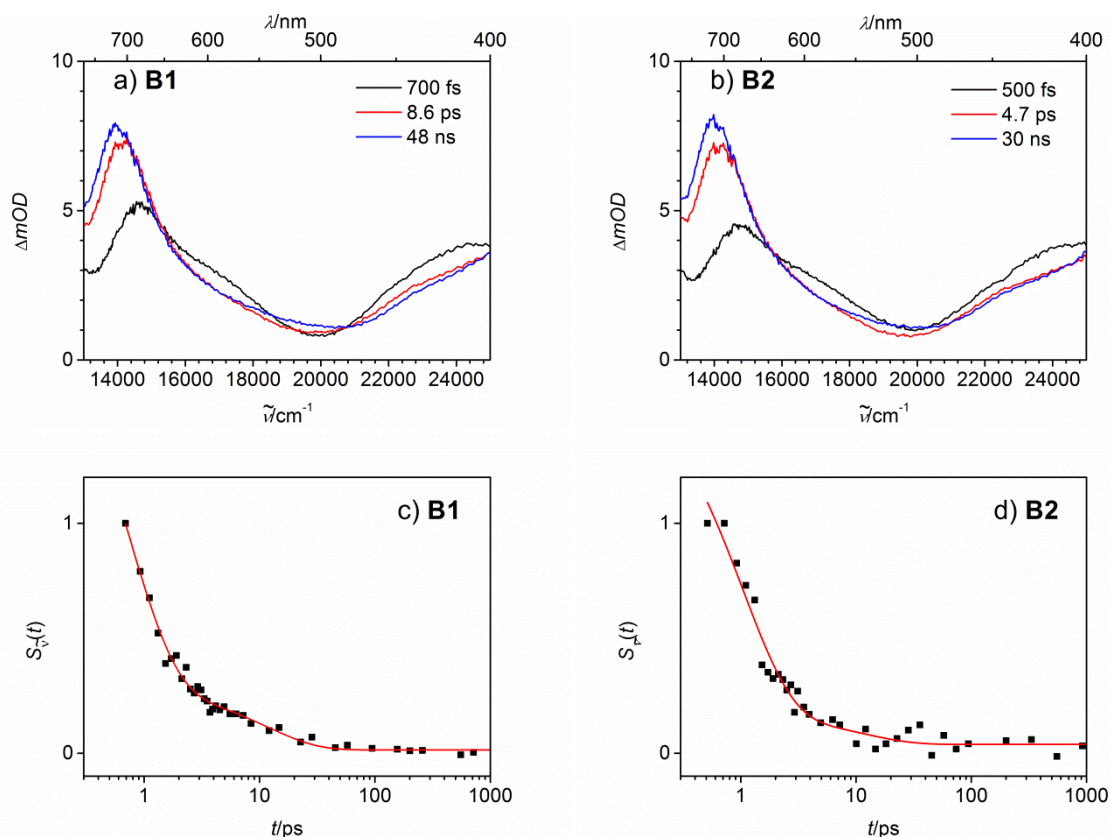


Figure 103 Evolution associated fs-transient absorption spectra (the decay times of the respective EADS are given in the legend) of a) **B1** and b) **B2** and the spectral response functions of the transient absorption of c) **B1** and d) **B2** in DCM. The compounds were pumped at 24700 cm^{-1} (405 nm).

Table 19 Decay time constants τ_1 - τ_3 of the evolution associated difference spectra EADS1 - EADS3, respectively, and time constants τ_{s1} and τ_{s2} and amplitudes a_{s1} and a_{s2} for the spectral response function $S_{\nu}(t)$ of **B1** and **B2** in DCM.

	τ_1	τ_2	τ_3	a_{s1}	τ_{s1}	a_{s2}	τ_{s2}
	/ps	/ps	/ns		/ps		/ps
B1	0.7	8.6	48	2.0	0.7	0.3	11.8
B2	0.5	4.7	30	2.0	0.9	0.2	9.6

The spectral response functions $S_{\nu}(t)$, calculated by the shift of the low energy transient absorption bands of **B1** and **B2**, showed in contrast to **B3** both a biexponential decay with time constants of $\tau_{s1} = 0.7 - 0.9\text{ ps}$ and $\tau_{s2} = 9.6 - 11.8\text{ ps}$. The short time constant is in good agreement to the time constant observed in **B3** and to the solvation time constants of coumarin 153 in DCM $\tau_b = 1.02\text{ ps}$. The low weighted, longer time constant τ_{s2} is only obtained for **B1** and **B2** and is ascribed to slow torsional geometry changes stabilising the CT state.^{67,77,259,260} This behavior is not observed for **B3** possibly because of one of the two following reasons. (i) HABs **B1** and **B2** are sterical much more demanding

compared to **B3** so that an additional relaxation process of the CT state seems reasonable. (ii) This longer time constant could be untraceable in **B3** due to the low weighted amplitude and low signal-to-noise ratio. This is supported by the fact that in all three HABs two EADS with similar time constants are needed to fit the evolution of the CT state. It has to be pointed out that due to the similar transient absorption characteristics of **B1**, **B2** and **B3**, the CT seems to be localised in all cases on one donor acceptor pair. This symmetry breaking in the excited state was observed before in the steady-state fluorescence anisotropy measurements.

Fluorescence Upconversion measurements were performed for **B1** and **B2** in PhCN to test for energy transfer between CT states within the lifetime of the excited state. They were carried out with the same specifications as used for **B3** except that the molecules were excited solely at 24700 cm^{-1} (405 nm) to circumvent degradation of the samples. For both **B1** and **B2**, three isotropic and 2 anisotropic decay time constants were obtained (see Figure 104 and Table 20).

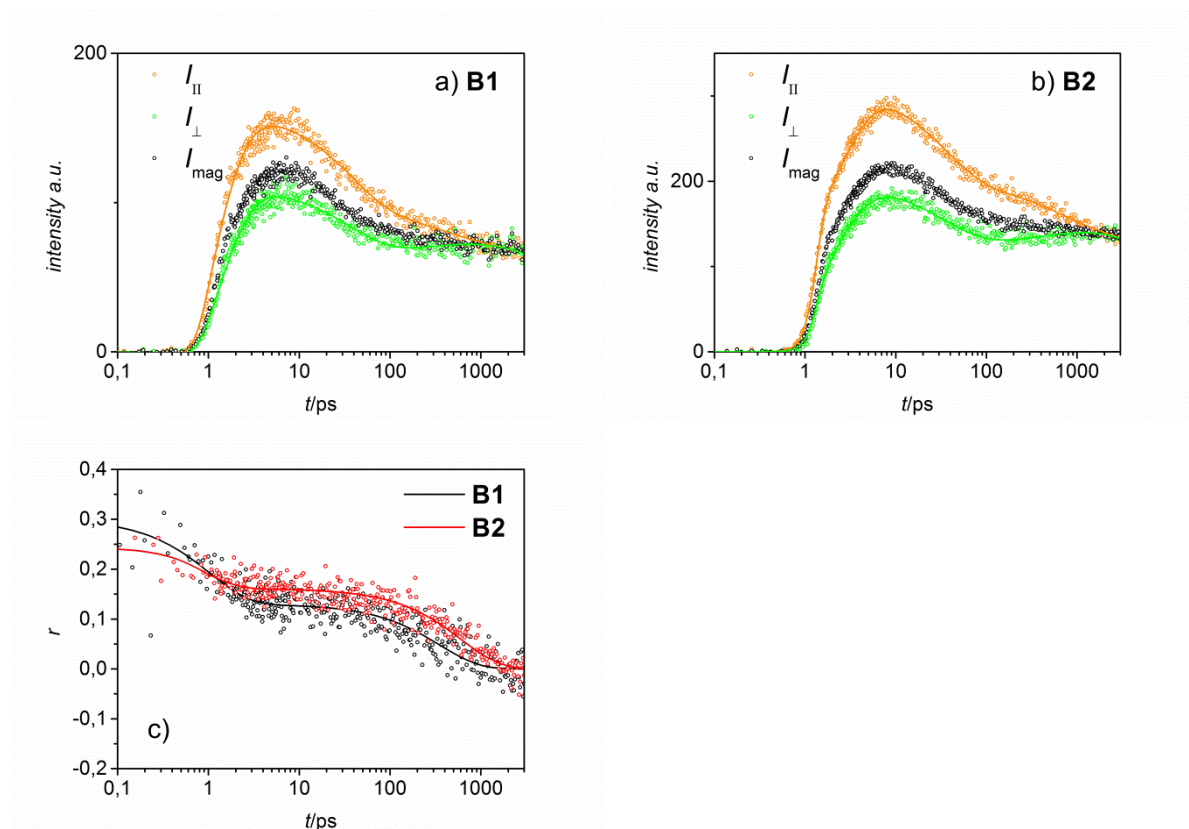


Figure 104 The fluorescence upconversion traces (circles) $I_{||}$, I_{\perp} and the reconstructed I_{mag} of a) **B1** and b) **B2** and c) the convoluted anisotropy decay curves of **B1** and **B2** excited at 24700 cm^{-1} (405 nm) in PhCN and the respective global fits (lines). In the case of the anisotropy the fit curve is deconvoluted.

Table 20 Isotropic (index i) and anisotropic (index a) time constants τ and amplitudes a of the fluorescence upconversion measurements of **B1** and **B2** in PhCN excited at 24700 cm^{-1} (405 nm).

	a_{i1}	τ_{i1} /ps	a_{i2}	τ_{i2} /ps	a_{i3}	τ_{i3} /ns	a_{a1}	τ_{a1} /ps	a_{a2}	τ_{a2} /ps
B1	-149	1.01	48	38.0	72	21	0.17	1.04	0.13	353
B2	-153	1.92	93	35.3	166	25	0.12	0.74	0.16	606

The isotropic time constants obtained for **B1** and **B2** are in good agreement to each other (Table 20) and are of the same order of magnitude as those obtained for **B3** ($\tau_1 = 1.96\text{ ps}$, $\tau_2 = 27.3\text{ ps}$ and $\tau_3 = 32\text{ ns}$). This strengthens the assumption, that in all HABs the same evolution, relaxation and decay of a localised CT state is observed. The anisotropy decays in the multidimensional HABs **B1** and **B2** biexponentially with a long time constant $\tau_{a1} = 350\text{-}600\text{ ps}$ and a short time constant $\tau_{a2} = 0.74\text{-}1.04\text{ ps}$. The long time constant is roughly of the same magnitude as the anisotropic time constant found for **B3**. Hence, it can be likewise attributed to rotational diffusion of the molecules. It has to be noted that the rotational diffusion of **B1** is fitted to be faster than that of **B3**. This is incompatible with the greater molecule size of **B1** in comparison to **B3** and is possible due to a poor signal-to-noise ratio of the fluorescence upconversion data of **B1** that may lead to considerable errors in the fitting process. In contrast, the rotational diffusion constant of **B2** is greater than that of **B1** and **B3** and the respective data has a much better signal-to-noise ratio. The short anisotropic decay is not observed in **B3**. It is therefore attributed to the energy transfer between the CT states in **B1** and **B2**. With this short time constant the anisotropy drops from values of 0.3 and 0.28 at zero time delay to values of 0.13 and 0.16 for **B1** and **B2**, respectively. The values at zero time delay of all HABs are similar ranging from 0.28 to 0.32, so there is no indication of ultrafast coherent energy transfer ($<100\text{ fs}$) in **B1** and **B2**. These anisotropy values deviate by at most 0.04 for several possible reasons. (i) In HABs **B1** - **B3** higher energy states might be excited unequally at the given excitation wavelength. (ii) The low signal-to-noise ratio at early time delays and small temporal shifts of the maxima of the differently polarised excitation pulses might result in errors of the observed anisotropy values. Nonetheless, the energy is assumed to hop between the localised CT states. The observed anisotropy values of 0.13 and 0.16 match the values of 0.1 and 0.175 expected for planar energy delocalisation in **B1** and **B2**, respectively (see below for the justification of the expected values). The small deviations of the observed and calculated limiting anisotropy values are possibly caused by the transition moment directions of the involved CT states slightly deviating from the assumed orientation along the N-B axis.

In the following the mechanism for this energy transfer shall be discussed. There are in general two possible ways how the CT states can interact. The energy can be transferred by exchanging electrons

and/or by Coulomb interactions.¹ In the case of electron exchange, energy transfer between neighbouring CT states coincide with the single charge transfer between degenerate redox centres *meta*-linked by the central benzene ring (see Figure 105).²⁵⁷

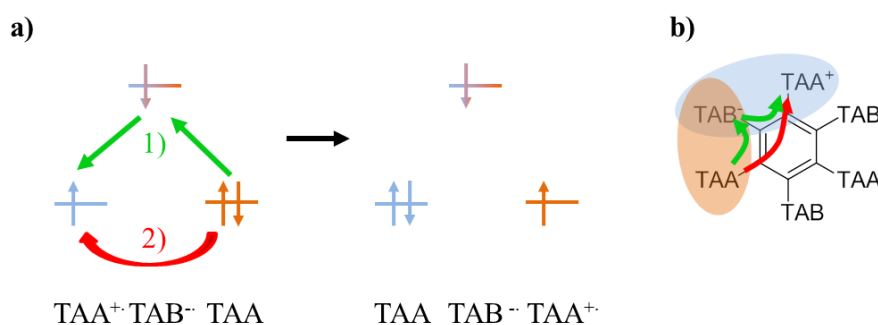


Figure 105 a) Orbital diagram of the energy transfer and b) the corresponding states in **B1** in the case of electron exchange between neighbouring states with a TAB⁻ as the centre. In analogy the following process is also conceivable: TAB⁻-TAA⁺-TAB → TAB-TAA⁺-TAB⁻.

Bonvoisin et al investigated charge transfer between TAA moieties linked in the exact same way¹⁹² and the obtained data indicate a charge transfer time constant of several hundreds of picoseconds. The charge transfer between TAB and TAB⁻ centres should have similar time constants as these redox centres are isoelectronic to the TAA-TAA⁺ couple and their molecular geometry is very similar. Hence, we assume that the electron exchange interactions in **B1** and **B2** are too slow to explain energy transfer time constants of ≤ 1 ps.

The Coulomb interactions between neighbouring CT states can be characterised by resonance energy transfer theory derived by Förster.^{191,261} In the case of energy hopping equation 28 was postulated, which is based on the dipole-dipole approximation.

$$k_{\text{EN}}^{\text{Coul}} = \frac{9000 \ln(10) \Phi_{\text{D}} \kappa^2 J}{128 \pi^5 N_{\text{A}} n^4 \tau_{\text{D}} r^6} \quad (28)$$

Accordingly, the energy transfer rate k_{FT} is dependent on the quantum yield Φ_{D} and lifetime τ_{D} of the donor state in absence of the acceptor state, the factor κ describing the mutual orientation of the transition moments of the donor and acceptor states, the centre to centre distance r of the two states and the overlap integral J . The latter is defined as the integral over the product of the area normalised fluorescence intensity of the donor $\bar{I}_{\text{fl},D}(\tilde{\nu})$ and the extinction coefficient of a single acceptor state $\varepsilon(\tilde{\nu})$ (equation 28).

$$J = \int_{-\infty}^{\infty} \bar{I}_{\text{fl},D}(\tilde{\nu}) \varepsilon(\tilde{\nu}) \frac{\partial \tilde{\nu}}{\tilde{\nu}^4} \quad (28)$$

With $n(\text{PhCN})=1.528$, $\Phi_D = 0.35$ and $\tau_D = 63$ ns (of **3** in PhCN), $\kappa=1.75$ for an angle of 120° between the transition moment directions of two neighbouring CT states, $r_{\text{DA}} = 6.279$ Å for the distance between the middle points of the C-B separation (from DFT optimised structures) and $J = 1.1 \cdot 10^{-18}$ and $3.2 \cdot 10^{-18}$ $\text{dm}^3 \text{mol}^{-1} \text{cm}^3$ (calculated for the steady state absorption and emission spectra in PhCN), energy transfer time constants of 42 ns and 79 ns were obtained for **B1** and **B2**, respectively (see Table 21).

Table 21 Overlap integrals J of **B1** and **B2**, calculated for PhCN and cyclohexane, and the respective energy transfer time constants τ_{EN} obtained by equation 28.

	J (PhCN)	J (cyclohexane)	τ_{EN}	τ_{EN}
	$/\text{dm}^3 \text{mol}^{-1} \text{cm}^3$	$/\text{dm}^3 \text{mol}^{-1} \text{cm}^3$	(PhCN)	(cyclohexane)
B1	$3.2 \cdot 10^{-18}$	$1.2 \cdot 10^{-15}$	42 ns	89 ps
B2	$1.1 \cdot 10^{-18}$	$1.5 \cdot 10^{-15}$	79 ns	75 ps

Furthermore, the energy transfer rate can directly be calculated from the transition moments of the donor (μ_D) and acceptor (μ_A) using equation 76.^{65,262,263}

$$k_{\text{EN}}^{\text{Coul}} = 4\pi^2 c (V_{\text{EN}}^{\text{Coul}})^2 \int_{-\infty}^{\infty} \bar{I}_{\text{fl},D}(\tilde{\nu}) \bar{\epsilon}(\tilde{\nu}) \frac{\partial \tilde{\nu}}{\tilde{\nu}^4} \quad (76)$$

$$\text{with } V_{\text{EN}}^{\text{Coul}} = \frac{\mu_D \mu_A \kappa}{4\pi \hbar c \epsilon_0 r^3}$$

where $\bar{I}_{\text{fl},D}(\tilde{\nu})$ is the area normalised fluorescence intensity of the donor and $\bar{\epsilon}(\tilde{\nu})$ the area normalised absorption of the acceptor. This method is however not applicable for **B1** and **B2**, because $\bar{\epsilon}(\tilde{\nu})$ cannot be determined due to band superposition.

To relate the calculated τ_{EN} to the measured values the dynamic hopping processes in the multidimensional chromophores have to be considered. The symmetric HAB **B1** shall be discussed first. There, the six CT states have each a time dependent probability to be excited $P_i(t)$ ($i = 1-6$) that is based on the assumption that one CT state ($i = 1$) is initially excited, the energy can be transferred between neighbouring CT states with an uniform rate constant k_{EN} and each CT state can relax to the ground state with the fluorescence time constant τ_{fl} (see Figure 106).

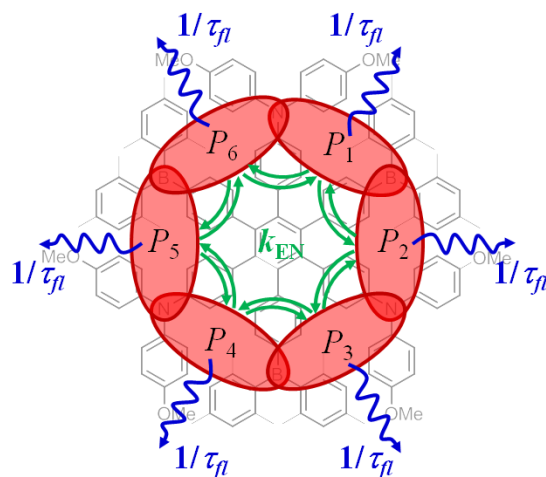


Figure 106 Energy transfer pathways in HAB **B1**.

The following Pauli master differential equations can be set up for each CT state (equation 77).

$$\begin{aligned} \frac{\partial P_1(t)}{\partial t} &= -\left(\frac{1}{\tau_{fl}} + 2k_{EN}\right)P_1 + k_{EN}P_2 + k_{EN}P_6 \\ \frac{\partial P_2(t)}{\partial t} &= -\left(\frac{1}{\tau_{fl}} + 2k_{EN}\right)P_2 + k_{EN}P_3 + k_{EN}P_1 \\ \frac{\partial P_3(t)}{\partial t} &= -\left(\frac{1}{\tau_{fl}} + 2k_{EN}\right)P_3 + k_{EN}P_4 + k_{EN}P_2 \\ \frac{\partial P_4(t)}{\partial t} &= -\left(\frac{1}{\tau_{fl}} + 2k_{EN}\right)P_4 + k_{EN}P_5 + k_{EN}P_3 \\ \frac{\partial P_5(t)}{\partial t} &= -\left(\frac{1}{\tau_{fl}} + 2k_{EN}\right)P_5 + k_{EN}P_6 + k_{EN}P_4 \\ \frac{\partial P_6(t)}{\partial t} &= -\left(\frac{1}{\tau_{fl}} + 2k_{EN}\right)P_6 + k_{EN}P_1 + k_{EN}P_5 \end{aligned} \quad (77)$$

This system of equations can be solved to derive terms for each probability $P_i(t)$ (equation 78)

$$\begin{aligned} P_1(t) &= \frac{P_1(0)}{6} e^{\frac{-t}{\tau_{fl}}} (1 + 2e^{-tk_{EN}} + 2e^{-3tk_{EN}} + e^{-4tk_{EN}}) \\ P_{2,6}(t) &= \frac{P_1(0)}{6} e^{\frac{-t}{\tau_{fl}}} (1 + e^{-tk_{EN}} - e^{-3tk_{EN}} - e^{-4tk_{EN}}) \end{aligned}$$

$$P_{3,5}(t) = \frac{P_1(0)}{6} e^{\frac{-t}{\tau_{fl}}} (1 - e^{-tk_{EN}} - e^{-3tk_{EN}} + e^{-4tk_{EN}})$$

$$P_4(t) = \frac{P_1(0)}{6} e^{\frac{-t}{\tau_{fl}}} (1 - 2e^{-tk_{EN}} + 2e^{-3tk_{EN}} - e^{-4tk_{EN}}) \quad (78)$$

The measured anisotropy $r(t)$ can then be obtained by summation of the anisotropy values of each CT state $r_i(t)$ ($i = 1 - 6$) weighted by the relative probability of each CT state being excited w_i (equation 59).

$$r(t) = \sum_{i=1}^6 r_i(t) w_i(t) \quad \text{with} \quad w_i(t) = \frac{P_i(t)}{\sum_{k=1}^6 P_k(t)} \quad (59)$$

If rotational diffusion is neglected the measured anisotropy is calculated to decay with equation 79

$$r(t) = 0.1 + 0.3e^{-3k_{EN}t} \quad (79)$$

Hence, in the case of the symmetric HAB **B1** the observed anisotropy decay time constant τ_{a1} ascribed to energy transfer is a third of the actual energy transfer time constant τ_{EN} between neighbouring CT states (equation 80).

$$\tau_{a1} = \frac{\tau_{EN}}{3} = \frac{1}{3k_{EN}} \quad (80)$$

In this consideration it was assumed that energy transfer between CT states being further apart is negligible in contrast to that between neighbouring chromophores. That is because the energy transfer rate constant decreases rapidly with the distance between the involved states (see equation 28). Furthermore, the derived anisotropy decay is only observable if the energy transfer ($\tau_{EN} \sim 3$ ps in **B1** and **B2**) is faster than the fluorescence lifetime ($\tau_{fl} \sim 60$ ns) and the rotational diffusion ($\tau_{a2} \sim 350-600$ ps), which is the case in all HABs. From equation 79 the anisotropy value of planar delocalisation is determined to be 0.1 for **B1**.

For the asymmetric HAB **B2** the set of Pauli Master differential equations is much more complex as the initial excitation of each CT state leads to a different system of equations. A detailed derivation of the time dependent anisotropy for **B2** is found appendix 4. With the same assumptions made for **B1** and following the same procedure in solving the differential equations, equation 81 can be obtained for the time dependent anisotropy of **B2**.

$$r(t) = 0.175 + 0.11e^{-k_{EN}t} + 0.115e^{-3k_{EN}t} \quad (81)$$

Consequently, two time constants are expected for the anisotropy decay of **B2** caused by energy transfer. However, as these time constants are of the same order of magnitude the observed single time constant may be the average of the calculated biexponential decay. It has to be noted that delocalisation of the CT states in **B2** leads to a limiting, calculated anisotropy of 0.175.

When considering equation 80, the calculated anisotropy time constants of **B1** and **B2** in PhCN have values of 14-26 ns. These are too long to be observed due to the faster rotational depolarisation ($\tau_{a2} \sim 350\text{-}600$ ps). Moreover, the fast anisotropy drop ($\tau_{a1} = 0.74\text{-}1.04$ ps) indicates that the energy transfer is present while the excited state relaxation processes take place. As the fluorescence energy shifts due to the solvent relaxation the overlap integral J becomes time dependent. An upper limit for J can be obtained by calculating the overlap integral for the steady state emission in cyclohexane, which should correspond to the emission spectrum in PhCN immediately after excitation (see Figure 100). Thus, overlap integrals are obtained which are by three orders of magnitude higher than those calculated for the steady state emission in PhCN (see Table 21). Consequently, the calculated resonance energy transfer time constants are likewise faster ($\tau_{\text{EN}}(\text{cyclohexane}) = 75\text{-}89$ ps). This corresponds to an anisotropy decay of 25 ps in **B1** and 30 ps in **B2** which still cannot explain the very fast anisotropy decays ($\tau_{a1} = 0.74\text{-}1.04$ ps) observed for the multidimensional HABs. There are two possible reasons that the Förster energy transfer theory cannot reproduce the measured energy transfer time constants. (i) The interchromophore distances in **B1** and **B2** ($r_{\text{DA}} = 6.279$ Å) are similar to the chromophore size (the centre-to-centre distance between neighbouring TAA and TAB moieties is 7.15 Å, obtained from DFT calculations of **B3**). As a result, the point-dipole approximation utilised by Förster is no more valid.^{4,72} In this case, improved electronic couplings can be obtained by calculating the interactions between the transition densities of the individual chromophores.^{65,73,74} Furthermore, for small interchromophore distances the dielectric screening is inaccurately described in equation 28. (ii) As the integral of the fluorescence intensity decreases with the solvent relaxation, see Figure 100, the same relationship might be speculated for the fluorescence transition moment. Förster describes the emission transition moment in equation 28 by the quantum yield, the fluorescence lifetime and the steady state emission energy of the donor state. All these values are obtained for the relaxed CT state of **B3** in PhCN and presumably underestimate the emission transition moment of the unrelaxed CT state involved in the energy transfer process. To approximate the transition moment of the unrelaxed CT, the before mentioned quantities should be determined in unpolar solvents (e.g. cyclohexane) as the solvent relaxation should be less distinct in an unpolar environment. However, the model compound **B3** showed complex, multiexponential decay characteristics in the range of the cyclohexane emission which rendered an analysis of the fluorescence lifetime and quantum yield in this solvent impossible. It is assumed that the complexed species of **B3** as well as products of decomposition emit in the wavelength range between 18200 – 25000 cm^{-1} (400 - 550 nm), which could be responsible for this obscure emission behavior. To conclude the energy transfer considerations, the Förster equation is presumably overestimating the energy transfer time constants in **B1** and **B2** because of the geometric

proximity of the individual CT states and as the charge transfer state adopts a rearrangement within the first 50 ps. However, as the anisotropy decay is much better described by Coulomb interactions compared to through bond interactions we assume the former to be the predominant mechanism of energy redistribution in **B1** and **B2**. It has to be noted that both the steady-state and the ultrafast fluorescence measurements prove energy transfer in **B1** and **B2**.

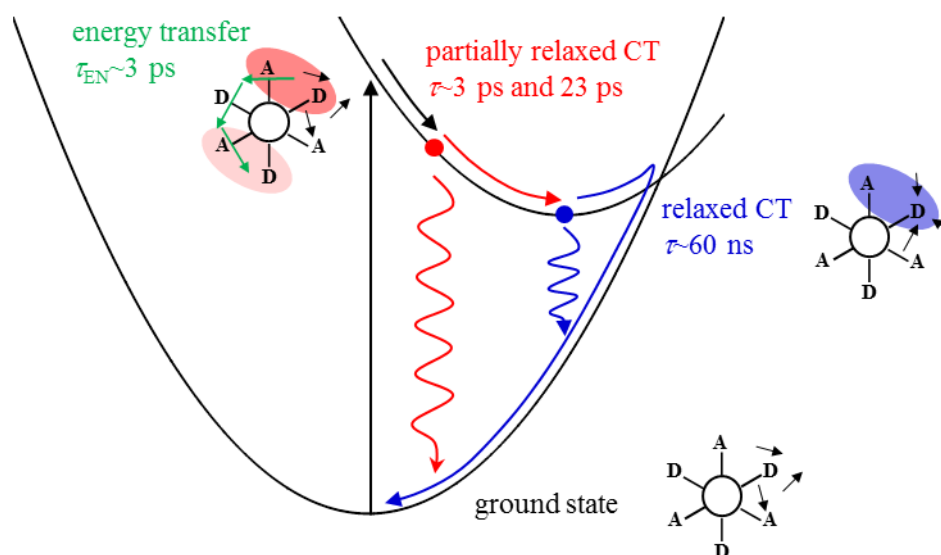


Figure 107 Potential energy diagram for the relaxation processes in the excited state of **1**. The molecule is sketched besides the relevant states, the small black arrows represent solvent molecules and the coloured ellipses highlight the spatial extent of the excited states.

The excited state processes of **B1** and **B2** in PhCN can be summarised as follows (see Figure 107). The first state observable is a localised, partially relaxed CT state because ultrafast relaxation processes (induced by e.g. inertial solvent motion) cannot be resolved by the used measurement setup. The energy of this partially relaxed CT state is redistributed within the multidimensional compounds **B1** and **B2** with energy transfer time constants of $\tau_{EN} \sim 2 - 3$ ps by a hopping mechanism. This might be due to strong Coulomb interactions between neighbouring partially relaxed CT states. The energy transfer process competes with the localisation of the excitation energy due to solvens dynamics. With two time constants of ~ 3 ps and ~ 23 ps for the reorientational motions of the PhCN molecules the excited state converts to the solvent stabilised, relaxed CT state. Due to the solvent relaxation a twisting motion of the aryl systems is presumably stimulated which reduces the electronic communication between donor and acceptor. This leads to a stronger charge localisation in the relaxed CT state. Moreover, the Coulomb coupling between the relaxed CT states is reduced so that the energy transfer is hampered. The competition of these two processes might be the reason that in case of **B1**

the anisotropy drops to a value of only 0.13 within the first picoseconds, whereas a value of 0.1 is expected for a complete energy delocalisation. Time constants for the hampered energy transfer of $\tau_{\text{EN,relaxed}} > 40$ ns were calculated by *Förster* energy transfer theory which are too slow to be observed by the presented anisotropy measurements. In addition, these calculated energy transfer time constants are so slow that it is in fact questionable if the energy can be redistributed between the relaxed CT states within the excited state lifetime of ~ 60 ns.

In the following the discrepancy in the energy transfer behavior of **B1** and **B2** in PhCN and **HAB-S** and **HAB-A** in DCM shall be addressed. Whereas in **B1** and **B2** energy transfer with a time constant of $\tau = 0.7\text{-}1.0$ ps in PhCN was observed, the excitation energy is not redistributed in **HAB-S** and **HAB-A** within the excited state lifetimes of ~ 4 ps in DCM. The discussion shall be restricted to Coulomb interactions as these are assumed to be responsible for the energy transfer in **B1** and **B2**. A precise comparison of these interactions is for two reasons difficult. (i) Due to the short excited state lifetimes and the absence of steady state fluorescence it is impossible to measure or calculate energy transfer rate constants for **HAB-S** and **HAB-A**. (ii) The discussion on energy transfer in **B1** and **B2** showed that the simple model of energy transfer derived by Förster is not able to describe the Coulomb interactions in **B1** and **B2** accurately. This might be due to the small interchromophore distances and ultrafast solvent relaxation processes. Nevertheless, the Coulomb interactions in **B1** and **HAB-S** shall be roughly compared by the Coulomb coupling elements between the respective CT states. In the case of **HAB-S** the calculations yield $V_{\text{EN}}^{\text{Coul}} = 20 \text{ cm}^{-1}$ (with $\mu_{\text{abs}} = 0.81 \text{ D}$, $\kappa = 1.75$ and $r_{\text{DA}} = 6.8 \text{ \AA}$) whereas for **B1** a Coulomb coupling of $V_{\text{EN}}^{\text{Coul}} = 40 \text{ cm}^{-1}$ was obtained (with $\mu_{\text{fl}} = 1.18 \text{ D}$, $\kappa = 1.75$ and $r_{\text{DA}} = 6.8 \text{ \AA}$). It has to be noted that for the calculation of the Coulomb coupling in **B1** the fluorescence transition moment was used, which was obtained by the *Strickler-Berg* relation. The absorption transition moment of the CT state in **B1** was not determinable due to band superposition. Although the values for $V_{\text{EN}}^{\text{Coul}}$ are very similar, the small deviation by a factor of 2 may be responsible for the observed energy transfer behaviours. That is because it is necessary to consider the solvent relaxation as a competing process. It has been shown that in the case of CT states the energy transfer rate is time dependent because the overlap integral $J(t)$ changes with the solvent relaxation process. Two limiting cases can be discussed. (i) If the solvent relaxation is faster than the energy transfer between the unrelaxed CT states, the excited state will first relax to the relaxed CT state and the energy transfer time constant between these relaxed states has to be considered (for **B1** calculated to be >40 ns). (ii) In the reversed case energy transfer between the unrelaxed CT states is observed in the time domain faster than solvent relaxation. It is evident that the choice of solvent is crucial in this consideration. Given that the energy transfer time constants in **B1** and **B2** in PhCN are in the range of solvent relaxation (intermediate case), it is very possible that the slightly smaller Coulomb coupling calculated for **HAB-S** leads to the first limiting case (i). That is, the energy transfer rate between the unrelaxed CT states in **HAB-S** and **HAB-A** is slower than the solvent relaxation processes in the less

viscous DCM. Consequently, the excited state in **HAB-S** and **HAB-A** would first relax to the relaxed CT state, which features an energy transfer time constant presumably much greater (> 1 ns) than the excited state lifetime of ~ 4 ps. This would explain the lack of energy transfer in **HAB-S** and **HAB-A**. To prove this theory, anisotropic transient absorption/fluorescence upconversion measurements should be performed for all HABs in solvents with varying viscosities.

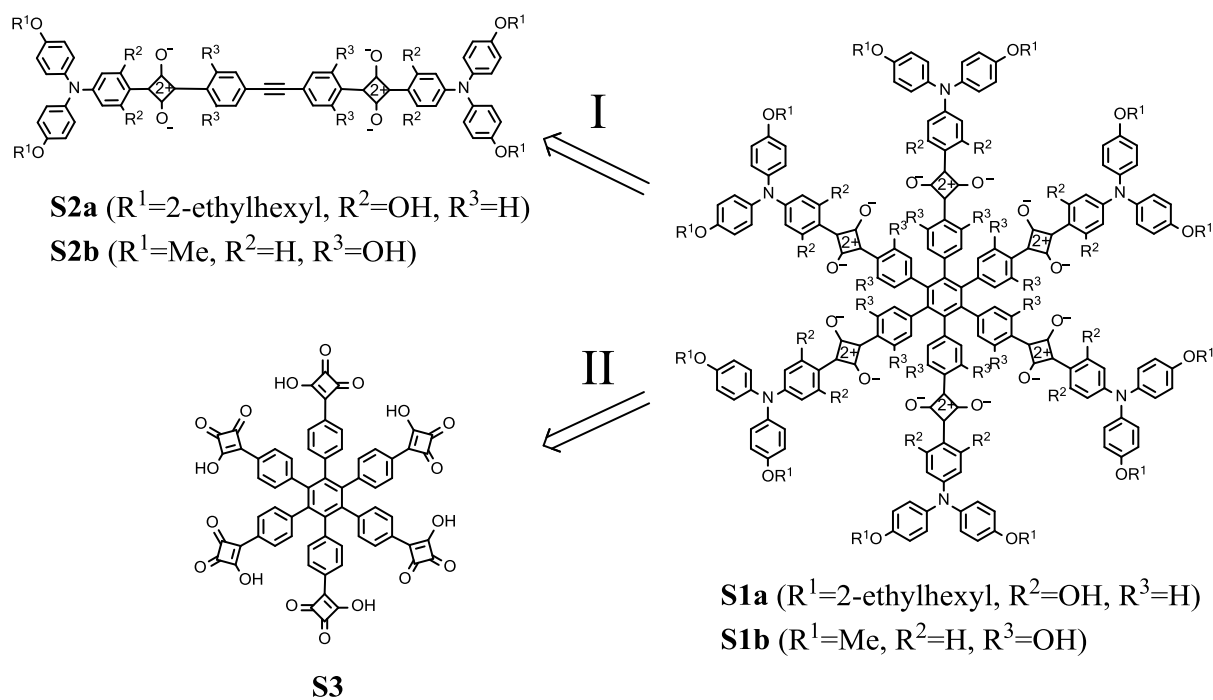
6. Hexaarylbenzene containing squaraine chromophores

6.1. Introduction

Due to the strong absorption characteristics in the near infrared region, squaraine dyes are used in organic photovoltaics,²⁶⁴⁻²⁶⁹ as photoconductors for xerographic devices,³⁶ in data imaging,²⁷⁰ in studies about nonlinear optics²⁷¹⁻²⁷⁵ and as sensors.²⁷⁶⁻²⁷⁹ Moreover, squaraine chromophores were incorporated into polymeric^{271,280} and multidimensional²⁸¹ structures to investigate excitonic interactions between the squaraines. In the case of **S1a/b** exciton theory shall be utilised to determine the interactions between neighbouring and further distant squaraine chromophores in the cyclic arrangement provided by the HAB framework.

6.2. Retrosynthetic analysis

From a retro synthetic point of view there are basically two pathways to obtain the symmetric HAB bearing six squaraine chromophores **S1a/b** (Figure 108). These pathways differ in the order the cyclotrimerisation reaction is performed. Pathway I describes the situation that first the tolan **S2a/b**, substituted with two squaraines, is synthesised and then the cyclotrimerisation reaction is carried out to yield **S1a/b**. $\text{Co}_2(\text{CO})_8$ is chosen as cyclotrimerisation catalysts as this kind of cobalt complex ranks among the most reactive catalysts for the cyclotrimerisation reaction.¹³⁹ In pathway II the HAB framework **S3** is at first synthesised by the cyclotrimerisation reaction and the squaraine chromophores are subsequently prepared by a sixfold condensation reaction. Although multiple reactions are often avoided in the last reaction step due to purification and yield issues, in this case it seems promising as a fourfold condensation reaction with reasonable yields of 20-35 % was reported by Gerold *et al.*²⁸¹

Figure 108 Retrosynthetic analysis of **S1a/b**.

Before going into more detail about pathway I, the basics of squaraine synthesis shall be discussed. In general, asymmetric squaraines are built up by two successive condensation reactions (Figure 109).²⁸² Thereby, di-*n*-butylestersquarate or squaric dichloride is used as starting material to guarantee a gradual reaction sequence. After reaction with the first nucleophile, in general an electron-rich aromatic compound, a semisquaric ester/chloride is obtained. Before the condensation with the second nucleophile can be executed, the ester/chloride has to be hydrolysed under acid or base catalysis.

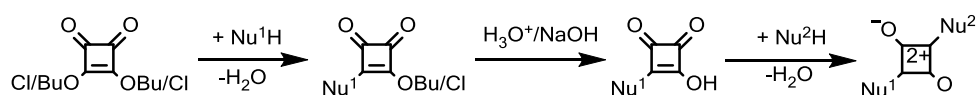


Figure 109 Synthesis of an asymmetric squaraine.

The first condensation reaction can be readily executed with a lithium organyle as nucleophile.²⁸³ The crucial point of the squaraine synthesis is the second condensation step. Thereby, the nucleophile has to be reactive enough to attack the more electron-rich semisquaric acid. This can be influenced by the order the nucleophiles are used. When regarding the synthesis of **S2a/b** (pathway I), the second nucleophile can accordingly be either the tolan spacer **S5** (pathway III) or the amine **S7** (pathway IV) (see Figure 110). The nucleophilicity of both molecules is strengthened by introducing hydroxyl groups into the reacting aryl unit.²⁶⁴ Moreover, the hydroxyl groups will improve thermal stability and guarantee structural rigidity.²⁶⁴ Pathway III is based on the synthesis of multiple squaraines by *Gerold et al*²⁸¹ and would provide squaraines with a more balanced electron distribution as two electron-rich moieties are vicinal to the electron poor four-ring-system. In contrast, the amine **S7** in pathway IV is

the undeniably better nucleophile but leads to squaraines with a strongly on-sided electron density. This might have an influence to the spectral properties of the synthesised squaraines.^{264,281} The respective semisquaric acids for the pathways III and IV are **S4** and **S6**, respectively.

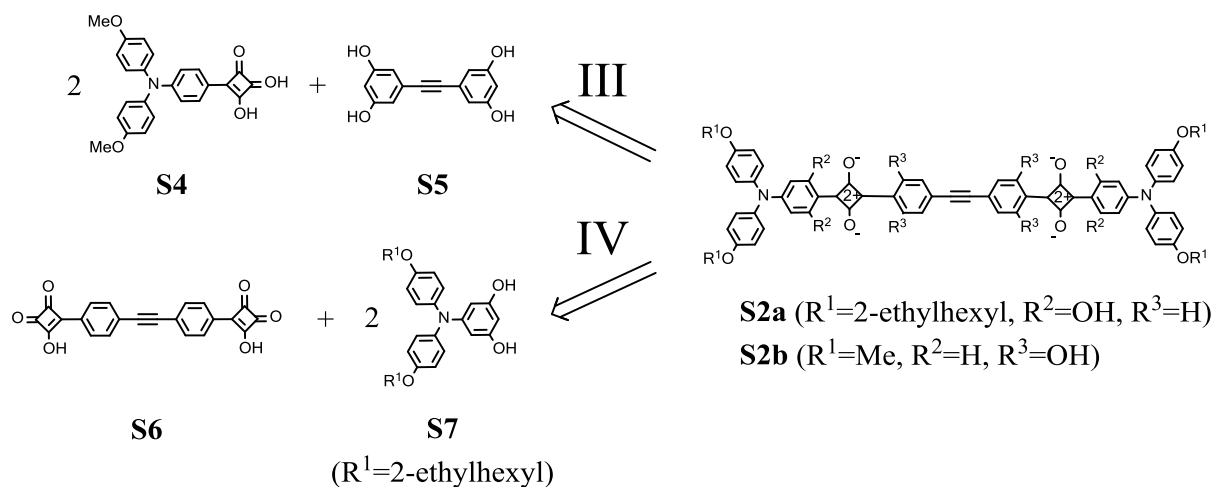


Figure 110 Retrosynthetic analysis of **S2a/b**.

The semisquaric esters **S8** and **S10** shall be synthesised from **S9** and **S11**, respectively, following the procedure of *Paquette et al.*²⁸⁴ To do so, **S9** and **S11** are converted to lithium organyles which in turn should readily attack di-*n*-butylestersquarate, as stated above (Figure 111). In the following **S8** and **S10** shall be hydrolysed under acidic conditions^{282,285} to yield **S4** and **S6**, respectively.

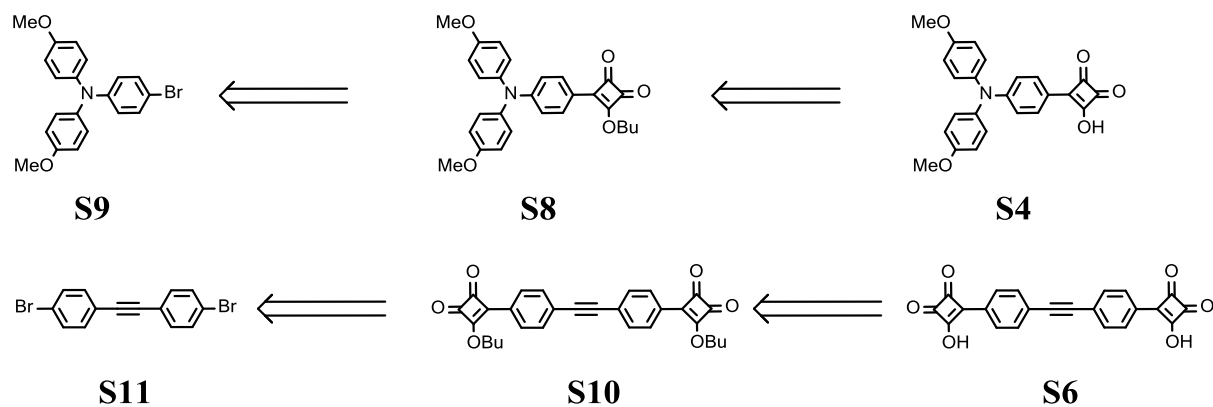


Figure 111 Retrosynthetic analysis of **S4** and **S6**.

In order to synthesise **S5** and **S7**, their hydroxyl groups need to be protected, because these might interfere with the coupling reactions involved in the synthesis of **S12** (shown elsewhere)²⁸⁶ and **S13** (see Figure 112).

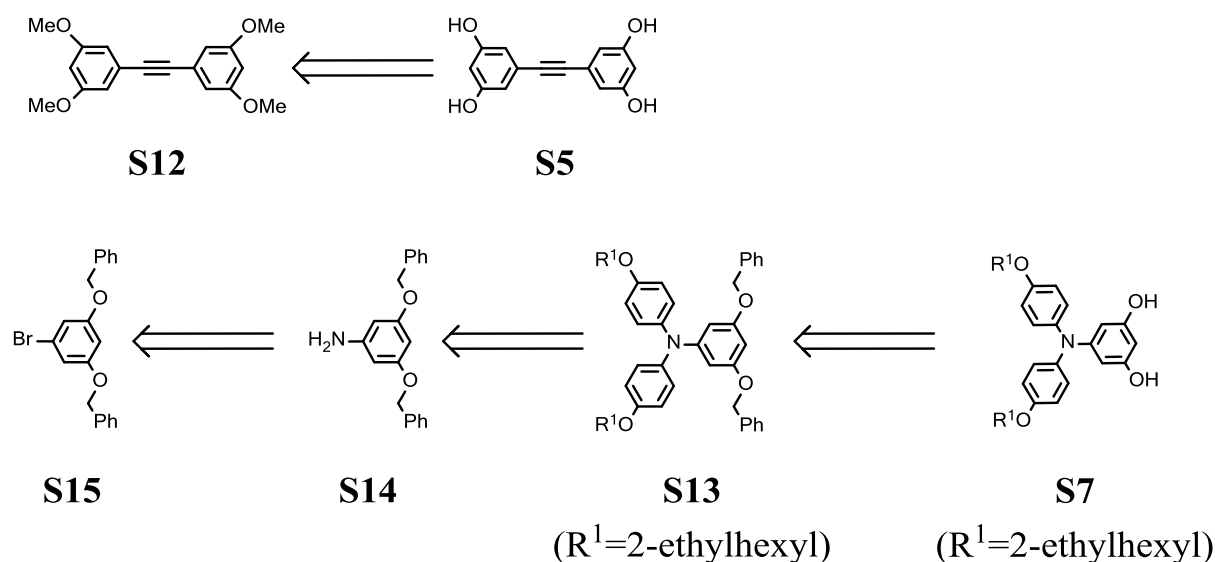


Figure 112 Retrosynthetic analysis of **S5** and **S7**.

In the case of **S5** a convenient protection strategy is to use methoxy ethers and then cleave the ether bond in **S12** with the strong Lewis acid BBr_3 at mild conditions according to the patent of *Docherty et al.*²⁸⁷ The protection of the aromatic alcohols in **S7** shall be realised by benzyl groups which can be removed by hydrogenation.²⁸⁸ This is to avoid BBr_3 , which would cleave all ether groups in the triarylamine **S13**. The latter shall be synthesised by two consecutive *Ullmann* coupling reactions of **S15**²⁸⁹ with ammonium hydroxide²⁹⁰ and **S14** with 1-(2-ethylhexyloxy)-4-iodobenzene.²⁸⁵

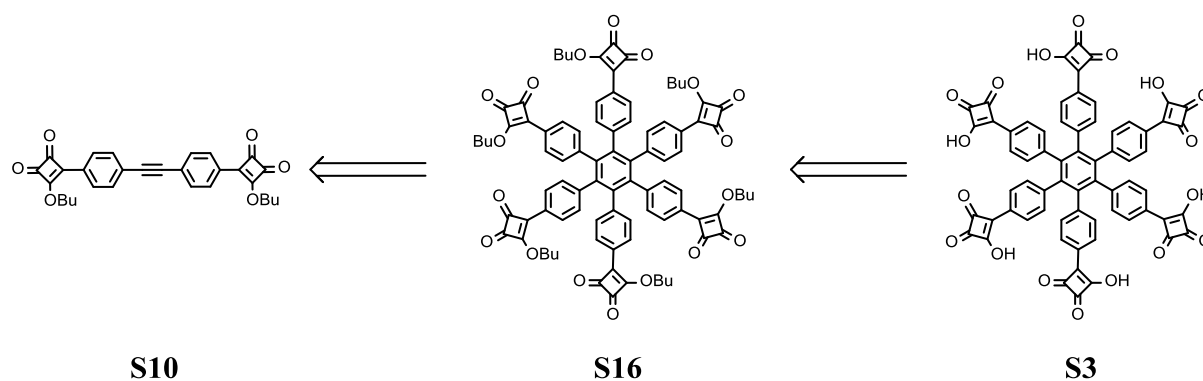


Figure 113 Retrosynthetic analysis of **S3**.

To realise pathway II (see Figure 113), HAB **S16** shall be synthesised by cyclotrimerisation of **S10** with $\text{Co}_2(\text{CO})_8$. Subsequently, **S17** shall be hydrolysed under acidic conditions to yield **S3**.

6.3. Synthesis

The attempts to synthesise **S1a/b** according to the retrosynthetic considerations are presented in the following. The approach is thereby structured by the different pathways.

6.3.1. Attempted synthesis of **S2b** (pathway III)

The starting material for the pathway III was **S12**, which could be synthesised as described elsewhere.²⁸⁶ The subsequent cleavage of the methyl ether groups (see Figure 114) was not achieved with the Lewis acid BBr_3 alone as described in ref.²⁸⁷ Only when dried Na_2CO_3 (freshly prepared by heating NaHCO_3 to 300°C in vacuo) was present during the reaction, **S5** was obtained with a yield of 62%.²⁹¹ The carbonate possibly scavenges HBr , which is formed when BBr_3 comes into contact with traces of moisture.

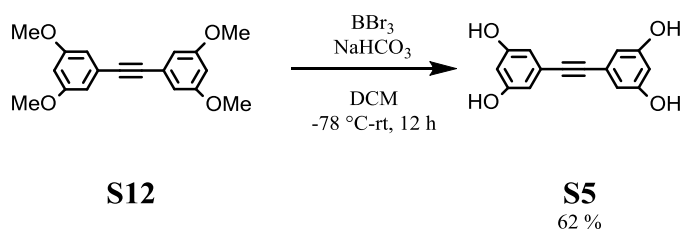


Figure 114 Synthesis of **S5**.

The semisquaric acid **S4** was prepared as shown in Figure 115. Lithiation of **S9**²⁸⁴ and the subsequent condensation reaction with di-*n*-butylsquarate gave **S8** with a yield of 40%. **S4** was obtained nearly quantitatively by acid catalysed hydrolysis of the semisquaric ester **S8**.

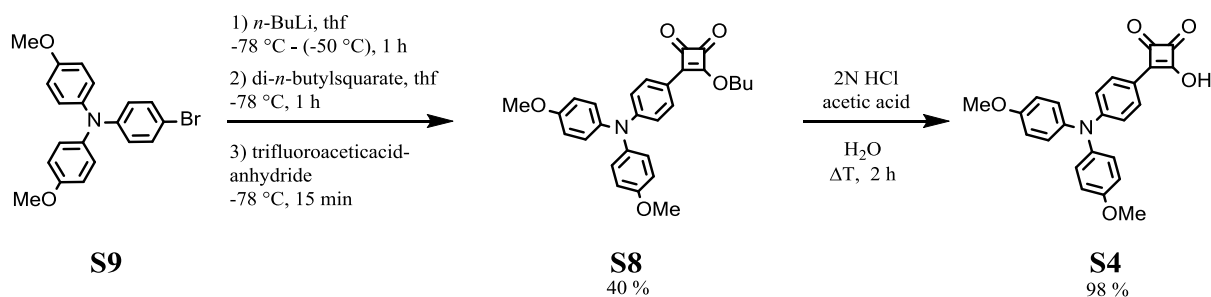


Figure 115. Synthesis of **S4**.

The squaraine **S2b** could however not be obtained by the reaction of the semisquaric acid **S4** with the electron rich tolan derivative **S5** (figure 116).

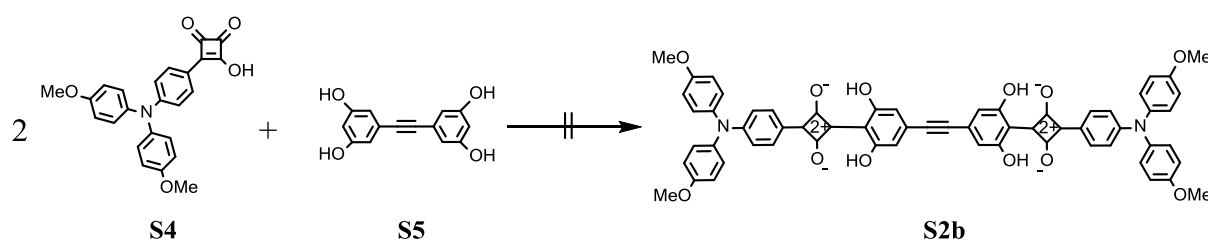


Figure 116 Attempted synthesis of **S2b**.

To identify possible reasons, the reaction progress was monitored by absorption spectroscopy (see Figure 117).

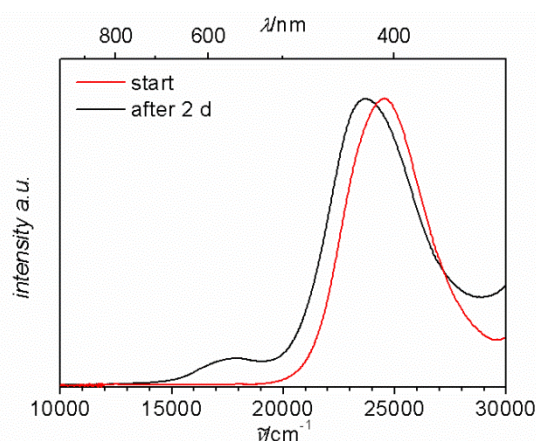


Figure 117. Absorption spectra of the reaction mixture synthesising **S2b** at the start of the reaction (red) and after 2 d (black).

The absorption band at 25500 cm^{-1} can be attributed to the semisquaraine **S4**. After stirring **S4** and **S5** in a *n*-butanol/toluene (1:3) mixture for 2 d at reflux the spectrum is nearly unchanged. Thereby, water was removed by azeotropic distillation using a Dean-Stark trap. A comparison to the absorption spectra of **S2a** and **S20**, a tolan substituted by only one squaraine, with absorption maxima at 16000 cm^{-1} and 17800 cm^{-1} , respectively, indicates that the low energy absorption band at 17800 cm^{-1} may be attributed to traces of a mono condensation product. Attempts to isolate this species chromatographically or by precipitating were however unsuccessful. The nucleophilicity of **S5** seems to be too poor to attack the semisquaraine **S4**. Consequently, attention was drawn to pathway IV where the much better nucleophile **S7** was synthesised.

6.3.2. Synthesis of **S2a** (pathway IV)

The triarylamine **S7** was obtained in three steps starting from **S15** (Figure 118). Firstly, the aromatic compound **S15**²⁹⁰ was aminated under copper catalysis with a yield of 64 %. The following *Ulmann* coupling with two equivalents of 1-(2-ethylhexyloxy)-4-iodobenzene gave **S13**. In the third step, the

two benzyl protection groups were removed by reduction with hydrogen in the presence of Pd/C to yield 84 % of **S7**.

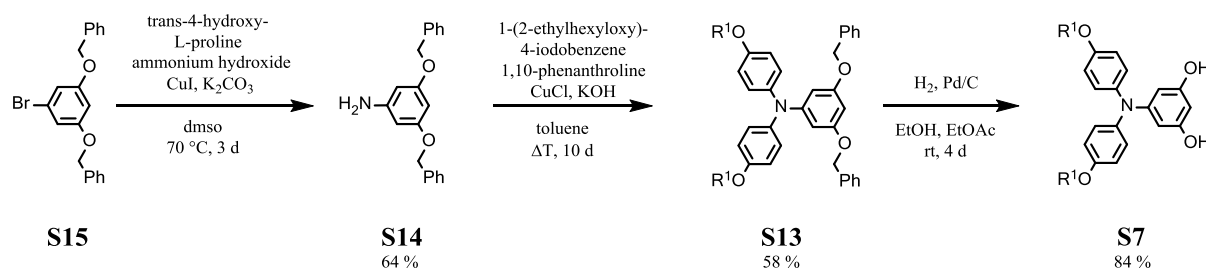


Figure 118 Synthesis of **S7**. $R^1 = 2$ -ethylhexyl.

The tolan derivative **S6** was synthesised using a similar procedure as described for **S4** (figure 119). That is the double lithiation of **S11**,²⁹² followed by the twofold condensation reaction with di-*n*-butylsquarate to yield **S10**. Hydrolysis to **S6** was executed nearly quantitatively under acidic conditions.

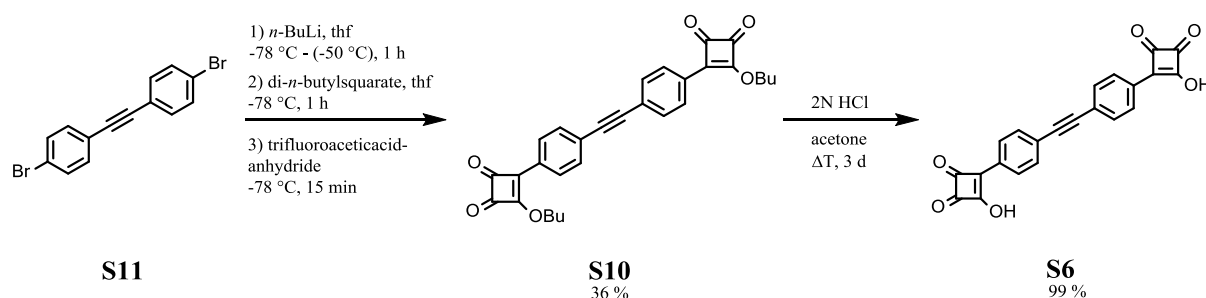


Figure 119 Synthesis of **S6**.

With the much better nucleophile **S7** the twofold condensations reaction with **S6** was successful (see Figure 120). Squaraine **S2a** was obtained in a yield of 51 %.

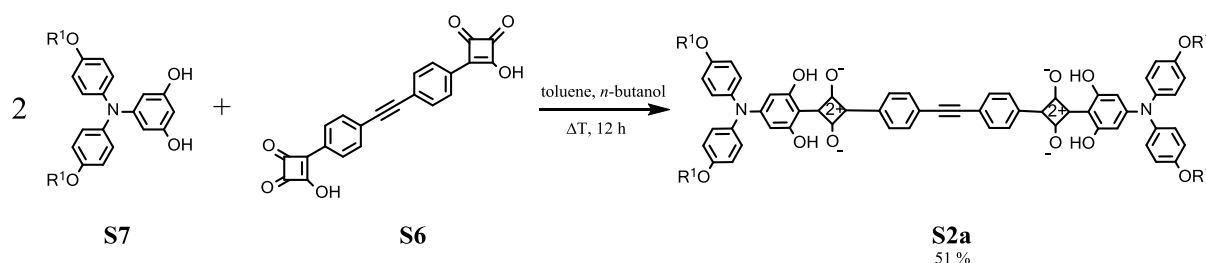


Figure 120. Synthesis of **S2a**. $R^1 = 2$ -ethylhexyl.

6.3.3. Attempted synthesis of S1a (pathway I)

The cyclotrimerisation of **S2a** was attempted with $\text{Co}_2(\text{CO})_8$ as catalyst in 1,4-dioxane (Figure 121). After several days stirring at reflux the tolan was completely consumed. However, **S1a** could not be evidenced by mass spectroscopy or NMR. As the solubility of **S2a** in 1,4-dioxane is poor, solubility issues possibly hamper the cyclotrimerisation by e.g. precipitation of insoluble intermediates. Therefore, the cyclotrimerisation was tested in several solvents. In chloroform at 61 °C and toluene at 100 °C no reaction could be observed so that the squaraine could be recovered in each case after 6 d reaction time. At last the cyclotrimerisation was performed in DCM in a sealed glass vessel, which was heated to 100 °C in a microwave oven (800 W). After 4 h neither reactant nor product could be identified in the reaction mixture. Although the exact reason why the trimerisation does not succeed is obscure, the following statements can be given. (i) The squaraine itself seems to be stable for several days at 100 °C in solution, when kept in the dark. (ii) The lack of cyclotrimerisation product in chloroform suggests that the cobalt catalyst is unreactive in this solvent. (iii) The reaction behavior in DCM and 1,4-dioxane cannot be comprehended. Both steric and energetic reasons do not argue against the cyclotrimerisation because the triple bond in **S2a** is not shielded by substituents of the linked benzene rings. Moreover, the cobalt catalyst should in general be able to convert both very electron-poor (e.g. **S10**, see below) or electron-rich²⁰ tolan derivatives to the respective substituted benzenes. It may however be possible that in the case of **S2a** the hydroxyl groups at the triaryl amines are not tolerated by the cobalt complex.

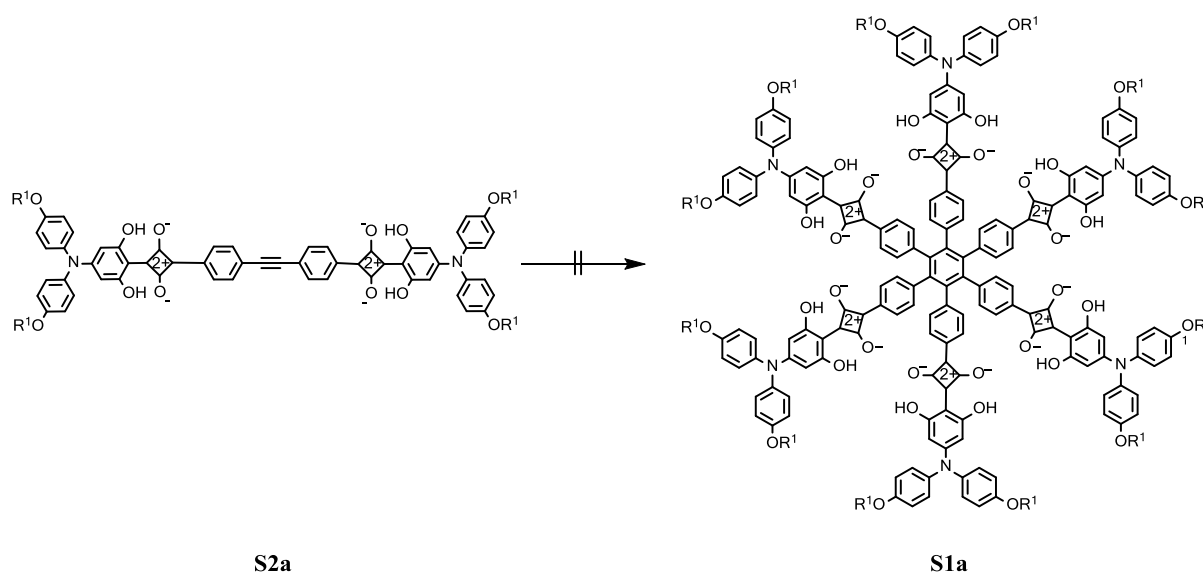


Figure 121 Attempted synthesis of **S1a**. $\text{R}^1 = 2\text{-ethylhexyl}$.

6.3.4. Attempted synthesis of S3 (pathway II)

As the cyclotrimerisation of **S2a** could not be achieved, the sequence of reactions was switched as stated for pathway II. Accordingly, the cyclotrimerisation of **S10** was tested (Figure 122). Thus, HAB **S16** was successfully synthesised when **S10** was stirred with $\text{Co}_2(\text{CO})_8$ in 1,4-dioxane for 6 d at reflux.

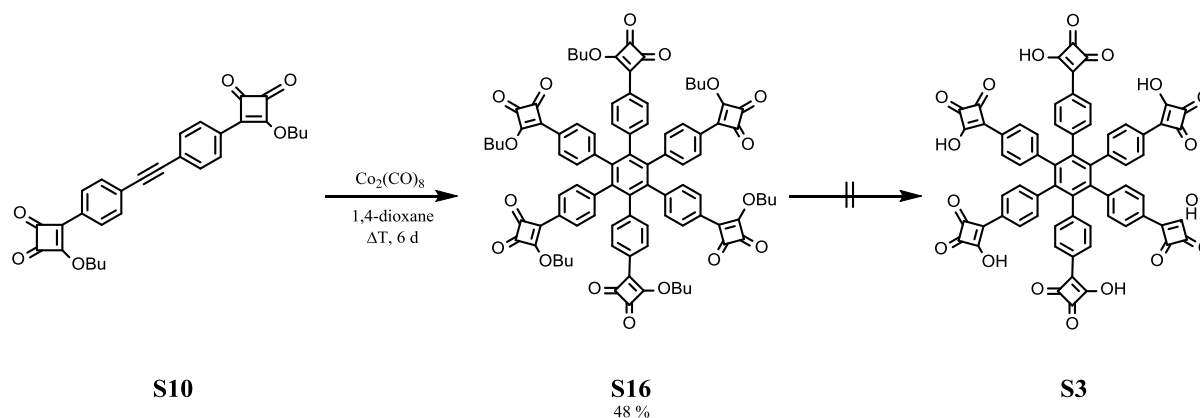


Figure 122 Attempted synthesis of **S3**.

The following sixfold hydrolysis to **S3** could not be realised. This reaction was performed either under acidic conditions with diluted HCl in acetone²⁸⁵ or 1,4-dioxane²⁹³ or under alkaline conditions with 40 % NaOH in ethanol.²⁹⁴ The obtained residue showed in all cases ambiguous, broad aromatic signals in the ¹H-NMR and moreover could not be identified by mass spectroscopy.

In conclusion, neither pathway I or II could lead to the desired HAB **S1a/b**. However, with **S2a** a dimeric squaraine dye could be synthesised, which was in the following analysed concerning energy transfer between the two containing chromophores.

6.3.5. Synthesis of model compound S20

For comparison reasons the tolan **S20** was synthesised with a similar framework compared to **S2a**, but featuring only one squaraine chromophore. The procedure resembles the synthetic approach to **S2a**, except that the starting material is the mono brominated tolan **S17** (Figure 123).

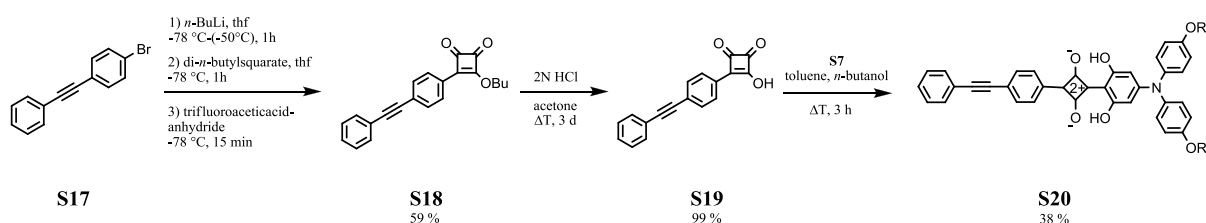


Figure 123 Synthesis of model compound **S20**. $\text{R}^1 = 2\text{-ethylhexyl}$.

As described before the semisquaric ester was obtained by lithiation of **S17** and the subsequent condensation reaction with di-*n*-butylsquarate. After hydrolysis of the ester **S18** to the semisquaric acid **S19**, the second condensation reaction was performed to yield of 38 % of **S20**.

6.4. Absorption spectroscopy

Absorption spectra were measured for the squaraine **S2a** and the respective model compound **S20** to investigate the EN interactions between the two squaraine chromophores in **S2a**. The respective spectra in toluene and DCM are given in Figure 124.

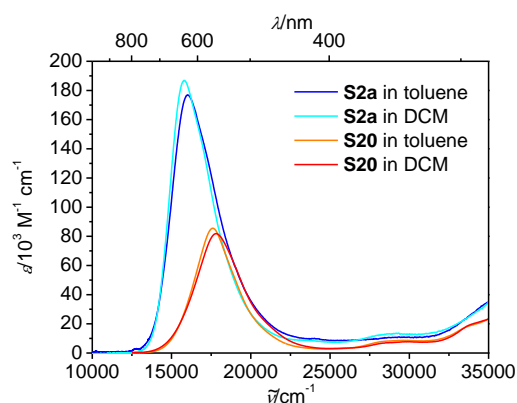


Figure 124 Absorption spectra of **S2a** and **S20** in toluene and DCM.

In all cases a broad, intense absorption band is observed at $\sim 16700 \text{ cm}^{-1}$, which is characteristic for squaraine dyes.^{264,281,285} For both compounds the absorption band in toluene is red-shifted by 200 cm^{-1} compared to DCM. The square of the transition moment of this absorption band in **S2a** ($\mu^2 = 302 \text{ D}^2$) is around twice as high as in **S20** ($\mu^2 = 131 \text{ D}^2$), resembling the number of squaraine chromophores per molecule. Moreover, the absorption band in **S2a** is shifted by 1800 cm^{-1} to lower energies. This indicates a strong Coulomb interaction between the two squaraine subchromophores, whose transition moments are presumably positioned “in line”. For this situation a red-shift is expected by theory (see EN theory section). The coupling strength can be calculated using the point-dipole approximation (equation 25).

$$V_{\text{EN}}^{\text{Coul}} = \frac{\kappa \mu_{\text{C1}} \mu_{\text{C2}}}{r^3} \quad (25)$$

$$\text{with } \kappa = (\mathbf{e}_{\text{C1}} \mathbf{e}_{\text{C2}}) - 3(\mathbf{e}_{\text{C1}} \mathbf{e}_{\text{C1C2}})(\mathbf{e}_{\text{C2}} \mathbf{e}_{\text{C1C2}})$$

where r is estimated by the distance between the squaraine cores ($\sim 14.7 \text{ \AA}$ was obtained from MM2 optimised structures).²⁹⁵ The orientation factor was determined to be 2 for the “in-line” configuration of the respective transition moments ($\mu_{\text{C1}} = \mu_{\text{C2}} = 11.4 \text{ D}$). Accordingly, a strong Coulomb coupling of $V_{\text{EN}}^{\text{Coul}} = 410 \text{ cm}^{-1}$ is obtained. The Coupling strength can be furthermore estimated from experiment, as

the energy difference between the absorption maxima of monomer and dimer equals $2V_{\text{EN}}^{\text{exp}}$. The experimentally obtained value ($V_{\text{EN}}^{\text{exp}} = 900 \text{ cm}^{-1}$) is around two times higher as the calculated one. This discrepancy cannot be solely explained by the inaccuracy of determining r . The charge transfer characterisation of **Star** and **StarModel** indicates that the tolan bridging unit may provide a considerable electronic communication between the linked chromophores. It is thus entirely possible that the “through bond” energy transfer contributes to the coupling of the squaraines in **S2a**.

A further investigation of the optical properties of **S2a** and **S20** was not possible, as steady state fluorescence was not observed. Moreover, the presented squaraines were not photo stable when irradiated with laser light. Spectroelectrochemistry could not be measured as all observed oxidation and reduction processes were irreversible.

7. Summary*

The focus of this work was the investigation of energy transfer between charge transfer states. For this purpose the multidimensional chromophores **HAB-S**, **HAB-A**, **B1** and **B2** were synthesised, each consisting of three electron donor and three electron acceptor redox centres linked symmetrically or asymmetrically by the hexaarylbenzene framework. Triarylamines represent in all these compounds the electron donors, whereas the electron poor centres were triarylboranes in **B1** and **B2** and PCTM centres in **HAB-S** and **HAB-A**, respectively. The hexaarylbenzenes were obtained by cobalt catalysed cyclotrimerisation of the respective tolan precursors. In addition, **Star** was synthesised, which consists of a central PCTM linked to three triarylamin centres by tolan bridging units in a star-like configuration. The hexaarylbenzene **S1a/b** substituted with six squaraine chromophores could not be realised. It is assumed that the cyclotrimerisation catalyst $\text{Co}_2(\text{CO})_8$ does not tolerate the essential hydroxyl groups in the tolan precursor **S2a**. The alternative reaction pathway to execute the cyclotrimerisation reaction first and introduce the hydroxyl groups thereafter failed as well, because the required hexaarylbenzene substituted by six semisquaric acid moieties could not be synthesised. However, energy transfer interactions could be investigated in the tolan precursor **S2a** with two squaraine units to obtain information about the electronic coupling provided by the tolan bridge. For all multidimensional compounds model molecules were synthesised with only a single donor-acceptor pair (**B3**, **Star-Model** and **HAB-Model**). This allows a separate consideration of energy and charge transfer processes. It has to be stressed that in all before mentioned multidimensional compounds the “through bond” energy transfer interaction between neighbouring IV-CT states is identical to a transfer of a single electron between two redox centres of the same kind (e.g. $\text{TAA} \rightarrow \text{TAA}^+$). The latter can be analysed by electron transfer theory. This situation is observed when the two IV-CT states transferring energy share one redox centre.

All compounds containing PCTM centres were characterised by paramagnetic resonance spectroscopy. Thereby, a weak interaction between the three PCTM units in **HAB-S** and **HAB-A** was observed. In addition, when oxidising **Star-Model**, a strongly interacting singlet or triplet state was obtained. In contrast, signals corresponding to a weakly interacting biradical were obtained for **HAB-Model**⁺. This indicates a strong electronic coupling between the redox centres provided by the tolan bridge and a weak coupling when linked by the hexaarylbenzene. This trend is supported by UV/Vis/NIR absorption measurements. The analysis of the observed IV-CT absorption bands by electron transfer theory reveals a weak electronic coupling of $V = 340 \text{ cm}^{-1}$ in **HAB-Model** and a distinctly stronger coupling of $V = 1190\text{-}2900 \text{ cm}^{-1}$ in **Star-Model**. In the oxidised **HAB-S**⁺, **Star**⁺ and **Star-Model**⁺ a

*Parts of this section have already been published in M. Steeger, S. Griesbeck, A. Schmiedel, M. Holzapfel, I. Krummenacher, C. Lambert and H. Braunschweig, *Phys. Chem. Chem. Phys.*, **2015**, submitted and M. Steeger and C. Lambert, *Chem. Eur. J.*, **2012**, *18*, 11937-11948.

charge transfer reversed from that of the neutral species, that is, from the PCTM radical to the electron poorer cationic TAA centre, was observed by spectroelectrochemistry. The temporal evolution of the excited states was monitored by ultrafast transient absorption measurements. Within the first picosecond stabilisation of the charge transfer state was observed, induced by solvent rotation. Anisotropic transient absorption measurements revealed that within the lifetime of the excited state ($\tau = 1-4$ ps) energy transfer does not occur in the HABs whereas in the star-like system ultrafast and possibly coherent energy redistribution is observed. Taken this information together the identity between energy transfer and electron transfer in the specific systems were made apparent. It has to be remarked that neither energy transfer nor charge transfer theory can account for the very fast energy transfer in **Star**.

The electrochemical and photophysical properties of **B1** and **B2** were investigated by cyclic voltammetry, absorption and fluorescence measurements and were compared to **B3** with only one neighbouring donor-acceptor pair. For the asymmetric **B2** CV measurements show three oxidations as well as three reduction peaks whose peak separation is greatly influenced by the conducting salt due to ion-pairing and shielding effects. Consequently, peak separations cannot be interpreted in terms of electronic couplings in the generated mixed valence species. Transient absorption, fluorescence solvatochromism and absorption spectra show that charge transfer states from the amine to the boron centres are generated after optical excitation. The electronic donor-acceptor interaction is weak though as the charge transfer has to occur predominantly through space. The electronic coupling could not be quantified as the CT absorption band is superimposed by $\pi-\pi^*$ transitions localised at the amine and borane centres. However, this trend is in good agreement to the weak coupling measured for **HAB-Model**. Both transient absorption and fluorescence upconversion measurements indicate an ultrafast stabilisation of the charge transfer state in **B1- B3** similar to the corresponding observations in **HAB-S** and **Star**. Moreover, the excitation energy of the localised excited charge transfer states can be redistributed between the aryl substituents of these multidimensional chromophores within fluorescence lifetime (ca. 60 ns). This was proved by steady state fluorescence anisotropy measurements, which further indicate a symmetry breaking in the superficially symmetric HAB. Anisotropic fluorescence upconversion measurements confirm this finding and reveal a time constant of $\tau_{EN} = 2-3$ ps for the energy transfer in **B1** and **B2**. It has to be stressed that, although the geometric structures of **B1** and **HAB-S** are both based on the same framework and furthermore the neighbouring CT states show in both cases similar Coulomb couplings and negligible “through bond” couplings, very fast energy transfer is observed in **B1** whereas in **HAB-S** the energy is not redistributed within the excited state lifetime. To explain this, it has to be kept in mind that the energy transfer and the relaxation of the CT state are competing processes. The latter is influenced moreover by the solvent viscosity. Hence, it is assumed that this discrepancy in energy transfer behaviour is caused by monitoring the excited state in solvents of varying viscosity. Adding fluoride ions causes the boron centres to lose their acceptor ability due to complexation. Consequently, the charge transfer character

in the donor-acceptor chromophores vanishes which could be observed in both the absorption and fluorescence spectra. However, the fluoride sensor ability of the boron centre is influenced strongly by the moisture content of the solvent possibly due to hydrogen bonding of water to the fluoride anions.

UV/Vis/NIR absorption measurements of **S2a** show a red-shift by 1800 cm^{-1} of the characteristic squarain band compared to the model compound **S20**. From exciton theory a Coulomb coupling of $V_{\text{EN}}^{\text{Coul}} = 410\text{ cm}^{-1}$ is calculated which cannot account for this strong spectral shift. Consequently, “through-bond” interactions have to contribute to the strong communication between the two squaraine chromophores in **S2a**. This is in accordance with the strong charge transfer coupling calculated for the tolan spacer in **Star-Model**.

8. Experimental section*

8.1. Methods

NMR

- Bruker Avance 400 FT-Spectrometer (^1H : 400.1 MHz, ^{13}C : 100.6 MHz)
- Bruker 600 DMX FT (^1H : 600.1 MHz, ^{13}C : 150.9 MHz)

When no temperature is explicitly given, the spectra were measured at rt. The chemical shift δ is given in ppm relative to tetramethylsilane (TMS) as internal standard. The coupling constants J are given in Hertz [Hz]. The multiplicity is abbreviated by s (singlet), d (doublet), t (triplet) and m (multiplet). The data is displayed in the following order: chemical shift (multiplicity, coupling constant, number of nuclei, assignment).

For molecules, which are based on the HAB framework and contain unradicalised PCTM units complex NMR spectra were obtained. This may be due to stereoisomers. As a result an assignment of peaks or integrals was not possible in these cases.

The analysis of NMR spectra of the synthesised radicals was not possible due to paramagnetic line broadening, so that in these cases only mass spectra are given.

Mass Spectrometry

- Bruker Daltonik micrOTOF focus (ESI)
- Finnigan MAT 90 (EI)
- Bruker Daltonics autoflex II (MALDI)

For compounds containing many chlorine atoms the mass signals were distributed over a broad m/z region so that the signal to noise ratio of the monoisotopic signal was too low for an accurate mass measurement. In these cases the most intensive signals ($X + n$) of the isotropic distribution were checked against values calculated with the software module “Bruker Daltonics IsotopePattern” of the software Compass 1.1 (Bruker Daltonik GmbH, Bremen, Germany).

*Parts of this section have already been published in M. Steeger, S. Griesbeck, A. Schmiedel, M. Holzapfel, I. Krummenacher, C. Lambert and H. Braunschweig, *Phys. Chem. Chem. Phys.*, **2015**, submitted and M. Steeger and C. Lambert, *Chem. Eur. J.*, **2012**, *18*, 11937-11948.

Electrochemistry

- GAMRY INSTRUMENTS potentiostat/galvanostat/ZRA model REFERENCE 600
- BAS CW-50W

The measurements were carried out under an argon atmosphere in a flame-dried cell with the standard three electrode setup. A platinum wire served as counter electrode, an Ag/AgCl “leak free” electrode (Innovative Instruments, Inc. Tampa, USA) as reference electrode or a platinum wire as pseudo reference electrode and a glass-sealed platinum wire of 1 mm diameter as working electrode. The ferrocene/ferrocenium redox couple served as an internal standard. The electrochemical cell was furthermore equipped with a column filled with aluminiumoxide (dried in vacuo at 300 °C for 30 min) which allowed in-situ drying of the solvent/solute/electrolyte mixture. DCM was dried over calcium hydride and distilled prior usage. THF was dried over Na and freshly distilled prior usage. The samples were measured at a concentration of $3 \cdot 10^{-4}$ - $1 \cdot 10^{-3}$ M. $[\text{Bu}_4\text{N}][\text{B}(\text{C}_6\text{F}_5)_4]$ was prepared according to a literature procedure²⁹⁶ from $\text{Li}[\text{B}(\text{C}_6\text{F}_5)_4]$ ²⁹⁷ and recovered by recrystallisation in hexane/DCM after usage. $[\text{Bu}_4\text{N}][\text{PF}_6]$ was prepared according to a literature procedure.²⁹⁸

UV/Vis/NIR absorption

- JASCO V-570
- JASCO V-670 UV/Vis/NIR

Absorption spectra were measured in 1 cm quartz cuvettes. All solvents were obtained in spectroscopic grade and used without further purification.

Spectroelectrochemistry

- EG & G Princeton Applied Research Model 283 potentiostat
- JASCO V670 spectrometer

Spectroelectrochemistry measurements were performed in a cylindrical quartz cell with a three electrode setup consisting of a platinum disc working electrode with a diameter of 6 mm, a gold-coated metal plate counter electrode and an Ag/AgCl pseudo reference electrode. The working electrode was positioned 100 μm above the quartz cell bottom by an μm -screw so that the adjusted thin-layer is completely electrolysed during the measurement. The light beam was directed through the optically transparent bottom of the quartz cell and the thin-layer and reflected at the working electrode. The oxidation or reduction process was assumed to be finished when no further change in the spectrum was observed by varying the voltage. The extinction coefficients of the oxidised and reduced species were determined by comparison to the neutral starting compound.

Steady state fluorescence spectroscopy

- PTI (Photon Technology International) QM-2000-4 fluorescence spectrometer with a cooled photomultiplier (R928 P).

All solvents were of spectroscopic grade and used as received. The samples ($\sim 10^{-6}$ M) were measured in 1 cm quartz cuvettes and freed of oxygen by degassing with argon for 5 min prior to use. Equation 82 was used to determine the fluorescence quantum yield (I_f , OD and n denote the intensity of the fluorescence, the optical density of the solution at the excitation wavelength and the refractive index of the solvent, respectively).

$$\Phi_f = \Phi_{f, \text{ref}} \left(\frac{\int I_f(\tilde{\nu})}{\int I_f(\tilde{\nu})_{\text{ref}}} \cdot \frac{OD_{\text{ref}}}{OD} \cdot \frac{n^2}{n_{\text{ref}}^2} \right) \quad (82)$$

A solution of chininsulfate in 1 N sulfuric acid with a quantum yield of 0.546 was used as the reference.²⁹⁹

Polarised steady-state fluorescence spectroscopy

- PTI (Photon Technology International) QM-2000-4
- Glan-Thompson polarisers (PTI)

The analyte was embedded in a sucrose octaacetate (SOA) matrix. SOA (Acros Organics) was recrystallised from ethanol prior usage. The sample was prepared as reported in literature.³⁰⁰ A Solution of SOA and the chromophore in DCM (Merck, Uvasol) was filtered through a syringe PTFE filter with 0.1 μm pore size (Whatman) in order to remove any traces of lints and dust and degassed with argon for 10 min. The solution was concentrated in vacuo until a viscous oil was obtained and then filled into a 1 cm fluorescence quartz cuvette. To remove the remaining DCM the cuvette was heated in an oven to 100°C for about 1 h and to 130°C for 4 h. The excitation anisotropy measurements were recorded at 21200 cm^{-1} (472 nm) emission energy.

Fluoride titration

Fluorescence and UV/Vis fluoride titration measurements were performed with the steady-state spectrometers mentioned above. Tetra-*n*-butylammonium fluoride was purchased from Sigma-Aldrich and used as received. THF was either dried over Na and freshly distilled before use or obtained from Acros in spectroscopic grade with a water content of ≤ 0.03 % and used without further purification. The samples were measured in 1 cm quartz cuvettes at concentrations of $\sim 5 \cdot 10^{-7}$ M (fluorescence measurements) and $1\text{--}4 \cdot 10^{-5}$ M (UV/Vis measurements) and the TBAF added in portions of 10-20 μl with concentrations of $1\text{--}3 \cdot 10^{-4}$ M and $0.6\text{--}1 \cdot 10^{-3}$ M, respectively. The fluorescence spectra were

normalised by the OD at the excitation wavelength of 29400 cm⁻¹ prior to fitting. For measurements under inert gas conditions the cuvettes were filled under an argon atmosphere and sealed by septa. The HypSpec software package, which is part of the Hyperquad suite,²⁵⁶ was used to fit the titration curves.

ns-Transient Absorption spectroscopy

- Edinburgh LP 920 Laser Flash
- Continuum Minilite II Nd:YAG laser
- pulsed Xe flash lamp

All solvents were obtained in spectroscopic grade and used as received. The instrument response function (IRF) of the setup is ca. 8 ns and was obtained by measuring the laser pulse scattered with an empty quartz cell. The decay curves were deconvoluted with the measured IRF and the quality of the fit was evaluated by the residuals and the χ^2 values.

Fluorescence lifetime measurements:

- Edinburgh LP 920 Laser Flash
- Continuum Minilite II Nd:YAG laser

The fluorescence lifetimes were determined in the same manner as in the transient absorption measurements.

Ultrafast transient absorption and fluorescence upconversion

The setups are described in section 1.3.4

EPR

- Bruker ELEXSYS E580 CW/FT

EPR measurements at X-band (9.8 GHz) were carried out at room temperature. Typical experimental conditions for the acquisition of CW EPR spectra were as follows: 0.6 mW microwave power, 0.1 G field modulation, 100 kHz modulation frequency. Low temperature experiments were conducted in a liquid-flow He cryostat (Oxford ESR900) and a mercury iTC controller. The spectral simulations were performed using MATLAB 8.2 and the EasySpin 4.5.3 toolbox.³⁰¹

Structure optimisations

- Gaussian09RevD.01.³⁰²

A global hybrid functional with an exact-exchange admixture of 30% and an SVP basis was used for all atoms.¹⁶⁴ Solvent effects of DCM have been taken into account by a continuum solvent model (CPCM). The excitation energies, transition moments and excited state dipole moments were

calculated by linear-response time-dependent density functional theory (TDDFT) using the same custom hybrids and SVP basis sets.

Differential Scanning Calorimetry

- TA Q1000 calorimeter

DSC measurements were recorded with a heating/cooling rate of 30°C min⁻¹. Two heating-cooling cycles were conducted.

Gel permeation chromatography (GPC)

Shimadzu GPC System

- Model SPD-M20A diode array detector
- CBM-20A system controller
- LC-20AD solvent delivery unit
- DGU 20A9 online degasser

Two preparative columns from PSS (SDV 50 Å and 500 Å, dimension 20 x 600 mm, particle size 10 µm) were used in recycling mode.

Melting points

- Tottoli melting point apparatus (Büchi)

All melting points are uncorrected.

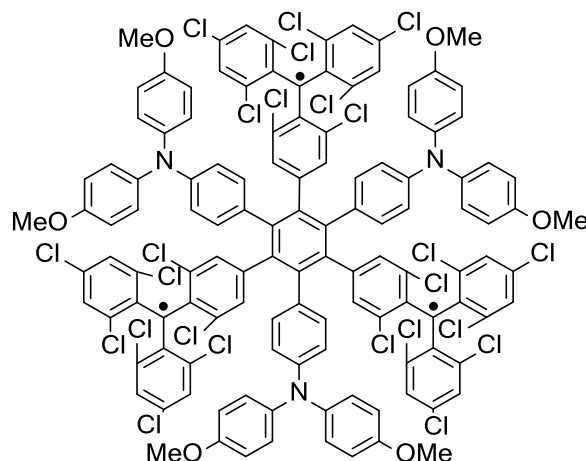
8.2. Synthesis

All reagents were purchased from commercial suppliers in standard quality and used as received. Reactions under a nitrogen-atmosphere were carried out in flame-dried Schlenk vessels and the solvents were dried according to common literature procedures.³⁰³ Silica gel (32-63 µm) was obtained from Merck (32-63 µm) or Acros Organics(35-70 µm). The precursors *N*-[4-(4-bromophenyl)ethynylphenyl]-*N,N*-di(4-methoxyphenyl)amine³³, *N,N*-Di(4-methoxyphenyl)-*N*(4-(ethynyl)phenyl)amine¹⁹, **S12**²⁸⁶ and **S15**²⁹⁰ were synthesised according to a literature procedure.

General Procedure (GP): Radicalisation of polychlorotriphenylmethanes: Under a nitrogen atmosphere the polychlorotriphenylmethane was dissolved in absolute THF (10 ml) and degassed. TBAOH (1 M solution in water, 2.33 equiv per reaction centre) was added and the dark blue mixture stirred at rt under exclusion of light for 3 d. Thereafter *p*-chloranil (5.50 equiv per reaction centre) was added and the now brown solution was stirred under exclusion of light at rt for further 3 d. The reaction mixture was poured in 2 N HCl (50 ml) and extracted with CHCl₃ (30 ml). The organic phase

was dried over MgSO_4 and the solvent removed in vacuo. The crude product was purified by gel permeation chromatography (Chloroform).

Synthesis of HAB-S



HAB-S was synthesised according to GP from **P7** (45 mg, 18 μmol).

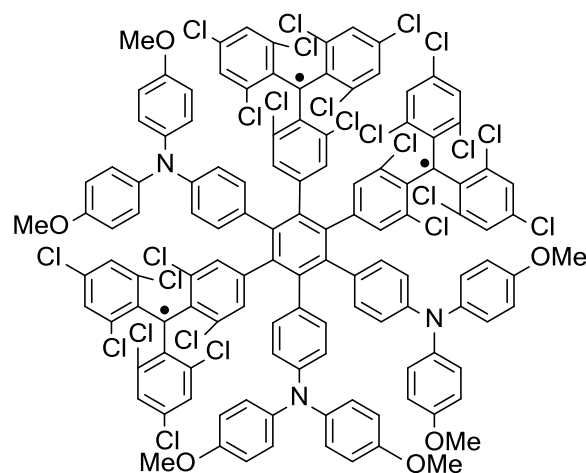
Yield: 18 mg (7.2 μmol , 40 %) of a brown solid

$\text{C}_{123}\text{H}_{72}\text{Cl}_{24}\text{N}_3\text{O}_6$ [2538.776]

SWV measurements proved a degree of radicalisation of 95 %.

HRMS (ESI): $[\text{M}^+ + 10]$ calc.: 2537.78172 m/z , found: 2537.78130 m/z , $\Delta = 0.17$ ppm.

Synthesis of HAB-A



HAB-A was synthesised according to GP from **P8** (40 mg, 16 μmol).

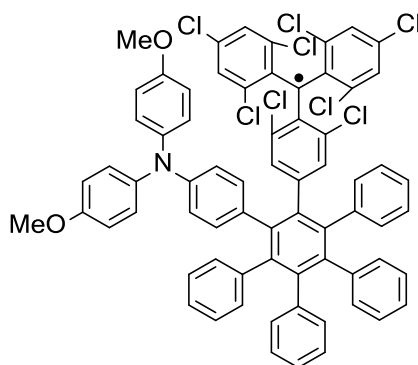
Yield: 31 mg (13 μmol , 78 %) of a brown solid

$C_{123}H_{72}Cl_{12}N_3O_6$ [2538.776]

SWV measurements proved a degree of radicalisation of 95 %.

HRMS (ESI): [$M^+ + 10$] calc.: 2537.78172 m/z , found: 2537.77993 m/z , $\Delta = 0.71$ ppm.

Synthesis of HAB-Model



HAB-Model was synthesised according to GP from **P9** (60 mg, 50 μ mol).

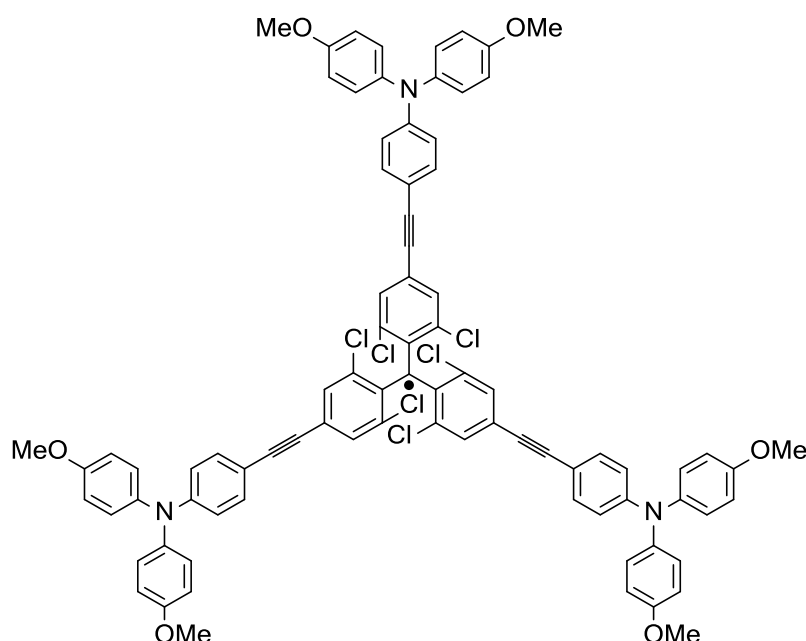
Yield: 33 mg (28 μ mol, 55 %) of a brown solid

$C_{69}H_{44}Cl_8NO_2$ [1202.717]

SWV measurements proved a degree of radicalisation of 99 %.

HRMS (ESI): [M^+] calc.: 1198.08748 m/z , found: 1198.08850 m/z , $\Delta = 0.85$ ppm.

Synthesis of Star



Star was synthesised according to GP from **P10** (36 mg, 25 μmol).

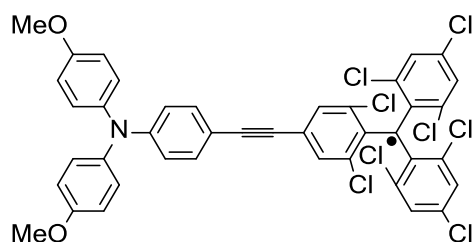
Yield: 16 mg (11 μmol , 44 %) of a brown solid

$\text{C}_{85}\text{H}_{60}\text{Cl}_4\text{N}_3\text{O}_6$ [1432.120]

SWV measurements proved a degree of radicalisation of 90 %.

HRMS (ESI): $[\text{M}^+]$ calc.: 1428.26078 m/z, found: 1428.26170 m/z, $\Delta=0.64$ ppm.

Synthesis of Star-Model



Under a nitrogen atmosphere **P6** (68 mg, 80 μmol) was dissolved in absolute THF (30 ml), TBAOH (1.5 M, 1.00 ml, 1.50 mmol) was added and the reaction mixture was stirred at rt under light exclusion over night. Afterwards the violet solution was poured in a hexane (30 ml), water (30 ml) mixture. The organic phase was separated and the solvent removed in vacuo. Under a nitrogen atmosphere the residue was dissolved in absolute DCM (10 ml). AgNO_3 (15 mg, 88 μmol) was added and the reaction

mixture was stirred at rt under light exclusion for 5 h. The brown solution was directly filtrated through silica gel (DCM).

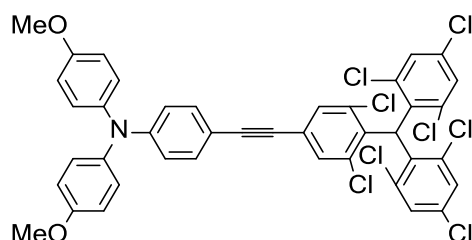
Yield: 30 mg (35 μmol , 44 %) of a brown solid

$\text{C}_{41}\text{H}_{24}\text{Cl}_8\text{NO}_2$ [846.259]

SWV measurements proved a degree of radicalisation of 97 %.

HRMS (ESI): $[\text{M}^+]$ calc.: 841.93098 m/z , found: 841.93138 m/z , $\Delta=0.48$ ppm.

Synthesis of P6



Under a nitrogen atmosphere *N,N*-Di(4-methoxyphenyl)-*N*-(4-(ethynyl)phenyl)amine (119 mg, 361 μmol), tris(2,4,6-trichlorophenyl)methane (100 mg, 180 μmol), Cs_2CO_3 (129 mg, 397 μmol) and DBU (27.0 μl , 180 μmol) were dissolved in a quartz pressure vessel in absolute DMF (5 ml) and degassed. After addition of $\text{Pd}(\text{PPh}_3)_2\text{Cl}_2$ (4 mg, 5 μmol) and $\text{P}(t\text{-Bu})_3$ (1 M in toluene, 11 μl , 11 μmol) the reaction mixture was stirred at 150 $^\circ\text{C}$ in a microwave oven for 8 min. After cooling, EA was added to reaction mixture and then washed with saturated NaCl solution (3 x 30 ml). The combined aqueous phases were extracted with EA (3 x 30 ml) and the combined organic phases dried over MgSO_4 . The solvent was removed in vacuo and the residue was purified by flash chromatography on silica gel (DCM/petrol ether 1:3). The crude product was purified further by gel permeation chromatography (Chloroform)

Yield: 46 mg (54 μmol , 30 %) of a yellow solid

$\text{C}_{41}\text{H}_{25}\text{Cl}_8\text{NO}_2$ [847.267]

M.p. 258 $^\circ\text{C}$

$^1\text{H NMR}$ (600 MHz, $[\text{D}_6]$ acetone):

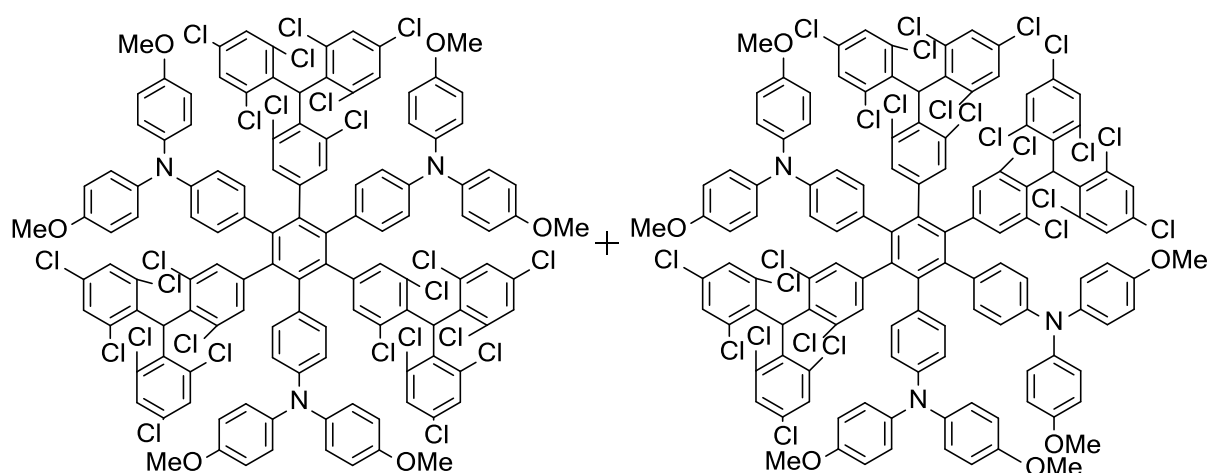
$\delta[\text{ppm}] =$ 7.63 (d, $^4J_{\text{HH}} = 2.3$ Hz, 2 H), 7.59 (d, $^4J_{\text{HH}} = 1.7$ Hz, 1 H), 7.46 (d, $^4J_{\text{HH}} = 1.4$ Hz, 2 H), 7.43 (d, $^4J_{\text{HH}} = 1.7$ Hz, 1 H), 7.35 (AA', 2 H), 7.13 (AA', 4 H), 6.96 (BB', 4 H), 6.79 (s, 1 H), 6.77 (BB', 2 H), 3.81 (s, 6 H)

^{13}C NMR (150.9 MHz, $[\text{D}_6]$ acetone):

$\delta[\text{ppm}] =$ 158.0, 150.8, 140.4, 138.8, 138.7, 138.00, 137.98, 137.92, 137.3, 135.3, 135.1, 134.71, 134.69, 133.6, 133.2, 131.5, 130.90, 130.87, 129.37, 129.35, 128.6, 126.4, 118.6, 115.9, 112.6, 94.6, 85.6, 55.8, 51.1, no carbons at the chlorinated benzene rings are chemical equivalent with the exception of one pair.

HRMS (ESI): $[\text{M}^+]$ calc.: 842.93880 m/z , found: 842.93884 m/z , $\Delta=0.05$ ppm.

Synthesis of P7 and P8



To a degassed solution of **P6** (155 mg, 0.182 mmol) in 1,4-dioxane (5 ml) dicobaltoctacarbonyl (6.0 mg, 0.02 mmol) was added and the reaction mixture stirred at 100 °C for 4 d. The solvent was removed in vacuo and the residue was purified by flash chromatography on silica gel (DCM/petrol ether 1:2→1:1→2:1) and by gel permeation chromatography (THF).

Yield (**P7**): 12 mg (4.7 μmol , 8 %) of a yellow solid

$\text{C}_{123}\text{H}_{75}\text{Cl}_{24}\text{N}_3\text{O}_6$ [2541.800]

^1H NMR (600 MHz, $[\text{d}_6]$ acetone, 323K):

$\delta[\text{ppm}] =$ 7.56 (3H), 7.46-7.43 (3H), 7.41 (3H), 7.28-7.26 (3H), 7.05-6.60 (45 H), 3.78-3.77 (18H).

^{13}C NMR (150.9 MHz, $[\text{D}_6]$ acetone, 323K):

$\delta[\text{ppm}] =$ 156.6-156.5, 148.0, 143.0-142.9, 142.1-142.0, 141.9-141.7, 139.1-139.0, 138.7-138.5, 138.0-137.9, 137.8-137.7, 136.3-136.2, 135.8, 135.4, 135.3-135.2, 134.5-134.0, 132.4-133.2, 131.1-

130.9, 130.7, 129.6-129.4, 129.2, 126.5-126.1, 123.4-122.9, 115.6-115.4, 55.7-55.6, 51.0, the existence of an unknown number of conformers causes the observation of signals of higher order

HRMS (ESI): $[M^{+}+12]$ calc.: 2540.80520 m/z , found: 2540.80117 m/z , $\Delta=1.59$ ppm

Yield (**P8**): 64 mg (25 μmol , 42 %) of a yellow solid

$\text{C}_{123}\text{H}_{75}\text{Cl}_{12}\text{N}_3\text{O}_6$ [2541.800]

^1H NMR (600 MHz, $[\text{d}_6]$ acetone, 313K):

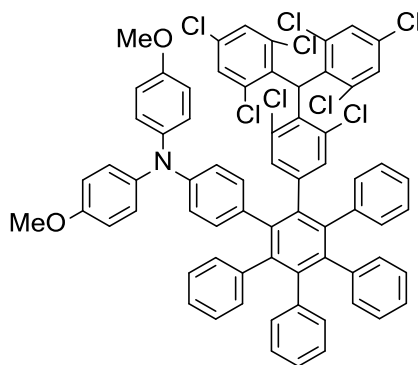
$\delta[\text{ppm}] =$ 7.58-7.53 (3H), 7.48-7.17 (8H), 7.12-6.57 (46 H), 3.78-3.76 (18H).

^{13}C NMR (150.9 MHz, $[\text{D}_6]$ acetone, 313K):

$\delta[\text{ppm}] =$ 156.9-156.7, 148.1-147.9, 143.4-141.7, 140.0-137.5, 137.1-135.0, 134.7-134.2, 133.6-132.5, 131.1-130.6, 129.7-129.0, 126.9-126.4, 123.3-123.0, 122.1-121.8, 115.7-115.5, 55.8, 51.2-51.1, the existence of a unknown number of conformers causes the observation of signals of higher order.

HRMS (ESI): $[M^{+}+12]$ calc.: 2540.80520 m/z , found: 2540.80937 m/z , $\Delta=1.64$ ppm.

Synthesis of P9



Under a nitrogen atmosphere **P6** (150 mg, 180 μmol) and tetraphenylcyclopentadienone (68.0 mg, 180 μmol) were dissolved in diphenyl ether (15 ml) and stirred at reflux for 3 d. After cooling, the residue was purified by flash chromatography on silica gel (DCM/petrol ether 1:2).

Yield: 65 mg (56 μmol , 31 %) of a yellow solid

$\text{C}_{69}\text{H}_{45}\text{Cl}_8\text{NO}_2$ [1203.725]

$^1\text{H NMR}$ (600 MHz, $[\text{d}_6]$ acetone, 323K):

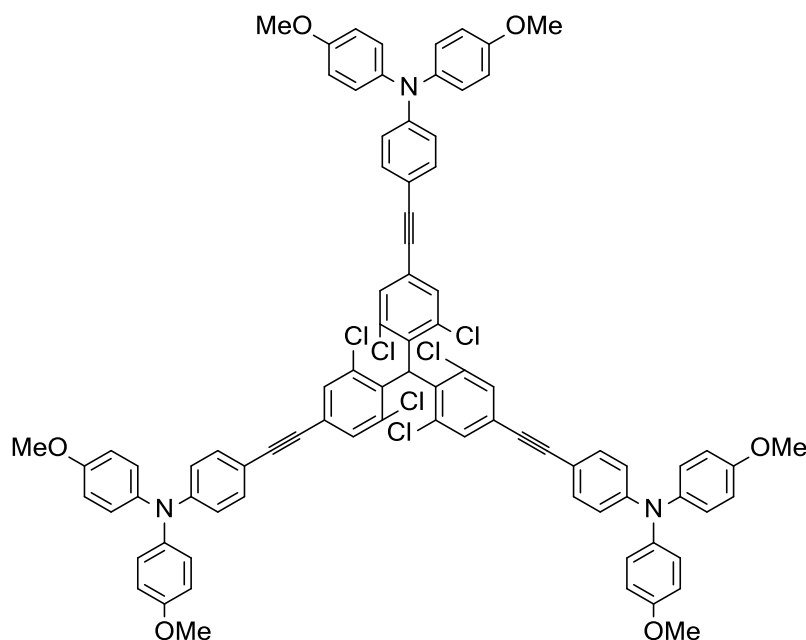
$\delta[\text{ppm}] =$ 7.52 (1.4 H), 7.38-7.35 (2H), 7.20-7.19 (0.5 H), 6.97-6.73 (31.6 H), 6.67-6.66 (0.7 H), 6.59-6.49 (3 H), 3.77-3.75 (6 H), due to the existence of at least two conformers, fractional integrals are observed.

$^{13}\text{C NMR}$ (150.9 MHz, $[\text{D}_6]$ acetone, 313K):

$\delta[\text{ppm}] =$ 156.8, 156.7, 147.5, 143.93, 143.88, 142.2, 142.13, 142.10, 141.9, 141.7, 141.44, 141.41, 141.34, 141.28, 141.25, 141.20, 141.17, 141.1, 141.02, 141.00, 139.4, 139.2, 138.7, 138.5, 138.3, 138.2, 137.8, 136.24, 136.19, 135.8, 135.7, 135.6, 135.4, 135.3, 134.41, 134.37, 134.36, 134.2, 134.0, 133.9, 133.0-132.9, 132.8-132.7, 132.6, 132.53, 132.47, 132.4-132.1, 130.94, 130.88, 130.7-130.6, 129.5, 129.3, 129.11-129.08, 128.1, 127.91-127.88, 127.82, 127.6-127.5, 126.8, 126.7, 126.6, 126.33-126.30, 121.7-121.5, 115.6, 115.5, 55.8, 51.0, the existence of at least two conformers causes the observation of signals of higher order.

HRMS (ESI): $[\text{M}^{+4}]$ calc.: 1203.09142 m/z , found: 1203.09206 m/z , $\Delta=0.53$ ppm.

Synthesis of P10



Under a nitrogen atmosphere tris(2,4,6-trichlorophenyl)methane (180 mg, 324 μmol), $\text{Pd}(\text{MeCN})_2\text{Cl}_2$ (3.0 mg, 13 μmol), *x*-Phos (12 mg, 26 μmol) and CuI (2 mg, 10 μmol) were suspended in a quartz pressure vessel in $(i\text{-Pr})_2\text{NH}$ (2 ml) and degassed. A degassed solution of *N,N*-Di(4-methoxyphenyl)-*N*-(4-(ethynyl)phenyl)amine (428 mg, 1.30 mmol) in absolute 1,4-dioxane (4 ml) was added and the reaction mixture stirred at 100 $^\circ\text{C}$ in a microwave oven for 1 h. After cooling, a degassed solution of

N,N-Di(4-methoxyphenyl)-*N*(4-(ethynyl)phenyl)amine (321 mg, 972 μ mol) in absolute 1,4-dioxane (2 ml) was added stirred at 100 °C in a microwave oven for further 1 h. This procedure was repeated one more time. After cooling, EA (100 ml) was added and the mixture washed with a saturated NaCl solution (3 x 50 ml). The combined aqueous phases were extracted with EA (3 x 50 ml) and the combined organic phases dried over MgSO₄. The solvent was removed in vacuo and the residue was purified by flash chromatography on silica gel (DCM/petrol ether 1:1->2:1->3:1) and by gel permeation chromatography (CHCl₃).

Yield: 160 mg (110 μ mol, 34 %) of a yellow solid

C₈₅H₆₁C₁₆N₃O₆ [1433.128]

M.p. 174 °C

¹H NMR (600 MHz, [D₆]acetone, 298 K):

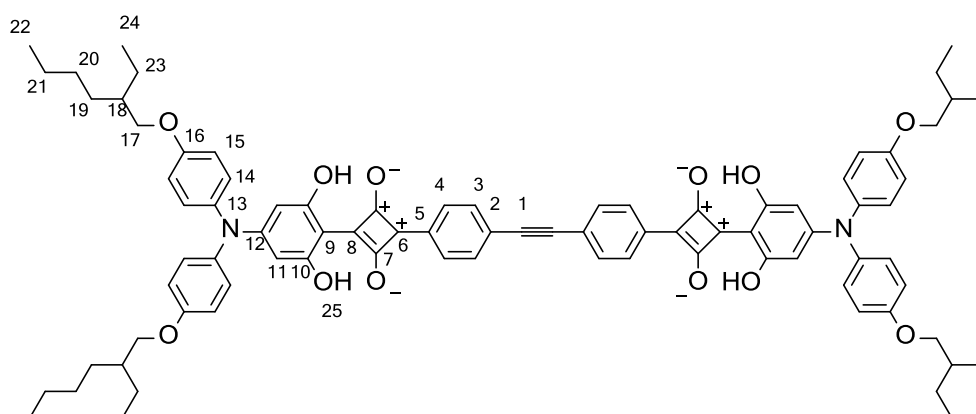
δ [ppm] = 7.59 (3 H), 7.43 (3 H), 7.36 (AA', 6 H), 7.13 (AA', 12 H), 6.95 (BB', 12 H), 6.86 (s, 1 H), 6.77 (BB', 6 H), 3.80 (s, 18 H).

¹³C NMR (150.9 MHz, [D₆]acetone, 298 K):

δ [ppm] = 157.9, 150.7, 140.4, 138.1, 137.3, 135.8, 133.5, 133.1, 131.4, 128.6, 126.2, 118.6, 115.8, 112.6, 94.4, 85.6, 55.7, 51.6.

HRMS (ESI): [M⁺] calc.: 1429.26860 *m/z*, found: 1429.26884 *m/z*, Δ =0.17 ppm.

Synthesis of S2a



S7 (400 mg, 749 μ mol) and **S6** (139 mg, 375 μ mol) were dissolved in a *n*-butanol/toluene mixture (100 ml, 1:3) and stirred at reflux over night. Water is removed by a Dean-Stark trap. The solvent is removed and the residue washed with hot acetone.

Yield: 270 mg (190 μmol , 51 %) of a metallic, green solid

$\text{C}_{90}\text{H}_{100}\text{N}_2\text{O}_{12}$ [1401.763]

$^1\text{H-NMR}$ (600 MHz, CD_2Cl_2):

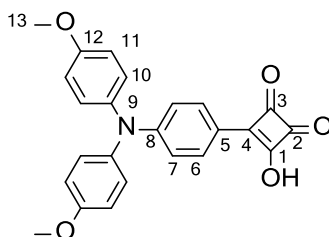
$\delta[\text{ppm}] =$ 12.97 (s, 4H, H-25), 8.04 (AA', 4H, H-3 oder H-4), 7.61 (BB', 4H, H-3 oder H-4), 7.16 (AA', 8H, H-14), 6.95 (BB', 8H, H-15), 5.75 (s, 4H, H-11), 3.89-3.85 (m, 8H, H-17), 1.73 (sept., 4H, H-18), 1.52-1.39 (16H, H-19 und H-23), 1.37-1.30 (16H, H-20 und H-21), 0.94-0.90 (24H, H-22 und H-24).

$^{13}\text{C-NMR}$ (150 MHz, CD_2Cl_2):

$\delta[\text{ppm}] =$ 183.3 (q, 4C, C-7), 181.5 (q, 2C), 166.3 (q, 4C, C-10), 165.0 (q, 2C), 159.6 (q, 4C, C-16), 157.0 (q, 2C, C-6), 135.9 (q, 4C, C-13), 132.7 (t, 4C, C-3), 130.4 (q, 2C, C-5), 128.7 (t, 8C, C-14), 127.9 (t, 4C, C-4), 125.9 (q, 2C, C-2), 115.9 (t, 8C, C-15), 113.1 (q, 2C, C-9), 98.4 (t, 4C, C-11), 93.9 (q, 2C, C-1), 71.2 (s, 4C, C-17), 39.7 (t, 4C, C-18), 30.8 (s, 4C, C-19), 29.4 (s, 4C, C-20), 24.2 (s, 4C, C-23), 23.4 (s, 4C, C-21), 14.3 (p, 4C, C22), 11.2 (p, 4C, C24).

HRMS (ESI): $[\text{M}^+\text{H}]$ calc.: 1401.73490 m/z , found: 1401.73519 m/z , $\Delta=0.21$ ppm.

Synthesis of S4



S8 (70 mg, 150 μmol) was stirred in a mixture of acetic acid (6.3 ml), water (6.3 ml) and 2N HCl (0.5 ml) at reflux for 2 h. The solvent was removed in vacuo.

Yield: 60 mg (150 μmol , 98 %) of a yellow solid

$\text{C}_{24}\text{H}_{19}\text{NO}_5$ [401.411]

$^1\text{H-NMR}$ (600 MHz, $\text{dmsO}[D_6]$):

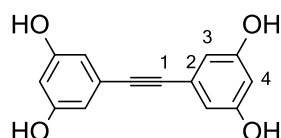
$\delta[\text{ppm}] =$ 7.83 (AA', 2H, H-6), 7.03 (AA', 4H, H-10), 6.91 (BB', 4H, H-11), 6.76 (BB', 2H, H-7), 3.74 (s, 6H, H-13).

$^{13}\text{C-NMR}$ (150 MHz, $\text{dms}_o[\text{D}_6]$):

$\delta[\text{ppm}] =$ 214.4 (q, 1C), 196.8 (q, 2C), 175.7 (q, 1C, C-4), 155.9 (q, 2C, C-12), 148.3 (q, 1C, C-8), 139.8 (q, 2C, C-9), 126.8 (t, 4C, C-10), 124.8 (t, 2C, C-6), 124.7 (q, 1C, C-5), 118.8 (t, 2C, C-7), 115.0 (t, 4C, C-11), 55.2 (p, 2C, C-13).

MALDI-MS: 400 m/z [$\text{M}^- - \text{H}$]

Synthesis of S5



Under a nitrogen atmosphere **S12** (500 mg, 1.68 mmol) and NaHCO_3 (5 g, heated to 300°C in vacuo for 30 min) were suspended in dry DCM (14 ml). Boron tribromide (10.1 ml, 10.1 mmol, 1M DCM) was added dropwise at -78°C . The temperature was slowly allowed to rise to rt over night. The reaction mixture was poured into water, extracted with EA (3 x 30 ml) and the combined organic phases dried over MgSO_4 . The solvent was removed in vacuo and the residue was purified by flash chromatography on silica gel (DCM/EA 4:1).

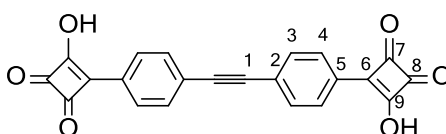
Yield: 250 mg (1.03 mmol, 62 %) of a colourless solid

$\text{C}_{14}\text{H}_{10}\text{O}_4$ [242.227]

$^1\text{H-NMR}$ (400 MHz, $\text{acetone}[\text{D}_6]$):

$\delta[\text{ppm}] =$ 8.42 (s, 4H, -OH), 6.51 (d, $^4\text{J}=2.23$ Hz, 4H, H-3), 6.39 (t, $^4\text{J}=2.20$ Hz, 2H, H-4).

Synthesis of S6



S10 (250 mg, 520 μmol) is dissolved in acetone (40 ml) and 2N HCl (10 ml) was added at reflux. The reaction mixture was stirred at reflux for 3 d. The solvent was removed in vacuo.

Yield: 190 mg (510 μmol , 99 %) of a yellow solid

$\text{C}_{22}\text{H}_{10}\text{O}_6$ [370.311]

¹H-NMR (600 MHz, [d₆]dms_o):

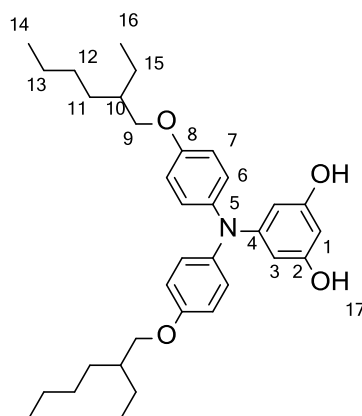
δ[ppm] = 8.02 (AA', 4H, H-4), 7.63 (BB', 4H, H-3).

¹³C-NMR (151 MHz, [d₆]dms_o):

δ[ppm] = 210.8 (q, 2C, C-7 or C-8, or C-9), 196.5 (q, 4C, C-7 or C-8, or C-9), 172.7 (q, 2C, C-6), 131.8 (t, 4C, C-3), 131.2 (q, 2C, C-5), 124.3 (t, 4C, C-4), 122.3 (q, 2C, C-2), 91.1 (q, 2C, C-1).

MALDI-MS: 369 *m/z* [M⁻ - H]

Synthesis of S7



S13 (1.00 g, 1.40mmol) and Pd/C (10 wt% palladium on activated carbon, 220 mg) were stirred in a mixture of EtOH (20 ml) and EtOAc (10 ml) under 1 atm H₂ (balloon) for 4 d. The reaction mixture was filtrated and the solvent removed in vacuo. The residue was purified by flash chromatography on silica gel (PE/EA 5:1).

Yield: 630 mg (1.18 mmol, 84 %) of a colorless solid

C₃₄H₄₇NO₄ [533.741]

¹H-NMR (400 MHz, acetone[D₆]):

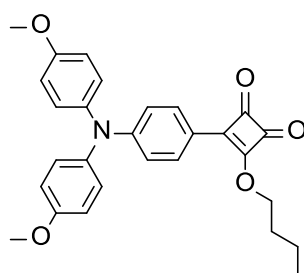
δ[ppm] = 7.93 (s, 2H, H-17), 7.02 (AA', 4H, H-6), 6.89 (BB', 4H, H-7), 5.89 (t, ⁴J=2.08 Hz, 1H, H-1), 5.82 (d, ⁴J=2.08 Hz, 2H, H-2), 3.88 (d, ³J=5.67 Hz, 4H, H-9), 1.76-1.67 (m, 2H, H-10), 1.58-1.28 (16H, H-11-13 and H-15), 0.96-0.88 (12 H, H-14 and H-16).

$^{13}\text{C-NMR}$ (101 MHz, acetone[D_6]):

$\delta[\text{ppm}] =$ 159.7 (q, 2C, C-2), 156.8 (q, 2C, C-8), 151.9 (q, 1C, C-4), 141.7 (q, 2C, C-5), 128.0 (t, 4C, C-6), 115.9 (t, 4C, C-7), 99.8 (t, 2C, C-3), 96.2 (t, 1C, C-1), 71.2 (s, 2C, C-9), 40.4 (t, 2C, C-10), 31.3 (s, 2C, C-11), 29.8 (s, 2C, C-12, superimposed by solvent signal, proved by HSQC, HMBC), 24.6 (s, 2C, C-15), 23.7 (s, 2C, C-13), 14.3 (p, 2C, C-14), 11.4 (p, 2C, C-16).

MALDI-MS: 533 m/z [M^+]

Synthesis of S8



Under a nitrogen atmosphere **S9** (170 mg, 0.44 mmol) was dissolved in THF (4 ml). *n*-BuLi (0.19 ml, 2.6 M in toluene, 0.49 mmol) was added dropwise at -78°C and the reaction mixture stirred for 30 min at -78°C and 30 min at -50°C . At 78°C a to -78°C cooled solution of di-*n*-butylsquarate (200 mg, 0.88 mmol) in THF (4 ml) was added dropwise. After stirring for 1 h at -78°C trifluoroacetic acid anhydride (125 mg, 0.08 ml, 0.48 mmol) was added and the reaction mixture stirred for 15 min at -78°C . A saturated NH_4Cl solution (5 ml) was added and the reaction mixture was warmed to rt. Subsequently, brine (5 ml) was added and the reaction mixture was extracted with diethyl ether (2 x 20 ml), the combined organic phases washed with brine and dried over MgSO_4 . The solvent was removed in vacuo and the residue was purified by flash chromatography on silica gel (PE/DCM 2:1 \rightarrow EA).

Yield: 80 mg (0.18 mmol, 40 %) of a yellow solid

$\text{C}_{28}\text{H}_{27}\text{NO}_5$ [457.518]

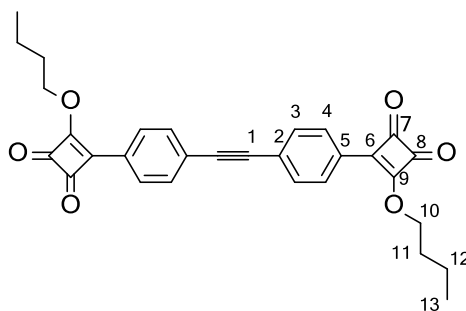
$^1\text{H-NMR}$ (400 MHz, CDCl_3):

$\delta[\text{ppm}] =$ 7.85-7.80 (AA', 2 H), 7.14-7.09 (AA', 4 H), 6.91-6.84 (6 H), 4.87 (t, $^3\text{J}=6.5$ Hz, 2 H, OCH_2), 3.82 (s, 6 H, OCH_3), 1.89-1.81 (m, 2 H, CH_2), 1.54-1.44 (m, 2 H, CH_2), 0.98 (t, $^3\text{J}=7.4$ Hz, 3 H, CH_3)

$^{13}\text{C-NMR}$ (150 MHz, CDCl_3):

$\delta[\text{ppm}] =$ 192.6 (q), 192.3 (q), 191.2 (q), 173.6 (q), 157.5 (q), 152.8 (q), 138.9 (q), 129.5 (t), 128.1 (t), 118.6 (t), 117.6 (t), 115.2 (q), 74.7(s), 55.7 (s), 32.2 (s), 18.8 (s), 13.8 (p).

Synthesis of S10



Under a nitrogen atmosphere **S11** (1.09 g, 3.24 mmol) was dissolved in THF (10 ml). *n*-BuLi (2.75 ml, 2.6 M in toluene, 7.14 mmol) was added dropwise at -78°C and the reaction mixture stirred for 30 min at -78°C and 30 min at -50°C . At 78°C a to -78°C cooled solution of di-*n*-butylsquarate (1.47 g, 6.49 mmol) in THF (10 ml) was added dropwise. After stirring for 1 h at -78°C trifluoroacetic acid anhydride (1.84 g, 1.23 ml, 8.76 mmol) was added and the reaction mixture stirred for 15 min at -78°C . A saturated NH_4Cl solution (20 ml) was added and the reaction mixture was warmed to rt. Subsequently, brine (20 ml) was added and the reaction mixture was extracted with diethyl ether (2 x 50 ml), the combined organic phases washed with brine and dried over MgSO_4 . The solvent was removed in vacuo and the residue was purified by flash chromatography on silica gel (PE/DCM 2:1→EA).

Yield: 560 mg (1.16 mmol, 36 %) of a yellow solid.

$\text{C}_{30}\text{H}_{26}\text{O}_6$ [482.524]

$^1\text{H-NMR}$ (600 MHz, CD_2Cl_2):

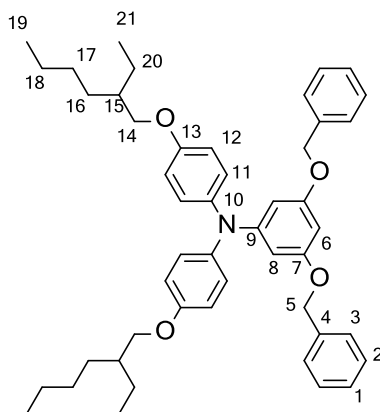
$\delta[\text{ppm}] =$ 8.05 (AA', 4H, H-4), 7.69 (BB', 4H, H-3), 4.93 (t, $^3\text{J}=6.7$ Hz, 4H, H-10), 1.93-1.88 (m, 4H, H-11), 1.57-1.50 (m, 4H, H-12), 1.01 (t, $^3\text{J}=7.4$ Hz, 6H, H-13).

$^{13}\text{C-NMR}$ (151 MHz, CD_2Cl_2):

$\delta[\text{ppm}] =$ 195.2 (q, 2C, C-9), 192.91 (q, 2C, C-7 or C-8), 192.88 (q, 2C, C-7 or C-8), 172.4 (q, 2C, C-6), 132.7 (t, 4C, C-3), 128.1 (q, 2C, C-5), 127.8 (t, 4C, C-4), 127.0 (q, 2C, C-2), 92.4 (q, 2C, C-1), 76.0 (s, 2C, C-10), 32.3 (s, 2C, C-11), 19.0 (s, 2C, C-12), 13.8 (p, 2C, C-13).

HRMS (ESI): $[M^+]$ calc.: 505.16216 m/z , found: 505.16155 m/z , $\Delta=1.21$ ppm.

Synthesis of S13



Under a nitrogen atmosphere CuCl (14 mg, 0.14 mmol) and KOH (1.56 g, 27.8 mmol) are added to a degassed solution of 1-(2-ethylhexyloxy)-4-iodobenzene (2.42 g, 7.29 mmol), 1,10-phenanthroline (25 mg, 0.14 mmol) and **S14** (1.06 g, 3.47 mmol) in dry toluene (5 ml). The suspension was stirred at reflux for 10 d. The solvent was removed in vacuo. Water (150 ml) and DCM (150 ml) were added to the residue. The phases were separated and the aqueous phase extracted with DCM (3 x 100 ml). The organic phases were combined, washed with water (2 x 100 ml) and dried over MgSO₄. The solvent was removed in vacuo and the residue was purified by flash chromatography on silica gel (PE/DCM 6:1).

Yield: 1.45 g (2.03 mmol, 59 %) of a colorless solid.

C₄₈H₅₉NO₄ [713.986]

¹H-NMR (400 MHz, acetone[D₆]):

δ [ppm] = 7.37-7.28 (10H, H-1 and H-2 and H-3), 7.01 (AA', 4H, H-11), 6.88 (BB', 4H, H-12), 6.22 (t, ⁴J=2.23 Hz, 1H, H-6), 6.07 (d, ⁴J=2.23 Hz, 2H, H-8), 4.96 (s, 4H, H-5), 3.88 (d, ³J=5.68 Hz, 4H, H-14), 1.75-1.67 (m, 2H, H-15), 1.58-1.28 (16H, H-16-18 and H-20), 0.96-0.88 (12 H, H-19 and H-21).

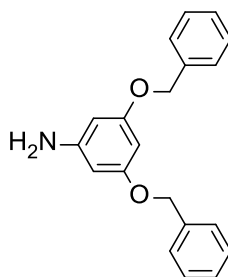
¹³C-NMR (101 MHz, acetone[D₆]):

δ [ppm] = 161.3 (q, 2C, C-7), 157.0 (q, 2C, C-13), 151.7 (q, 1C, C-9), 141.3 (q, 2C, C-10), 138.4 (q, 2C, C-4), 129.2 (t, 4C, C-2 or C-3), 128.5 (t, 2C, C-1), 128.4 (t, 4C, C-2 or C-3), 128.0 (t, 4C, C-11), 116.2 (t, 4C, C-12), 100.3 (t, 2C, C-8), 94.8 (t, 1C, C-6), 71.3 (s, 2C, C-14), 70.4 (s, 2C, C-5),

40.4 (t, 2C, C-15), 30.3 (s, 2C, C-16), 29.8 (s, 2C, C-17, superimposed by solvent signal, proved by HSQC, HMBC), 24.6 (s, 2C, C-20), 23.7 (s, 2C, C-18), 14.4 (p, 2C, C-19), 11.5 (p, 2C, C-21);

MALDI: 713.362 m/z [M^+]

Synthesis of S14



Under a nitrogen atmosphere a degassed solution of **S15** (2.00, 5.42 mmol), ammonium hydroxide (28 %, 5.50ml, 5.42 mmol), CuI (210 mg, 1.08 mmol), trans-4-hydroxy L-proline (284 mg, 2.17 mmol) and K_2CO_3 (2.25 g, 16.2 mmol) in DMSO (10 ml) was stirred at 70 °C for 3 d. Water (50 ml) and EA (50 ml) were added and the phases separated. The aqueous phase was extracted with EA (2 x 50 ml) and the combined organic phases dried over $MgSO_4$. The solvent was removed in vacuo and the residue was purified by flash chromatography on silica gel (DCM).

Yield: 1.06 g (3.47 mmol, 64 %) of a colorless solid.

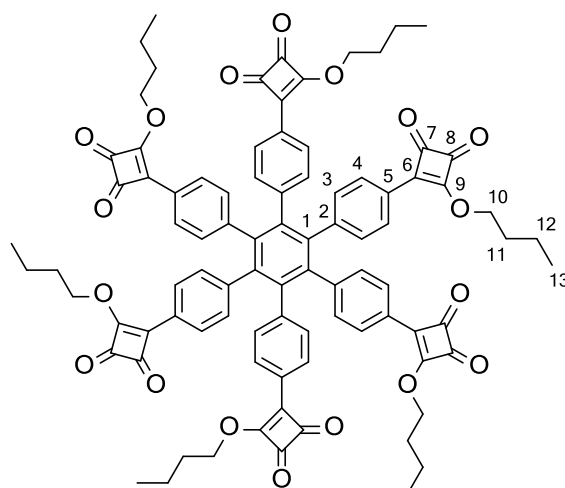
$C_{20}H_{19}NO_2$ [305.370]

1H -NMR (400 MHz, acetone- d_6):

δ [ppm] = 7.45-7.43 (4 H), 7.39-7.35 (4 H), 7.32-7.29 (2 H), 6.01 (3 H), 5.00 (4 H).

MALDI-MS: 305.139 m/z [M^+]

Synthesis of S16



Under a nitrogen atmosphere a degassed solution of **S10** (250 mg, 0.518 mmol) and $\text{Co}_2(\text{CO})_8$ (18 mg, 51 μmol) in 1,4-dioxane (15 ml) was stirred at reflux for 6 d. The solvent was removed in vacuo and the residue was purified by flash chromatography on silica gel (PE/EA 10:1).

Yield: 120 mg (83 μmol , 48 %) of a yellow solid.

$\text{C}_{90}\text{H}_{78}\text{O}_{18}$ [1447.572]

$^1\text{H-NMR}$ (400 MHz, CD_2Cl_2):

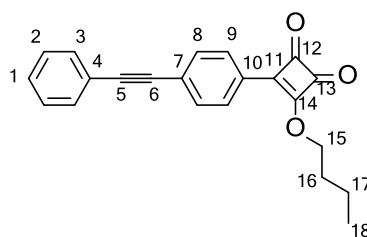
$\delta[\text{ppm}] =$ 7.61 (AA', 12H, H-4), 7.06 (BB', 12H, H-3), 4.81 (t, $^3J=6.6$ Hz, 12H, H-10), 1.85-1.78 (m, 12H, H-11), 1.48-1.41 (m, 12H, H-12), 0.96 (t, $^3J=7.4$ Hz, 18H, H-13).

$^{13}\text{C-NMR}$ (100 MHz, CD_2Cl_2):

$\delta[\text{ppm}] =$ 195.0 (q, 6C, C-9), 193.2 (q, 6C, C-7 or C-8), 192.7 (q, 6C, C-7 or C-8), 173.0 (q, 6C, C-6), 144.2 (q, 6C, C-2), 140.3 (q, 6C, C-5), 132.3 (t, 12C, C-3), 126.8 (t, 12C, C-4), 126.3 (q, 6C, C-1), 75.8 (s, 6C, C-10), 32.3 (s, 6C, C-11), 19.0 (s, 6C, C-12), 13.7 (p, 6C, C-13).

HRMS (ESI): $[\text{M}^+ + \text{Na}]$ calc.: 1469.50804 m/z , found: 1469.50925 m/z , $\Delta=0.82$ ppm.

Synthesis of S18



Under a nitrogen atmosphere **S17** (750 mg, 2.92 mmol) was dissolved in THF (20 ml). *n*-BuLi (1.23 ml, 2.6 M in toluene, 3.21 mmol) was added dropwise at -78°C and the reaction mixture stirred for 30 min at -78°C and 30 min at -50°C . At 78°C a to -78°C cooled solution of di-*n*-butylsquarate (660 mg, 2.92 mmol) in THF (20 ml) was added dropwise. After stirring for 1 h at -78°C trifluoroacetic acid anhydride (830 mg, 0.560 ml, 3.94 mmol) was added and the reaction mixture stirred for 15 min at -78°C . A saturated NH_4Cl solution (80 ml) was added and the reaction mixture was warmed to rt. Subsequently, brine (60 ml) was added and the reaction mixture was extracted with diethyl ether (2 x 60 ml), the combined organic phases washed with brine and dried over MgSO_4 . The solvent was removed in vacuo and the residue was purified by flash chromatography on silica gel (PE/EA 5:1→2:1→0:1). The raw product was recrystallised from hexane.

Yield: 570 mg (1.73 mmol, 59 %) of a yellow solid.

$\text{C}_{22}\text{H}_{18}\text{O}_3$ [330.377]

$^1\text{H-NMR}$ (400 MHz, acetone- d_6):

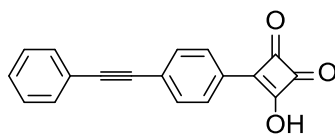
δ [ppm] = 8.04 (AA', 2H, H-9), 7.73 (BB', 2H, H-8), 7.61-7.58 (m, 2H, H-3), 7.45-7.44 (3H, H-1 and H-2), 4.99 (t, $^3\text{J}=6.6$ Hz, 2H, H-15), 1.98-1.91 (m, 2H, H-16), 1.61-1.51 (m, 2H, H-17), 1.01 (t, $^3\text{J}=7.4$ Hz, 3H, H-18).

$^{13}\text{C-NMR}$ (101 MHz, acetone- d_6):

δ [ppm] = 196.2 (q, 1C, C-14), 193.33 (q, 1C, C-12 or C-13), 193.28 (q, 1C, C-12 or C-13), 171.7 (q, 1C, C-11), 133.0 (t, 2C, C-8), 132.5 (t, 2C, C-3), 130.0 (t, 1C, C-1), 129.6 (t, 2C, C-2), 128.6 (q, 1C, C-10), 128.0 (t, 2C, C-9), 127.7 (q, 1C, C-7), 123.5 (q, 1C, C-4), 93.2 (q, 1C, C-5), 89.6 (q, 1C, C-6), 76.2 (s, 1C, C-15), 32.6 (s, 1C, C-16), 19.3 (s, 1C, C-17), 13.9 (p, 1C, C-18).

MALDI: $[\text{M}^+ + \text{Na}] = 353.025$ *m/z*

Synthesis of S19



S18 (200 mg, 604 μmol) was dissolved in acetone (40 ml) and 2N HCl (10 ml) was added at reflux. The reaction mixture was stirred at reflux for 3 d. The solvent was removed in vacuo.

Yield: 165 mg (600 μmol , 99 %) of a yellow solid

$\text{C}_{18}\text{H}_{10}\text{O}_3$ [274.270]

$^1\text{H-NMR}$ (400 MHz, $\text{dms}\text{O}[\text{D}_6]$):

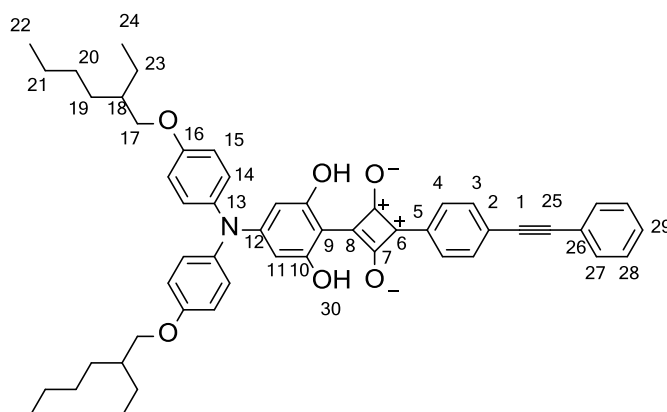
$\delta[\text{ppm}] =$ 8.01 (AA', 2H), 7.60 (BB', 2H), 7.57-7.54 (2H), 7.44-7.40 (3H).

$^{13}\text{C-NMR}$ (101 MHz, $\text{dms}\text{O}[\text{D}_6]$):

$\delta[\text{ppm}] =$ 212.1 (q, 1C), 197.1 (q, 2C), 173.5 (q, 1C), 132.0 (t, 2C), 131.6 (t, 2C), 131.5 (q, 1C), 129.2 (t, 1C), 129.1 (t, 2C), 124.4 (t, 2C), 122.5 (q, 1C), 122.4 (q, 1C), 90.8 (q, 1C), 90.0 (q, 1C).

MALDI: $[\text{M}^- - \text{H}^+] =$ 273 m/z

Synthesis of S20



S7 (45 mg, 84 μmol) and **S19** (25 mg, 84 μmol) were dissolved in a *n*-butanol/toluene mixture (50 ml, 1:3) and stirred at reflux for 3 h. Water is removed by a Dean-Stark trap. The solvent is removed and the residue washed with hexane.

Yield: 25 mg (32 μmol , 59 %) of a metallic, green solid.

$\text{C}_{52}\text{H}_{55}\text{NO}_6$ [789.996]

¹H-NMR (400 MHz, CD₂Cl₂):

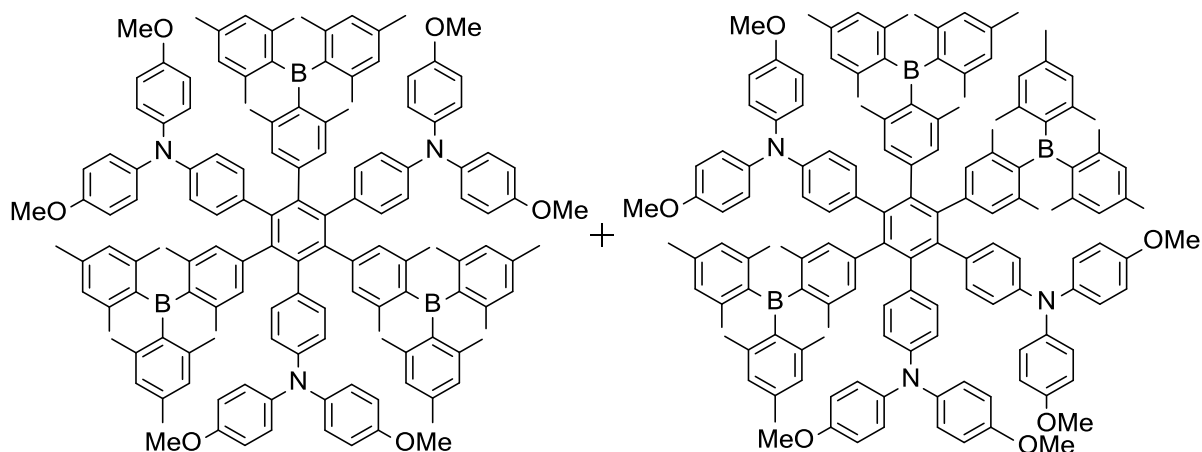
δ[ppm] = 12.98 (s, 2H, H-30), 8.04 (AA', 2H, H-4), 7.61 (BB', 2H, H-3), 7.57-7.55 (m, 2H, H27), 7.39-7.37 (3H, H-28 and H-29), 7.17 (AA', 4H, H-14), 6.95 (BB', 4H, H-15), 5.75 (s, 2H, H-11), 3.89-3.85 (m, 4H, H-17), 1.74 (sept., 2H, H-18), 1.52-1.27 (16H, H-19, H-20, H-21 and H-23), 0.96-0.94 (12H, H-22 and H-24).

¹³C-NMR (101 MHz, CD₂Cl₂):

δ[ppm] = 183.3 (q, 2C, C-7), 181.7 (q, 1C), 166.4 (q, 2C, C-10), 165.1 (q, 1C), 159.7 (q, 2C, C-16), 157.4 (q, 1C, C-6), 136.0 (q, 2C, C-13), 132.5 (t, 2C, C-3), 132.1 (t, 2C, C-27), 130.1 (q, 1C, C-5), 129.2 (t, 1C, C-29), 128.9 (t, 2C, C-28), 128.7 (t, 4C, C-14), 128.0 (t, 2C, C-4), 126.4 (q, 1C, C-2), 123.3 (q, 1C, C-26), 116.0 (t, 4C, C-15), 113.1 (q, 1C), 98.4 (t, 2C, C-11), 93.5 (q, 1C, C-25), 90.1 (q, 1C, C-1), 71.3 (s, 2C, C-17), 39.8 (t, 2C, C-18), 30.9 (s, 2C, C-19), 29.5 (s, 2C, C-20), 24.2 (s, 2C, C-23), 23.5 (s, 2C, C-21), 14.3 (p, 2C, C-22), 11.2 (p, 2C, C-24).

HRMS (ESI): [M⁺+H] calc.: 790.41021 *m/z*, found: 790.41058 *m/z*, Δ=0.47 ppm.

Synthesis of B1 and B2



Under a nitrogen atmosphere compound **B4** (193 mg, 0.30 mmol) was dissolved in absolute 1,4-dioxane (8 ml) and degassed. Dicobaltoctacarbonyl (15.1 mg, 44 μmol) was added and the reaction mixture stirred at reflux for 5 d. The solvent was removed in vacuo and the crude product was purified by flash chromatography on silica gel with (DCM/petrol ether 2:3→2:5). Pure compound **B1** was obtained as by dropping a concentrated DCM solution into acetone.

Yield: 32 mg (16 μmol, 17 %) of a yellow solid.

C₁₃₈H₁₃₂B₃N₃O₆ [1960.974]

M.p. 290°C (decomp.);

¹H NMR (600 MHz, [D₂]DCM):

δ[ppm] = 7.06 (AA', 6 H), 6.85-6.88 (18 H), 6.77 (s, 12 H), 6.74 (BB', 12 H), 6.59 (AA', 6 H), 6.38 (BB', 6 H), 3.76 (s, 18 H, MeO), 2.28 (s, 18 H), 1.89 (s, 36 H).

¹³C NMR (150.9 MHz, [D₂]DCM):

δ[ppm] = 155.9, 146.4, 145.5, 143.5, 142.2, 141.6, 141.0, 140.7, 140.3, 138.8, 134.7, 133.5, 132.3, 131.7, 128.4, 126.4, 120.1, 114.8, 55.7, 23.6, 21.3.

HRMS (ESI): [M²⁺] calc.: 980.052241 *m/z*, found: 980.051541 *m/z*, Δ=0.71 ppm.

Pure compound **B2** was obtained by dropping a concentrated DCM solution into methanol.

Yield: 120 mg (61 μmol, 62 %) of a yellow solid.

C₁₃₈H₁₃₂B₃N₃O₆ [1960.974]

T_g = 151°C

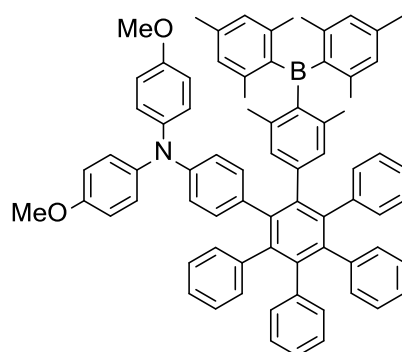
¹H NMR (600 MHz, [D₆]acetone):

δ[ppm] = 7.08 (AA', 2 H), 7.01-7.04 (2 AA', 4 H), 6.97 (BB', 4 H), 6.94 (BB', 2 H), 6.90 (AA', 4 H), 6.85-6.87 (8 H), 6.77-6.83 (24 H), 6.70-6.72 (2 AA', 4 H), 6.67 (AA', 2 H), 6.49-6.52 (2 BB', 4 H), 6.39 (BB', 2 H), 3.77 (s, 6 H, MeO), 3.76 (s, 6 H, MeO), 3.75 (s, 6 H, MeO), 2.27 (s, 6 H), 2.26 (s, 12 H), 1.87-1.95 (36 H).

¹³C NMR (150.9 MHz, [D₆]acetone):

δ[ppm] = 156.63, 156.59, 156.5, 147.2, 147.12, 147.07, 146.3, 146.0, 145.9, 144.3, 142.63, 142.56, 142.04, 142.01, 141.97, 141.6, 141.32, 141.26, 141.1, 140.9, 140.8, 140.7, 139.34, 139.33, 135.0, 134.94, 134.93, 134.4, 134.3, 134.2, 133.1, 133.04, 132.96, 132.4, 132.3, 129.1, 129.0, 126.8, 126.7, 126.5, 121.1, 120.9, 120.8, 115.5, 115.4, 55.68, 55.67, 23.9, 21.3, 21.26, 21.25.

HRMS (ESI): [M⁺+H] calc.: 1961.04536 *m/z*, found: 1961.04309 *m/z*, Δ=1.16 ppm.

Synthesis of B3

Compound **B6** (190 mg, 0.23 mmol) was dissolved in dry THF (6 ml) under a nitrogen atmosphere. A solution of t-BuLi in pentane (0.3 ml, 0.51 mmol, 1.7 M) was added slowly at -78°C . The mixture was stirred for 30 min at -78°C and then Mes_2BF (91.0 mg, 0.34 mmol) dissolved in dry THF (4 ml) was added slowly at -78°C . The reaction mixture was allowed to warm up to RT and was stirred at RT for further 2 d. The pale yellow suspension was hydrolysed with water (20 ml) and extracted with DCM (2 x 30 ml). The combined organic phases were washed with water (2 x 50 ml) and dried over MgSO_4 . The solvent was removed in vacuo and the residue was purified by flash chromatography on silica gel (DCM/petrol ether 1:4 \rightarrow 1:3 \rightarrow 1:2). The pure product was obtained by dropping a concentrated DCM solution into hexane.

Yield: 66 mg (65 μmol , 29 %) of a white solid.

$\text{C}_{74}\text{H}_{64}\text{BNO}_2$ [1010.116]

M.p. 246°C .

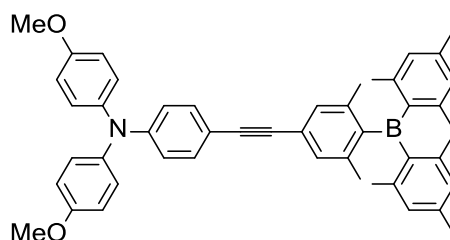
$^1\text{H NMR}$ (600 MHz, $[\text{D}_2]$ DCM):

$\delta[\text{ppm}] =$ 6.99 (AA', 2H), 6.93-6.95 (3H), 6.84-6.90 (19 H), 6.80 (AA', 4H), 6.75 (s, 4H), 6.74 (BB', 4H), 6.63 (AA', 2H), 6.41 (BB', 2H), 3.75 (s, 6H, OMe), 2.27 (s, 6H), 1.83 (s, 12H).

$^{13}\text{C NMR}$ (150.9 MHz, $[\text{D}_2]$ DCM):

$\delta[\text{ppm}] =$ 155.8, 146.3, 145.5, 143.6, 142.1, 141.5, 141.19, 141.15, 141.07, 141.0, 140.9, 140.8, 140.7, 140.5, 140.4, 140.3, 138.8, 134.6, 133.7, 132.3, 131.9, 131.80, 131.78, 131.76, 131.6, 128.4, 126.92, 126.89, 126.2, 125.62, 125.58, 125.56, 125.5, 120.2, 114.7, 55.8, 23.5, 21.3.

HRMS (ESI): $[\text{M}^+]$ calc.: 1008.50609 m/z , found: 1008.50609 m/z , $\Delta=0.00$ ppm.

Synthesis of B4

N-[4-(4-bromophenyl)ethynylphenyl]-*N,N*-di(4-methoxyphenyl)amine (200 mg, 0.41 mmol) was dissolved in dry THF (7 ml) under a nitrogen inert gas atmosphere. A solution of *t*BuLi in pentane (0.5 ml, 0.85 mmol, 1.7 M) was added slowly at -78°C . The mixture was stirred for 30 min at -78°C and then Mes_2BF (166 mg, 0.62 mmol) dissolved in dry THF (4 ml) was added slowly at -78°C . The reaction mixture was allowed to warm up to RT and was stirred for further 4 d at RT. The brown suspension was hydrolysed with water (20 ml) and extracted with DCM (2 x 30 ml). The combined organic phases were washed with water (2 x 50 ml), dried over MgSO_4 and the solvent was removed in vacuo. The residue was purified by flash chromatography on silica gel (DCM/petrol ether 2:3). The pure product was obtained by dropping a concentrated DCM solution into methanol.

Yield: 110 mg (170 μmol , 42 %) of a yellow solid.

$\text{C}_{46}\text{H}_{44}\text{BNO}_2$ [653.658]

M.p. 104°C

$^1\text{H NMR}$ (600 MHz, $[\text{D}_6]$ acetone):

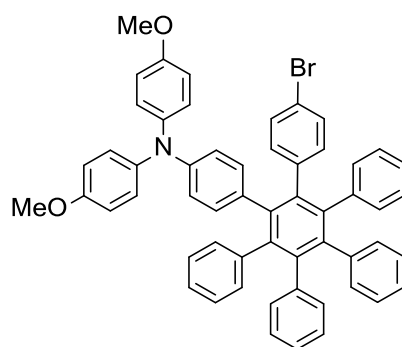
$\delta[\text{ppm}] =$ 7.52 (AA', 2 H), 7.45 (BB', 2 H), 7.35 (AA', 2 H), 7.12 (AA', 4 H), 6.95 (BB', 4 H), 6.84-6.85 (4 H), 6.77 (BB', 2 H), 3.80 (s, 6 H, MeO), 2.28 (s, 6 H), 2.00 (s, 12 H).

$^{13}\text{C NMR}$ (150.9 MHz, $[\text{D}_6]$ acetone):

$\delta[\text{ppm}] =$ 157.8, 150.4, 146.1, 142.2, 141.3, 140.5, 139.6, 136.9, 133.3, 131.53, 129.1, 128.5, 128.3, 118.8, 115.8, 114.8, 93.5, 88.9, 55.7, 23.6, 21.2.

HRMS (EI): $[\text{M}^+]$ calc.: 652.34959 m/z , found: 652.34908 m/z , $\Delta=0.78$ ppm.

Synthesis of B6



N-[4-(4-bromophenyl)ethynylphenyl]-*N,N*-di(4-methoxyphenyl)amine (200 mg, 0.41 mmol) and tetraphenylcyclopentadiene (159 mg, 0.41 mmol) were dissolved in diphenyl ether (6 ml) under a nitrogen atmosphere. The reaction mixture was stirred under reflux for 3 d. The crude product was purified by flash chromatography on silica gel (DCM/petrol ether 1:4→1:2).

Yield: 190 mg (226 μ mol, 55 %) of a white solid.

$C_{56}H_{42}BrNO_2$ [840.842]

M.p. 241 °C

1H NMR (600 MHz, $[D_2]DCM$):

δ [ppm] = 7.07 (AA', 2 H), 6.84-6.94 (20 H), 6.75-6.77 (10 H), 6.61 (AA', 2 H), 6.46 (BB', 2 H), 3.74 (s, 6 H, MeO).

^{13}C NMR (150.9 MHz, $[D_2]DCM$):

δ [ppm] = 155.8, 146.5, 141.6, 141.1, 141.04, 141.00, 140.88, 140.87, 140.8, 140.7, 140.6, 140.5, 140.4, 139.7, 133.9, 133.6, 132.3, 131.8, 131.69, 131.67, 130.0, 127.1, 126.93, 126.90, 126.89, 125.84, 125.79, 125.6, 120.9, 119.5, 114.7, 55.8.

HRMS (ESI): $[M^+]$ calc.: 839.23934 m/z , found: 839.23934 m/z , $\Delta=0.00$ ppm.

9. Literature

- (1) May, V. *Dalton Trans.* **2009**, 10086.
- (2) Thompson, A. L.; Gaab, K. M.; Xu, J.; Bardeen, C. J.; Martínez, T. J. *J. Phys. Chem. A* **2004**, *108*, 671.
- (3) Lin, S. H.; Xiao, W. Z.; Dietz, W. *Phys. Rev. E* **1993**, *47*, 3698.
- (4) Gudipati, M. S. *J. Phys. Chem.* **1994**, *98*, 9750.
- (5) Pullerits, T.; Sundström, V. *Acc. Chem. Res.* **1996**, *29*, 381.
- (6) Damjanović, A.; Ritz, T.; Schulten, K. *Int. J. Quant. Chem.* **2000**, *77*, 139.
- (7) Hsu, C.-P.; Walla, P. J.; Head-Gordon, M.; Fleming, G. R. *J. Phys. Chem. B* **2001**, *105*, 11016.
- (8) Salverda, J. M.; Vengris, M.; Krueger, B. P.; Scholes, G. D.; Czarnoleski, A. R.; Novoderezhkin, V.; Amerongen, H. v.; Grondelle, R. v. *Biophys. J* **2003**, *84*, 450.
- (9) Balzani, V.; Credi, A.; Venturi, M. *Molecular Devices and Machines Vol. 2*; Wiley-VCH: Weinheim, 2008.
- (10) Balzani, V.; Bergamini, G.; Ceroni, P.; Marchi, E. *New J. Chem.* **2011**, *35*, 1944.
- (11) Nakamura, Y.; Aratani, N.; Osuka, A. *Chem. Soc. Rev.* **2007**, *36*, 831.
- (12) Lambert, C. *Angew. Chem. Int. Ed.* **2005**, *44*, 7337.
- (13) Cho, H. S.; Rhee, H.; Song, J. K.; Min, C.-K.; Takase, M.; Aratani, N.; Cho, S.; Osuka, A.; Joo, T.; Kim, D. *J. Am. Chem. Soc.* **2003**, *125*, 5849.
- (14) Kodis, G., Y. Terazono, P. A. Liddell, J. Andreasson, V. Garg, M. Hambourger, T. A. Moore, A. L. Moore, D. Gust *J. Am. Chem. Soc.* **2006**, *128*, 1818.
- (15) Morandeira, A.; Vauthey, E.; Schuwey, A.; Gossauer, A. *J. Phys. Chem. A* **2004**, *108*, 5741.
- (16) Biemans, H. A. M.; Rowan, A. E.; Verhoeven, A.; Vanoppen, P.; Latterini, L.; Foekema, J.; Schenning, A. P. H. J.; Meijer, E. W.; de Schryver, F. C.; Nolte, R. J. M. *J. Am. Chem. Soc.* **1998**, *120*, 11054.
- (17) Gust, D.; Moore, T. A.; Moore, A. L.; Gao, F.; Luttrull, D.; DeGraziano, J. M.; Ma, X. C.; Makings, L. R.; Lee, S. J. *J. Am. Chem. Soc.* **1991**, *113*, 3638.
- (18) Kuroda, Y.; Sugou, K.; Sasaki, K. *J. Am. Chem. Soc.* **2000**, *122*, 7833.
- (19) Steeger, M.; Lambert, C. *Chem. Eur. J.* **2012**, *18*, 11937.
- (20) Lambert, C.; Nöll, G. *Chem. Eur. J.* **2002**, *8*, 3467.
- (21) Rausch, D.; Lambert, C. *Org. Lett.* **2006**, *8*, 5037.
- (22) Liddell, P. A.; Kodis, G.; de la Garza, L.; Moore, A. L.; Moore, T. A.; Gust, D. *J. Phys. Chem. B* **2004**, *108*, 10256.
- (23) Keirstead, A. E.; Bridgewater, J. W.; Terazono, Y.; Kodis, G.; Straight, S.; Liddell, P. A.; Moore, A. L.; Moore, T. A.; Gust, D. *J. Am. Chem. Soc.* **2010**, *132*, 6588.
- (24) Sun, D., S. V. Rosokha, J. K. Kochi *Angew. Chem. Int. Ed.* **2005**, *44*, 5133.

-
- (25) Chebny, V. J.; Shukla, R.; Rathore, R. *J. Phys. Chem. A* **2006**, *110*, 13003.
- (26) Rosokha, S. V., I. S. Neretin, D. Sun, J. K. Kochi *J. Am. Chem. Soc.* **2006**, *128*, 9394.
- (27) Chebny, V. J.; Dhar, D.; Lindeman, S. V.; Rathore, R. *Org. Lett.* **2006**, *8*, 5041.
- (28) Traber, B.; Wolff, J. J.; Rominger, F.; Oeser, T.; Gleiter, R.; Goebel, M.; Wortmann, R. *Chem. Eur. J.* **2004**, *10*, 1227.
- (29) Rathore, R.; Burns, C. L.; Abdelwahed, S. A. *Org. Lett.* **2004**, *6*, 1689.
- (30) Rathore, R.; Burns, C. L.; Deselnicu, M. I. *Org. Lett.* **2001**, *3*, 2887.
- (31) Heckmann, A.; Lambert, C. *Angew. Chem. Int. Edit.* **2012**, *51*, 326.
- (32) Amthor, S.; Noller, B.; Lambert, C. *Chem. Phys.* **2005**, *316*, 141.
- (33) Lambert, C.; Nöll, G.; Schelter, J. *Nat. Mater.* **2002**, *1*, 69.
- (34) Lambert, C.; Nöll, G. *J. Chem. Soc.-Perkin Trans. 2* **2002**, 2039.
- (35) Heckmann, A.; Amthor, S.; Lambert, C. *Chem. Commun.* **2006**, 2959.
- (36) Law, K. Y. *Chem. Rev.* **1993**, *93*, 449.
- (37) Jungermann, S.; Riegel, N.; Müller, D.; Meerholz, K.; Nuyken, O. *Macromolecules* **2006**, *39*, 8911.
- (38) Nuyken, O.; Jungermann, S.; Wiederhirn, V.; Bacher, E.; Meerholz, K. *Monatsh. Chem.* **2006**, *137*, 811.
- (39) Zhao, H.; Tanjutco, C.; Thayumanavan, S. *Tetrahedron Lett.* **2001**, *42*, 4421.
- (40) Shirota, Y.; Kageyama, H. *Chem. Rev.* **2007**, *107*, 953.
- (41) Ning, Z.; Tian, H. *Chem. Commun.* **2009**, 5483.
- (42) Thelakkat, M. *Macromol. Mater. Eng.* **2002**, *287*, 442.
- (43) Veciana, J.; Ratera, I. *Polychlorotriphenylmethyl Radicals: Towards Multifunctional Molecular Materials*; John Wiley & Sons, 2010.
- (44) Heitele, H. *Angew. Chem. Int. Edit.* **1993**, *32*, 359.
- (45) Marcus, R. A. *J. Chem. Phys.* **1956**, *24*, 966.
- (46) Marcus, R. A.; Sutin, N. *Biochim. Biophys. Acta* **1985**, *811*, 265.
- (47) Brunshwig, B. S.; Sutin, N. *Coord. Chem. Rev.* **1999**, *187*, 233.
- (48) Marcus, R. A. *J. Chem. Phys.* **1965**, *43*, 679.
- (49) Marcus, R. A. *Discuss. Faraday Soc.* **1960**, *29*, 21.
- (50) Hänggi, P.; Talkner, P.; Borkovec, M. *Reviews of Modern Physics* **1990**, *62*, 251.
- (51) Horng, M. L.; Gardecki, J. A.; Papazyan, A.; Maroncelli, M. *J. Phys. Chem.* **1995**, *99*, 17311.
- (52) Jortner, J.; Bixon, M. *J. Chem. Phys.* **1988**, *88*, 167.
- (53) Cortes, J.; Heitele, H.; Jortner, J. *J. Phys. Chem.* **1994**, *98*, 2527.
- (54) Marcus, R. A. *J. Phys. Chem.* **1989**, *93*, 3078.
- (55) Creutz, C.; Newton, M. D.; Sutin, N. *J. Photochem. Photobiol. A: Chem.* **1994**, *82*, 47.
- (56) Brunshwig, B. S.; Creutz, C.; Sutin, N. *Chem. Soc. Rev.* **2002**, *31*, 168.
- (57) Hush, N. S. *Coord. Chem. Rev.* **1985**, *64*, 135.

-
- (58) Cave, R. J.; Newton, M. D. *Chem. Phys. Lett.* **1996**, *249*, 15.
- (59) Amthor, S.; Lambert, C. J. *J. Phys. Chem. A* **2005**, *110*, 1177.
- (60) Amthor, S.; Lambert, C. J. *J. Phys. Chem. A* **2006**, *110*, 3495.
- (61) Bixon, M.; Jortner, J. *J. Chem. Phys.* **1997**, *107*, 5154.
- (62) Newton, M. D. *Chem. Rev.* **1991**, *91*, 767.
- (63) Bixon, M.; Jortner, J.; Michel-Beyerle, M. E.; Ogrodnik, A. *Biochim. Biophys. Acta* **1989**, *977*, 273.
- (64) Bixon, M.; Jortner, J. *Chem. Phys.* **1993**, *176*, 467.
- (65) Scholes, G. D. *Annu. Rev. Phys. Chem.* **2003**, *54*, 57.
- (66) Kim, Y. H.; Jeong, D. H.; Kim, D.; Jeoung, S. C.; Cho, H. S.; Kim, S. K.; Aratani, N.; Osuka, A. *J. Am. Chem. Soc.* **2000**, *123*, 76.
- (67) Zieschang, F.; Schmiedel, A.; Holzapfel, M.; Ansorg, K.; Engels, B.; Lambert, C. J. *J. Phys. Chem. C* **2013**, *117*, 19816.
- (68) Kimura, A.; Kakitani, T.; Yamato, T. *J. Phys. Chem. B* **2000**, *104*, 9276.
- (69) Speiser, S. *Chem. Rev.* **1996**, *96*, 1953.
- (70) Förster, T. *Naturwiss.* **1946**, *33*, 166.
- (71) Stevens, J. A.; Link, J. J.; Zang, C.; Wang, L.; Zhong, D. *J. Phys. Chem. A* **2011**, *116*, 2610.
- (72) Förster, T. *Discuss. Faraday Soc.* **1959**, *27*, 7.
- (73) Hwang, I.; Scholes, G. D. *Chem. Mater.* **2010**, *23*, 610.
- (74) Beenken, W. J. D.; Pullerits, T. *J. Chem. Phys.* **2004**, *120*, 2490.
- (75) Sissa, C.; Manna, A. K.; Terenziani, F.; Painelli, A.; Pati, S. K. *Phys. Chem. Chem. Phys.* **2011**, *13*, 12734.
- (76) Scholes, G. D.; Curutchet, C.; Mennucci, B.; Cammi, R.; Tomasi, J. *J. Phys. Chem. B* **2007**, *111*, 6978.
- (77) Glasbeek, M.; Zhang, H. *Chem. Rev.* **2004**, *104*, 1929.
- (78) Toele, P.; van Gorp, J. J.; Glasbeek, M. *J. Phys. Chem. A* **2005**, *109*, 10479.
- (79) Maus, M.; Rettig, W.; Depaemelaere, S.; Onkelinx, A.; De Schryver, F. C.; Iwai, K. *Chem. Phys. Lett.* **1998**, *292*, 115.
- (80) Dexter, D. L. *J. Chem. Phys.* **1953**, *21*, 836.
- (81) Kasha, M.; Rawls, H. R.; Ashaf El-Bayoumi, M. *Pure Appl. Chem.* **1965**, *11*, 371.
- (82) McRae, E. G.; Kasha, M. *The molecular exciton model*; Academic Press, New York 3, 1964.
- (83) Rullière, C. *Femtosecond Laser Pulses*; Springer: New York, 2004.
- (84) Banerji, N. R. PhD Thesis, 2009.
- (85) van Stokkum, I. H. M.; Larsen, D. S.; van Grondelle, R. *Biochim. Biophys. Acta* **2004**, *1657*, 82.
- (86) Berera, R.; van Grondelle, R.; Kennis, J. M. *Photosynth Res* **2009**, *101*, 105.
- (87) Wynne, K.; Hochstrasser, R. M. *Chem. Phys.* **1993**, *171*, 179.

-
- (88) Jonas, D. M.; Lang, M. J.; Nagasawa, Y.; Joo, T.; Fleming, G. R. *J. Phys. Chem.* **1996**, *100*, 12660.
- (89) Ekvall, K.; van der Meulen, P.; Dhollande, C.; Berg, L.-E.; Pommeret, S.; Naskrecki, R.; Mialocq, J.-C. *Journal of Applied Physics* **2000**, *87*, 2340.
- (90) Liu, H.; Zhang, H.; Si, J.-H.; Yan, L.-H.; Chen, F.; Hou, X. *Chin. Phys. Lett.* **2011**, *28*, 86602.
- (91) The MathWorks Inc.: Natick, MA, 2005.
- (92) Dmitriev, V. G.; Gurzadyan, G. G.; Nikogosyan, D. N. *Handbook of Nonlinear Optical Crystals*; Springer-Verlag: Berlin, New York, Heidelberg, 1999.
- (93) Shen, Y. R. *The Principles of Nonlinear Optics*; John Wiley & Sons: New York, 1984.
- (94) Stegeman, G. I.; Stegeman, R. A. *Nonlinear Optics*; John Wiley & Sons, Inc.: New Jersey, 2012.
- (95) *Springer Handbook of Lasers and Optics*; Träger, F., Ed.; Springer: Berlin, 2007.
- (96) Saleh, B. E. A.; Teich, M. C. *Fundamentals of Photonics*; John Wiley & Sons, Inc., 1991.
- (97) Brodeur, A.; Chin, S. L. *J. Opt. Soc. Am. B* **1999**, *16*, 637.
- (98) Fork, R. L.; Tomlinson, W. J.; Shank, C. V.; Hirlimann, C.; Yen, R. *Opt. Lett.* **1983**, *8*, 1.
- (99) Wittmann, M.; Penzkofer, A. *Opt. Commun.* **1996**, *126*, 308.
- (100) *Coherent Raman Scattering Microscopy*; Cheng, J.; Xie, X. S., Eds.; CRC Press/Taylor & Francis Group, LLC., 2013.
- (101) Alfano, R. R.; Shapiro, S. L. *Physical Review Letters* **1970**, *24*, 592.
- (102) Midorikawa, K.; Kawano, H.; Suda, A.; Nagura, C.; Obara, M. *Applied Physics Letters* **2002**, *80*, 923.
- (103) Tayyab, I.; Gonçalo, F. *Journal of Optics* **2012**, *14*, 035201.
- (104) Lakowicz, J. R. *Principles of Fluorescence Spectroscopy*; 2nd ed.; Kluwer Academic/Plenum: New York, 1999.
- (105) Kawski, A. *Critical Reviews in Analytical Chemistry* **1993**, *23*, 459.
- (106) Liu, C.; Tang, K.-C.; Zhang, H.; Pan, H.-A.; Hua, J.; Li, B.; Chou, P.-T. *J. Phys. Chem. A* **2012**, *116*, 12339.
- (107) Wynne, K.; Hochstrasser, R. M. *Chemical Physics* **1993**, *171*, 179.
- (108) Knox, R. S.; Gülen, D.; Lotterhos, K. E. *Chem. Phys. Lett.* **2002**, *361*, 285.
- (109) Vanderwerf, D. F. *Applied Prismatic and Reflective Optics*; SPIE Press, 2010.
- (110) Litfin, G. *Technische Optik in der Praxis, 3. Ed.*; Springer, 2004.
- (111) Feynman, P. F.; Leighton, R. B.; Sands, M. *Feynman Lectures on Physics, Vol. II*; Basic Books, 2011.
- (112) Yeh, P. *Opt. Commun.* **1978**, *26*, 289.
- (113) Subrahmanyam, N.; Lal, B.; Avadhanulu, M. N. *A Textbook of Optics*; S. Chand & Company Ltd.: New Delhi, 2006.

-
- (114) Gross, H.; Dörband, B.; Müller, H. *Handbook of Optical Systems: Volume 5: Metrology and Optical Components and Systems*; Wiley-VCH Verlag GmbH & Co. KGaA: Weinheim, 2012.
- (115) Eimerl, D.; Davis, L.; Velsko, S.; Graham, E. K.; Zalkin, A. *Journal of Applied Physics* **1987**, *62*, 1968.
- (116) Personal communication with an employee of Ultrafast Systems.
- (117) Goldstein, D. *Polarized Light, Revised and Expanded*; CRC Press, 2003.
- (118) Ratera, I.; Ruiz-Molina, D.; Sporer, C.; Marcen, S.; Montant, S.; Letard, J. F.; Freysz, E.; Rovira, C.; Veciana, J. *Polyhedron* **2003**, *22*, 1851.
- (119) Ballester, M.; Molinet, C.; Castaner, J. *J. Am. Chem. Soc.* **1960**, *82*, 4254.
- (120) Ballester, M.; Riera, J.; Castaner, J.; Rodriguez, A.; Rovira, C.; Veciana, J. *J. Org. Chem.* **1982**, *47*, 4498.
- (121) Armet, O.; Veciana, J.; Rovira, C.; Riera, J.; Castaner, J.; Molins, E.; Rius, J.; Miravittles, C.; Olivella, S.; Brichfeus, J. *J. Phys. Chem.* **1987**, *91*, 5608.
- (122) Heckmann, A.; Lambert, C.; Goebel, M.; Wortmann, R. *Angew. Chem. Int. Edit.* **2004**, *43*, 5851.
- (123) Heckmann, A.; Dummmler, S.; Pauli, J.; Margraf, M.; Kohler, J.; Stich, D.; Lambert, C.; Fischer, I.; Resch-Genger, U. *J. Phys. Chem. C* **2009**, *113*, 20958.
- (124) Heckmann, A.; Lambert, C. *J. Am. Chem. Soc.* **2007**, *129*, 5515.
- (125) Rovira, C.; Ruiz-Molina, D.; Elsner, O.; Vidal-Gancedo, J.; Bonvoisin, J.; Launay, J. P.; Veciana, J. *Chem. Eur. J.* **2001**, *7*, 240.
- (126) Lloveras, V.; Vidal-Gancedo, J.; Figueira-Duarte, T. M.; Nierengarten, J.-F.; Novoa, J. J.; Mota, F.; Ventosa, N.; Rovira, C.; Veciana, J. *J. Am. Chem. Soc.* **2011**, *133*, 5818.
- (127) Lloveras, V.; Vidal-Gancedo, J.; Ruiz-Molina, D.; Figueira-Duarte, T. M.; Nierengarten, J. F.; Veciana, J.; Rovira, C. *Farad. Discuss.* **2006**, *131*, 291.
- (128) Reitzenstein, D.; Quast, T.; Kanal, F.; Kullmann, M.; Ruetzel, S.; Hammer, M. S.; Deibel, C.; Dyakonov, V.; Brixner, T.; Lambert, C. *Chem. Mater.* **2010**, *22*, 6641.
- (129) Ratera, I.; Veciana, J. *Chem. Soc. Rev.* **2012**, *41*, 303.
- (130) Crivillers, N.; Mas-Torrent, M.; Vidal-Gancedo, J.; Veciana, J.; Rovira, C. *J. Am. Chem. Soc.* **2008**, *130*, 5499.
- (131) Crivillers, N.; Mas-Torrent, M.; Perruchas, S.; Roques, N.; Vidal-Gancedo, J.; Veciana, J.; Rovira, C.; Basabe-Desmonts, L.; Ravoo, B. J.; Crego-Calama, M.; Reinhoudt, D. N. *Angew. Chem. Int. Edit.* **2007**, *46*, 2215.
- (132) Mas-Torrent, M.; Crivillers, N.; Mugnaini, V.; Ratera, I.; Rovira, C.; Veciana, J. *J. Mater. Chem.* **2009**, *19*, 1691.
- (133) Roques, N.; Maspoch, D.; Dăteu, A.; Wurst, K.; Ruiz-Molina, D.; Rovira, C.; Veciana, J. *Polyhedron* **2007**, *26*, 1934.

-
- (134) MasPOCH, D.; Domingo, N.; Ruiz-Molina, D.; WurSt, K.; Vaughan, G.; Tejada, J.; Rovira, C.; Veciana, J. *Angew. Chem. Int. Edit.* **2004**, *43*, 1828.
- (135) MasPOCH, D.; Ruiz-Molina, D.; WurSt, K.; Domingo, N.; Cavallini, M.; Biscarini, F.; Tejada, J.; Rovira, C.; Veciana, J. *Nature Materials* **2003**, *2*, 190.
- (136) Dang, V.; Wang, J.; Feng, S.; Buron, C.; Villamena, F. A.; Wang, P. G.; Kuppusamy, P. *Bioorg. Med. Chem. Lett.* **2007**, *17*, 4062.
- (137) Kutala, V. K.; Villamena, F. A.; Ilangovan, G.; MasPOCH, D.; Roques, N.; Veciana, J.; Rovira, C.; Kuppusamy, P. *J. Phys. Chem. B* **2008**, *112*, 158.
- (138) Mesa, J. A.; Velazquez-Palenzuela, A.; Brillas, E.; Coll, J.; Torres, J. L.; Julia, L. *J. Org. Chem.* **2012**, *77*, 1081.
- (139) Schore, N. E. *Chem. Rev.* **1988**, *88*, 1081.
- (140) Markina, N. A.; Mancuso, R.; Neuenswander, B.; Lushington, G. H.; Larock, R. C. *Acc. Comb. Sci.* **2011**, *13*, 265.
- (141) Huang, H.; Liu, H.; Jiang, H.; Chen, K. *J. Org. Chem.* **2008**, *73*, 6037.
- (142) Ehlers, P.; Neubauer, A.; Lochbrunner, S.; Villinger, A.; Langer, P. *Org. Lett.* **2011**, *13*, 1618.
- (143) Rudolph, M.; ElchSoft.com: 2011.
- (144) Torres, J. L.; Varela, B.; Brillas, E.; Julia, L. *Chem. Commun.* **2003**, *0*, 74.
- (145) Castellanos, S.; Velasco, D.; Lopez-Calahorra, F.; Brillas, E.; Julia, L. *J. Org. Chem.* **2008**, *73*, 3759.
- (146) The MM2 optimisation is not able to handle radical centres. We exchanged therefore all radical centres by nitrogen atoms to get rough estimates for the distances in the molecules.
- (147) CambridgeSoft Corp: Cambridge, MA, 1999, p CS Chem3D Pro.
- (148) Barriere, F.; Geiger, W. E. *J. Am. Chem. Soc.* **2006**, *128*, 3980.
- (149) Wienk, M. M.; Janssen, R. A. J. *J. Am. Chem. Soc.* **1997**, *119*, 4492.
- (150) Margerum, J. D. *J. Am. Chem. Soc.* **1965**, *87*, 3772.
- (151) Ballester, M.; Pascual, I.; Carreras, C.; Vidal-Gancedo, J. *J. Am. Chem. Soc.* **1994**, *116*, 4205.
- (152) Sato, K.; Yano, M.; Furuichi, M.; Shiomi, D.; Takui, T.; Abe, K.; Itoh, K.; Higuchi, A.; Katsuma, K.; Shirota, Y. *J. Am. Chem. Soc.* **1997**, *119*, 6607.
- (153) Ballester, M.; Castaner, J.; Riera, J.; Pascual, I. *J. Am. Chem. Soc.* **1984**, *106*, 3365.
- (154) Reitz, D. C.; Weissman, S. I. *J. Chem. Phys.* **1960**, *33*, 700.
- (155) Weil, J. A.; Bolton, J. R. *Electron Paramagnetic Resonance: Elementary Theory and Practical Applications Ed. 2*; John Wiley & Sons, 2006.
- (156) Kattnig, D. R.; Mladenova, B.; Grampp, G.; Kaiser, C.; Heckmann, A.; Lambert, C. *J. Phys. Chem. C* **2009**, *113*, 2983.
- (157) Koshechko, V. G.; Titov, V. E.; Pokhodenko, V. D. *Theor. Exp. Chem.* **1983**, *19*, 143.
- (158) Gerson, F.; Walter, H. *Electron Spin Resonance Spectroscopy of Organic Radicals* Wiley-VCH: Weinheim, 2003.

-
- (159) *Mixed Valence Compounds*; Brown, E. D., Ed.; D. Reidel Publishing Company: Dordrecht, 1980.
- (160) Hupp, J. T.; Dong, Y.; Blackburn, R. L.; Lu, H. *J. Phys. Chem.* **1993**, *97*, 3278.
- (161) Nelsen, S. F. *Chem. Eur. J.* **2000**, *6*, 581.
- (162) Nelsen, S. F.; Ismagilov, R. F.; Trieber, D. A. *Science* **1997**, *278*, 846.
- (163) Balzani, V. *Electron Transfer in Chemistry*; Wiley-VCH: Weinheim, 2001; Vol. 2.
- (164) Kaupp, M.; Renz, M.; Parthey, M.; Stolte, M.; Wurthner, F.; Lambert, C. *Phys. Chem. Chem. Phys.* **2011**, *13*, 16973.
- (165) Because the radicalisation process in **Star** and in **Star-Model** was not quantitative their spectra are contaminated to a certain degree with the α -H precursor. However, these “impurities” should have no influence on the position and shape of the IV-CT bands and this is what we are mainly interested in.
- (166) Gould, I. R.; Noukakis, D.; Gomez-Jahn, L.; Young, R. H.; Goodman, J. L.; Farid, S. *Chem. Phys.* **1993**, *176*, 439.
- (167) Nelsen, S. F.; Ramm, M. T.; Wolff, J. J.; Powell, D. R. *J. Am. Chem. Soc.* **1997**, *119*, 6863.
- (168) Stahl, R.; Lambert, C.; Kaiser, C.; Wortmann, R.; Jakober, R. *Chem. Eur. J.* **2006**, *12*, 2358.
- (169) Kapturkiewicz, A.; Herbich, J.; Karpiuk, J.; Nowacki, J. *J. Phys. Chem. A* **1997**, *101*, 2332.
- (170) The least squares fit of the reduced IV-CT band of **Star-Model** in acetonitrile is not shown because the signal-to-noise ratio as well as the intensity of the absorption is much lower due to low solubility.
- (171) Mataga, N.; Kaifu, Y.; Koizumi, M. *Bull. Chem. Soc. Jpn.* **1956**, *29*, 465.
- (172) Lippert, E. *Z. Elektrochem. Angew. Phys. Chem.* **1957**, *61*, 962.
- (173) Both approaches to calculate $\Delta\mu_{12}$ have to be used with care. The methodology according to Lippert and Mataga is highly dependent on the estimated magnitude of a_0 which can lead to high errors due to its third power. Its applicability was nevertheless proven for **V2** by comparison to EOA measurements.¹²⁴ In contrast, the TDDFT calculations gave in fact reasonable results for bistriarylamine based intervalence compounds though no dipole moment differences have been calculated for compounds with a PCTM acceptor centre.¹⁶⁴
- (174) Spectrum Software Associates 1999–2004
- (175) Maksimenka, R.; Margraf, M.; Köhler, J.; Heckmann, A.; Lambert, C.; Fischer, I. *Chem. Phys.* **2008**, *347*, 436.
- (176) Duvanel, G.; Grilj, J.; Chaumeil, H.; Jacques, P.; Vauthey, E. *Photochem. Photobiol. Sci.* **2010**, *9*, 908.
- (177) Maus, M.; Rettig, W.; Jonusauskas, G.; Lapouyade, R.; Rullière, C. *J. Phys. Chem. A* **1998**, *102*, 7393.
- (178) Mohammed, O. F.; Sarhan, A. A. O. *Chem. Phys.* **2010**, *372*, 17.
- (179) Ramakrishna, G.; Goodson, T. *J. Phys. Chem. A* **2007**, *111*, 993.

-
- (180) Ramakrishna, G.; Bhaskar, A.; Goodson, T. *J. Phys. Chem. B* **2006**, *110*, 20872.
- (181) Sung, J.; Kim, P.; Lee, Y. O.; Kim, J. S.; Kim, D. *J. Phys. Chem. Lett.* **2011**, *2*, 818.
- (182) Malval, J.-P.; Chaumeil, H.; Rettig, W.; Kharlanov, V.; Diemer, V.; Ay, E.; Morlet-Savary, F.; Poizat, O. *Phys. Chem. Chem. Phys.* **2012**, *14*, 562.
- (183) Banerji, N.; Angulo, G.; Barabanov, I.; Vauthey, E. *J. Phys. Chem. A* **2008**, *112*, 9665.
- (184) Kovalenko, S. A.; Schanz, R.; Hennig, H.; Ernsting, N. P. *J. Chem. Phys.* **2001**, *115*, 3256.
- (185) Kanal, F.; Ruetzel, S.; Han, L.; Moos, M.; Holzapfel, M.; Brixner, T.; Lambert, C. *J. Phys. Chem. C* **2014**, submitted.
- (186) Ratera, I.; Sporer, C.; Ruiz-Molina, D.; Ventosa, N.; Baggerman, J.; Brouwer, A. M.; Rovira, C.; Veciana, J. *J. Am. Chem. Soc.* **2007**, *129*, 6117.
- (187) Efrima, S.; Bixon, M. *Chem. Phys. Lett.* **1974**, *25*, 34.
- (188) Ulstrup, J.; Jortner, J. *J. Chem. Phys.* **1975**, *63*, 4358.
- (189) The fitting routine was programmed using the MatLab software package. See the SI for the script.
- (190) The structural model was obtained by MMFF94 optimisation using CS Chem3D Pro; CambridgeSoft Corp: 1999. Therefore the radical carbon atoms had to be exchanged by nitrogen atoms.
- (191) Förster, T. *Ann. Phys.* **1948**, *437*, 55.
- (192) Bonvoisin, J.; Launay, J.-P.; Van der Auweraer, M.; De Schryver, F. C. *J. Phys. Chem.* **1994**, *98*, 5052.
- (193) Varnavski, O.; Yan, X.; Mongin, O.; Blanchard-Desce, M.; Goodson, T. *J. Phys. Chem. C* **2006**, *111*, 149.
- (194) Goodson, T. *Annu. Rev. Phys. Chem.* **2005**, *56*, 581.
- (195) Banerji, N. *J. Mater. Chem. C* **2013**, *1*, 3052.
- (196) Collini, E.; Scholes, G. D. *Science* **2009**, *323*, 369.
- (197) Leegwater, J. A. *J. Phys. Chem.* **1996**, *100*, 14403.
- (198) Zhou, G.; Ho, C.-L.; Wong, W.-Y.; Wang, Q.; Ma, D.; Wang, L.; Lin, Z.; Marder, T. B.; Beeby, A. *Adv. Funct. Mater.* **2008**, *18*, 499.
- (199) Noda, T.; Shirota, Y. *J. Lumin.* **2000**, *87-89*, 1168.
- (200) Noda, T.; Shirota, Y. *J. Am. Chem. Soc.* **1998**, *120*, 9714.
- (201) Doi, H.; Kinoshita, M.; Okumoto, K.; Shirota, Y. *Chem. Mater.* **2003**, *15*, 1080.
- (202) Yamaguchi, S.; Wakamiya, A. *Pure Appl. Chem.* **2006**, *78*, 1413.
- (203) Zhao, C. H.; Sakuda, E.; Wakamiya, A.; Yamaguchi, S. *Chem. Eur. J.* **2009**, *15*, 10603.
- (204) Hudson, Z. M.; Wang, S. N. *Acc. Chem. Res.* **2009**, *42*, 1584.
- (205) Yamaguchi, S.; Shirasaka, T.; Tamao, K. *Org. Lett.* **2000**, *2*, 4129.
- (206) Bai, D.-R.; Liu, X.-Y.; Wang, S. *Chem. Eur. J.* **2007**, *13*, 5713.
- (207) Reitzenstein, D.; Lambert, C. *Macromolecules* **2009**, *42*, 773.

- (208) Yuan, Z.; Collings, J. C.; Taylor, N. J.; Marder, T. B.; Jardin, C.; Halet, J.-F. *J. Solid State Chem.* **2000**, *154*, 5.
- (209) Jia, W.-L.; Song, D.; Wang, S. *J. Org. Chem.* **2003**, *68*, 701.
- (210) Liu, Z.-Q.; Fang, Q.; Wang, D.; Cao, D.-X.; Xue, G.; Yu, W.-T.; Lei, H. *Chem. Eur. J.* **2003**, *9*, 5074.
- (211) Sun, Y.; Wang, S. N. *Inorganic Chemistry* **2010**, *49*, 4394.
- (212) Zhao, S. B.; Wucher, P.; Hudson, Z. M.; McCormick, T. M.; Liu, X. Y.; Wang, S. N.; Feng, X. D.; Lu, Z. H. *Organomet.* **2008**, *27*, 6446.
- (213) Jaekle, F. *Chem. Rev.* **2010**, *110*, 3985.
- (214) Heilmann, J. B.; Scheibitz, M.; Qin, Y.; Sundararaman, A.; Jäkle, F.; Kretz, T.; Bolte, M.; Lerner, H.-W.; Holthausen, M. C.; Wagner, M. *Angew. Chem. Int. Edit.* **2006**, *45*, 920.
- (215) Yuan, Z.; Taylor, N. J.; Marder, T. B.; Williams, I. D.; Kurtz, S. K.; Cheng, L. T. *J. Chem. Soc., Chem. Commun.* **1990**, 1489.
- (216) Yuan, Z.; Taylor, N. J.; Sun, Y.; Marder, T. B.; Williams, I. D.; Cheng, L.-T. *J. Organomet. Chem.* **1993**, *449*, 27.
- (217) Yuan, Z.; Entwistle, C. D.; Collings, J. C.; Albesa-Jove, D.; Batsanov, A. S.; Howard, J. A. K.; Taylor, N. J.; Kaiser, H. M.; Kaufmann, D. E.; Poon, S.-Y.; Wong, W.-Y.; Jardin, C.; Fathallah, S.; Boucekkine, A.; Halet, J.-F.; Marder, T. B. *Chem. Eur. J.* **2006**, *12*, 2758.
- (218) Lequan, M.; Lequan, R. M.; Ching, K. C. *J. Mater. Chem.* **1991**, *1*, 997.
- (219) Yuan, Z.; Taylor, N. J.; Ramachandran, R.; Marder, T. B. *Appl. Organomet. Chem.* **1996**, *10*, 305.
- (220) Entwistle, C. D.; Marder, T. B. *Chem. Mater.* **2004**, *16*, 4574.
- (221) Lequan, M.; Lequan, R. M.; Ching, K. C.; Barzoukas, M.; Fort, A.; Lahoucine, H.; Bravic, G.; Chasseau, D.; Gaultier, J. *J. Mater. Chem.* **1992**, *2*, 719.
- (222) Charlot, M.; Porres, L.; Entwistle, C. D.; Beeby, A.; Marder, T. B.; Blanchard-Desce, M. *Phys. Chem. Chem. Phys.* **2005**, *7*, 600.
- (223) Liu, Y.; Xu, X.; Zheng, F. K.; Cui, Y. *Angew. Chem. Int. Ed.* **2008**, *47*, 4538.
- (224) Collings, J. C.; Poon, S. Y.; Le Droumaguet, C.; Charlot, M.; Katan, C.; Palsson, L. O.; Beeby, A.; Mosely, J. A.; Kaiser, H. M.; Kaufmann, D.; Wong, W. Y.; Blanchard-Desce, M.; Marder, T. B. *Chem. Eur. J.* **2009**, *15*, 198.
- (225) Entwistle, C. D.; Collings, J. C.; Steffen, A.; Palsson, L.-O.; Beeby, A.; Albesa-Jove, D.; Burke, J. M.; Batsanov, A. S.; Howard, J. A. K.; Mosely, J. A.; Poon, S.-Y.; Wong, W.-Y.; Ibersiene, F.; Fathallah, S.; Boucekkine, A.; Halet, J.-F.; Marder, T. B. *J. Mater. Chem.* **2009**, *19*, 7532.
- (226) Pron, A.; Baumgarten, M.; Müllen, K. *Org. Lett.* **2010**, *12*, 4236.
- (227) Wade, C. R.; Broomsgrove, A. E. J.; Aldridge, S.; Gabbai, F. P. *Chem. Rev.* **2010**, *110*, 3958.
- (228) Pron, A.; Zhou, G.; Norouzi-Arasi, H.; Baumgarten, M.; Müllen, K. *Org. Lett.* **2009**, *11*, 3550.

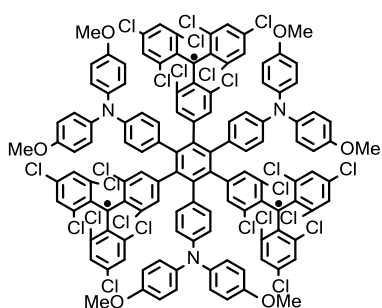
- (229) Zhou, G.; Baumgarten, M.; Müllen, K. *J. Am. Chem. Soc.* **2008**, *130*, 12477.
- (230) Schmidt, H. C.; Reuter, L. G.; Hamacek, J.; Wenger, O. S. *J. Org. Chem.* **2011**, *76*, 9081.
- (231) Hudnall, T. W.; Gabbai, F. P. *J. Am. Chem. Soc.* **2007**, *129*, 11978.
- (232) Chiu, C. W.; Gabbai, F. P. *Dalton Trans.* **2008**, 814.
- (233) Agou, T.; Sekine, M.; Kobayashi, J.; Kawashima, T. *J. Organomet. Chem.* **2009**, *694*, 3833.
- (234) Huh, J. O.; Do, Y.; Lee, M. H. *Organometallics* **2008**, *27*, 1022.
- (235) Wade, C. R.; Gabbai, F. P. *Inorganic Chemistry* **2010**, *49*, 714.
- (236) Megerle, U.; Selmaier, F.; Lambert, C.; Riedle, E.; Lochbrunner, S. *Phys. Chem. Chem. Phys.* **2008**, *10*, 6245.
- (237) Megerle, U.; Lambert, C.; Riedle, E.; Lochbrunner, S. *Springer Ser. Chem. Phys.* **2009**, *92*, 316.
- (238) Entwistle, C. D.; Marder, T. B. *Angew. Chem. Int. Ed.* **2002**, *41*, 2927.
- (239) Doty, J. C.; Babb, B.; Grisdale, P. J.; Glogowski, M.; Williams, J. L. R. *J. Organometal. Chem.* **1972**, *38*, 229.
- (240) Kaim, W.; Schulz, A. *Angew. Chem. Int. Ed.* **1984**, *23*, 615.
- (241) Ester, C.; Maderna, A.; Pritzkow, H.; Siebert, W. *Eur. J. Inorg. Chem.* **2000**, 1177.
- (242) Steffen, A.; Ward, R. M.; Jones, W. D.; Marder, T. B. *Coord. Chem. Rev.* **2010**, *254*, 1950.
- (243) Kiesele, H. *Anal. Chem.* **1981**, *53*, 1952.
- (244) Schulz, A.; Kaim, W. *Chem. Ber.* **1989**, *122*, 1863.
- (245) Curtis, J. C.; Roberts, J. A.; Blackbourn, R. L.; Dong, Y. H.; Massum, M.; Johnson, C. S.; Hupp, J. T. *Inorganic Chemistry* **1991**, *30*, 3856.
- (246) Yuan, M. S.; Liu, Z. Q.; Fang, Q. *J. Org. Chem.* **2007**, *72*, 7915.
- (247) Strickler, S. J.; Berg, R. A. *J. Chem. Phys.* **1962**, *37*, 814.
- (248) Fiedler, J.; Zalis, S.; Klein, A.; Hornung, F. M.; Kaim, W. *Inorganic Chemistry* **1996**, *35*, 3039.
- (249) Hall, R. D.; Valeur, B.; Weber, G. *Chem. Phys. Lett.* **1985**, *116*, 202.
- (250) Verbouwe, W.; Van der Auweraer, M.; De Schryver, F. C.; Piet, J. J.; Warman, J. M. *J. Am. Chem. Soc.* **1998**, *120*, 1319.
- (251) Demidov, A. A.; Andrews, D. L. *Photochem. Photobiol.* **1996**, *63*, 39.
- (252) Sohn, H.; Letant, S.; Sailor, M. J.; Trogler, W. C. *J. Am. Chem. Soc.* **2000**, *122*, 5399.
- (253) Zhang, S. W.; Swager, T. M. *J. Am. Chem. Soc.* **2003**, *125*, 3420.
- (254) Rao, Y. L.; Amarne, H.; Zhao, S. B.; McCormick, T. M.; Martic, S.; Sun, Y.; Wang, R. Y.; Wang, S. N. *J. Am. Chem. Soc.* **2008**, *130*, 12898.
- (255) Wolfram Research; Inc. *Mathematica, Version 7.0* Champaign, IL, 2008.
- (256) Gans, P.; Sabatini, A.; Vacca, A. *Talanta* **1996**, *43*, 1739.
- (257) Steeger, M.; Griesbeck, S.; Schmiedel, A.; Holzapfel, M.; Krummenacher, I.; Lambert, C.; Braunschweig, H. *Phys. Chem. Chem. Phys.* **2015**, submitted.

- (258) Grabowski, Z. R.; Rotkiewicz, K.; Rettig, W. *Chem. Rev.* **2003**, *103*, 3899.
- (259) van der Meer, M. J.; Zhang, H.; Glasbeek, M. *J. Chem. Phys.* **2000**, *112*, 2878.
- (260) van Veldhoven, E.; Zhang, H.; Rettig, W.; Brown, R. G.; Hepworth, J. D.; Glasbeek, M. *Chem. Phys. Lett.* **2002**, *363*, 189.
- (261) Braslavsky, S. E.; Fron, E.; Rodriguez, H. B.; Roman, E. S.; Scholes, G. D.; Schweitzer, G.; Valeur, B.; Wirz, J. *Photochem. Photobiol. Sci.* **2008**, *7*, 1444.
- (262) Völker, S. F.; Schmiedel, A.; Holzapfel, M.; Renziehausen, K.; Engel, V.; Lambert, C. *J. Phys. Chem. C* **2014**, *118*, 17467.
- (263) Pullerits, T.; Hess, S.; Herek, J. L.; Sundström, V. *J. Phys. Chem. B* **1997**, *101*, 10560.
- (264) Wang, S.; Hall, L.; Diev, V. V.; Haiges, R.; Wei, G.; Xiao, X.; Djurovich, P. I.; Forrest, S. R.; Thompson, M. E. *Chem. Mater.* **2011**, *23*, 4789.
- (265) Wei, G.; Wang, S.; Renshaw, K.; Thompson, M. E.; Forrest, S. R. *ACS Nano* **2010**, *4*, 1927.
- (266) Wei, G.; Xiao, X.; Wang, S.; Zimmerman, J. D.; Sun, K.; Diev, V. V.; Thompson, M. E.; Forrest, S. R. *Nano Letters* **2011**, *11*, 4261.
- (267) Kuang, D.; Walter, P.; Nüesch, F.; Kim, S.; Ko, J.; Comte, P.; Zakeeruddin, S. M.; Nazeeruddin, M. K.; Grätzel, M. *Langmuir* **2007**, *23*, 10906.
- (268) Mayerhöffer, U.; Deing, K.; Groß, K.; Braunschweig, H.; Meerholz, K.; Würthner, F. *Angew. Chem. Int. Edit.* **2009**, *48*, 8776.
- (269) Deing, K. C.; Mayerhoffer, U.; Wurthner, F.; Meerholz, K. *Phys. Chem. Chem. Phys.* **2012**, *14*, 8328.
- (270) Emmelius, M.; Pawlowski, G.; Vollmann, H. W. *Angew. Chem. Int. Edit.* **1989**, *28*, 1445.
- (271) Scherer, D.; Dörfler, R.; Feldner, A.; Vogtmann, T.; Schwoerer, M.; Lawrentz, U.; Grahn, W.; Lambert, C. *Chemical Physics* **2002**, *279*, 179.
- (272) Ohira, S.; Rudra, I.; Schmidt, K.; Barlow, S.; Chung, S.-J.; Zhang, Q.; Matichak, J.; Marder, S. R.; Brédas, J.-L. *Chem. Eur. J.* **2008**, *14*, 11082.
- (273) Webster, S.; Odom, S. A.; Padilha, L. A.; Przhonska, O. V.; Peceli, D.; Hu, H.; Nootz, G.; Kachkovski, A. D.; Matichak, J.; Barlow, S.; Anderson, H. L.; Marder, S. R.; Hagan, D. J.; Van Stryland, E. W. *J. Phys. Chem. B* **2009**, *113*, 14854.
- (274) Webster, S.; Fu, J.; Padilha, L. A.; Przhonska, O. V.; Hagan, D. J.; Van Stryland, E. W.; Bondar, M. V.; Slominsky, Y. L.; Kachkovski, A. D. *Chemical Physics* **2008**, *348*, 143.
- (275) Collini, E.; Carlotto, S.; Ferrante, C.; Bozio, R.; Polimeno, A.; Bloino, J.; Barone, V.; Ronchi, E.; Beverina, L.; Pagani, G. A. *Phys. Chem. Chem. Phys.* **2011**, *13*, 12087.
- (276) Ajayaghosh, A.; Arunkumar, E.; Daub, J. *Angew. Chem. Int. Edit.* **2002**, *41*, 1766.
- (277) Ros-Lis, J. V.; Martinez-Manez, R.; Soto, J. *Chem. Commun.* **2002**, *0*, 2248.
- (278) Ros-Lis, J. V.; Marcos, M. D.; Martínez-Máñez, R.; Rurack, K.; Soto, J. *Angew. Chem. Int. Edit.* **2005**, *44*, 4405.

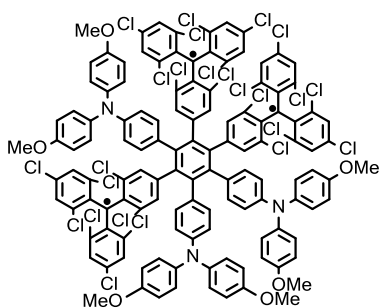
- (279) Ros-Lis, J. V.; Martínez-Máñez, R.; Sancenón, F.; Soto, J.; Spieles, M.; Rurack, K. *Chem. Eur. J.* **2008**, *14*, 10101.
- (280) Völker, S. F.; Uemura, S.; Limpinsel, M.; Mingeback, M.; Deibel, C.; Dyakonov, V.; Lambert, C. *Macromolecular Chemistry and Physics* **2010**, *211*, 1098.
- (281) Gerold, J.; Holzenkamp, U.; Meier, H. *Eur. J. Org. Chem.* **2001**, 2757.
- (282) Keil, D.; Hartmann, H. *Dyes Pigm.* **2001**, *49*, 161.
- (283) Reed, M. W.; Pollart, D. J.; Perri, S. T.; Foland, L. D.; Moore, H. W. *J. Org. Chem.* **1988**, *53*, 2477.
- (284) Paquette, L. A.; Morwick, T. M. *J. Am. Chem. Soc.* **1997**, *119*, 1230.
- (285) Völker, S. PhD Thesis, 2014.
- (286) Bertrand, G.; Tortech, L.; Fichou, D.; Malacria, M.; Aubert, C.; Gandon, V. *Organometallics* **2011**, *31*, 126.
- (287) J., D.; C., T. US, 2002; Vol. WO0213764 (A2) - METHODS FOR TREATING SUBJECTS INFECTED WITH A HERPES VIRUS OR NEISSERIA GONORRHEAE
- (288) Frost, J. M.; Dart, M. J.; Tietje, K. R.; Garrison, T. R.; Grayson, G. K.; Daza, A. V.; El-Kouhen, O. F.; Miller, L. N.; Li, L.; Yao, B. B.; Hsieh, G. C.; Pai, M.; Zhu, C. Z.; Chandran, P.; Meyer, M. D. *Journal of Medicinal Chemistry* **2008**, *51*, 1904.
- (289) Huang, S.; Petersen, T. B.; Lipshutz, B. H. *J. Am. Chem. Soc.* **2010**, *132*, 14021.
- (290) Jiang, L.; Lu, X.; Zhang, H.; Jiang, Y.; Ma, D. *J. Org. Chem.* **2009**, *74*, 4542.
- (291) Busch-Petersen, J.; Hill, W. A.; Fan, P.; Khanolkar, A.; Xie, X.-Q.; Tius, M. A.; Makriyannis, A. *Journal of Medicinal Chemistry* **1996**, *39*, 3790.
- (292) Rakshit, S.; Patureau, F. W.; Glorius, F. *J. Am. Chem. Soc.* **2010**, *132*, 9585.
- (293) Enhnen, A.; Karabelas, K.; Heerding, J. M.; Moore, H. W. *J. Org. Chem.* **1990**, *55*, 1177.
- (294) Kim, S.; Mor, G. K.; Paulose, M.; Varghese, O. K.; Baik, C.; Grimes, C. A. *Langmuir* **2010**, *26*, 13486.
- (295) The MM2 optimisation is not able to handle the formal charges at the squaraine core. So the squaraine was calculated in its doubly reduced form to get rough estimates for the distances in the molecules.
- (296) LeSuer, R. J.; Buttolph, C.; Geiger, W. E. *Anal. Chem.* **2004**, *76*, 6395.
- (297) Santi, S.; Orian, L.; Durante, C.; Bencze, E. Z.; Bisello, A.; Donoli, A.; Ceccon, A.; Benetollo, F.; Crociani, L. *Chem. Eur. J.* **2007**, *13*, 7933.
- (298) Salbeck, J. PhD Thesis, 1988.
- (299) Melhuish, W. H. *J. Phys. Chem.* **1961**, *65*, 229.
- (300) Dorfman, R. C.; Lin, Y.; Fayer, M. D. *J. Phys. Chem.* **1989**, *93*, 6388.
- (301) Stoll, S.; Schweiger, A. *Journal of Magnetic Resonance* **2006**, *178*, 42.
- (302) Frisch, M. J., et. al. *Gaussian 09*; Revision D.01: Gaussian, Inc., Wallingford CT, 2013.

- (303) Leonard, J.; Lygo, B.; Procter, G. *Advanced Practical Organic Chemistry*; 2nd ed.; CRC Press Inc., 1994.

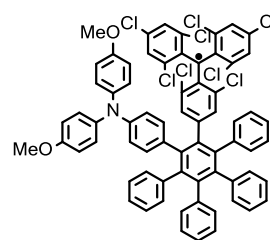
10. Table of formulas



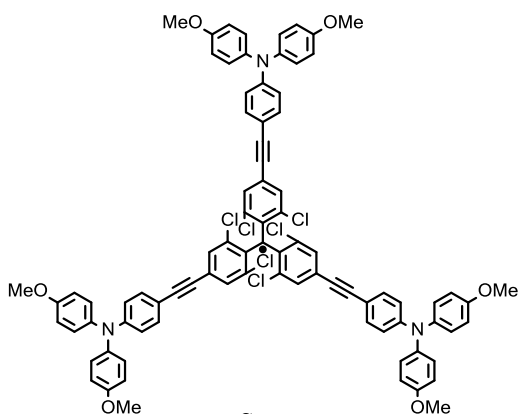
HAB-S



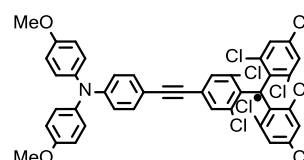
HAB-A



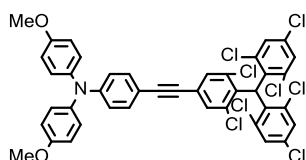
HAB-Model



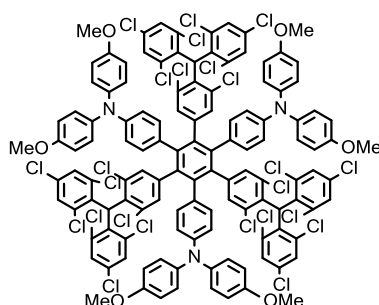
Star



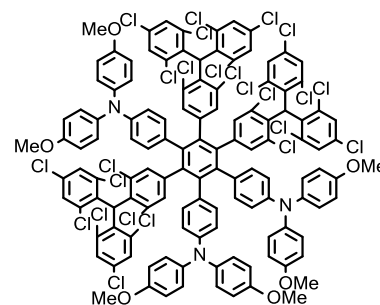
Star-Model



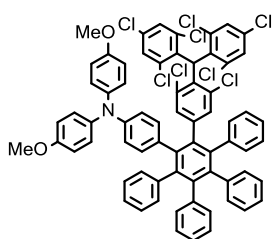
P6



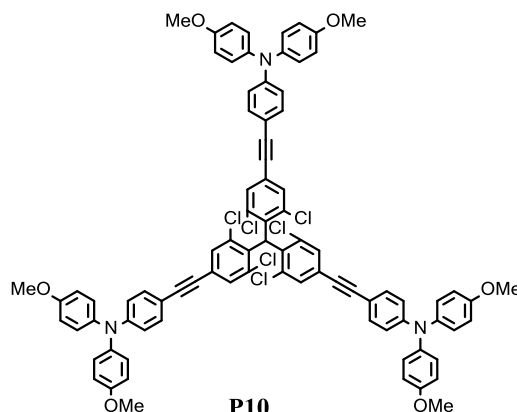
P7



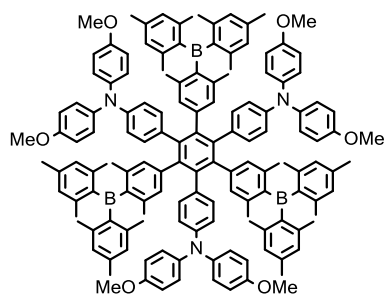
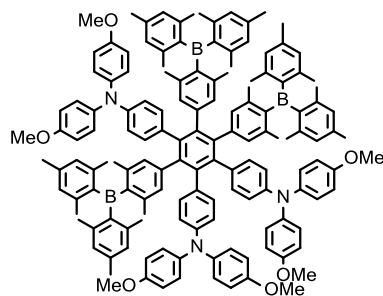
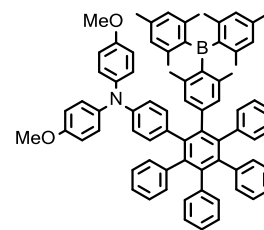
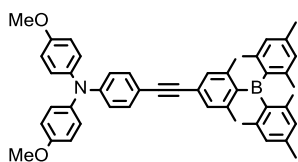
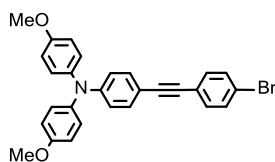
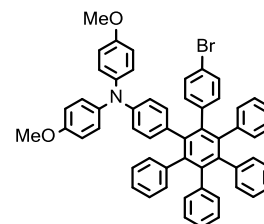
P8

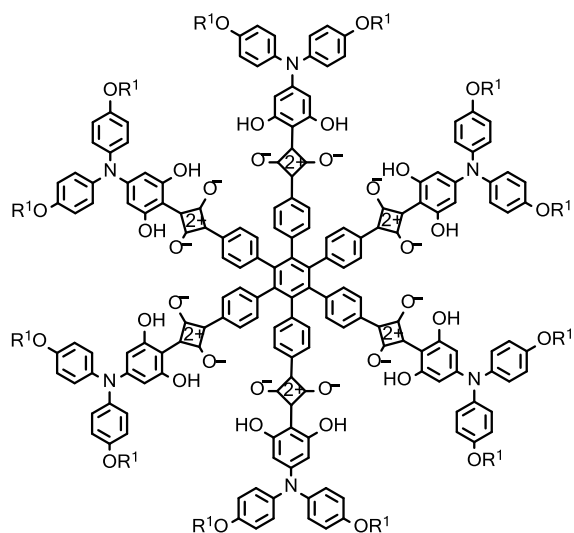


P9

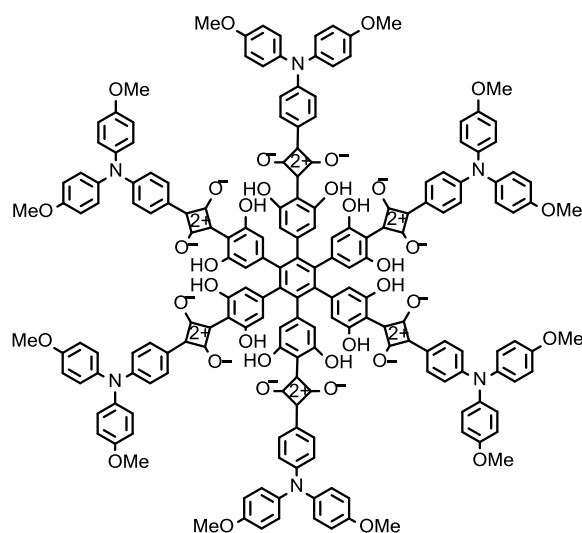
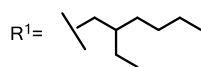


P10

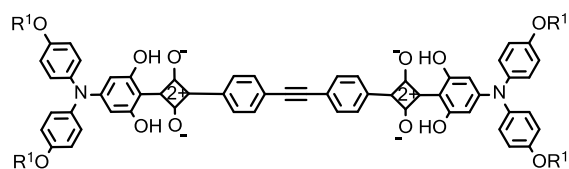
**B1****B2****B3****B4****B5****B6**



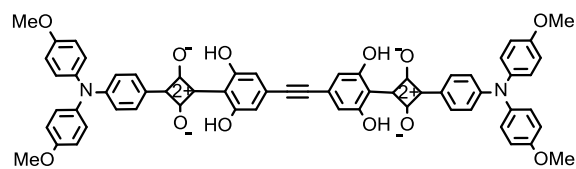
S1a



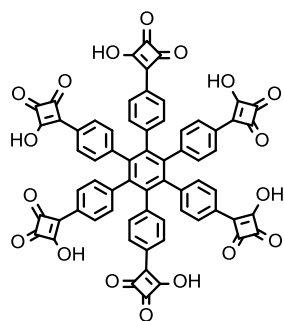
S1b



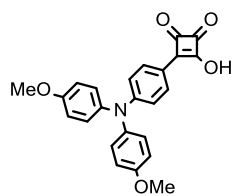
S2a



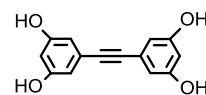
S2b



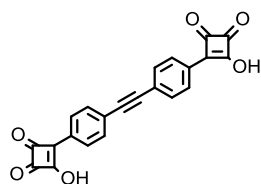
S3



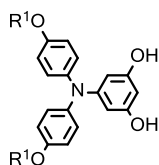
S4



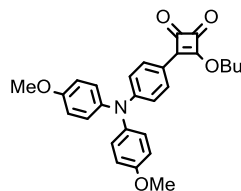
S5



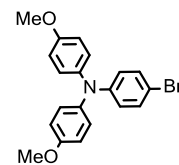
S6



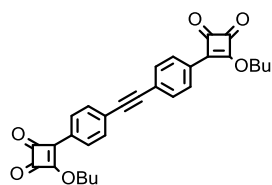
S7



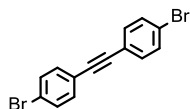
S8



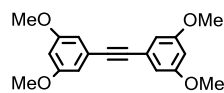
S9



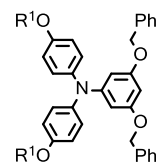
S10



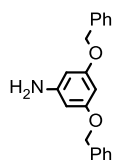
S11



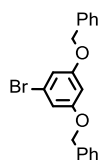
S12



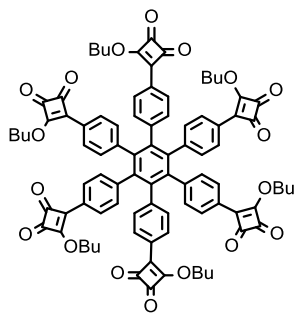
S13



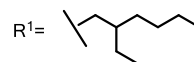
S14



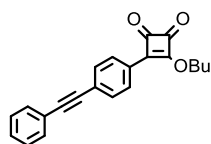
S15



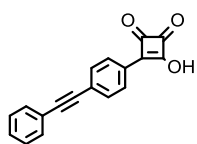
S16



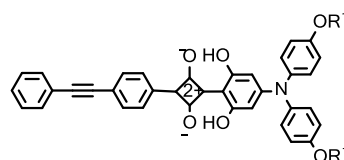
S17



S18



S19



S20

11. Zusammenfassung

Ziel dieser Arbeit war die Untersuchung des Energietransfers zwischen Ladungstransfer-Zuständen in multidimensional Donor-Akzeptor Systemen. Zu diesem Zweck wurden die Chromophore **HAB-S**, **HAB-A**, **B1** und **B2** synthetisiert. Diese bestehen jeweils aus drei Elektronen-Donoren und Elektronen-Akzeptoren, die über das Hexaarylbenzol-Gerüst symmetrisch oder asymmetrisch verknüpft sind. Triarylamine stellen dabei die Elektronen-Donoren dar, während Triarylborane in **B1** und **B2** und PCTM-Zentren in **HAB-S** und **HAB-A** die Aufgabe der Elektronen-Akzeptoren übernehmen. Die Hexaarylbenzole konnten durch Cobalt-katalysierte Cyclotrimerisierung der entsprechenden Tolan-Vorstufen hergestellt werden. Zusätzlich wurde das multidimensionale Chromophor **Star** synthetisiert. Dieses besteht aus einem zentralen PCTM, welches über Tolan-Brückeneinheiten sternförmig mit drei Triarylamin Zentren verknüpft ist. Das Hexaarylbenzol **S1a/b**, das mit sechs Squarain Chromophoren substituiert ist, konnte nicht realisiert werden. Möglicherweise werden die essentiellen Hydroxygruppen der Tolan-Vorstufe **S2a** nicht von dem Cyclotrimerisierungs-Katalysator $\text{Co}_2(\text{CO})_8$ toleriert. Der alternative Reaktionsweg, die Cyclotrimerisierung zuerst durchzuführen und anschließend die Hydroxygruppen einzuführen, schlug ebenfalls fehl. Grund dafür war, dass das Hexaarylbenzol, welches mit sechs Quadratsäure-Einheiten substituiert ist, nicht synthetisiert werden konnte. Nichtsdestotrotz konnten Energietransfer Wechselwirkungen in der Tolan-Vorstufe **S2a** untersucht werden. Dabei konnte die elektronische Kopplung zwischen den zwei Squarain-Zentren charakterisiert werden. Zu allen multidimensionalen Verbindungen wurden zusätzlich Modelverbindungen mit nur einem einzelnen Donor-Akzeptor-Paar hergestellt (**B3**, **Star-Model** und **HAB-Model**). Dadurch konnten die Energie- und Ladungstransferprozesse getrennt betrachten werden. Es soll noch angemerkt werden, dass in allen genannten multidimensionalen Verbindungen der Energietransfer „über Bindungen“ zwischen zwei benachbarten IV-CT Zuständen identisch ist mit dem Transfer eines einzelnen Elektrons zwischen zwei gleichartigen Redoxzentren (z.B. $\text{TAA} \rightarrow \text{TAA}^+$). Diese Situation ist immer dann zu beobachten, wenn sich die zwei IV-CT Zustände, zwischen denen Energie übertragen wird, ein Redox-Zentrum teilen.

Alle Verbindungen, die PCTM Zentren beinhalten, wurden durch Elektronenspinrezonanz Experimente charakterisiert. Dabei wurde eine schwache Wechselwirkung zwischen den drei PCTM Einheiten in **HAB-S** und **HAB-A** beobachtet. Durch die Oxidation von **Star-Model** konnten zudem stark wechselwirkende Singlett- bzw. Triplettzustände erhalten werden. Dagegen wurden für **HAB-Model**⁺ Signale beobachtet, die einem schwach wechselwirkendem Biradikal entsprechen. Das lässt darauf hindeuten, dass die Tolan-Brückeneinheit eine starke Kopplung zwischen den Redox-Zentren gewährleistet, während die Verknüpfung über das Hexaarylbenzol-Gerüst eine schwache Kopplung zur Folge hat. Dieser Trend wurde durch UV/Vis/NIR Absorptionmessungen gestützt. Durch die Analyse der beobachteten IV-CT Absorptionsbanden mittels Elektronentransfer-Theorie konnte eine

schwache Kopplung von $V = 340 \text{ cm}^{-1}$ in **HAB-Model** und eine deutlich stärkere Kopplung von $V = 1190\text{-}2900 \text{ cm}^{-1}$ in **Star-Model** ermittelt werden. In spektroelektrochemischen Untersuchungen wurde in den oxidierten Verbindungen **HAB-S⁺**, **Star⁺** und **Star-Model⁺**, im Vergleich zu den neutralen Verbindungen, der Ladungstransfer in entgegengesetzter Richtung beobachtet. D.h. vom PCTM-Radikal zum elektronenärmeren, kationischen TAA-Zentrum. Die zeitliche Entwicklung der angeregten Zustände wurde mit transienter Absorptionsspektroskopie verfolgt. Innerhalb der ersten Pikosekunden konnte eine Stabilisierung des Ladungstransferzustands, verursacht durch Umorientierungen des Lösungsmittels, beobachtet werden. Anisotrope, transiente Absorptionsmessungen konnten zeigen, dass innerhalb der Lebenszeit des angeregten Zustands ($\tau = 1\text{-}4 \text{ ps}$) kein Energietransfer in den HABs stattfindet, während in dem sternförmigen System eine ultraschnelle und möglicherweise kohärente Energieumverteilung beobachtet wurde. Letztendlich konnte klargelegt werden, dass Energietransfer und Ladungstransfer in diesen speziellen Systemen identisch sind. Jedoch konnte weder die Energie-, noch die Ladungstransfertheorie den sehr schnellen Energietransfer in **Star** erklären.

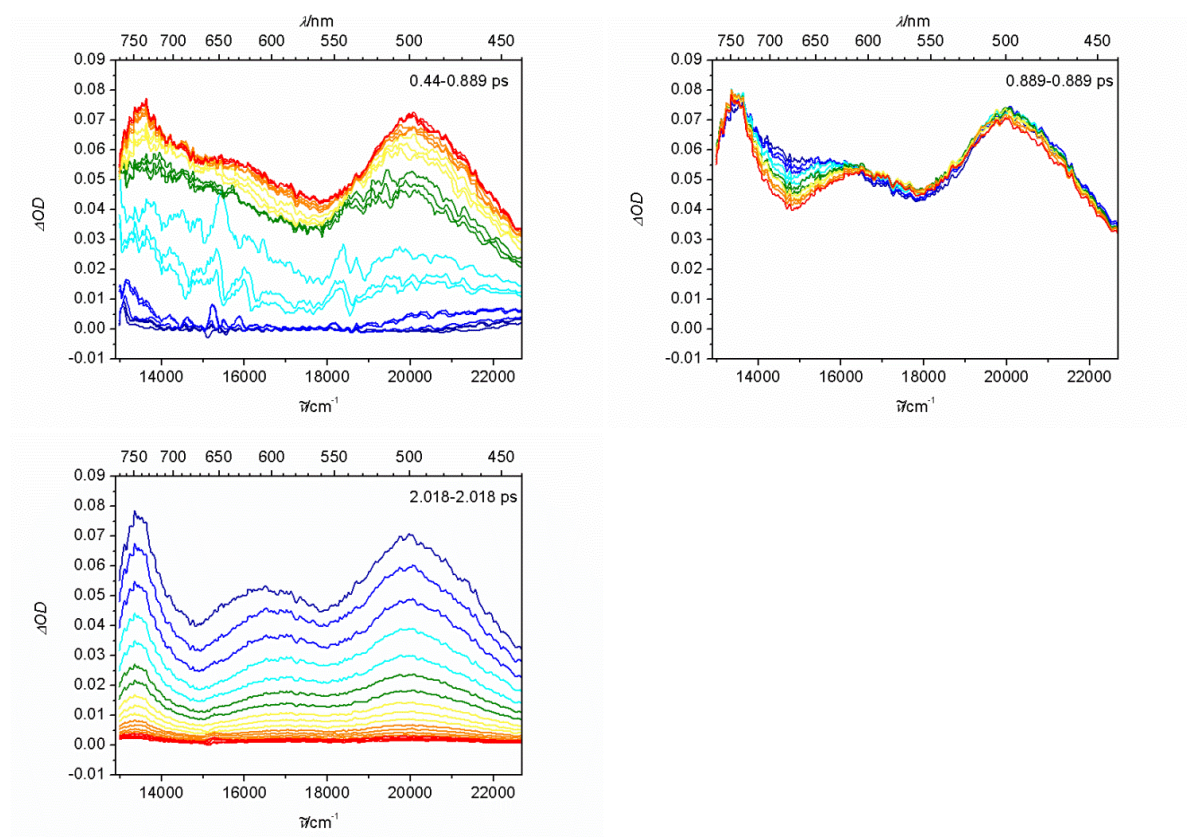
Die elektrochemischen und photophysikalischen Eigenschaften von **B1** und **B2** wurden mittels Cyclovoltammetrie, Absorptions- und Fluoreszenzmessungen untersucht und mit **B3** verglichen. Im Fall vom asymmetrischen **B2** zeigten CV Messungen drei Oxidations- und drei Reduktionspeaks, wobei der Abstand zwischen den Peaks stark vom Leitsalz abhing. Dies lässt sich auf Ionenpaar und Abschirmungseffekte zurückführen. Folglich konnten die Abstände zwischen den Peaks nicht in Bezug auf elektronische Kopplungen in den erzeugten, gemischtvalenten Verbindungen interpretiert werden. Transiente Absorption, Fluoreszenz Solvatochromie sowie Absorptionsspektren zeigten, dass nach optischer Anregung Ladungstransferzustände vom Amin- zum Borzentrum bevölkert werden. Die elektronische Donor-Akzeptor Wechselwirkung war jedoch schwach, da der Ladungstransfer hauptsächlich über den Raum stattfindet. Die elektronische Kopplung konnte nicht quantifiziert werden, weil die CT Absorptionsbande von $\pi\text{-}\pi^*$ Übergängen, die an den Amin- und Borzentren lokalisiert sind, überlagert war. Der Trend ist jedoch in guter Übereinstimmung mit der schwachen Kopplung, die für **HAB-Model** gemessen wurde. Sowohl transiente Absorptions- wie auch Fluoreszenz-Aufkonversionsmessungen deuten auf eine ultraschnelle Stabilisierung des Ladungstransferzustandes in **B1 - B3**, ähnlich dem Verhalten von **HAB-S** und **Star**, hin. Des Weiteren kann die Anregungsenergie der lokalisierten, angeregten Ladungstransferzustände innerhalb der Fluoreszenzlebensdauer (ca. 60 ns) zwischen den Arylsubstituenten dieser multidimensionalen Chromophore umverteilt werden. Dies wurde mit stationären Fluoreszenz-Anisotropiemessungen bewiesen, die weiterhin einen Symmetriebruch im vermeintlich symmetrischen HAB andeuten. Anisotrope Fluoreszenz-Aufkonversionsmessungen bestätigten diese Schlussfolgerung und zeigten eine Zeitkonstante von $\tau_{\text{EN}} = 2\text{-}3 \text{ ps}$ für den Energietransfer in **B1** und **B2**. Es soll darauf hingewiesen werden, dass obwohl die geometrischen Strukturen von **B1** und **HAB-S** beide auf dem gleichen Grundgerüst basieren und weiterhin benachbarte CT Zustände in beiden Fällen ähnliche Coulomb

Kopplungen und vernachlässigbare Kopplungen „über Bindungen“ aufweisen, in **B1** ein sehr schneller Energietransfer beobachtet werden konnte, während in **HAB-S** die Anregungsenergie innerhalb der Fluoreszenzlebenszeit nicht umverteilt wird. Um dies zu erklären, muss berücksichtigt werden, dass Energietransfer und die Relaxation des CT Zustands konkurrierende Prozesse darstellen. Letzteres wird zudem von der Viskosität des Lösungsmittels beeinflusst. Demnach wird angenommen, dass der Unterschied im Ladungstransferverhalten auf die Verwendung von unterschiedlich viskosen Lösungsmitteln zurückzuführen ist. Wenn Fluorid-Ionen zugesetzt wurden, verloren die Borzentren auf Grund von Komplexbildung die Akzeptoreigenschaften. Folglich ging der Ladungstransfercharakter in den Donor-Akzeptor-Verbindungen verloren, was mittels Absorptions- und Fluoreszenzspektroskopie verfolgt wurde. Die Fluorid-Sensor-Eigenschaften der Borzentren war jedoch stark vom Feuchtigkeitsgehalt des Lösungsmittels beeinflusst. Dies ist wahrscheinlich auf starke Wasserstoffbindungen zwischen Wasser Molekülen und Fluorid-Ionen zurückzuführen.

UV/Vis/NIR Absorptionsmessungen von **S2a** zeigten im Vergleich zur Modelverbindung **S20** eine Rotverschiebung der charakteristischen Squarain Bande um 1800 cm^{-1} . Anhand der Excitonen-Theorie konnte eine Coulomb Kopplung von $V_{\text{EN}}^{\text{Coul}} = 410\text{ cm}^{-1}$ berechnet werden, die jedoch diese starke Verschiebung nicht erklären kann. Demnach müssen Wechselwirkungen „durch Bindungen“ mit zu dieser guten Kommunikation zwischen den beiden Squarain Chromophoren in **S2a** beitragen. Diese Annahme stimmt mit der starken Ladungstransfer Kopplung überein, die für die Tolan-Brücke in **Star-Model** berechnet wurde.

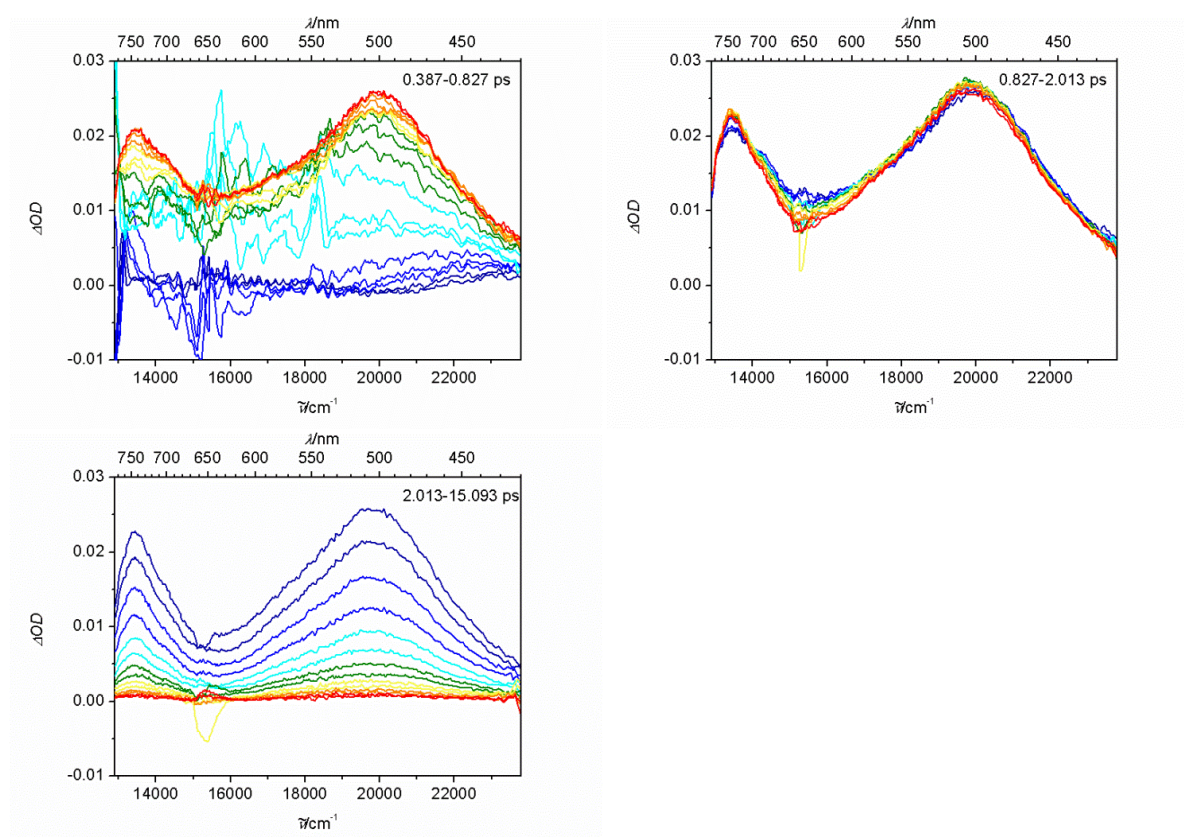
12. Appendix 1*

Transient absorption raw data for HAB-S, HAB-A, HAB-Model, Star and Star-Model

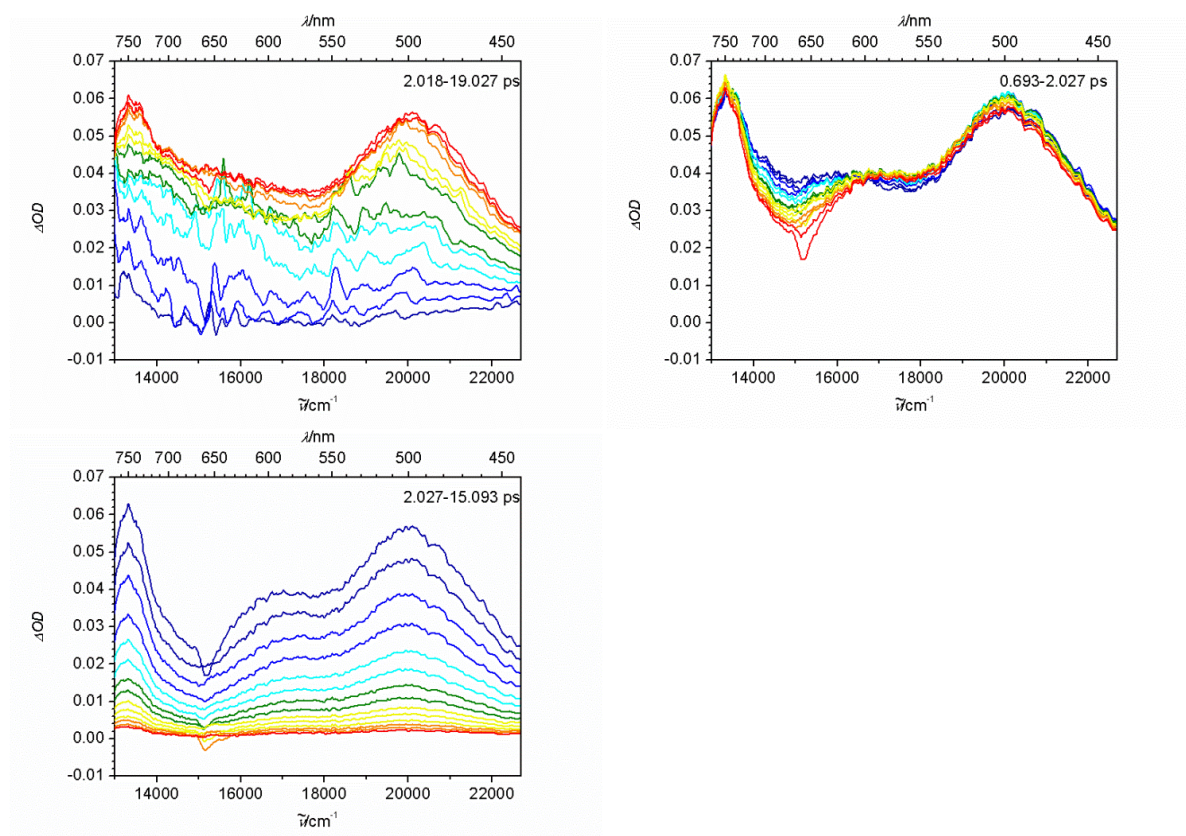


Raw data of the fs-transient absorption corrected for chirp and scattered light of **HAB-Model** in DCM excited at 15200 cm^{-1} . The spectra are coloured from blue to red.

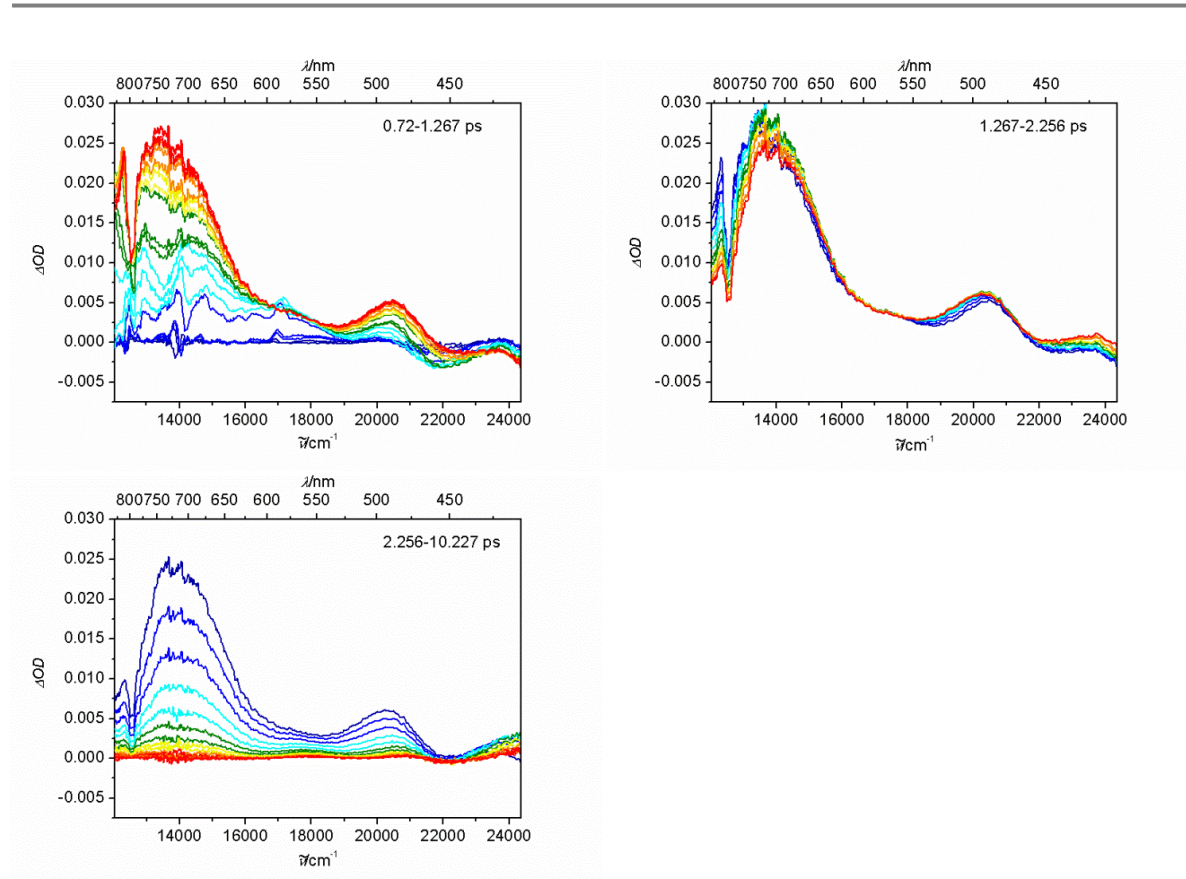
*Parts of this section have already been published in M. Steeger, S. Griesbeck, A. Schmiedel, M. Holzapfel, I. Krummenacher, C. Lambert and H. Braunschweig, *Phys. Chem. Chem. Phys.*, **2015**, submitted.



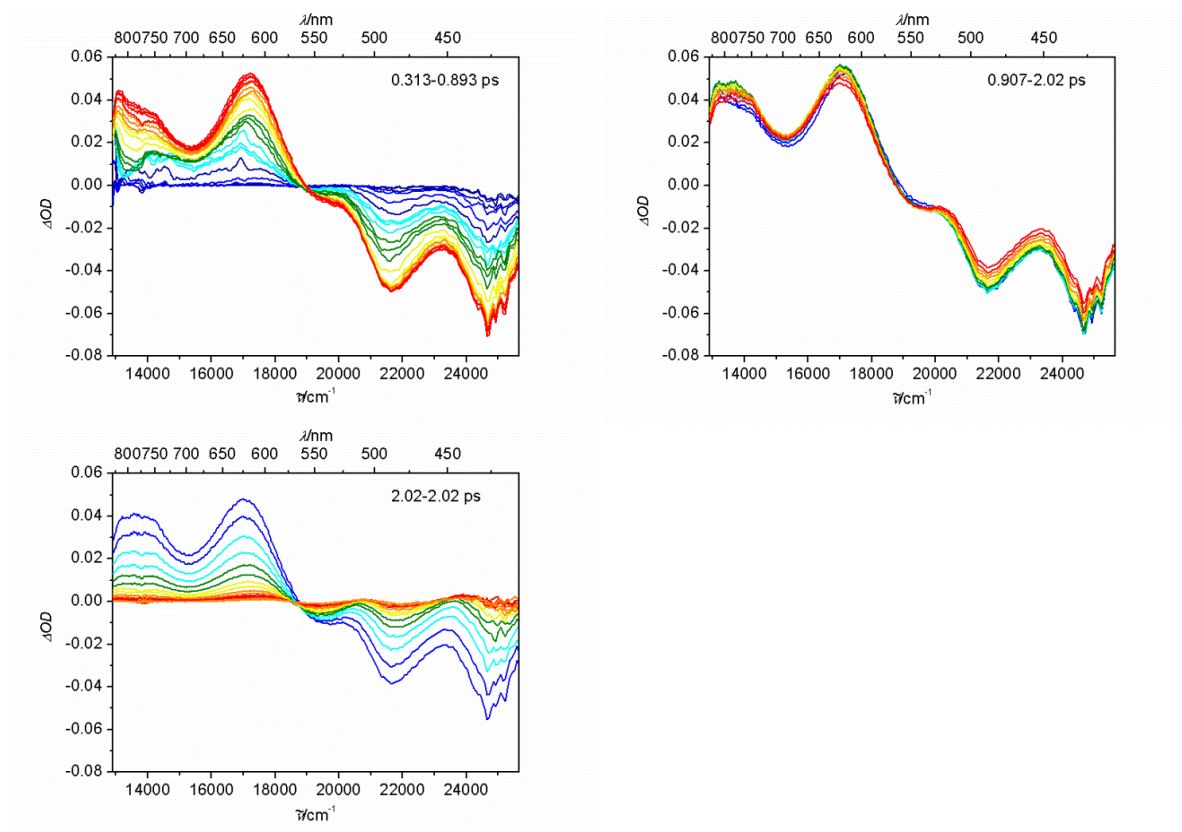
Raw data of the fs-transient absorption corrected for chirp and scattered light of **HAB-A** in DCM excited at 15200 cm^{-1} . The spectra are coloured from blue to red.



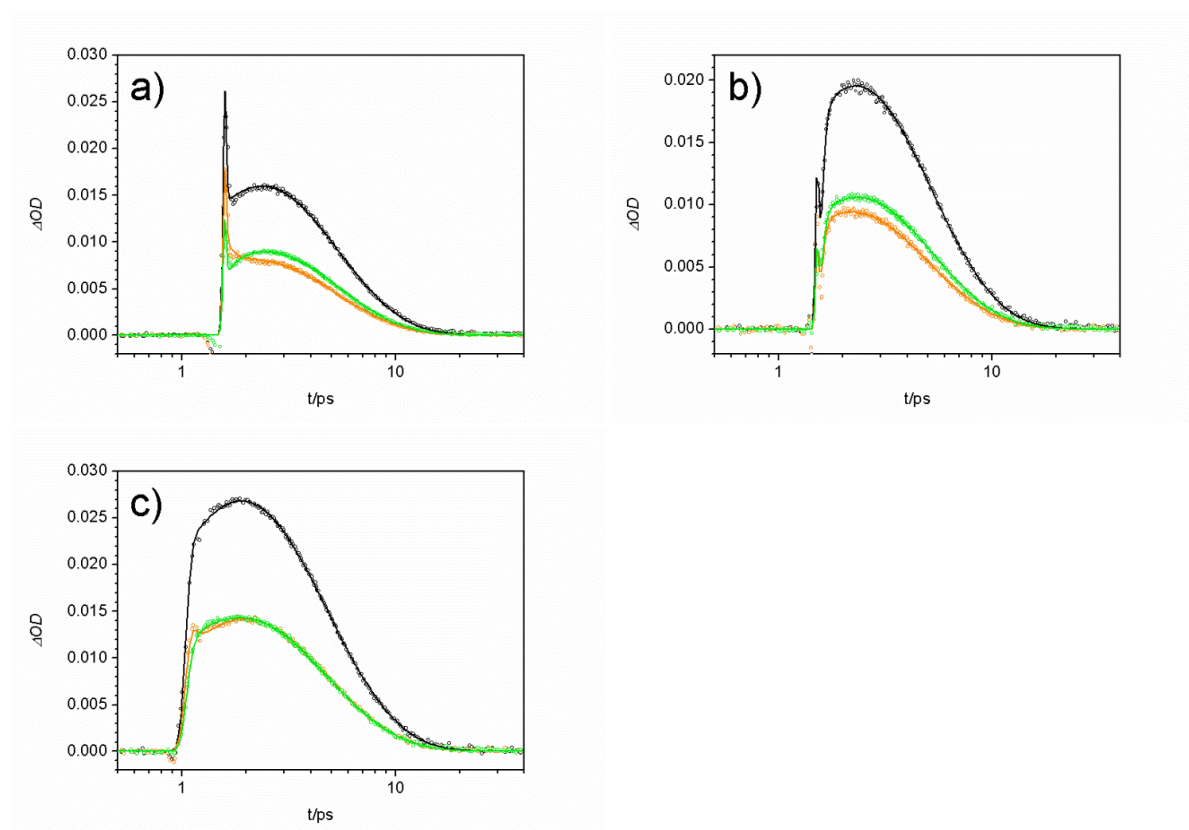
Raw data of the fs-transient absorption corrected for chirp and scattered light of **HAB-S** in DCM excited at 15200 cm^{-1} . The spectra are coloured from blue to red.



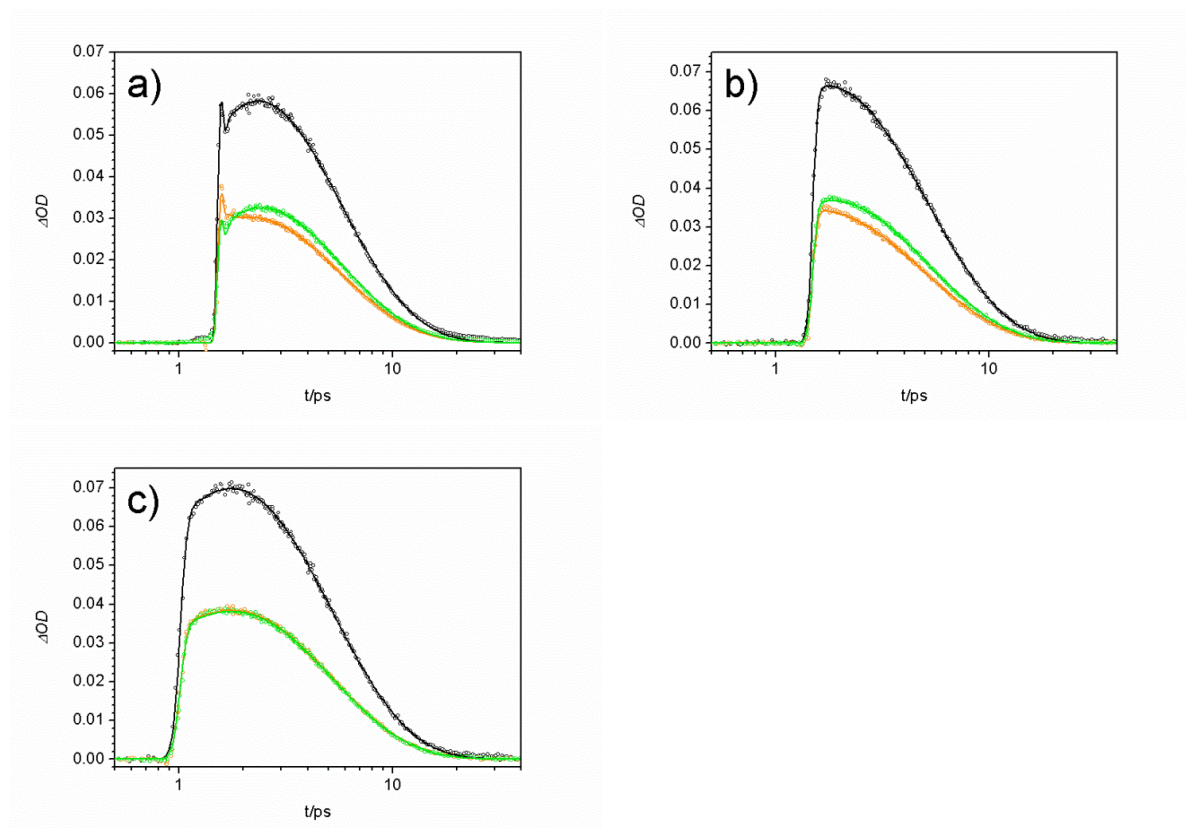
Raw data of the fs-transient absorption corrected for chirp and scattered light of **Star-Model** in DCM excited at 13800 cm⁻¹. The spectra are coloured from blue to red.



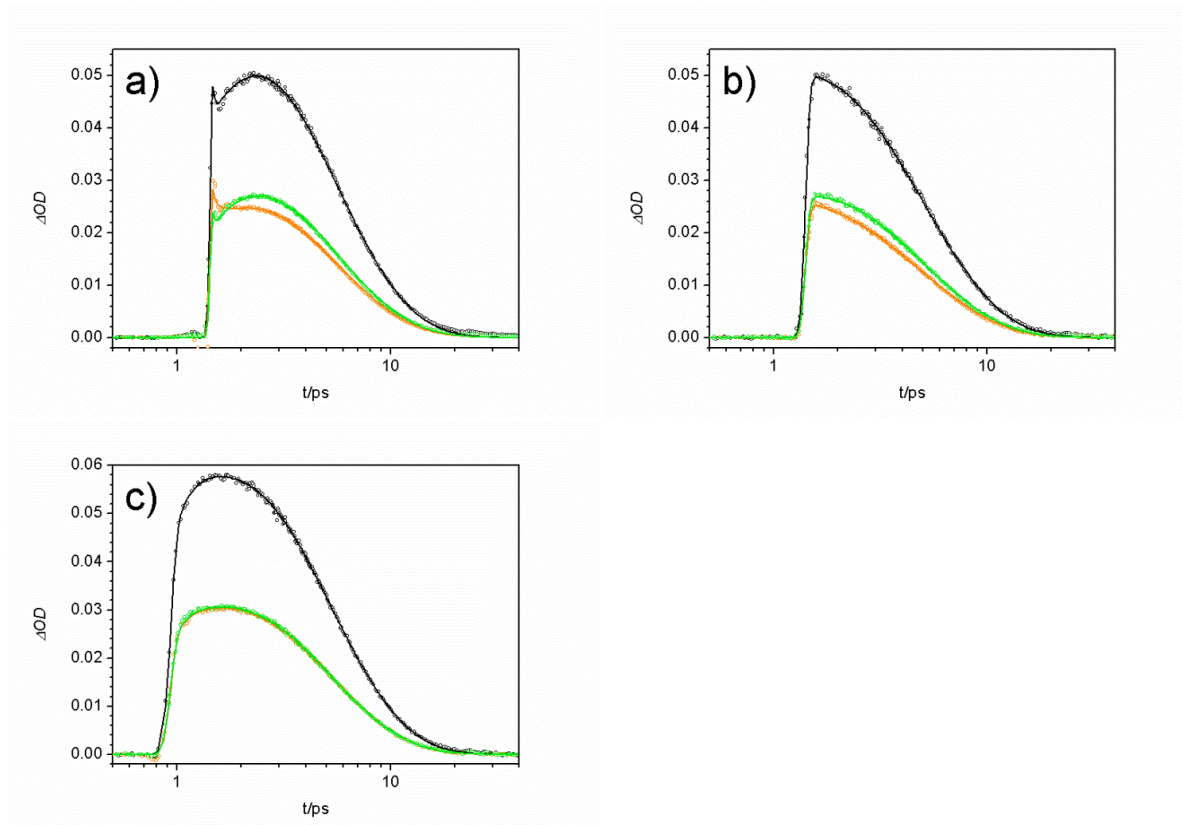
Raw data of the fs-transient absorption corrected for chirp and scattered light of **Star** in DCM excited at 13800 cm⁻¹. The spectra are coloured from blue to red.

Transient absorption anisotropy measurements

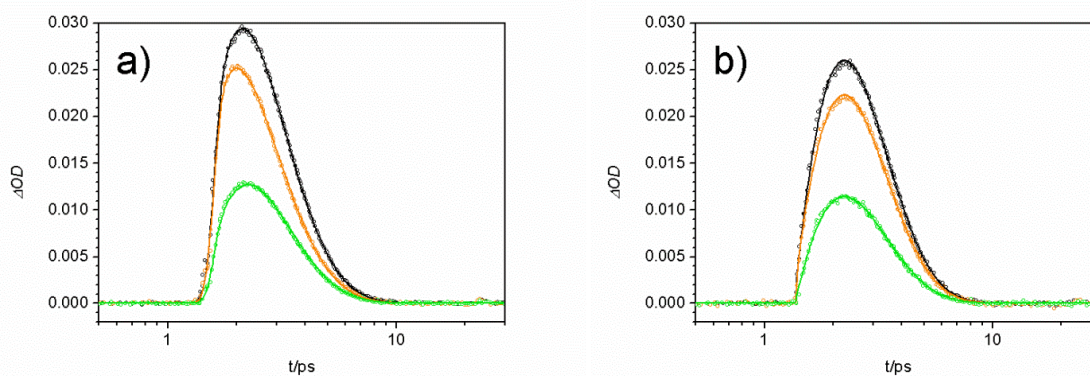
The transient absorption traces (circles) I_{mag} (black), I_{II} (orange) and I_{\perp} (green) of **HAB-Model** pumped at 15200 cm^{-1} and probed at 13000 cm^{-1} (a), 13900 cm^{-1} (b) and 19600 cm^{-1} (c) in DCM and the respective fits (lines) performed with a self written procedure based on MatLab (S36). All fit parameters are summarised below.



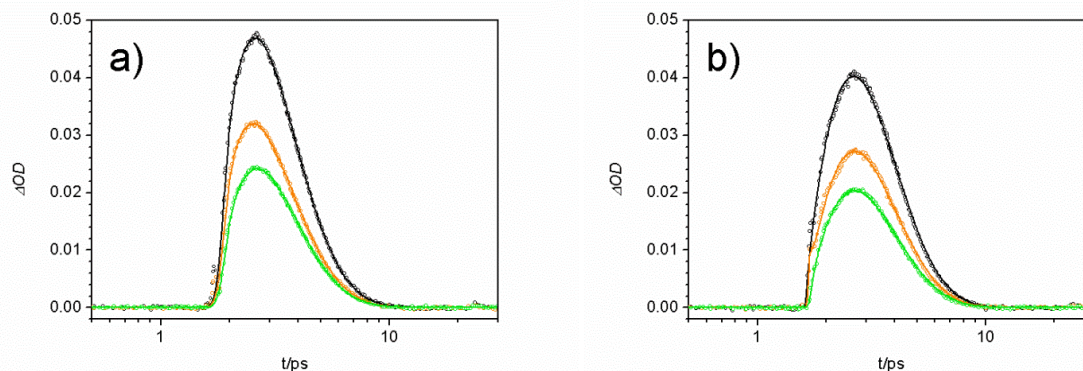
The transient absorption traces (circles) I_{mag} (black), I_{II} (orange) and I_{\perp} (green) of **HAB-A** pumped at 15200 cm^{-1} and probed at 13000 cm^{-1} (a), 13900 cm^{-1} (b) and 19600 cm^{-1} (c) in DCM and the respective fits (lines) performed with a self written procedure based on MatLab (S36). All fit parameters are summarised below.



The transient absorption traces (circles) I_{mag} (black), I_{II} (orange) and I_{\perp} (green) of **HAB-S** pumped at 15200 cm^{-1} and probed at 13000 cm^{-1} (a), 13900 cm^{-1} (b) and 19600 cm^{-1} (c) in DCM and the respective fits (lines) performed with a self written procedure based on MatLab (S36). All fit parameters are summarised below.



The transient absorption traces (circles) I_{mag} (black), I_{II} (orange) and I_{\perp} (green) of **Star-Model** pumped at 13800 cm^{-1} and probed at 13300 cm^{-1} (a) and 14300 cm^{-1} (b) in DCM and the respective fits (lines) performed with a self written procedure based on MatLab (S36). All fit parameters are summarised below.



The transient absorption traces (circles) I_{mag} (black), I_{\parallel} (orange) and I_{\perp} (green) of **Star** pumped at 13800 cm^{-1} and probed at 13300 cm^{-1} (a) and 14300 cm^{-1} (b) in DCM and the respective fits (lines) performed with a self written procedure based on MatLab (S36). All fit parameters are summarised below.

Isotropic amplitudes a and decay time constants τ of the global fits of the transient absorption traces I_{mag} , I_{\parallel} and I_{\perp} measured for the presented compounds at the given probe wavelength $\tilde{\nu}_{\text{probe}}$.

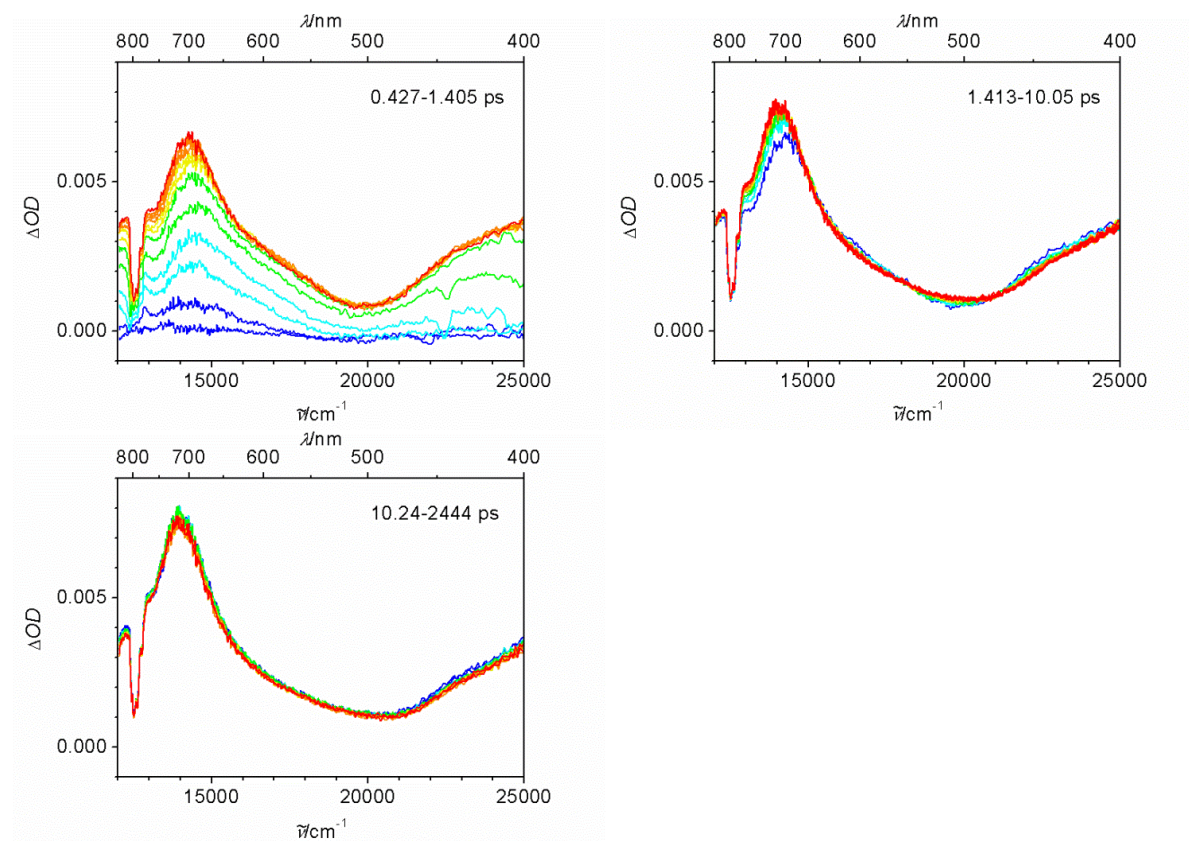
$\tilde{\nu}_{\text{probe}}$ / cm^{-1}		a_1	τ_1 /ps	a_2	τ_2 /ps	a_3	τ_3 /ps	a_4	τ_4 /ps	a_5	τ_5 /ps
13300	StarModel	-0.07	0.59	0.09	1.23						
	Star	-0.38	0.02	-0.15	0.69	0.17	1.33				
14300	StarModel	-3.00	0.88	3.00	0.90						
	Star	-4.19	1.03	4.12	1.06						
13000	HAB-Model	-0.17	0.01	240	0.01	-35.4	0.01	-0.02	1.12	0.03	3.27
	HAB-A	-0.17	0.01	240	0.02	-35.4	0.02	-0.04	0.98	0.09	4.21
	HAB-S	-0.17	0.01	240	0.01	-35.4	0.01	-0.04	1.01	0.08	4.08
13900	HAB-Model	2.45	0.04	-2.30	0.04	-0.02	1.02	0.04	3.28		
	HAB-A	0.01	0.01	-0.02	0.86	0.09	4.15				
	HAB-S	0.01	0.01	-0.01	1.01	0.06	4.00				
19600	HAB-Model	1.98	0.01	0.68	0.06	-0.03	0.91	0.05	3.34		
	HAB-A	0.02	0.02	-0.05	0.93	0.11	4.07				
	HAB-S	-0.02	0.16	0.5	0.76	-0.50	0.79	0.09	3.93		

S35. Anisotropic amplitudes a and decay time constants τ of the global fits of the transient absorption traces I_{mag} , I_{II} and I_{\perp} measured for the presented compounds at the given probe wavelength $\tilde{\nu}_{\text{probe}}$.

$\tilde{\nu}_{\text{probe}}$ /cm ⁻¹		a_1	τ_1 /ps	a_2	τ_2 /ps	a_3	τ_3 /ps
13300	StarModel	0.22	0.97	0.12	100		
	Star	0.07	0.97	0.06	100		
14300	StarModel	0.16	0.12	0.24	100		
	Star	0.88	0.05	0.10	100		
13000	HAB-Model	0.26	0.13	0.06	0.90	-0.06	140
	HAB-A	0.22	0.10	0.04	0.91	-0.04	139
	HAB-S	0.12	0.18	0.03	1.04	-0.04	139
13900	HAB-Model	0.04	1.15	-0.06	101		
	HAB-A	0.04	1.38	-0.06	49.3		
	HAB-S	0.03	1.28	-0.05	49.3		
19600	HAB-Model	-0.04	0.39	0.001	100		
	HAB-A	0.002	100				
	HAB-S	-0.002	100				

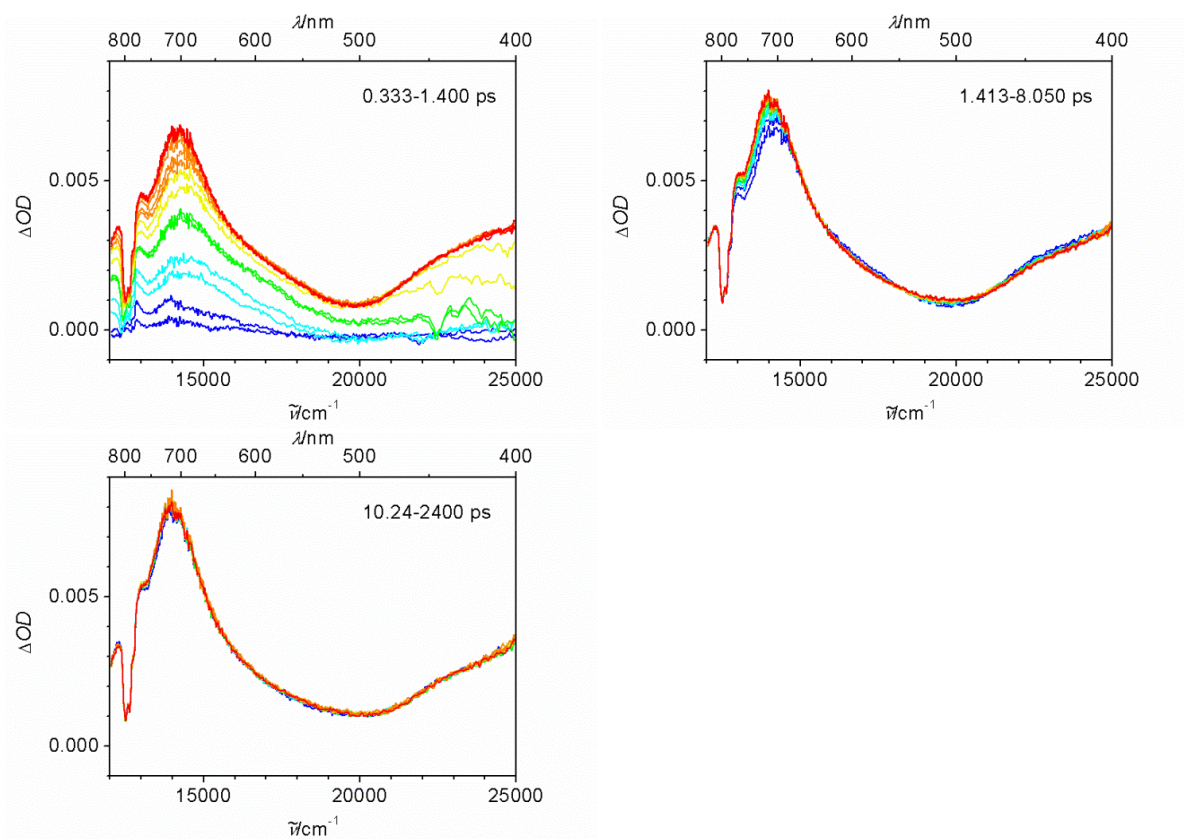
13. Appendix 2*

Transient absorption raw data for B1, B2 and B3

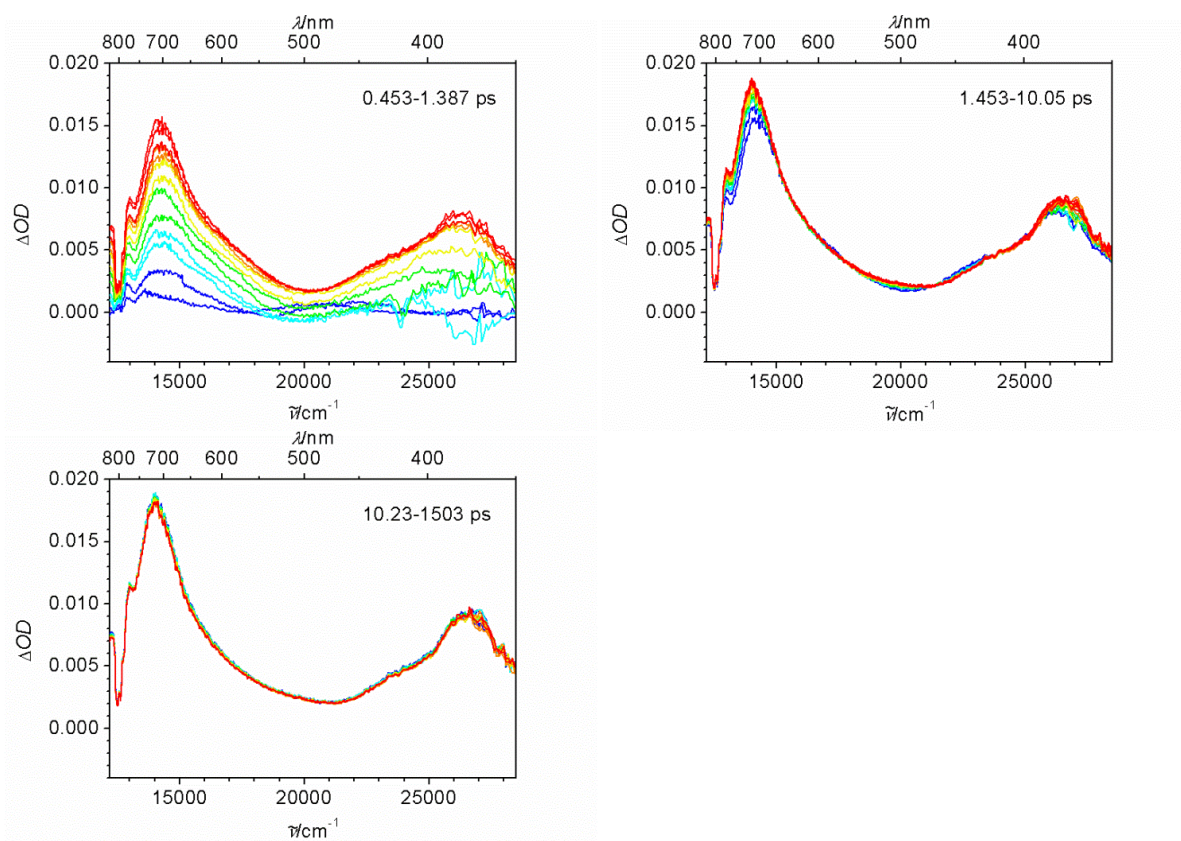


Raw data of the fs-transient absorption corrected for chirp and scattered light of **B1** in DCM excited at 24700 cm^{-1} . The spectra are coloured from blue to red.

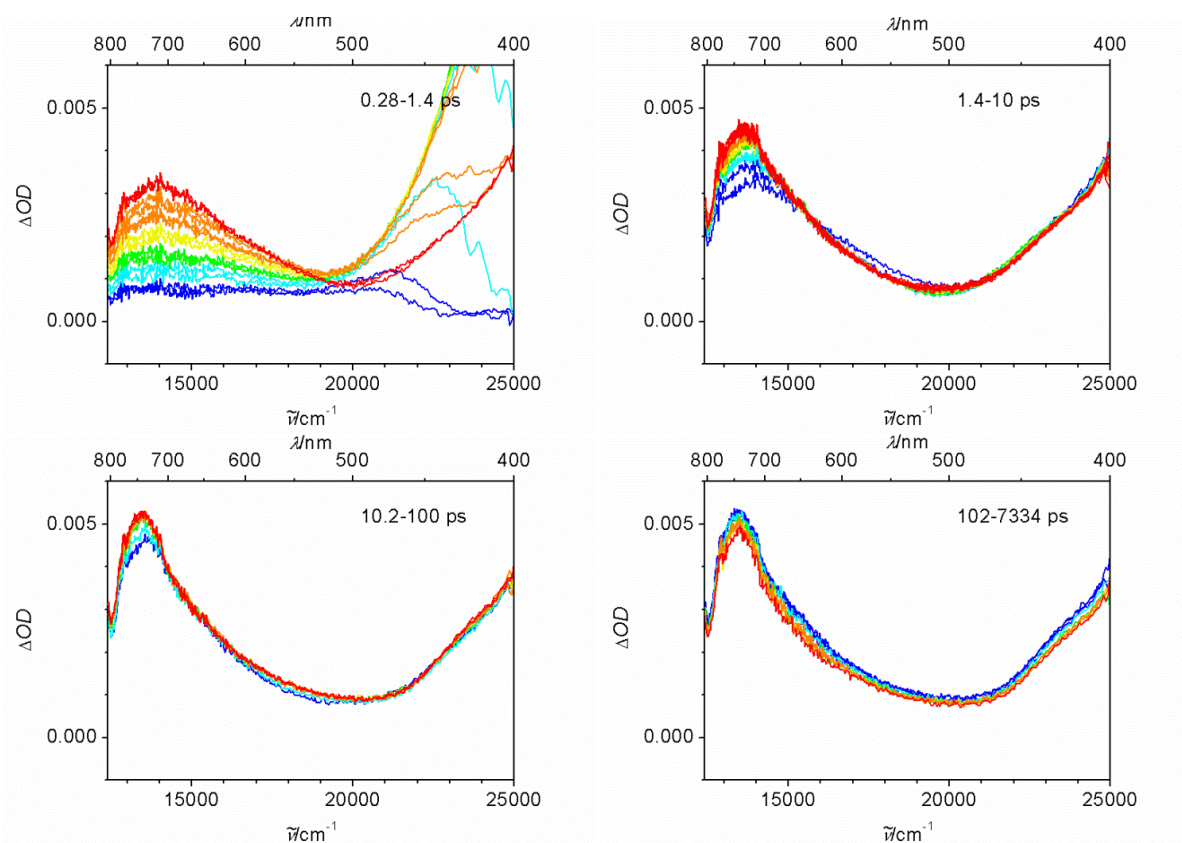
*Parts of this section have already been published in M. Steeger and C. Lambert, *Chem. Eur. J.*, **2012**, *18*, 11937-11948.



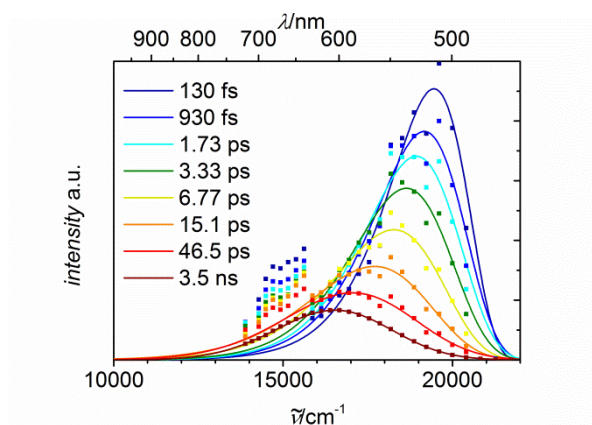
Raw data of the fs-transient absorption corrected for chirp and scattered light of **B2** in DCM excited at 24700 cm^{-1} . The spectra are coloured from blue to red.



Raw data of the fs-transient absorption corrected for chirp and scattered light of **B3** in DCM excited at 26700 cm^{-1} . The spectra are coloured from blue to red.



Raw data of the fs-transient absorption corrected for chirp and scattered light of **B3** in PhCN excited at 26700 cm^{-1} . The spectra are coloured from blue to red.



Log-normal functions (lines) fitted to the fluorescence upconversion map (squares) of **B3** in PhCN at various delay times (colour given in the legend).

14. Appendix 3*

MATLAB script used for the global analysis of the transient absorption traces I_{mag} , I_{II} and I_{\perp} .

```
function [x,resnorm,residual,exitflag,output] = FitA(n,b,xo,fucAx,fucAy)
options=optimset('Display','off','LargeScale','off','LevenbergMarquardt','on');
[x,resnorm,residual,exitflag,output] = lsqcurvefit(@nestedfun,xo,fucAx,fucAy,[],[],options);
function [Fo] = nestedfun(x,fucAx)

l(1) = find(fucAx(:,1)>0,1,'last');
l(2) = find(fucAx(:,2)>0,1,'last');
l(3) = find(fucAx(:,3)>0,1,'last');

fucMAx=fucAx(1:l(1),1);
fucPx=fucAx(1:l(2),2);
fucSx=fucAx(1:l(3),3);

F{1,1}=zeros(max(l),3);

m=1;
while m <= n;
    IMA{m}=x(1,2*m+1)/2.*exp(-(fucMAx-x(1,1))/x(1,2*m+2)).*exp(-
x(1,2).^2./(2.*x(1,2*m+2)^2)).*(1+erf((fucMAx-x(1,1)-x(1,2).^2/(x(1,2*m+2)))/((2^0.5).*x(1,2))));
    %#ok<AGROW>
    IP{m}=x(1,2*m+1)/2.*exp(-(fucPx-x(2,1))/x(1,2*m+2)).*exp(-
x(2,2).^2./(2.*x(1,2*m+2)^2)).*(1+erf((fucPx-x(2,1)-x(2,2).^2/(x(1,2*m+2)))/((2^0.5).*x(2,2))));
    %#ok<AGROW>
    IS{m}=x(1,2*m+1)/2.*exp(-(fucSx-x(3,1))/x(1,2*m+2)).*exp(-
x(3,2).^2./(2.*x(1,2*m+2)^2)).*(1+erf((fucSx-x(3,1)-x(3,2).^2/(x(1,2*m+2)))/((2^0.5).*x(3,2))));
    %#ok<AGROW>

    F{1,1}(1:l(1),1)=F{1,1}(1:l(1),1)+IMA{1,m}(:,1);
    F{1,1}(1:l(2),2)=F{1,1}(1:l(2),2)+IP{1,m}(:,1);
    F{1,1}(1:l(3),3)=F{1,1}(1:l(3),3)+IS{1,m}(:,1);

a=1;
while a <= b;

    AP{a+b*(m-1)}=x(1,2*m+1)*x(1,2*n+1+2*a)/2.*exp(-(fucPx-
x(2,1))/(x(1,2*m+2)*x(1,2*n+2+2*a)/(x(1,2*m+2)+x(1,2*n+2+2*a)))).*exp(-
x(2,2).^2./(2.*(x(1,2*m+2)*x(1,2*n+2+2*a)/(x(1,2*m+2)+x(1,2*n+2+2*a)))^2)).*(1+erf((fucPx-
x(2,1)-x(2,2).^2/((x(1,2*m+2)*x(1,2*n+2+2*a)/(x(1,2*m+2)+x(1,2*n+2+2*a)))/((2^0.5).*x(2,2))));
    %#ok<AGROW>
    AS{a+b*(m-1)}=x(1,2*m+1)*x(1,2*n+1+2*a)/2.*exp(-(fucSx-
x(3,1))/(x(1,2*m+2)*x(1,2*n+2+2*a)/(x(1,2*m+2)+x(1,2*n+2+2*a)))).*exp(-
x(3,2).^2./(2.*(x(1,2*m+2)*x(1,2*n+2+2*a)/(x(1,2*m+2)+x(1,2*n+2+2*a)))^2)).*(1+erf((fucSx-
x(3,1)-x(3,2).^2/((x(1,2*m+2)*x(1,2*n+2+2*a)/(x(1,2*m+2)+x(1,2*n+2+2*a)))/((2^0.5).*x(3,2))));
    %#ok<AGROW>
```

*Parts of this section have already been published in M. Steeger, S. Griesbeck, A. Schmiedel, M. Holzapfel, I. Krummenacher, C. Lambert and H. Braunschweig, *Phys. Chem. Chem. Phys.*, **2015**, submitted.

```

F{1,1}(1:l(2),2)=F{1,1}(1:l(2),2)+2*AP{1,a+b*(m-1)}(:,1);
F{1,1}(1:l(3),3)=F{1,1}(1:l(3),3)-AS{1,a+b*(m-1)}(:,1);

a=a+1;
    end
m=m+1;
    end

Fo=cell2mat(F);
Fo(:,2)=Fo(:,2).*x(2,2*n+3+2*b);
Fo(:,3)=Fo(:,3).*x(3,2*n+3+2*b);

P(:,1)=Fo(:,2);
S(:,1)=Fo(:,3);

    End

%calculation of the anisotropy

    u = round((x(2,1)-x(3,1))*1000);

fucPi(:,1)=(0:0.001:30);
fucSi(:,1)=(0:0.001:30);
fucAxi(:,1)=(0:0.001:30);
fucAxi(:,2)=(0:0.001:30);
fucAxi(:,3)=(0:0.001:30);

fucPi(:,2) = interp1(fucAx(1:l(2),2),fucAy(1:l(2),2),fucPi(:,1));
fucSi(:,2) = interp1(fucAx(1:l(3),3),fucAy(1:l(3),3),fucSi(:,1));

if u>=0
AniM=((fucPi(1+u:end,2)-fucSi(1:end-u,2))./(fucPi(1+u:end,2)+2*fucSi(1:end-u,2)));
else
AniM=((fucPi(1:end+u,2)-fucSi(1-u:end,2))./(fucPi(1:end+u,2)+2*fucSi(1-u:end,2)));
end

fucFi=nestedfun(x,fucAxi);

if u>=0
AniF=((fucFi(1+u:end,2)-fucFi(1:end-u,3))./(fucFi(1+u:end,2)+2*fucFi(1:end-u,3)));
else
AniF=((fucFi(1:end+u,2)-fucFi(1-u:end,3))./(fucFi(1:end+u,2)+2*fucFi(1-u:end,3)));
end

ii=isnan(AniF);
AniF(ii)=0;

%grafic Output

figure(1)
semilogx(fucAx(:,1),fucAy(:,1),'k',fucAx(:,2),fucAy(:,2),'b',fucAx(:,3),fucAy(:,3),'g',fucAx,nestedfu
n(x,fucAx),'-r')
title('Fit mit Exponentialfunktionen');
axis([0.5 10 0 0.03])

```

```

xlabel('t in ps');
ylabel('intensity a. u. ');
legend('MA','P','S');

figure(2)
if u>=0
semilogx(fucPi(1+u:end,1),AniM(:,1),'.b',fucAxi(1+u:end,1),AniF(:,1),'-r')
else
semilogx(fucPi(1:end+u,1),AniM(:,1),'.b',fucAxi(1:end+u,1),AniF(:,1),'-r')
end
axis([0.5 10 -0.25 0.45])
xlabel('t in ps');
ylabel('anisotropy');
legend('Messdaten', 'FIT')

%save the data as ASCII

if u>=0
SAniso(:,1)=fucPi(1+u:end,1);
SAniso(:,2)=AniM(:,1);
SAniso(:,3)=AniF(:,1);
else
SAniso(:,1)=fucPi(1:end+u,1);
SAniso(:,2)=AniM(:,1);
SAniso(:,3)=AniF(:,1);
end

TFit=nestedfun(x,fucAx);
SFit(:,1)=fucAx(:,1);
SFit(:,2)=fucAy(:,1);
SFit(:,3)=TFit(:,1);
SFit(:,4)=fucAx(:,2);
SFit(:,5)=fucAy(:,2);
SFit(:,6)=TFit(:,2);
SFit(:,7)=fucAx(:,3);
SFit(:,8)=fucAy(:,3);
SFit(:,9)=TFit(:,3);

dlmwrite('Fit.txt',SFit,')
dlmwrite('Anisotropie.txt',SAniso,')

dlmwrite('xo.txt',x,')
dlmwrite('fucAx.txt',fucAx,')
dlmwrite('fucAy.txt',fucAy,')

display(resnorm)
display(output)
display(u);

end

```


MATLAB script used for the global analysis of the fluorescence upconversion traces I_{Π} and I_{\perp}

```

function [x,resnorm,residual,exitflag,output] = FitA(n,b,xo,fucAx,fucAy)

options=optimset('Display','off','LargeScale','off','LevenbergMarquardt','on');
[x,resnorm,residual,exitflag,output] = lsqcurvefit(@nestedfun,xo,fucAx,fucAy,[],[],options);
    function [Fo] = nestedfun(x,fucAx)

l(1) = find(fucAx(:,1)>0,1,'last');
l(2) = find(fucAx(:,2)>0,1,'last');

fucPx=fucAx(1:l(1),1);
fucSx=fucAx(1:l(2),2);

F{1,1}=zeros(max(l),2);

m=1;
while m <= n;

    IP{m}=x(1,2*m+1)/2.*exp(-(fucPx-x(1,1))/x(1,2*m+2)).*exp(-
x(1,2).^2./(2.*x(1,2*m+2)^2)).*(1+erf((fucPx-x(1,1)-x(1,2).^2/(x(1,2*m+2)))/((2^0.5).*x(1,2))));
    %#ok<AGROW>
    IS{m}=x(1,2*m+1)/2.*exp(-(fucSx-x(2,1))/x(1,2*m+2)).*exp(-
x(2,2).^2./(2.*x(1,2*m+2)^2)).*(1+erf((fucSx-x(2,1)-x(2,2).^2/(x(1,2*m+2)))/((2^0.5).*x(2,2))));
    %#ok<AGROW>

    F{1,1}(1:l(1),1)=F{1,1}(1:l(1),1)+IP{1,m}(:,1);
    F{1,1}(1:l(2),2)=F{1,1}(1:l(2),2)+IS{1,m}(:,1);
    a=1;
    while a <= b;

        AP{a+b*(m-1)}=x(1,2*m+1)*x(1,2*n+1+2*a)/2.*exp(-(fucPx-
x(1,1))/(x(1,2*m+2)*x(1,2*n+2+2*a)/(x(1,2*m+2)+x(1,2*n+2+2*a)))).*exp(-
x(1,2).^2./(2.*(x(1,2*m+2)*x(1,2*n+2+2*a)/(x(1,2*m+2)+x(1,2*n+2+2*a)))^2)).*(1+erf((fucPx-
x(1,1)-x(1,2).^2/(x(1,2*m+2)*x(1,2*n+2+2*a)/(x(1,2*m+2)+x(1,2*n+2+2*a)))/((2^0.5).*x(1,2))));
        %#ok<AGROW>
        AS{a+b*(m-1)}=x(1,2*m+1)*x(1,2*n+1+2*a)/2.*exp(-(fucSx-
x(2,1))/(x(1,2*m+2)*x(1,2*n+2+2*a)/(x(1,2*m+2)+x(1,2*n+2+2*a)))).*exp(-
x(2,2).^2./(2.*(x(1,2*m+2)*x(1,2*n+2+2*a)/(x(1,2*m+2)+x(1,2*n+2+2*a)))^2)).*(1+erf((fucSx-
x(2,1)-x(2,2).^2/(x(1,2*m+2)*x(1,2*n+2+2*a)/(x(1,2*m+2)+x(1,2*n+2+2*a)))/((2^0.5).*x(2,2))));
        %#ok<AGROW>

        F{1,1}(1:l(1),1)=F{1,1}(1:l(1),1)+2*AP{1,a+b*(m-1)}(:,1);
        F{1,1}(1:l(2),2)=F{1,1}(1:l(2),2)-AS{1,a+b*(m-1)}(:,1);
        a=a+1;
    end
    m=m+1;
end

```

```

Fo=cell2mat(F);
Fo(:,2)=Fo(:,2).*x(2,2*n+3+2*b);

P(:,1)=Fo(:,1);
S(:,1)=Fo(:,2);

    end

fucAxi(:,1)=fucPx;
fucAxi(:,2)=fucPx;

fucFi=nestedfun(x,fucAxi);

AniF=((fucFi(:,1)-fucFi(:,2)/x(2,2*n+3+2*b))./(fucFi(:,1)+2*fucFi(:,2)/x(2,2*n+3+2*b)));

ii=isnan(AniF);
AniF(ii)=0;

figure(1)
semilogx(fucAx(:,1),fucAy(:,1),'k',fucAx(:,2),fucAy(:,2),'b',fucAx,nestedfun(x,fucAx),'-r')
title('Fit mit Exponentialfunktionen');
xlabel('t in ps');
ylabel('intensity a. u. ');
legend('P','S');

r(1,1)=length(fucAx(:,1));
r(1,2)=length(fucAx(:,2));

c=1;
for k=1:r(1,1);

for l=1:r(1,2) ;
    if fucAx(k,1)==fucAx(l,2);

        Zeile(c,1)=k;
        Zeile(c,2)=l;
        c=c+1;
        end
    end
end

for o=1:length(Zeile(:,1));
    fucAxt(o,1)=fucAx(Zeile(o,1),1);
    fucAxt(o,2)=fucAx(Zeile(o,2),2);
    fucAyt(o,1)=fucAy(Zeile(o,1),1);
    fucAyt(o,2)=fucAy(Zeile(o,2),2);
end

for o=1:length(Zeile(:,1));

```

```

aniso(o,1)=((fucAyt(o,1)-
fucAyt(o,2)./x(2,2*n+3+2*b))./(fucAyt(o,1)+2*fucAyt(o,2)./x(2,2*n+3+2*b)));
end

```

```

figure(2)
semilogx(fucAxt(:,1),aniso(:,1),'b',fucAxi(:,1),AniF(:,1),'-r')
axis([0.0 8000 -0.25 0.45])
xlabel('t in ps');
ylabel('anisotropy');
legend('Messdaten')

```

```

TFit=nestedfun(x,fucAx);
SFit(:,1)=fucAx(:,1);
SFit(:,2)=fucAy(:,1);
SFit(:,3)=TFit(:,1);
SFit(:,4)=fucAx(:,2);
SFit(:,5)=fucAy(:,2);
SFit(:,6)=TFit(:,2);

```

```

SANiso(1:length(Zeile(:,1)),1)=fucAxt(1:length(Zeile(:,1)),1);
SANiso(1:length(Zeile(:,1)),2)=aniso(1:length(Zeile(:,1)),1);
SANiso(1:l(1),3)=fucAxi(1:l(1),1);
SANiso(1:l(1),4)=AniF(1:l(1),1);

```

```

dlmwrite('Fit.txt',SFit,');
dlmwrite('Anisotropie.txt',SANiso,');

```

```

dlmwrite('xo.txt',x,');
dlmwrite('fucAx.txt',fucAx,');
dlmwrite('fucAy.txt',fucAy,');

```

```

display(resnorm)
display(output)

```

```

end

```

15. Appendix 4

Equation 81 for the time dependent anisotropy of **B2** is obtained in the following way. As **B2** is asymmetric (see Figure 125), four cases have to be treated corresponding to the excitation of the four CT states. In the following it is assumed that the energy transfer is only observed between adjacent CT states.

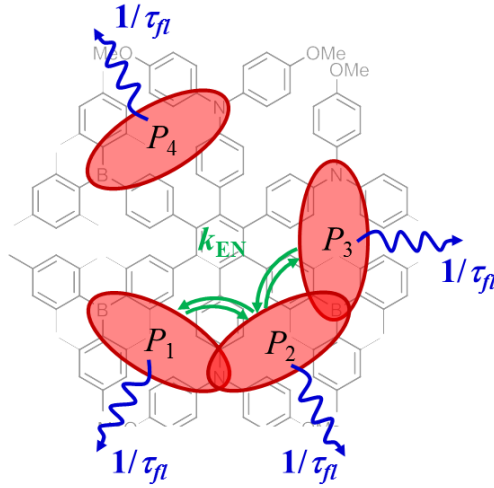


Figure 125 Energy transfer pathways in HAB **B2**.

(i) Excitation of CT state 1:

The following Pauli master differential equations can be set up for each CT state (equation 83).

$$\begin{aligned}\frac{\partial P_1(t)}{\partial t} &= -\left(\frac{1}{\tau_{fl}} + k_{EN}\right)P_1 + k_{EN}P_2 \\ \frac{\partial P_2(t)}{\partial t} &= -\left(\frac{1}{\tau_{fl}} + 2k_{EN}\right)P_2 + k_{EN}P_3 + k_{EN}P_1 \\ \frac{\partial P_3(t)}{\partial t} &= -\left(\frac{1}{\tau_{fl}} + k_{EN}\right)P_3 + k_{EN}P_2\end{aligned}\quad (83)$$

CT state 4 is not considered as it is not populated in this case. This system of equations can be solved to derive terms for each probability $P_i(t)$ (equation 84)

$$P_1(t) = \frac{P_1(0)}{6} e^{\frac{-t}{\tau_{fl}}} (2 + e^{-3tk_{EN}} + 3e^{-tk_{EN}})$$

$$P_2(t) = \frac{P_1(0)}{6} e^{\frac{-t}{\tau_{fl}}} (2 - 2e^{-3tk_{EN}})$$

$$P_3(t) = \frac{P_1(0)}{6} e^{\frac{-t}{\tau_{fl}}} (2 + e^{-3tk_{EN}} - 3e^{-tk_{EN}}) \quad (84)$$

The measured anisotropy $r(t)$ can then be obtained by summation of the anisotropy values of each CT state $r_i(t)$ ($i = 1 - 3$) weighted by the relative probability of each CT state being excited w_i (equation 59) and equation 85 is obtained.

$$r(t) = 0.1 + 0.225e^{-k_{EN}t} + 0.075e^{-3k_{EN}t} \quad (85)$$

(ii) Excitation of CT state 2:

In the same way as shown for (i) Pauli master differential equations can be set up for each CT state (equation 83).

$$\frac{\partial P_1(t)}{\partial t} = -\left(\frac{1}{\tau_{fl}} + k_{EN}\right)P_1 + k_{EN}P_2$$

$$\frac{\partial P_2(t)}{\partial t} = -\left(\frac{1}{\tau_{fl}} + 2k_{EN}\right)P_2 + k_{EN}P_3 + k_{EN}P_1$$

$$\frac{\partial P_3(t)}{\partial t} = -\left(\frac{1}{\tau_{fl}} + k_{EN}\right)P_3 + k_{EN}P_2 \quad (83)$$

CT state 4 is again not considered as it is not populated in this case. This system of equations can be solved to derive terms for each probability $P_i(t)$ (equation 86).

$$P_1(t) = \frac{P_2(0)}{6} e^{\frac{-t}{\tau_{fl}}} (2 - 2e^{-3tk_{EN}})$$

$$P_2(t) = \frac{P_2(0)}{6} e^{\frac{-t}{\tau_{fl}}} (2 + 4e^{-3tk_{EN}})$$

$$P_3(t) = \frac{P_2(0)}{6} e^{\frac{-t}{\tau_{fl}}} (2 - 2e^{-3tk_{EN}}) \quad (86)$$

The measured anisotropy $r(t)$ can then be obtained by summation of the anisotropy values of each CT state $r_i(t)$ ($i = 1 - 3$) weighted by the relative probability of each CT state being excited w_i (equation 59) and equation 87 is obtained.

$$r(t) = 0.1 + 0.3e^{-3k_{\text{EN}}t} \quad (87)$$

(iii) Excitation of CT state 3:

The same result as in (i) is obtained.

(iv) Excitation of CT state 4:

As there is no adjacent CT state, no energy transfer is possible and hence equation 88 is obtained.

$$r(t) = 0.4 \quad (88)$$

The overall anisotropy (equation 81) is calculated by averaging the cases (i)-(iv).

$$r(t) = \frac{2(0.1 + 0.225e^{-k_{\text{EN}}t} + 0.075e^{-3k_{\text{EN}}t}) + 0.1 + 0.3e^{-3k_{\text{EN}}t} + 0.4}{4} = 0.175 + 0.11e^{-k_{\text{EN}}t} + 0.115e^{-3k_{\text{EN}}t}$$

(81)

16. Appendix 5

Publications

On the relation of Energy Transfer Between IV-CT States and Electron Transfer Between Redox Centres in Multidimensional Chromophores Based on Polychlorinated Triphenylmethyl Radicals and Triarylamines, Steeger, M.; Griesbeck, S.; Schmiedel, A.; Holzapfel, M.; Krummenacher, I.; Lambert, C.; Braunschweig, H. *Phys. Chem. Chem. Phys.* **2015**, submitted.

Charge-Transfer Interactions in Tris-Donor-Tris-Acceptor Hexaarylbenzene Redox Chromophores, Steeger, M.; Lambert, C. *Chem. Eur. J.* **2012**, *18*, 11937-11948. DOI 10.1002/chem.201104020

Charge-Transfer Interactions in a Multichromophoric Hexaarylbenzene Containing Pyrene and Triarylamines, Lambert, C.; Ehbets, J.; Rausch, D.; Steeger, M. *J. Org. Chem.* **2012**, *77*, 6147-6154. DOI 10.1021/jo300924x

Mixed-valence interactions in triarylamine-gold-nanoparticle conjugates, Müller, C. I.; Lambert, C.; Steeger, M.; Forster, F.; Wiessner, M.; Schöll, A.; Reinert, F.; Kamp, M. *Chem. Commun.* **2009**, *41*, 6213-6215. DOI 10.1039/b909715e

Talks

ENERGY TRANSFER IN SUBSTITUTED HEXAARYLBENZENES, “GRK-1221 Tagung”, Zeilitzheim, Germany, **2010**.

ENERGY TRANSFER IN MULTIDIMENSIONAL CHROMOPHORS, „Tagung über Konjugierte Polymere und Oligomere“, Blaubeuren, Germany, **2009**.

Poster

PHOTOPHYSICAL PROPERTIES OF DONOR AND ACCEPTOR SUBSTITUTED HEXAARYLBENZENES, Steeger, M.; Lambert, C. “Gordon Research Conference on Electron Donor-Acceptor Interactions”, Newport/RI, United States of America, **2012**.

ELECTRON AND ENERGY TRANSFER IN DONOR AND ACCEPTOR SUBSTITUTED HEXAARYLBENZENES, Steeger, M.; Lambert, C. “Electronic Properties of π -conjugated Materials II”, Würzburg, Germany, **2011**.

CHARGE AND ENERGY TRANSFER IN DONOR AND ACCEPTOR SUBSTITUTED HEXAARYLBENZENES, Steeger, M.; Lambert, C. “22nd Lecture Conference of the GDCh-division of Photochemie”, Erlangen, Germany, **2010**.

ENERGY TRANSFER IN SUBSTITUTED HEXAARYLBENZENES, Steeger, M.; Lambert, C. “XXIII IUPAC Symposium on Photochemistry”, Ferrara, Italy, **2010**.

OPTICAL PROPERTIES OF DONOR- AND ACCEPTOR SUBSTITUTED HEXAARYLBENZENES, Steeger, M.; Lambert, C. “XXIV International Conference on Photochemistry”, Toledo, Spain, **2009**.

SYNTHESIS AND PHOTOCHEMISTRY OF ELECTRON DONOR- AND ACCEPTOR SUBSTITUTED HEXAARYLBENZENES, Steeger, M.; Lambert, C. “Electronic Processes in π -conjugated Materials”, Würzburg, Germany, **2008**.